



HAL
open science

Use of squeezed states of light for the reduction of quantum noise in Advanced Virgo

Marc Eisenmann

► **To cite this version:**

Marc Eisenmann. Use of squeezed states of light for the reduction of quantum noise in Advanced Virgo. Astrophysics [astro-ph]. Université Savoie Mont Blanc, 2020. English. NNT : 2020CHAMA032 . tel-03560691

HAL Id: tel-03560691

<https://theses.hal.science/tel-03560691>

Submitted on 7 Feb 2022

HAL is a multi-disciplinary open access archive for the deposit and dissemination of scientific research documents, whether they are published or not. The documents may come from teaching and research institutions in France or abroad, or from public or private research centers.

L'archive ouverte pluridisciplinaire **HAL**, est destinée au dépôt et à la diffusion de documents scientifiques de niveau recherche, publiés ou non, émanant des établissements d'enseignement et de recherche français ou étrangers, des laboratoires publics ou privés.

THÈSE

Pour obtenir le grade de

Docteur de l'université Savoie Mont Blanc

Spécialité : **Physique Subatomique et Astroparticules**

Arrêté ministériel : 25 Mai 2016

Présentée par

Marc Eisenmann

Thèse dirigée par **Raffaele Flaminio**
et coencadrée par **Romain Gouaty**

Préparée au sein du **Laboratoire d'Annecy de Physique des Particules** et de l'**École doctorale de physique de Grenoble**

Use of squeezed vacuum states to reduce the quantum noise of the Advanced Virgo gravitational wave detector

Thèse soutenue publiquement le **10 Novembre 2020**,
devant le jury composé de :

Antoine Heidmann

LKB, Rapporteur

Jean-Pierre Zendri

INFN Padova, Rapporteur

Cécile Renault

LPSC, Examinatrice

Peter Wolf

SYRTE, Examinateur

Raffaele Flaminio

LAPP, Directeur de thèse

Romain Gouaty

LAPP, Co-Encadrant de thèse

Remerciements

J'aimerais ici remercier toutes les personnes qui ont pu faire de ces trois années de thèse une expérience si enrichissante et passionnante. Sans vous je n'aurais pas pu en profiter si pleinement.

A Antoine Heidmann et Jean-Pierre Zendri qui ont accepté la lourde tâche d'être les rapporteurs de ces travaux. Merci d'avoir relu ce manuscrit et d'avoir pris le temps d'échanger avec moi sur son contenu. A Cécile Renault et Peter Wolf qui ont si gentiment accepté d'examiner mes travaux de thèse malgré ce contexte sanitaire si particulier. Vos questions ont, je l'espère, permis d'affiner le contenu de ce manuscrit tel que vous le souhaitiez.

A Raffaele Flaminio qui m'a fait découvrir le monde des ondes gravitationnelles, depuis l'installation des miroirs de TAMA jusqu'aux dernières lignes de ce manuscrit. Merci de m'avoir laissé orienter mes travaux de thèse sur les différents thèmes qui me tenaient à coeur tout en prenant tout le temps nécessaire pour répondre à mes nombreuses questions et me remettre sur le droit chemin quand il le fallait.

A Romain Gouaty pour avoir si gentiment accepté de co-encadrer mes travaux de thèse et de m'avoir ouvert en grand les portes du système de détection. Depuis le premier jour de ma thèse passé dans SDB1 jusqu'aux derniers instants de rédaction, j'ai pu profiter de ta grande patience à répondre à toutes mes questions et de ta positivité à toute épreuve.

A mes collègues du LAPP, ce fut un plaisir de travailler à vos côtés et de profiter des portes ouvertes pour pouvoir échanger des sujets des plus variés. En particulier, à l'équipe de détection : A Alain pour toujours voir le bon côté des choses malgré les boxons. A Michal pour avoir toujours pris le temps de répondre à mes trop nombreuses questions malgré les souffrances que j'ai pu faire subir à tes plantes. A Romain Bonnard pour toutes nos discussions, des ondes gravitationnelles les plus lointaines aux meilleures blagues (?). A Edwige et Stéphane ainsi que Brigitte et Myriam qui ont toujours eu une oreille attentive quand il le fallait.

To the Virgo squeezing team, it has been a pleasure working with you. Especially to Jean-Pierre to have welcome me so warmly inside the team and had always taken time to discuss with me. To Marco for these long but exciting shifts, it has been super nice to learn by your side. To Fiodor, Henning, Livia, Martina, Moritz and Sheon for all these nice shifts and the patience you had to explain and work with me.

A Matteo Tacca pour m'avoir montré comment toujours apprendre quelque soit la situation ou l'expérience et de m'avoir toujours aidé à voir le bon côté des choses.

A Jérôme et Matteo Barsuglia d'avoir si gentiment pris le temps de répondre à toutes mes questions.

To the people on Virgo site that made all my stay so nice. En particulier à Camilla,

Gabriel, Julia and Mathieu pour m'avoir accueilli si chaleureusement malgré mes questions.

To the TAMA dream team, Eleonora, Manuel and Yuefan that welcomed me so warmly. It was really nice to work with you between the merenda or sleeping in front of a movie. To Matteo Leonardi and Yuhang that join the team later on for all the interesting discussions about the filter cavity and nice time spent together.

Aux amies et amis du LAPP pour tous ces moments passés ensemble : A Dimitri et Florian pour ces cafés toujours enrichissants et ces doux souvenirs du chalet. A Alix, Anne, Jordan et MÉRIL pour avoir partagé nos pires comme nos meilleurs moments entrecoupés de fourberies sur notre bateau. Aux nouvelles et aux nouveaux qui sont arrivées en cours de route, Alexandre, Anthony, Camille, Carole, Eleonora, Iuri, Loïc, Matteo, Monica, Nicolas, Pablo, Paul et Victor. Aux amies et amis du SYMME, Marine, Mathias et Tigran pour s'être serrés les coudes entre symmiens et lappins.

A Laura pour les meilleurs cafés (et presque meilleure tartiflette) et m'avoir tellement aidé à arriver au bout de ce manuscrit. Entre le flipbook et les trop nombreuses corrections de typos j'espère que tu pourras trouver au moins une page à ton goût dans ce manuscrit.

A tous mes amies et amis qui me supportent depuis bien trop longtemps. En particulier aux crewpains et crewpines qui n'ont jamais refusé que je leur ré-explique mes travaux ou mes cours de catane.

A ma famille qui a toujours encouragé et soutenu dans mes choix et mes expériences malgré des distances plus ou moins lointaines.

Pictograms

All the optical scheme presented in this document are based on the Optical Component Library created by A. Franzen [1].

	Laser source
	Faraday isolator
	Electro-Optic Modulator (EOM)
	Beam Splitter mirror (BS)
	Optical fiber and couplers
	Mirror
	Beam-dump
	Photodiode
	Dichroic mirror
	Laser beams
	Monolithic cavity
	Frequency generator
	Mixer
	Sum
	Difference

Acronyms

AdV	Advanced Virgo detector.
AEI	Albert Einstein Institute <i>Hannover (Germany)</i> .
AOM	Acousto-Optic Modulator.
ASD	Amplitude Spectral Density.
BAB	Bright Alignment Beam.
BBH	Binary Black Holes.
BNS	Binary Neutron Stars.
BRMS	Band Root Mean Square.
BS	Beam Splitter mirror.
CC	Coherent Control.
CD	Contrast Defect.
EGO	European Gravitational wave Observatory (Italy).
EMFC	End Mirror Filter Cavity.
EMFCB	End Mirror Filter Cavity Bench.
EOM	Electro-Optic Modulator.
ESQB	External SQueuezing Bench.
ESQB1	External SQueuezing Bench 1.
ESQB2	External SQueuezing Bench 2.
GEO600	German English gravitational wave Observatory.
HOM	Higher Order Mode.
IMC	Input Mode Cleaner.
IMFC	Input Mirror Filter Cavity.

KAGRA	KAmioka GRAvitational wave detector.
LAPP	Laboratoire d'Annecy de Physique des Particules (France).
LIGO	Laser Interferometric Gravitational wave Observatories (USA).
LMA	Laboratoire des Materiaux Avances (France).
LO	Local Oscillator.
MC	Mode Cleaner.
MZ	Mach-Zehnder interferometer.
NE	North End mirror.
NI	North Input mirror.
NSBH	Neutron Star Black Hole binaries.
OMC	Output Mode Cleaner.
OPO	Opto-Parametric Oscillator.
PDH	Pound-Drever Hall.
PLL	Phase-Locked Loop.
PR	Power Recycling.
PSD	Power Spectral Density.
RH	Ring Heater.
RIN	Relative Intensity Noise.
RoC	Radius of Curvature.
RoC	Radius of Curvature.
RTL	Round-Trip Losses.
SDB1	Suspended Detection Bench 1.
SDB2	Suspended Detection Bench 2.
SHG	Second Harmonic Generator.
SNR	Signal-to-Noise Ratio.
SQB1	Suspended sQueezing Bench 1.
SQB2	Suspended sQueezing Bench 2.
SR	Signal Recycling.
WE	West End mirror.
WI	West Input mirror.

Contents

Remerciements	iii
Pictograms	v
Acronyms	vii
Table of contents	xiii
Introduction	xv
1 Gravitational Wave detection	1
1.1 Introduction	1
1.2 Gravitational waves	2
1.2.1 Introduction	2
1.2.2 Gravitational waves sources	3
1.2.3 Impacts of gravitational waves detection	5
1.3 Gravitational waves detectors	6
1.3.1 Interferometric gravitational waves detectors	7
1.3.2 Michelson interferometer	7
1.3.3 Advanced configurations	9
1.3.4 Sensitivity	13
1.4 The Advanced Virgo detector	18
1.5 The gravitational wave detectors network	22
1.6 Gravitational wave detections	25
1.7 Conclusion	25
2 Quantum description of the interferometer	27
2.1 The electromagnetic field	28
2.1.1 The quantization of the electromagnetic field	28
2.1.2 The coherent states	31
2.1.3 The quadrature operators and Heisenberg uncertainty principle	31
2.1.4 The quantum states representation	36
2.2 The quantum states in experiments	42
2.2.1 The squeezed states generation	42
2.2.2 The beam-splitter model	44
2.2.3 The squeezing detection	45

2.2.4	The squeezing degradation	46
2.3	The interferometer quantum noise	50
2.3.1	Michelson	50
2.3.2	The Advanced Virgo quantum noise	54
2.3.3	The frequency dependent squeezing generation	55
2.4	Conclusion	57
3	Frequency Independent Squeezing commissioning for O3	59
3.1	Introduction	59
3.2	The External Squeezer Bench	60
3.2.1	The Squeezer	60
3.2.2	The injection optics	62
3.3	Alignment and mode-matching	65
3.4	The squeezer controls	70
3.4.1	The Phase Locked Loops	70
3.4.2	Phase control	72
3.4.3	The Alignment Controls	77
3.5	Conclusion	82
4	Frequency Independent Squeezing during O3	83
4.1	Introduction	83
4.2	The stray light mitigation	84
4.2.1	First squeezed light injection and scattered-light	84
4.2.2	Mechanical resonances and Virgo sensitivity	97
4.3	The shot-noise decrease	99
4.3.1	Characterization of the squeezing performances	100
4.3.2	Degradation budget	101
4.3.3	Conclusion	112
4.4	The radiation-pressure increase	112
4.4.1	Virgo quantum noise model	112
4.4.2	Experimental results	115
4.4.3	Conclusion	118
4.5	The O3 performances	118
4.5.1	Median squeezing level	118
4.5.2	Duty cycle	121
4.6	Conclusion	123
5	Filter Cavity design	125
5.1	Introduction	125
5.2	From Advanced Virgo to Advanced Virgo+	126
5.2.1	The phase I : lowering the quantum noise	126
5.2.2	The phase II : lowering the thermal noise	130
5.2.3	Other upgrades	130
5.3	The Filter Cavity degradation mechanisms	131
5.3.1	The Filter Cavity round-trip losses	131
5.3.2	The optimal rotation	131
5.3.3	The degradation mechanisms	135
5.3.4	The Filter Cavity length	143

5.4	The impact of frequency-dependent squeezing on the sensitivity	144
5.5	The Filter Cavity length and the Advanced Virgo+ ranges	147
5.6	Conclusion	148
6	The Filter Cavity optical design	151
6.1	Introduction	151
6.2	The Filter Cavity optical configuration	152
6.2.1	The beam size	152
6.2.2	The alignment	153
6.3	The mirrors maps characterization	157
6.3.1	The surface defects	157
6.3.2	Realistic mirror maps	159
6.4	Single Round-Trip simulation	161
6.4.1	Fabry-Perot round-trip losses	161
6.5	The Filter Cavity degeneracy	166
6.6	The etalon effect	171
6.7	Conclusion and Mirror specifications	172
7	Frequency dependent squeezing for Advanced Virgo+	175
7.1	Introduction	175
7.2	The integration overview	176
7.2.1	The Filter Cavity location	176
7.2.2	The benches overview	177
7.2.3	The optical paths	180
7.3	The matching telescopes	185
7.3.1	The infrastructure and beam parameters	185
7.3.2	The matching telescopes design	189
7.3.3	The matching telescope tolerances	195
7.4	Conclusion	196
	Conclusion	199
	Appendix A	203
	Bibliography	207

Introduction

More than a billion years ago in a galaxy far, far away, two black holes make space-time vibrate as they orbit around each other. This space-time vibration or gravitational wave increases in amplitude and frequency as the two black holes get closer until they coalesce. This gravitational wave propagates through the Universe carrying information about the sources that generated it. This gravitational wave was detected by the LIGO-Virgo collaboration on September 14, 2015, which was the first direct detection of a gravitational wave.

The theory of general relativity unifies space and time into a single entity that can be deformed by the presence of mass or energy. The gravitational waves are a prediction of theory of general relativity. Thus their detection allows to test this theory. On the other hand, gravitational waves can be used to study black holes predicted by the general theory of relativity. Furthermore, the combined detection of gravitational waves with electromagnetic waves emitted during the coalescence of two neutron stars has also shown the importance of gravitational waves in the multi-messenger astronomy.

The direct detection of gravitational waves is a particularly ambitious challenge. Indeed, the effect of a gravitational wave is to generate length variations of the order of 10^{-18} m over distances of a few kilometers. It has thus taken more than 40 years of development for detectors to reach sensitivities sufficient to observe the passage of a gravitational wave. All current gravitational wave detectors such as the LIGO, Virgo and KAGRA detectors are kilometer-long laser interferometers. They alternate between periods of observation and periods of improvement of their sensitivity. This has allowed to go from the detection of one gravitational wave signal every few months in 2015 to one per week in 2019.

The laser interferometry consists in converting relative length variations of the two arms of the interferometer into power variations of the light at the output port of the interferometer. The sensitivity of such detectors is limited at high frequency by the shot noise and at low frequency by the radiation pressure noise. These two noises arise from the quantum nature of light and their quadratic sum is the so-called quantum noise.

The quantum noise can be understood from the quantum description of light in which any electromagnetic field is affected by quantum fluctuations in amplitude and phase. Even for the so-called vacuum state that has a null mean power, these quantum fluctuations are present. This means that quantum fluctuations are introduced from the interferometer

output port. These quantum fluctuations are responsible for the quantum noise of the interferometer. In particular, the phase fluctuations of this vacuum state are responsible for the shot noise while the amplitude fluctuations are responsible for the radiation pressure noise.

The sensitivity of all gravitational waves detectors is currently largely limited by the shot noise. It is therefore particularly interesting to reduce quantum noise in order to improve the sensitivity of gravitational wave detectors. One technique for reducing quantum noise consists in replacing the vacuum state entering through the detector's output port by particular states called squeezed vacuum states. Such squeezed vacuum states have the peculiarity of having their phase (or amplitude) fluctuations reduced and on the other hand to have their amplitude (or phase) fluctuations increased. As current detectors are limited only by the shot noise, squeezed vacuum states with reduced phase fluctuations are injected into the interferometer.

However, future gravitational wave detectors will also be limited at low frequencies by the radiation pressure noise. It is therefore planned to inject frequency-dependent squeezed vacuum states with reduced amplitude fluctuations at low frequencies and reduced phase fluctuations at high frequencies. The use of these states thus make it possible to reduce the overall quantum noise of gravitational wave detectors. This frequency dependence can be imprinted on the squeezed states of the vacuum by reflecting them onto a special optical cavity called a filter cavity. The installation of such filter cavities is thus planned for the O4 observation period for the LIGO and Virgo detectors.

The work presented in this manuscript took place between the end of 2017, which corresponds to the preparation of the O3 observation period, and the end of 2020, which corresponds to the beginning of the preparation of the O4 observation period. This work aims at reducing the quantum noise of the Virgo detector by using squeezed vacuum states. In particular, squeezed vacuum states were injected for the first time into the Virgo detector during the O3 observation period. It is planned to use frequency-dependent squeezed vacuum states for the observation period O4.

Chapter 1 describes the gravitational waves from their generation up to their detection. The Advanced Virgo interferometric detector is introduced through its optical configuration and the noises that affect its sensitivity. The quantum noise that affects this detector is introduced through a semi-classical description of light.

Chapter 2 describes the electromagnetic fields in the quantum theory. It describes how quantum fluctuations in the vacuum state can be responsible for quantum noise. The squeezed vacuum states are also introduced, from their generation to their detection. This description makes it possible to demonstrate that these states can improve quantum noise. Finally, the effect of a filter cavity is also presented.

Chapter 3 presents the implementation of the source of frequency-independent squeezed vacuum states in Virgo. The different control loops necessary for the optimal injection of squeezed vacuum states are described.

Chapter 4 describes how the injection of squeezed vacuum states was performed during

the O3 observation period while making sure that the squeezing source did not introduce additional noise due to scattered light. The improvement of the shot noise has been measured and is in agreement with the expected performances. The increase in radiation pressure noise was also observed.

This observation further demonstrates the need to use frequency dependent squeezed vacuum states. The realization of a filter cavity that allows this frequency dependence to be imprinted on the squeezed vacuum states is therefore required. Chapter 5 presents the design of the filter cavity necessary for the generation of frequency-dependent squeezed vacuum states. For this purpose, the mechanisms that degrade the performances of a realistic filter cavity are presented. This is used to define the length of the filter cavity that most efficiently improves the sensitivity of Virgo.

The choice of the length of the filter cavity is strongly related to the optical losses of this cavity. Chapter 6 describes how mirror parameters such as the quality of their surfaces or their radii of curvature define the optical losses of the filter cavity. These mirrors parameters are chosen in order to reduce as much as possible the optical losses of the filter cavity.

Chapter 7 presents how to implement the filter cavity in Virgo. This requires the addition of numerous optics and control beams that are introduced. In particular, the performance of the mode-matching telescope between the filter cavity and the interferometer is studied.

Finally, the future prospects to achieve quantum noise reduction over the entire detection spectrum of Advanced Virgo are discussed in the conclusion.



Gravitational Wave detection

Contents

1.1	Introduction	1
1.2	Gravitational waves	2
1.2.1	Introduction	2
1.2.2	Gravitational waves sources	3
1.2.3	Impacts of gravitational waves detection	5
1.3	Gravitational waves detectors	6
1.3.1	Interferometric gravitational waves detectors	7
1.3.2	Michelson interferometer	7
1.3.3	Advanced configurations	9
1.3.4	Sensitivity	13
1.4	The Advanced Virgo detector	18
1.5	The gravitational wave detectors network	22
1.6	Gravitational wave detections	25
1.7	Conclusion	25

1.1 Introduction

Gravitational waves are predicted by the theory of general relativity developed by Albert Einstein in 1915 [2] [3]. More than a century after the prediction of gravitational waves, their first direct detection has been performed by the LIGO and Virgo scientific collaboration [4]. This chapter briefly introduces gravitational waves before presenting the

detectors that achieved this first direct detection. Finally, the Advanced Virgo detector sensitivity is derived from the noises that affect its performances.

1.2 Gravitational waves

1.2.1 Introduction

The theory of general relativity marked a shift in the description of the gravitation. Until the development of this theory, it was Newton's description of gravitation that successfully described the gravitation as an instantaneous force. Despite being precise enough to predict the existence of Neptune from perturbation in Uranus orbit [5], some flaws began to affect this theory. There were for instance some troubles with theoretical considerations (eg. instantaneous force versus finite speed of light [6]) to experimental ones (eg. the slight anomaly in the precession of Mercury's orbit [5]).

On the other hand, the theory of general relativity redefines the gravity as a consequence of curved space-time. Indeed, the Einstein equation links the space-time geometry with the mass (and energy) that it contains as:

$$R_{\mu\nu} - \frac{1}{2}R g_{\mu\nu} = \frac{8\pi G}{c^4}T_{\mu\nu} \quad (1.1)$$

In this equation, the left term describes the space-time geometry. $g_{\mu\nu}$ is the space-time metric tensor while $R_{\mu\nu}$ and R are the Ricci tensor and the scalar curvature both dependent on the metric tensor $g_{\mu\nu}$ and its derivatives. In the right side of this equation, $T_{\mu\nu}$ is the stress-energy tensor that corresponds to a generalization of the mass. It represents the source of the gravitational wave interaction while the metric tensor $g_{\mu\nu}$ is equivalent to the gravitational potential.

The equation 1.1 can be linearized in the weak field approximation. This weak field approximation consists in expressing the metric tensor as :

$$g_{\mu\nu} = \eta_{\mu\nu} + h_{\mu\nu} \quad (1.2)$$

where $h_{\mu\nu}$ is a small perturbative quantity describing a deviation from the Minkowski metric $\eta_{\mu\nu}$ of flat space-time such that $h_{\mu\nu} \ll 1$. Introducing this metric in the equation 1.1 far away from any source ($T_{\mu\nu} = 0$) and choosing an adequate system of coordinates allows to rewrite the equation as :

$$\left(\nabla^2 - \frac{1}{c^2} \frac{\partial}{\partial t^2} \right) h_{\mu\nu} = 0 \quad (1.3)$$

This corresponds to a wave equation for the space-time perturbation $h_{\mu\nu}$. $h_{\mu\nu}$ is therefore the gravitational waves strain. The general solution of equation 1.3 is a superposition of monochromatic plane waves that propagate at the speed of light c and modify the space-time metric according to the following equation :

$$h_{\mu\nu} = \epsilon_{\mu\nu} e^{ik(ct-z)} \quad (1.4)$$

where z is the direction of propagation of the gravitational wave, $\epsilon_{\mu\nu}$ is the polarization tensor and k the wave vector. These waves can be defined by two independent polarizations orthogonal to the wave direction of propagation [6] [7]. The gravitational waves are then expressed as

$$h_{\mu\nu} = \left(h_+ \epsilon_+ + h_\times \epsilon_\times \right) e^{ik(ct-z)} \quad (1.5)$$

with ϵ_+ and ϵ_\times the two polarization states known respectively as $+$ and \times polarizations.

The effects of a gravitational wave on free test masses located on a transversal plane with respect to the wave direction of propagation is shown in figure 1.1.

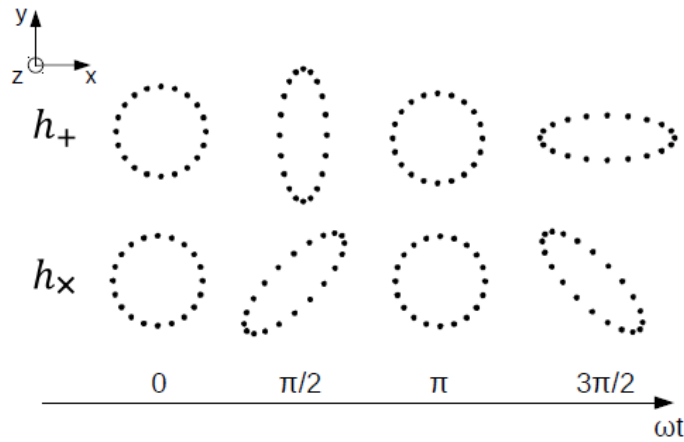


Figure 1.1: Effect of a gravitational wave propagating along the z direction on free test masses arranged in a circle in the (O, x, y) plane. The deformations are shown for the $+$ and \times polarizations

Each polarization modifies the distances between the test masses in phase opposition along orthogonal directions. By noting L the diameter of the initial test masses circle, its variation due to a gravitational wave δL is linked to the gravitational wave strain h by the relation :

$$h = \frac{2\delta L}{L} \quad (1.6)$$

The effect of gravitational waves as length variations between free test masses in phase opposition along orthogonal directions is at the heart of the laser interferometric detectors.

1.2.2 Gravitational waves sources

The sources of gravitational waves can be derived from the equation 1.1 by considering the presence of a mass ($T_{\mu\nu} \neq 0$). This can give the gravitational strain h at a distance r from the source of mass M , characteristic speed v and asymmetry factor ϵ ($0 < \epsilon < 1$ where $\epsilon = 0$ for a symmetrical mass distribution) as :

$$h \sim \epsilon \frac{G M}{c^2 r} \left(\frac{v}{c} \right)^2 \quad (1.7)$$

The scaling factor $\frac{G}{c^2} \sim 10^{-29}$ m/kg shows that it is not possible to generate significant gravitational waves on Earth[6]. Instead, there are astrophysical objects that are able to generate significantly stronger gravitational waves. This is highlighted by computing the gravitational wave power and introducing the Schwarzschild radius $R_S = \frac{2GM}{c^2}$ and the astrophysical object characteristic dimension R :

$$P \sim \frac{c^5}{G} \epsilon^2 \left(\frac{R_S}{R} \right)^2 \left(\frac{v}{c} \right)^6 \quad (1.8)$$

This estimation implies that the gravitational wave power is maximized for asymmetric ($\epsilon \sim 1$), compact ($\frac{R_S}{R} \sim 1$) and relativistic sources ($\frac{v}{c} \sim 1$). Therefore, astrophysical objects as well as cataclysmic phenomena in the Universe are preferred sources to generate gravitational waves detectable on Earth. Some of these sources are listed below :

Compact binary coalescence The compact binaries are divided into three categories depending on their composition :the Binary Black Holes (BBH),the Binary Neutron Stars (BNS) and the Neutron Star Black Hole binaries (NSBH). All these binary objects are highly compact and asymmetric. They are thus ideal sources for the emission of gravitational waves.

Compact binaries orbit around each other during millions of years and emit gravitational waves. Therefore they lose energy and get closer to each other. For instance, the first indirect detection of gravitational waves has been observed with the binary system PSR1913+16 where the energy lost through gravitational waves perfectly matched the predictions of the theory of general relativity [8].

Finally, the compact binaries coalesce. A compact binary coalescence corresponds to the merger of the two objects and the last moments before the merger. The time evolution of the compact binary coalescence is composed of three phases : the inspiral, the merger and the ring-down.

First, the inspiral phase happens when the two objects rotate one around the other. With time, they accelerate and their separation reduces due to energy lost through gravitational waves emission. It is possible to compute the gravitational waves frequency of the last stable orbit of these two objects (or equivalently at the last moment of the inspiral phase) with total mass M which corresponds to the highest frequency of gravitational waves emitted during this phase.

$$f_{GW} \sim 2.2\text{kHz} \frac{1M_{\odot}}{M} \quad (1.9)$$

where M_{\odot} is equal to one Solar mass.

It can be deduced from this equation that the gravitational waves frequency decreases with an increase of the mass of the compact binary. Therefore, the gravitational wave signals are expected at lower frequency for a BBH system than for a BNS system.

For a BNS the total mass is of the order of $2.8 M_{\odot}$ and so the maximal gravitational wave frequency is at about 800 Hz. On the other hand, a BBH system of total mass of the

order of $50 M_{\odot}$ leads to a frequency of the order of 45 Hz. As described in the section 1.3.4, this means that these signals will be within the detectable frequency range of ground based detectors such as the Laser Interferometric Gravitational wave Observatories (USA) (LIGO) or Virgo detector.

Then, during the merger phase, the two objects reach relativistic speed and merge into a single new object (so-called remnant). Finally, during the ring-down this remnant settles down from a highly asymmetrical state to a symmetrical and stationary state.

The theory of general relativity allows to predict the gravitational waveform emitted by such compact binaries. Thus the search for these signals can be performed using the match-filtering technique [9].

Burst sources This category includes unmodeled short gravitational wave signals. The search for such signals is performed by analyzing short high Signal-to-Noise Ratio (SNR) events [10] [11]. This category includes phenomena where large and dense amount of energy undergo quick variations. For example supernovae which are the explosion of a dying star when the nuclear reactions are not sufficient to compensate the gravitational force. However, there is only limited knowledge on this process and therefore on the evolution of the gravitational wave signal.

Continuous sources This category of sources is characterized by quasi-monochromatic gravitational wave emission and quasi-constant amplitude. For example, fast rotating neutron stars can emit gravitational waves if they present asymmetry in their masses distribution [12] [13]. Despite an estimated number of such rotating neutron stars of the order of 10^8 within our Galaxy [14], the gravitational wave amplitude is below $h \sim 10^{-25}$ which has prevented their detection up to now.

1.2.3 Impacts of gravitational waves detection

Because the effects of gravitational waves are so small ($h \sim 10^{-20}$), the direct detection of gravitational waves is extremely challenging. However, the detection of gravitational waves is interesting for several fields in physics. This section gives a non-exhaustive list of these benefits.

Theory of general relativity The general theory of relativity predicts precisely several parameters linked to the gravitation wave emission and propagation. In a similar manner to the Newton's theory of the gravitation, finding discrepancies between measurement and theory could hint to another underlying theory of gravitation.

Gravitational waves allow to perform many tests of general relativity in strong field [15]. For instance the polarizations and speed of gravitational waves can be compared with their predicted values [16]. The theory of general relativity also predicts the waveform of

gravitational waves. By comparing the detected signals with their predicted waveform, it is possible to look for deviations which could favor other gravity theories.

Cosmology As gravitational waves propagate through the Universe with little interaction with matter, they allow to probe the Universe at cosmological scale. Therefore, compact binary coalescences that provide direct measurement of the luminosity distance of the source, can be used as standard candles. If it is possible to also measure the redshift of these objects, it is then possible to measure the Hubble constant H_0 . The observation of GW170817 allowed to measure a Hubble constant of $H_0 = 68_{-7}^{+14}$ km/s/Mpc [17] [18]. While this measurement is not yet precise enough with respect to the Planck or SHoES measurements [19] [20], it paves the way for a new independent measurement of this constant. With more detections similar to GW170817, the precision on the gravitational wave measurement could help to understand the discrepancy between Planck and SHoES measurements [21].

Astrophysics The gravitational waves emitted by compact binary systems are a probe to objects that were mostly invisible using other kind of detectors so far. The detection of such gravitational waves allow therefore to study these objects, from their formation [22] to their population [23]. Any further detections should allow to estimate the variation of the black holes population in function of the redshift.

Moreover, the BNS coalescences are also expected to emit both gravitational waves, electromagnetic waves and neutrino. The coincident detection of gravitational and electromagnetic waves also linked (at least part of) the origin of short gamma ray bursts to BNS coalescences [16]. Furthermore, this combined measurement allowed to study the mechanisms responsible for the emission of such gamma ray bursts as well as the internal structure of the relativistic jet emitted during the coalescence [24] [25].

1.3 Gravitational waves detectors

The previous section presented that a variety of astrophysical sources should generate gravitational waves. The gravitational waves emitted by these objects cover a wide range in frequency, from nanohertz to several kilohertz. In order to probe all this gravitational wave spectrum, several detector configurations are foreseen; each aiming for different kind of sources. This variety of gravitational wave sources and detectors is represented in figure 1.2. The work presented in this manuscript focused on the Advanced Virgo detector (an upgraded configuration of the Virgo detector) that aims for gravitational wave signals between 10 Hz and 10 kHz.

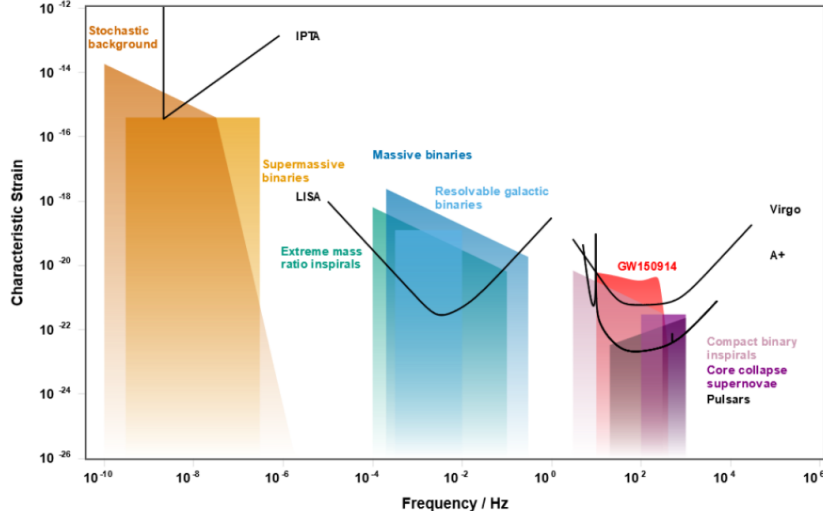


Figure 1.2: Sensitivity curves of current and future gravitational wave detectors together with the expected sources of gravitational waves. IPTA : International Pulsar Timing Array, LISA : Laser Interferometer Space Antenna, A+ : Advanced LIGO+, ET : Einstein Telescope. Credits : [26]

1.3.1 Interferometric gravitational waves detectors

Current ground-based detectors are km-scale Michelson interferometers. Indeed, as first proposed in the 1960's [27], a Michelson interferometer translates a variation of the mirrors relative positions into power variation at the interferometer's output. If the mirrors of such interferometer are suspended by pendula, they behave as free test masses in the horizontal plane for frequencies higher than the pendulum resonance frequency. In 1972, Reiner Weiss precisely described the performances of such detector which paved the way to their implementation [28].

1.3.2 Michelson interferometer

A Michelson interferometer (see figure 1.3) is composed of a laser source, a BS, two end mirrors (here labeled North End mirror (NE) and West End mirror (WE)) and a photo-detector. The optical path between the BS and the NE is called the north arm while the optical path between the BS and the WE is called the west arm. The laser beam is propagated towards a BS which transmits half of the beam and reflects the other half. Both beams propagate in the interferometer arm up to their respective end mirror that reflects the beams toward the BS where they interfere. The power of the beam resulting from this interference is measured on a photo-detector.

This output power P_{out} is expressed as a function of the interferometer input power P_{in} , a phase ϕ that depends on the relative length of the two arms and the interferometer contrast C that characterizes the similarity between the two interfering beams such that $0 \leq C \leq 1$ (and $C = 1$ for an ideal Michelson interferometer ,here meaning identical

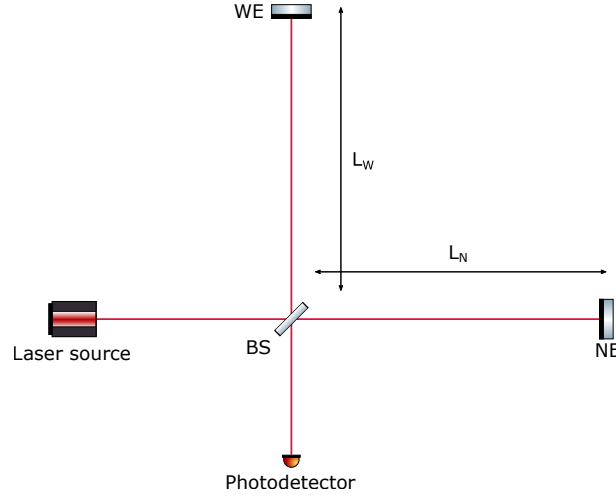


Figure 1.3: Schematic representation of a Michelson interferometer. A laser beam is split by the BS. One beam travels along the north arm and is reflected of the NE while the other beam travels along the west arm and is reflected of the WE. The two beams are recombined at the BS and the beam resulting from their interference is measured on a photo-detector

reflectivity of the end mirrors without losses) as

$$P_{out} = \frac{P_{in}}{2} (1 + C \cos(\phi)) \quad (1.10)$$

Assuming a '+' polarized gravitational wave propagating in the direction orthogonal to the interferometer plane, it is possible to see from equation 1.6 that such gravitational wave induces a length variation of the west and north arms in phase opposition. Meaning that one arm is elongated while the other one is shrunk. For a gravitational wave with an amplitude $h(t)$, the arm length varies as

$$\delta L_W(t) = -\delta L_N(t) = \frac{1}{2} h(t) L \quad (1.11)$$

where L is the mean length of the two arms, δL_W and δL_N the west and north arm length variations. This affects the optical path of the beam in each arm which in return generates a variation of the phase difference when these two beams interfere at the BS. The phase difference variation due to the gravitational wave $\phi_{GW}(t)$ can be expressed as a function of the laser wavelength λ as

$$\phi_{GW}(t) = \frac{4\pi}{\lambda} (\delta L_W(t) - \delta L_N(t)) = \frac{4\pi}{\lambda} h(t) L \quad (1.12)$$

This means that the effect of a gravitational wave on a Michelson interferometer can be represented by a phase change as

$$\phi(t) = \phi_0 + \phi_{GW}(t) \quad (1.13)$$

Where ϕ_0 is a static phase that depends on the relative length between the two arms of the interferometer. And because the gravitational wave strain is so small (it can be

recalled that the expected gravitational wave strain is at the order of $h \sim 10^{-21}$), one can assume $\phi_{GW} \ll \phi_0$ and therefore

$$P_{GW} = \frac{P_{in}}{2} (1 + C \cos(\phi_0) - C \sin(\phi_0) \phi_{GW}) \quad (1.14)$$

Finally, the variation of the output power due to the gravitational wave can be expressed as

$$\delta P_{GW}(t) \sim \frac{P_{in}}{2} C \sin(\phi_0) \phi_{GW} \quad (1.15)$$

$$\sim \frac{P_{in}}{2} C \sin(\phi_0) \frac{4\pi}{\lambda} Lh \quad (1.16)$$

The equation 1.16 shows that the variation of the output power due to gravitational waves increases with larger input power, better contrast and longer arms. For instance, all ground-based laser interferometric gravitational waves detectors have their arm length of few kilometers. It can also be derived from this equation that the fraction of the power due to gravitational waves at the interferometer output increases when $\phi_0 \rightarrow \pi/2$ which corresponds to the mid-fringe condition.

However, this working point means that the interferometer output signal is containing a large static component depending on the interferometer input power. Any noise that affect this input power might hide the effect of a gravitational wave on the interferometer. It is therefore convenient to use a working point close to the dark-fringe condition (where the beams circulating inside two interferometer arms interfere destructively and no light is present at its output port) with a so-called dark-fringe offset with respect to the dark-fringe. This working point allows to drastically reduce the effects of noise affecting the input power (among others) [29].

1.3.3 Advanced configurations

By modifying the optical configuration of the Michelson interferometer, it is possible to improve the effect of a gravitational wave on the interferometer output signal.

Fabry-Perot arm cavities

A schematic drawing of a Fabry-Perot cavity is presented in figure 1.4. It is composed of two mirrors M_1 and M_2 defined by their respective amplitude reflection coefficients r_1 and r_2 and amplitude transmission coefficients t_1 and t_2 and separated by a distance L .

The electromagnetic field can be written at different points of the cavity such as

- E_{in} the input electromagnetic field

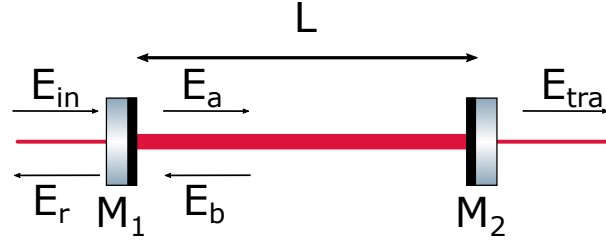


Figure 1.4: Schematic representation of a Fabry-Perot cavity

- $E_r = r_1 \cdot E_{in} + t_1 \cdot E_b$ the reflected electromagnetic field
- $E_a = t_1 \cdot E_{in} - r_1 \cdot E_b$ the intra-cavity electromagnetic field
- $E_b = -r_2 \cdot E_a \cdot e^{-2ikL}$ the second intra-cavity electromagnetic field
- $E_{tra} = t_2 \cdot E_a \cdot e^{ikL}$ the transmitted electromagnetic field

where k is the wave-number defined as $k = 2\pi/\lambda$.

Combining the different expressions of the electromagnetic fields it is possible to express the Fabry-Perot cavity transmissivity, reflectivity and gain as

$$t_{FP} = \frac{E_{tra}}{E_{in}} = \frac{t_1 t_2 e^{-ikL}}{1 - r_1 r_2 e^{-2ikL}} \quad (1.17)$$

$$r_{FP} = \frac{E_r}{E_{in}} = r_1 - \frac{r_2 t_1^2 e^{-2ikL}}{1 - r_1 r_2 e^{-2ikL}} \quad (1.18)$$

$$g_{FP} = \frac{E_a}{E_{in}} = \frac{t_1}{1 - r_1 r_2 e^{-2ikL}} \quad (1.19)$$

From equation 1.19 it is possible to express the power circulating inside the Fabry-Perot cavity as a function of the optical gain G and the finesse \mathcal{F} of the Fabry-Perot cavity as

$$P_{cav} = P_{in} G \frac{1}{1 + \left(\frac{2\mathcal{F}}{\pi}\right)^2 \sin^2(kL)} \quad (1.20)$$

with $G = \left(\frac{t_1}{1-r_1 r_2}\right)^2$ and $\mathcal{F} \sim \frac{\pi\sqrt{r_1 r_2}}{1-r_1 r_2}$ where the approximation holds for high finesse (meaning $r_1, r_2 \sim 1$). Note that the average number of round-trip inside a Fabry-Perot cavity N is directly related to its finesse : $N = 2\mathcal{F}/\pi$.

The resonance condition of a Fabry-Perot cavity is given by the maximum of the equation 1.20. This corresponds to a phase $\phi_0 = 2\pi n$ with n an integer. This is equivalent to consider that the Fabry-Perot cavity length is a multiple of $\lambda/2$.

For a Fabry-Perot cavity near resonance, the reflectivity phase can be expressed as a function of the phase at resonance ϕ_0 and a phase $\delta\phi$ induced by a small length variation δL as

$$\phi_{FP} = \phi_0 + \delta\phi = \phi_0 + \frac{4\pi}{\lambda} \frac{2\mathcal{F}}{\pi} \delta L \quad (1.21)$$

This means that the phase shift induced by a small length variation is amplified by the number of light round-trip inside the Fabry-Perot cavity. This can be used in interferometric gravitational waves detector by placing such Fabry-Perot cavity inside each Michelson arm cavity. This is represented in figure 1.5.

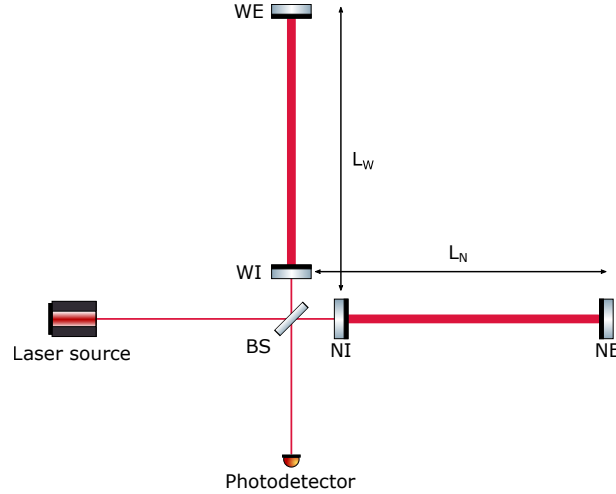


Figure 1.5: Michelson interferometer with Fabry-Perot arm cavities

If the propagation time of the light inside the arm cavity is not negligible with respect to the time period of the gravitational waves, the effect of a small length variation δL is averaged over several round-trips. The equation 1.21 then becomes in the frequency domain

$$\delta\phi(f) = \frac{4\pi}{\lambda} \frac{2\mathcal{F}}{\pi} \frac{\delta L}{1 + i\frac{f}{f_p}} \quad (1.22)$$

with $f_p = \frac{c}{4\mathcal{F}L}$ the Fabry-Perot cavity pole. This shows that this cavity is filtering the effect of small length variation at high frequency in exchange of an amplification of the small length variation at low frequency. This corresponds to a filtering effect, hence this cavity is also known as filter cavity as presented later on when discussing about frequency dependent squeezing generation.

Power recycling

It can be seen from equation 1.16, that an increase of the interferometer input power P_{in} increases its sensitivity.

Since the interferometer operates near the dark fringe condition, there is almost no light reaching the photo-detector. It means that almost all the light circulating inside the interferometer is reflected toward the laser source. By placing a mirror between the laser source and the BS, a large amount of the light reflected toward the laser source is re-injected into the interferometer which corresponds to an increase of the power circulating inside the interferometer. This mirror is thus known as Power Recycling (PR).

By properly tuning the PR position, it is possible to form a resonant cavity that has the PR as input mirror and the overall interferometer as output mirror. In this condition, the power at the BS, P_{BS} , is :

$$P_{BS} = P_{in} G_{PR} \quad (1.23)$$

with $G_{PR} = (t_{PR}/(1 - r_{PR}r_{arm}))^2$ the gain of this newly formed cavity that depends on the PR amplitude transmission t_{PR} , the PR amplitude reflection r_{PR} and the mean amplitude reflection of the Fabry-Perot arm cavities r_{arm} .

This means that the power due to a gravitational wave at the interferometer output is increased by G_{PR} .

Signal recycling

By analogy to the installation of the power recycling technique, a mirror can be placed between the BS and the photo-detector.

This configuration known as dual recycling [30] configuration is represented in figure 1.6.

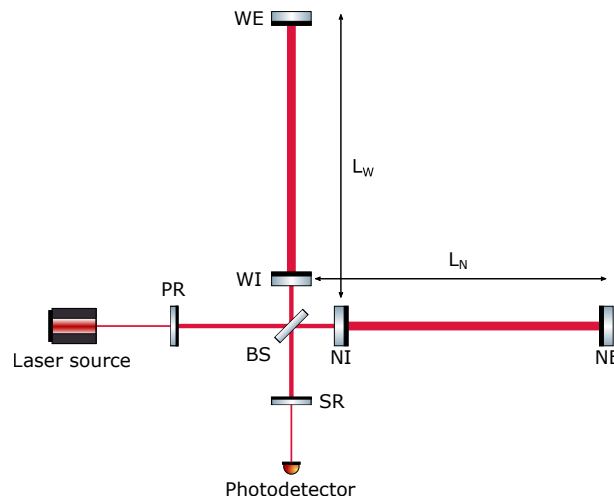


Figure 1.6: Schematic representation of Michelson interferometer with Fabry-Perot arm cavities, PR and Signal Recycling (SR)

This mirror, named SR is forming a cavity together with the Fabry-Perot mirrors that affects only the differential signals [31]. In particular, as the gravitational wave signals are encoded into differential signal when the interferometer is locked on dark-fringe, this SR cavity will affect the gravitational wave signal.

The role of the SR mirror can be understood by considering that the SR mirror and the interferometer arm end mirrors form an equivalent mirror. The reflectivity of this equivalent mirror depends on the detuning ϕ of the SR mirror and this detuning depends on the position of the SR mirror.

Especially, for $\phi = 0$, the reflectivity of this equivalent mirror is the lowest possible. This

corresponds to a reduction of the equivalent Fabry-Perot arm cavity finesse. And therefore, it can be seen from equation 1.22 that the interferometer bandwidth is increased at the expense of the low-frequency gain. The two LIGO detectors have already installed the SR mirror. The detectors Virgo and KAGRA are foreseeing to install the SR mirror for the O4 run. All these detectors should use the SR mirror to improve their detection bandwidths.

1.3.4 Sensitivity

Because the effect of gravitational waves are so weak, the detection of gravitational wave is highly linked with the noises that affect the performances of gravitational waves detectors. In order to detect gravitational waves, it is required that the gravitational wave signal is larger than random fluctuations, or noise, present without the gravitational wave signal. This noise can be described by a random time series $n(t)$ and its single-sided Power Spectral Density (PSD) is defined as

$$S(f) = \lim_{T \rightarrow \infty} \frac{2}{T} \left| \int_{-T}^{+T} n(t) e^{-2\pi i f t} dt \right|^2 \quad (1.24)$$

The PSD characterizes indeed the amount of time variation at the frequency f of the time series $n(t)$. One can also define the Amplitude Spectral Density (ASD) as

$$S^{1/2}(f) = \sqrt{S(f)} \quad (1.25)$$

Our convention will be to use the symbol S_n for the PSD and $h_n = S^{1/2}$ for the ASD of a noise n .

The noises can be divided into two sets of noises : the fundamental noises and the technical noises. First the fundamental noises arise because of the interferometer design. They are represented in figure 1.7.

Shot noise

As the gravitational wave signal is encoded into a laser power variation at the interferometer output, any uncertainty on this power measurement is directly limiting the ability to detect gravitational wave. The laser beam reaching the output photo-detector can be described by a flow of photons¹, and measuring the power of this laser beam consists in a counting of these photons. The arrival of the photons on the photo-detector being discrete independent events, it is described by a Poissonian distribution. If the mean number of photons verifies $\bar{N} \gg 1$, which is the case for the output power used in gravitational wave interferometer, the standard deviation σ_N of the Poissonian distribution is

$$\sigma_N = \sqrt{\bar{N}} \quad (1.26)$$

¹This chapter follows a semi-classical description of the light but a quantum description of the interferometer is presented in the next chapter

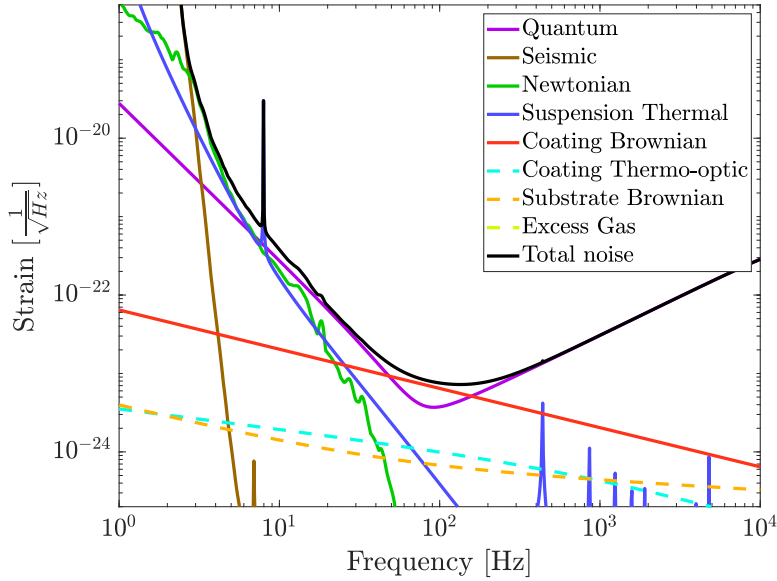


Figure 1.7: Advanced Virgo fundamental noises for the O3 run with an input laser power of 18 W and power-recycling. This configuration corresponds to a BNS range 90 Mpc. Their quadratic sum is represented by the black line. In practice, the sensitivity is lower due to technical noises

Since the gravitational wave signal scales with the output laser power, it is interesting to rewrite this uncertainty as a function of P_{out} . First, the average number of photons for a power P_{out} detected by a photo-detector during the time interval τ can be rewritten as

$$\bar{N} = \frac{P_{out} \tau \lambda}{2\pi \hbar c} \quad (1.27)$$

with \hbar being the reduced Planck constant. Then, the uncertainty on the power can be expressed as

$$\delta P_{out} = \sqrt{\bar{N}} \frac{2\pi \hbar c}{\lambda \tau} = \sqrt{\frac{P_{out} 2\pi \hbar c}{\lambda \tau}} \quad (1.28)$$

This power fluctuation is called shot noise. And because it originates from the quantum behavior of light, it is always present for interferometric gravitational wave detectors.

For a Michelson interferometer, combining the equations eq:pvar and 1.28 defines the minimal detectable gravitational wave signal as

$$h = \frac{1}{2L} \sqrt{\frac{\hbar c \lambda}{\pi i \tau P_{in}}} \frac{\sqrt{1 + C \cos(\phi_0)}}{C \sin(\phi_0)} \quad (1.29)$$

If one assumes a perfect contrast ($C = 1$) the relative arm length can be tuned to improve the sensitivity. By setting the relative arm length to a multiple of half the laser wavelength, the static phase becomes $\phi_0 = (2k + 1)\pi$ with k an integer and the output power is null. This configuration is named dark-fringe. In practice, the interferometer contrast can be

spoiled by non-perfect optical components inside the interferometer. The impact of non perfect contrast on the sensitivity are presented paragraph 1.3.4.

Finally, the shot noise of a power recycled Michelson interferometer with Fabry-Perot arm cavities expressed in units of gravitational wave amplitude is given by

$$h_{sn} = \frac{1}{(4\mathcal{F}L)} \cdot \sqrt{\frac{\pi\hbar\lambda c}{P_{in}G_{PR}}} \cdot \frac{1}{\sqrt{g(f)}} \quad (1.30)$$

with $g(f) = [1 + (f/f_p)^2]^{-1}$ is the frequency response of the Fabry-Perot arm cavity with pole frequency $f_p = c/4\mathcal{F}L$.

Radiation-pressure noise

Because photons are not equally spaced in time and because they each carry a non-null momentum, they generate fluctuating radiation pressure on the test masses. This fluctuating radiation pressure is related to the power fluctuation δP as

$$\delta F = \frac{2\delta P}{c} \quad (1.31)$$

This induces fluctuations in the position of the test masses known as radiation pressure noise. In terms of gravitational wave strain, it can be expressed as

$$h_{rpm} = \left(\frac{4\mathcal{F}}{ML} \right) \cdot \sqrt{\frac{\hbar P_{in} G_{PR}}{\pi^5 \lambda c}} \cdot \frac{\sqrt{g(f)}}{f^2} \quad (1.32)$$

where M is the mirror mass.

The quantum noise is defined by the sum of the shot noise and the radiation pressure noise :

$$h_{qn} = \sqrt{h_{sn}^2 + h_{rpm}^2} \quad (1.33)$$

It can be seen that the radiation pressure noise dominates at low frequency while the shot noise dominates at high frequency. Also, while the shot noise is proportional to $\sqrt{\frac{1}{P_{in}}}$, the radiation pressure noise is proportional to $\sqrt{P_{in}}$. This means that within the semi classical description of light, it is not possible to reduce at the same time the shot noise and the radiation pressure noise. Figure 1.8 shows the Advanced Virgo quantum noise for 20 W (solid line) and 60 W (dashed line) of input power with a power recycling gain $G_{PR} = 33$.

Seismic noise

Earth ground is always shaking, either from natural or human activities. This is inducing test masses motions known as seismic noise. For instance, the noise below 1 Hz is mainly due to natural factors [32], while human activities are responsible for seismic noises above 1 Hz [33].

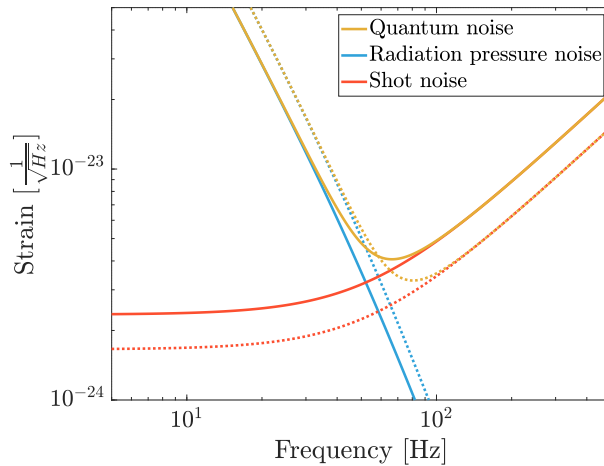


Figure 1.8: Advanced Virgo quantum noise with an input laser power 20 W (solid line) and input power 60 W (dashed line) with power recycling gain of 33

The seismic noise is the dominant noise at low frequency below 1 Hz. It is required to reduce seismic noise by ten orders of magnitude to reach sensitivity $h \sim 10^{-23}$ at 100 Hz. This reduction can be achieved by suspending the test masses with a cascade of inverted pendula.

Newtonian noise

Variations in the local gravity field surrounding the interferometer couple to test masses motions [34]. This noise, known as Newtonian noise will be limiting the future ground-based detectors below 20 Hz. This noise can be mitigated by placing the detectors in quiet place. For instance, building detectors underground reduces the Newtonian noise by more than two orders of magnitude (as for the KAGRA detector [35]). Another strategy is to measure and subtract the Newtonian noise [36] from the detector output signal.

Thermal noises

The fluctuation-dissipation theorem states that any mechanical system suffering dissipation see a fluctuation of its position [37]. The amplitude of this fluctuation is directly related to the system temperature. Furthermore, the equi-partition theorem relates that the system thermal energy is spread over the system mechanical modes. The combination of these two theorems means that the thermal energy of a mechanical system causes fluctuations of this system position spread over its mechanical modes. This results as a displacement noise of the system (in our case the test masses) known as thermal noise. Future ground-based laser interferometric detectors such as KAGRA are planning to operate with cryogenic mirrors to reduce the thermal noise.

There are two main sources of thermal noise in laser interferometric gravitational wave detectors.

Suspension thermal noise The suspension thermal noise consists of the excitations of the suspension system mechanical modes. These excitations translate into fluctuations in the test-masses positions. There are two kinds of suspension mechanical modes that affect the test-masses position.

First, the excitation of the suspension longitudinal modes induces a longitudinal displacement of the test-masses. The noise induced by these longitudinal excitations was limiting the low frequency sensitivity below 50 Hz during the O2 run. It has been reduced by a factor 5 for the O3 run by replacing the suspension steel wires for monolithic fused silica wires.

The suspension vibration modes of the suspension can also be excited. They are called the suspension violin modes. Their effects appear on the suspension thermal noise as a serie of a fundamental resonance at a frequency of the order of 450 Hz and its harmonics.

Mirror thermal noise There are several sources of thermal noise from the test masses themselves. Despite representing only few nanometers on the 42 kg test masses, the coating thermal noise is the main source of mirror thermal noise.

The coating thermal noise corresponds to the excitation of the mechanical modes of the coating due to its thermal energy. This corresponds to an effective vibration of the mirror surface. This noise is limiting the sensitivity around 100 Hz.

This noise can be reduced by increasing the laser beam size as the vibrations of the coating are averaged over a larger surface.

Technical noises

In addition to the fundamental noises, there is another set of noises known as technical noises. This name comes from the fact that these noises arise from the technical implementation of the detector. Technical noises could in principle be reduced to negligible levels through proper design.

Residual gas Residual gas present along the laser beam path induces variations of the refractive index of the air. This means that the laser beam acquires a fluctuating phase along its path. To mitigate this noise, most of the interferometer optical components are placed inside vacuum. The vacuum level ranges between 10^{-9} mbar to 10^{-6} mbar depending on the location.

Scattered light As presented in more details in section 6.3.1, mirror defects can reflect part of an incident beam in random directions. If this randomly reflected beam hits a mechanical component (eg vacuum chamber walls, chambers,...), the vibration of the mechanical component is imprinted on the phase of the beam. Finally, if this beam recombines with the main beam, it generates phase noise. This noise is known as scattering

noise and can be mitigated by avoiding spurious reflection and placing critical optical components on suspended benches inside vacuum.

Laser noises Because the laser beam is used to extract the gravitational wave signal, any fluctuations in the laser frequency, intensity or direction is responsible for noises that affect the gravitational wave signal. These noises can be reduced by implementing control loops or optical filtering before the injection of the laser into the interferometer.

Contrast defect In the derivation of the shot noise, we supposed that the interferometer contrast C was perfect. In practice, the interferometer contrast is not unity (for instance due to difference in reflectivities between the arm cavity input mirrors). This means that part of the photons reaching the output photo-detector have not traveled inside the arm cavities and do not carry information on the gravitational wave signal.

Electronic noises The interferometer output photodiode is used to convert the gravitational wave signal from optical power to electrical signal. Therefore, any fluctuations in the number of generated electrons can mask the gravitational wave signal. All these fluctuations are gathered in the electronic noise. They can be mitigated in the design of the electronic chain of the photo-detector.

1.4 The Advanced Virgo detector

Advanced Virgo is the first major upgrade of the Virgo interferometer. It is a power recycled Michelson interferometer with Fabry-Perot arm cavities. Figure 1.9 is an aerial picture of the detector.

This chapter gives an overview of the main components of the detector.

A simplified schematic of the Advanced Virgo detector (AdV) is presented in figure 1.10.

The injection system

The main laser source is a Nd:YAG emitting a laser with 500 mW of power and a wavelength $\lambda = 1064$ nm. The laser beam propagate through an amplifier that increases the laser power to 90 W.

The laser is also modulated to generate side-bands used to generate the control signals required to keep the interferometer in its nominal condition as briefly described in this section.

As the laser source and the laser amplifiers are not suspended nor under vacuum, the acoustic and seismic noises can affect the quality of the produced laser beam. The defects



Figure 1.9: Aerial view of the Advanced Virgo detector. The two 3 km arms of the interferometer meet in the central building where the laser beam is generated, and five mirrors, including the BS, are hosted. Optical benches used to acquire the interference pattern are also hosted in this building. On the left part, the other buildings host the European Gravitational wave Observatory (Italy) (EGO) offices.

Credits : Virgo collaboration/N. Baldocchi

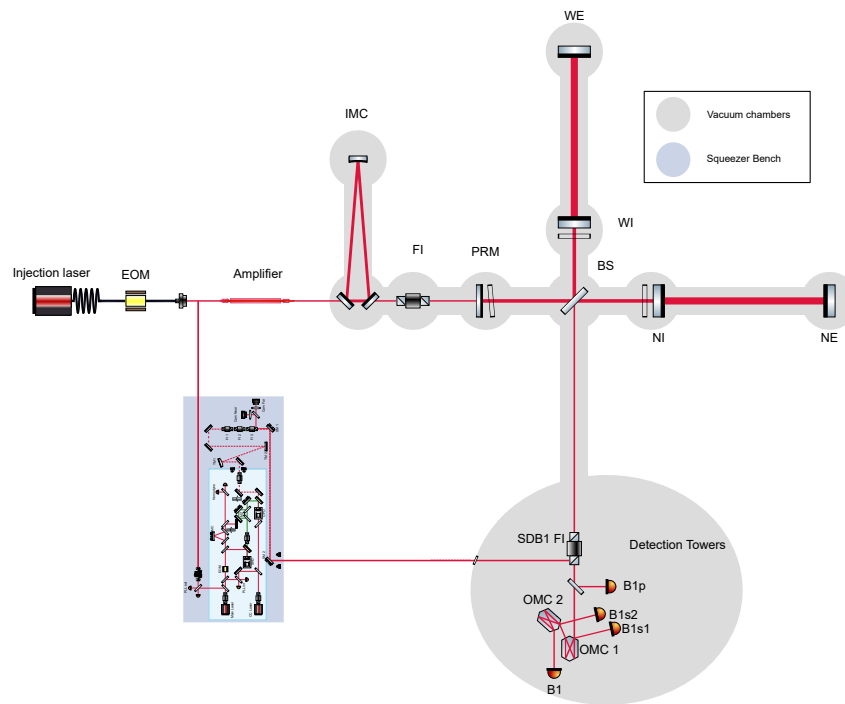


Figure 1.10: Simplified optical scheme of the Advanced Virgo detector during the O3 run. The detection benches Suspended Detection Bench 1 (SDB1) and Suspended Detection Bench 2 (SDB2) are represented by the Detection Towers on this scheme

are composed of beam jitter, laser frequency noise and Higher Order Mode (HOM) appearing on the produced beam. In order to correct these defects, the beam is sent to the Input Mode Cleaner (IMC). The IMC is a 150 m long triangular optical cavity mounted under vacuum with suspended mirrors. The role of this optical cavity is to filter the geometrical defect of the laser beam and mitigate the beam jitter. The output of the IMC

corresponds to the power entering the interferometer. Finally, a Faraday isolator is used to prevent back-reflected light to interfere with the input laser beam as this could spoil the beam quality. Note in figure 1.10 that from the IMC, all the main optical components are located inside vacuum.

The power recycling cavity

The PR has a Radius of Curvature (RoC) of 1430 m and a transmission of 5%. Together with the North Input mirror (NI), the West Input mirror (WI) and the BS it forms the power recycling cavity. When this cavity is locked, the power recycling gain is at the order of $G_{PR} \sim 33$.

The Fabry-Perot arm cavities

The Advanced Virgo arms are composed of Fabry-Perot cavities of length 3 km. Both end mirrors are fully reflectives while both input mirrors have a transmission of the order of $\sim 1.4\%$. This makes the arm cavity finesse of the order of $\mathcal{F} \sim 450$; Meaning that the arm cavity pole is at $f_p \sim 55$ Hz.

Because of the high power circulating inside the arm cavities (of the order of 100 kW), thermal gradient might appear inside the optics. This produces a deformation of the mirror surface and changes their Radius of Curvature (RoC). The optical path inside the mirror is also deformed which acts as a lens (so-called thermal lens). The change in RoC is compensated by installing Ring Heater (RH) around the mirrors. This system heats the mirror in a manner to reach a uniform heating of the mirror, thus canceling the effect of the circulating beam. The thermal lens is compensated by shining a CO₂ laser with a ring shape on a plate located in front of the mirror. This plate (so-called compensating plate), will also form a thermal lens that cancel the thermal lens generated inside the mirror.

The suspended mirrors

Six mirrors are suspended in the Advanced Virgo detector : the BS, the PR, the NI, the WI, the NE and the WE. The mirrors are made of fused silica with thin layers coatings made at Laboratoire des Matériaux Avancés (France) (LMA). The diameter of the mirrors is 35 cm except for the BS which diameter is 55cm. The mirrors have a state of the art polishing with roughness at the order of 0.4 nm so to not deform the circulating beam.

All these mirrors are suspended using the so-called super-attenuator system [38]. The super-attenuator consists of a serie of pendula together with blade springs. This allow to consider the suspended mirror as free test-masses on the horizontal plane above the super-attenuator resonant frequencies. Also, the super-attenuator isolates the suspended mirrors from seismic noise as the pendula and the blade springs respectively attenuate the horizontal and vertical motions of the mirrors.

The detection system

The Advanced Virgo detection system is composed of several optical benches which functions is to extract the gravitational wave signal and the control signals required to maintain the interferometer in nominal condition. In particular, two suspended benches placed under vacuum, the SDB1 and the SDB2 are hosting several optical components in order to extract the output signal of the interferometer. Roughly speaking, the goal of the SDB1 is to clean the interferometer output beam and insure manageable beam sizes on the bench while the goal of the SDB2 is to detect the interferometer output beam and various control beams.

First, SDB1 is hosting the so-called dark-fringe telescope (not represented in figure 1.10) that reduces the beam size from 22 mm to 1 mm. Then, the beam is filtered by the Output Mode Cleaner (OMC). In Advanced Virgo, the OMC is composed of two monolithic cavities in series. Each cavity is a bow-tie monolithic cavity of half round-trip length equal to 124 mm with finesse $F \sim 121$ [39]. The goal of the OMC is to filter the HOM in order to improve the interferometer contrast as well as filtering the control sidebands present on the beam. The HOM are induced by optical defects inside the interferometer. The OMC cavities are placed above Peltier cells that can stabilize the OMC temperature. This is especially useful to control the OMC length.

The SDB1 is also hosting a Faraday isolator, so-called the SDB1 Faraday isolator, that prevents back-scattered light on these optical benches to interfere with the interferometer output beam. There are also five windows on the vacuum chamber hosting SDB1 : four between the SDB1 and the SDB2 (not represented in figure 1.10) and another one between the SDB1 and the in-air squeezer.

Finally, the SDB2 is hosting several photodiodes. The interferometer output beam is detected by the B1 photodiodes. Several other photo-detectors are also present on the SDB2. Here, only the photodiodes that are used in this manuscript are presented. The B1p photodiodes is looking at a 1.5% pick-off of the interferometer output beam before the OMC. The B1s1 photodiode is looking at the beam reflected by the first OMC. The B1s2 is looking at the beam reflected of the second OMC (or equivalently to the beam transmitted by the first OMC).

The squeezer

In January 2018, a squeezer constructed at the Albert Einstein Institute *Hannover (Germany)* (AEI) has been installed on the Advanced Virgo detector [40]. The squeezer generates squeezed vacuum states and provides the control signals (described in more details in next chapter). It is installed on an in-air optical bench located close to the detection system. This squeezer can deliver up to 14 dB of squeezing over the entire sensitivity spectrum of Advanced Virgo.

The interferometer controls

As we have seen, a power-recycled Michelson interferometer with Fabry-Perot arm cavities can be described as the combination of several cavities. The maximum sensitivity is achieved by having the main laser beam resonant inside the PR and Fabry-Perot arm cavities and having the Michelson interferometer set in dark-fringe. These three degrees of freedom are sensed using frequency modulations of the main laser beam at 6 MHz, 8 MHz and 56 MHz [41]

Moreover, the modulation of the main laser frequency at 56 MHz allowed to stabilize the input laser frequency with respect to the Fabry-Perot arm cavities.

1.5 The gravitational wave detectors network

The relationship 1.16 has been obtained by assuming a gravitational wave propagating in the direction orthogonal to the interferometer plane. This is the most favorable case for a laser interferometer gravitational wave detector. But in general, gravitational waves can come from any direction, and the interferometer response to a gravitational wave is not isotropic. For instance, if one considers a gravitational wave propagating in the interferometer plane inclined by 45° with respect to the two arms, there is no differential variation of the arm length and therefore no detectable gravitational wave signal at the interferometer output.

In general, the interferometer response can be expressed for both the '+' and '×' polarizations by the antenna patterns [42] represented in figure 1.11.

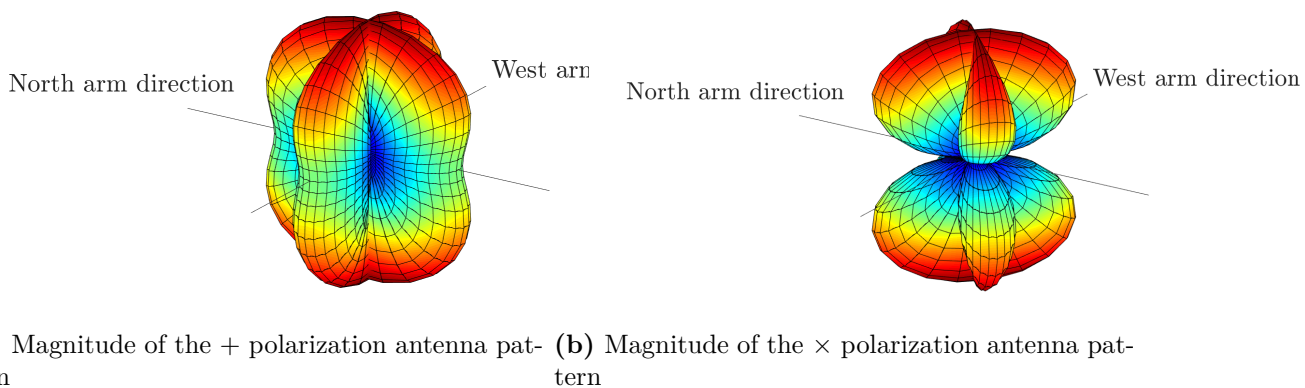


Figure 1.11: Magnitude of the plus (left) and cross (right) antenna response pattern for a Michelson interferometer with arms aligned with the North and West directions. The form and color represent both the magnitude of the antenna pattern going from a minimum in blue to a maximum in red

This figure represents the sensitivity of a gravitational wave detector to either a '+' or a '×' polarized gravitational wave coming from a given arbitrary direction.

The consequences of these antenna patterns are twofold.

First, an interferometric gravitational wave detector is sensitive to several positions on the sky. A single detector is therefore not able to pinpoint the gravitational wave source localization. For this reason, it is interesting to associate several detectors within a common network. Indeed, the gravitational wave source can be located using triangulation by comparing the arrival time of the gravitational wave signal. The localization of the gravitational wave source improves with the number of detectors within the network.

Combining several detectors together also allow to remove the local noises affecting each detectors.

Figure 1.12 shows the current and future gravitational wave detectors in the world. Currently, the Virgo and LIGO detectors have already started their observation together with German English gravitational wave Observatory (GEO600).



Figure 1.12: Location of current and future ground-based gravitational wave detectors. Credits : P. Shawhan [43]

The Virgo detector is located in Italy. It is a power recycled interferometer with 3 km long Fabry-Perot arm cavities [44]. The first direct detection of a gravitational wave signal involving the Virgo detector happened the August 14th 2017 jointly with LIGO [45].

The LIGO collaboration operates two detectors : One located in Hanford (Washington) and the other one in Livingston (Louisiana). Both detectors are dual recycled interferometers with 4 km long Fabry-Perot arm cavities [46].

KAGRA is a Japanese detector located inside the Kamioka mine. It will be a dual-recycled interferometer with 3 km long Fabry-Perot cavity arms. It will be the first underground detector with cryogenic mirrors. It is currently in commissioning and will soon take data together with the LIGO and Virgo detectors [47].

GEO600 is a British-German detector located in Hannover (Germany). It is a dual recycled with 600 m long folded arms interferometer. It is extensively used for research and development of new techniques (for instance the signal recycling technique or the frequency-independent squeezing injection) [48] [49].

LIGO India will be a third detector of the LIGO collaboration. It will share a similar

design to the LIGO detectors already installed. It should start to operate in 2024.

This network is looking for coincident detections that help determining if an event is from astrophysical origin. The data analysis is shared between the Virgo and LIGO collaboration, with KAGRA joining them soon.

A second consequence of the antenna patterns of the detector is that a gravitational wave signal amplitude is dependent on the location of the source with respect to the detector. Thus two ways of characterizing the detector performances appear. One is the maximal distance observable by the detector for a source perfectly oriented with respect to the detector. However, because the network is constituted of detectors with different orientations to increase the sky coverage, it is not possible to have a gravitational wave source in the perfect orientation for all detectors.

Therefore, another figure of merit has been chosen. It consist to define the radius of the sphere around the detector that has the same area as the detector antenna pattern. The radius of this sphere is called the range of the detector. In general, the BNS range is defined by two neutron stars with each masses of $1.4 M_{\odot}$ detected with an SNR of 8. The BBH range is defined by two black holes with each masses of $30 M_{\odot}$ also detected with an SNR of 8.

This gravitational wave network is sharing common observations periods and upgrades period as represented in figure 1.13 based on [50].

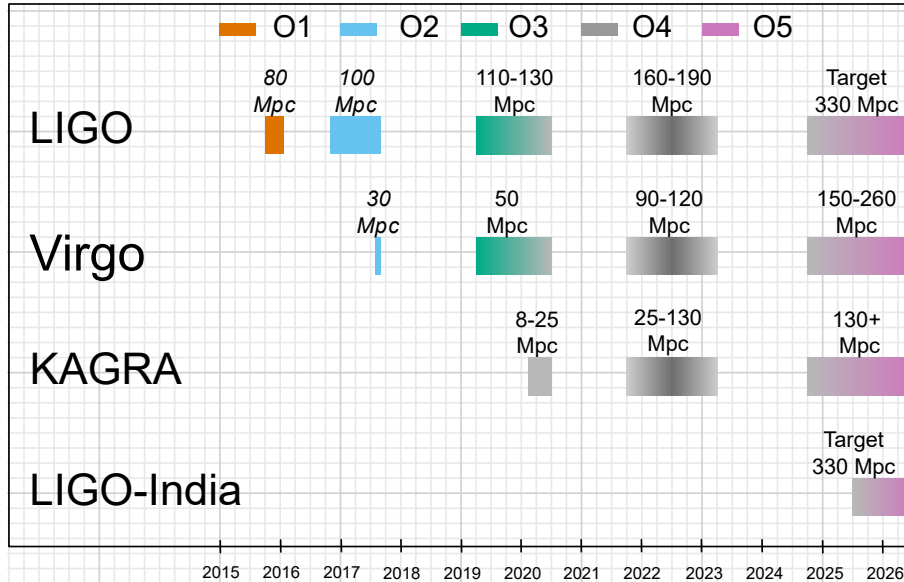


Figure 1.13: Planned sensitivity evolution and observing runs of the LIGO, Virgo and KAGRA detectors. Credits : [50]

It can be seen that all the detectors alternate between observing periods with commissioning periods. Improving the detectors sensitivity is indeed of particular interest as the numbers of events can be approximated by $\Delta T \cdot R^3$ with ΔT the observing duration and R the detector range.

1.6 Gravitational wave detections

On September 14th 2015 at 09:50:45 UTC, both LIGO interferometers detected the first gravitational wave signal during the O1 run. In this section, a non-exhaustive list of the various gravitational wave events are presented.

GW150914 : The first direct detection of gravitational wave GW150914 is the first direct detection of gravitational wave performed by the LIGO detectors. It was emitted by a BBH each with mass $30M_{\odot}$. This detection demonstrated that BBH could merge and started the gravitational wave astronomy [4].

GW170817 : The first gravitational wave detection with electromagnetic counterparts GW170817 is the first direct detection of gravitational wave emitted by a BNS system [51]. It was a major discovery for the scientific community as it was the first gravitational wave signal detected in coincidence with a short gamma ray burst named GRB 170817A [16]. This confirmed the hypothesis that short gamma ray bursts can originate from the merger of a BNS. Since the gamma ray burst was detected 1.7 s after the gravitational wave, the gravitational wave speed could be highly constrained which lead to high constraints on alternate gravitation theory. Furthermore, because both LIGO and Virgo detectors were in observing mode, this allowed a good sky localization (the error bar was 16 deg²) and thus the host galaxy could be identified as NGC 4993. This provided an estimate of the Hubble constant to $H_0 = 70_{-8}^{+12}$ km/s/Mpc.

More than 70 electromagnetic observatories participated to the follow-up campaign of this event. This represents the first multi-messenger observation combining electromagnetic signals and direct gravitational wave signal. These electromagnetic observations from ultra violet to near infra red showed the formation of a kilonova due to the r-processes where many chemical elements heavier than iron are produced.

Other detections During the O1 and O2 runs, nine other gravitational wave signals emitted by BBH have been detected [52]. Since the O3 run, the gravitational wave community decided to promptly release informations about the gravitational wave signal candidates such as the source origin and sky localization. This should allow a more rapid follow-up of these sources. During the O3 run, 50 gravitational wave candidates have been shared. This increase in the number of gravitational wave candidates highlights the benefit of improving the sensitivity of the detectors.

1.7 Conclusion

This chapter has introduced the gravitational waves predicted by the theory of general relativity. The principle of interferometric gravitational wave detectors which first directly

detected gravitational wave were also presented. The sensitivity of such detectors has also been derived from the various noise sources that affect their performances. Among these noises, the shot noise is a fundamental noise that arises from the quantum nature of light. It is therefore always present, even for a perfect detector. Reducing the quantum noise brings direct improvement on the detector sensitivity. This translates into the increase of the gravitational wave detections as well as the ability to detect gravitational wave sources further away in the Universe. The work presented in this manuscript focuses on reducing the Advanced Virgo detector quantum noise.

2

Quantum description of the interferometer

Contents

2.1	The electromagnetic field	28
2.1.1	The quantization of the electromagnetic field	28
2.1.2	The coherent states	31
2.1.3	The quadrature operators and Heisenberg uncertainty principle	31
2.1.4	The quantum states representation	36
2.2	The quantum states in experiments	42
2.2.1	The squeezed states generation	42
2.2.2	The beam-splitter model	44
2.2.3	The squeezing detection	45
2.2.4	The squeezing degradation	46
2.3	The interferometer quantum noise	50
2.3.1	Michelson	50
2.3.2	The Advanced Virgo quantum noise	54
2.3.3	The frequency dependent squeezing generation	55
2.4	Conclusion	57

The last chapter has shown that the quantum noise is a fundamental noise of the interferometric gravitational wave detectors. This noise is limiting the sensitivity of these detectors above 100 Hz. Following a semi-classical description of the fields of light present in the interferometer, it appeared that it is not possible to decrease the quantum noise over the entire sensitivity spectrum. In this chapter, the quantum behavior of the interferometer is described. It is also shown that the use of peculiar states of light known as squeezed vacuum states, allows to decrease the quantum noise over the entire sensitivity

spectrum of gravitational wave detectors.

2.1 The electromagnetic field

The electromagnetic field is at the heart of the interferometric measurement. In this section, the quantum states useful for the interferometer are derived.

2.1.1 The quantization of the electromagnetic field

The classical description of light arises from the Maxwell equations as an electromagnetic field. Assuming x polarized light propagating along the z direction, a single mode of the electrical field can be written as

$$E_x(z, t) = \mathcal{E}_0 \sin(kz) \sin(\omega t + \phi) \quad (2.1)$$

with E_0 the electrical field amplitude, k its wave vector, ω its angular frequency and ϕ a phase factor.

Introducing the two field quadratures $\mathcal{E}_1 = \mathcal{E}_0 \sin(\omega t)$ and $\mathcal{E}_2 = \mathcal{E}_0 \cos(\omega t)$, it can be represented in the phasor diagram as represented in figure 2.1. In this representation, the electrical field is represented by a vector of length \mathcal{E}_0 that rotates counter-clockwise as a function of time. The electrical field can therefore be perfectly known from its projections onto the two field quadratures. Note that from the equation 2.1, a field with null amplitude is represented by a point in the phasor representation.

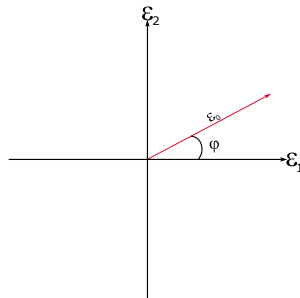


Figure 2.1: The phasor representation of a single mode of the electrical field along its two quadratures

The Ampere-Maxwell equation gives a relationship between the electrical field E and the magnetic field B in vacuum as a function of the vacuum permittivity ϵ_0 and vacuum permeability μ_0 as

$$\frac{1}{\mu_0} \nabla \times B = \epsilon_0 \frac{\partial E}{\partial t} \quad (2.2)$$

Combining the two previous equations allows to express the magnetic field as

$$B_y(z, t) = \mathcal{B}_0 \cos(kz) \cos(\omega t) \quad (2.3)$$

where $\mathcal{B}_0 = \mathcal{E}_0 \cdot \sqrt{\epsilon_0 \mu_0}$ is the magnetic field amplitude and the phase factor has been set to zero.

The equations 2.1 and 2.3 show that the electrical and magnetic fields oscillate 90 °out of phase with respect to each other. This behavior is similar to the behavior of a harmonic oscillator where its position and momentum also oscillate 90 °out of phase with each other. Thus a single mode of the electromagnetic field can be quantized following the same method as for the harmonic oscillator.

The quantization of a single mode of the electromagnetic field yields :

$$\begin{aligned} \hat{E}_x(z, t) &= \mathcal{E}_0 \left(\hat{a}(t) e^{-i\omega t} + \hat{a}^\dagger(t) e^{i\omega t} \right) \\ \hat{B}_y(z, t) &= \mathcal{B}_0 \left(\hat{a}(t) e^{-i\omega t} + \hat{a}^\dagger(t) e^{i\omega t} \right) \end{aligned} \quad (2.4)$$

with the non-Hermitian annihilation operator \hat{a} and creation operator \hat{a}^\dagger that verify the commutation relationship

$$[\hat{a}, \hat{a}^\dagger] = 1 \quad (2.5)$$

From equations 2.4, the Hamiltonian for a single mode of the electromagnetic field writes

$$\hat{\mathcal{H}} = \hbar\omega \left(\hat{a}^\dagger \hat{a} + \frac{1}{2} \right) \quad (2.6)$$

This Hamiltonian depends on the product of the ladder operators that is also known as the number operator defined by $\hat{n} = \hat{a}^\dagger \hat{a}$. The eigenstates of the number operators $|n\rangle$ are the eigenstates of the Hamiltonian defined in the equation 2.6 :

$$\hat{\mathcal{H}} |n\rangle = E_n |n\rangle \quad (2.7)$$

with E_n the eigenstate energy.

These eigenstates are called Fock states and form a complete orthogonal set. Applying the annihilation operator and the creation operator to the equation 2.7 an using the commutation relationship defined in equation 2.5, it becomes

$$\begin{aligned} \hat{\mathcal{H}} \hat{a} |n\rangle &= (E_n - \hbar\omega) \hat{a} |n\rangle \\ \hat{\mathcal{H}} \hat{a}^\dagger |n\rangle &= (E_n + \hbar\omega) \hat{a}^\dagger |n\rangle \end{aligned} \quad (2.8)$$

Therefore, the action of the annihilation operator is to remove one quantum of energy from the total energy of the field (hence the name of this operator). In a similar fashion, the creation operator adds a quantum of energy (or photon) to the field total energy. From this equation, it is also possible to derive the relationship between the energy of different eigenstates as $E_{n+1} = E_n + \hbar\omega$. This also means that the number operator corresponds to the number n of photons in a Fock state :

$$E_n = \hbar\omega \left(n + \frac{1}{2} \right) \quad (2.9)$$

with n a positive integer. This equation exhibits the quantization of the energy of a single mode of the electromagnetic field as discrete multiple levels defined by the number of photons they contain.

Furthermore, because the energy of a single mode of the electromagnetic field is positive, there is a lower energy state defined by

$$\hat{\mathcal{H}} |0\rangle = E_0 |0\rangle = \frac{1}{2}\hbar\omega |0\rangle \quad (2.10)$$

This state $|0\rangle$ is the vacuum state as it corresponds to the state without photons.

It is also possible to express the action of the ladder operators on the Fock states as [53]

$$\begin{aligned} \hat{a} |n\rangle &= \sqrt{n} |n-1\rangle \\ \hat{a}^\dagger |n\rangle &= \sqrt{n+1} |n+1\rangle \end{aligned} \quad (2.11)$$

These relationships allow to compute the average value of a single mode of the electrical field :

$$\langle n | \hat{E}_x | n \rangle = \mathcal{E}_0 \sin(kz) \langle n | \hat{a} + \hat{a}^\dagger | n \rangle = 0 \quad (2.12)$$

This null average value of the electrical field is not suited to represent electromagnetic fields with large numbers of photons (eg the input laser of the Virgo detector for the O3 run contained approximately $P/(\hbar \omega) \sim 10^{20}$ photons). It is therefore required to introduce other quantum states in order to fully describe the interferometer.

2.1.2 The coherent states

The coherent states were introduced by Roy J. Glauber in 1963 [54]. These states correspond to the eigenstates of the annihilation operator

$$\hat{a}|\alpha\rangle = \alpha|\alpha\rangle \quad (2.13)$$

where the eigenvalues α are complex (and thus we can write $\alpha = |\alpha|e^{i\theta}$).

A coherent state can be obtained by applying on a vacuum state the displacement operator $\hat{D}(\alpha) = \exp(\alpha\hat{a} - \alpha^*\hat{a}^\dagger)$. A coherent state is then given by

$$|\alpha\rangle = \hat{D}(\alpha)|0\rangle \quad (2.14)$$

Because the number states form a complete set, it is possible to expand the coherent state $|\alpha\rangle$ over the number states as [53]

$$|\alpha\rangle = e^{-\frac{1}{2}|\alpha|^2} \sum_{n=0}^{\infty} \frac{\alpha^n}{\sqrt{n!}} |n\rangle \quad (2.15)$$

This allows to derive the expectation value of the number operator \bar{n} and the fluctuations in this number $\Delta\hat{n}$ as

$$\begin{aligned} \bar{n} &= \langle\alpha|\hat{n}|\alpha\rangle = |\alpha|^2 \\ \Delta\hat{n} &= \sqrt{\langle\hat{n}^2\rangle - \langle\hat{n}\rangle^2} = \sqrt{\bar{n}} \end{aligned} \quad (2.16)$$

The equation 2.16 exhibits the interest of the coherent states. First, their expectation value corresponds to the expected behavior of a powerful laser field : The power increases with the number of photons in the field. Also, the fluctuations in this number (and therefore in the field power) follow a Poissonian distribution as for a classical laser field. Coherent fields are therefore the fields that best approximate a laser field. In order to make this similarity more apparent, it is interesting to express the coherent states over quadratures as was done for the classical electrical field.

2.1.3 The quadrature operators and Heisenberg uncertainty principle

Because the annihilation and creation operators are not Hermitian, they do not represent observable quantities. It is therefore convenient to introduce the Hermitian quadrature operators as

$$\begin{aligned}\hat{X}_1 &= (\hat{a} + \hat{a}^\dagger) \\ \hat{X}_2 &= i(\hat{a}^\dagger - \hat{a})\end{aligned}\quad (2.17)$$

Their commutation relationship can be derived from the equation 2.5 as

$$[\hat{X}_1, \hat{X}_2] = 2i \quad (2.18)$$

Using the equation 2.4, a single mode of the electric field is expressed as a function of the quadrature operators as

$$\hat{E}_x(z, t) = \mathcal{E}_0 (\hat{X}_1 \cos(\omega t) + \hat{X}_2 \sin(\omega t)) \quad (2.19)$$

From equation 2.19, one can recognize that the \hat{X}_1 and \hat{X}_2 corresponds respectively to the amplitude and phase quadratures.

It is also possible to define an arbitrary quadrature operator as

$$\begin{aligned}\hat{X}_\theta &= \hat{X}_1 \cos(\theta) + \hat{X}_2 \sin(\theta) \\ &= \hat{a}(t) e^{i\theta} + \hat{a}^\dagger(t) e^{-i\theta}\end{aligned}\quad (2.20)$$

where the amplitude and phase quadrature correspond respectively to $\theta = 0$ and $\theta = \pi/2$.

This expression of the electrical field over these two quadratures is similar to the one of a classical field. However, the Heisenberg uncertainty principle states that for two non commuting operators, it is not possible to measure with arbitrary precision their physical quantities. It can be applied to the two quadratures operators as

$$\begin{aligned}(\Delta \hat{X}_1)^2 (\Delta \hat{X}_2)^2 &\geq \frac{1}{4} |[\hat{X}_1, \hat{X}_2]|^2 \\ &\geq 1\end{aligned}\quad (2.21)$$

where $(\Delta \hat{X}_1)^2$ and $(\Delta \hat{X}_2)^2$ are the standard deviation of the operators \hat{X}_1 and \hat{X}_2 respectively.

The standard deviation can be also expressed as a function of their variances as

$$\Delta \hat{X}_1 \Delta \hat{X}_2 \geq 1 \quad (2.22)$$

This means that it is not possible to measure with an arbitrary precision the amplitude and phase quadratures simultaneously. This always present uncertainty is called the

quantum fluctuations of the electromagnetic field. It can be shown [53] that the energy of the quantum fluctuations correspond to the energy of the vacuum state that appears as the factor $\frac{1}{2}\hbar\omega$ in the Hamiltonian for the total energy of the electrical field (eg in the equation 2.9). It also means that the vacuum state corresponds only to quantum fluctuations.

The states that achieve the equality in equation 2.21, are called the minimum uncertainty states.

The squeezed states

The Heisenberg uncertainty principle presented in the equation 2.21 places only a limit on the product of two non-commuting observables. There is therefore no constraint on the individual variance. For instance, it is possible to have states where the variance of one quadrature is below the one of a minimum uncertainty states. Because of the Heisenberg uncertainty principle, this comes at the expense of having an increased variance in the orthogonal quadrature.

$$\begin{aligned}\Delta\hat{X}_\theta &< 1 \\ \Delta\hat{X}_{\theta+\frac{\pi}{2}} &> 1\end{aligned}\tag{2.23}$$

The states described by the relationships 2.23 are called squeezed states.

The previous sections have introduced two quantum states that will be useful to describe the quantum noise of a gravitational wave interferometric detector. First, the vacuum state that describe an electromagnetic field with no photons and a coherent state that describe a powerful laser field. Because of the Heisenberg uncertainty principle, these two states present quantum fluctuations over their amplitude and phase quadratures. Recalling that the gravitational wave signal is encoded into the phase of the laser field at the output of the interferometric detector, it could mean that the fluctuations along the phase quadrature could limit the detection of gravitational wave. Squeezed states, that are quantum states with quantum fluctuations over one quadrature reduced below the one of a coherent state, are therefore particularly appealing for gravitational wave interferometric detectors.

The squeezed states can be generated from a coherent state by applying the unitary squeezing operator defined by

$$\hat{S}(\xi) = \exp\left[\frac{1}{2}\left(\xi^*\hat{a}^2 - \xi\hat{a}^{\dagger 2}\right)\right]\tag{2.24}$$

The squeezing operator is a unity operator that destroys and creates photon by pair. It depends on the complex parameter $\xi = re^{2i\theta}$ with r being the squeezing factor and θ the squeezing angle.

For instance, the squeezed vacuum states are generated by applying the squeezing operator to the vacuum state : $|\xi\rangle = \hat{S}(\xi)|0\rangle$. And the bright squeezed states are generated by further applying the displacement operator : $|\xi, \alpha\rangle = \hat{D}(\alpha)\hat{S}(\xi)|0\rangle$ and correspond therefore to quantum states with photons ($n = |\alpha|^2$) and quadrature fluctuations reduced below the one of a coherent state.

The effect of the squeezing operator on two orthogonal quadratures with one of the two being aligned with the squeezing angle θ is :

$$\hat{S}^\dagger(\xi) \left(\hat{X}_\theta + i\hat{X}_{\theta+\frac{\pi}{2}} \right) \hat{S}(\xi) = \hat{X}_\theta e^{-r} + i\hat{X}_{\theta+\frac{\pi}{2}} e^r \quad (2.25)$$

This highlights that one quadrature is attenuated while the orthogonal quadrature is amplified. Their fluctuations can then be derived as

$$\begin{aligned} (\Delta\hat{X}_\theta)^2 &= e^{-2r} \\ (\Delta\hat{X}_{\theta+\frac{\pi}{2}})^2 &= e^{2r} \end{aligned} \quad (2.26)$$

which corresponds to the expected behavior of a squeezed state : the fluctuations of the quadrature aligned with the squeezing angle are reduced below one while the fluctuations of the orthogonal quadrature are increased above one. The value of the squeezing factor r gives the reduction or augmentation of the fluctuations with respect to the one of a coherent state.

When the squeezing angle θ is not aligned with the quadrature angle ϕ , the uncertainty is given by

$$\Delta\hat{X}_\phi = \cos(\phi - \theta)^2 e^{-2r} + \sin(\phi - \theta)^2 e^{2r} \quad (2.27)$$

This is represented in figure 2.2. This highlights the fact that the squeezing operator is dependent on the phase.

It is convenient to introduce the variances of the squeezed and anti-squeezed quadratures which correspond to the minimum and maximum of the variance of a squeezed states over the squeezing angle respectively as [55]

$$\begin{aligned} V_+ &= \max_{\theta} (\Delta X_\theta)^2 \\ V_- &= \min_{\theta} (\Delta X_\theta)^2 \end{aligned} \quad (2.28)$$

Also, as the squeezing factor impacts the variance level with respect to the vacuum variance V_{vac} , the squeezing is often characterized through its squeezing ratio :

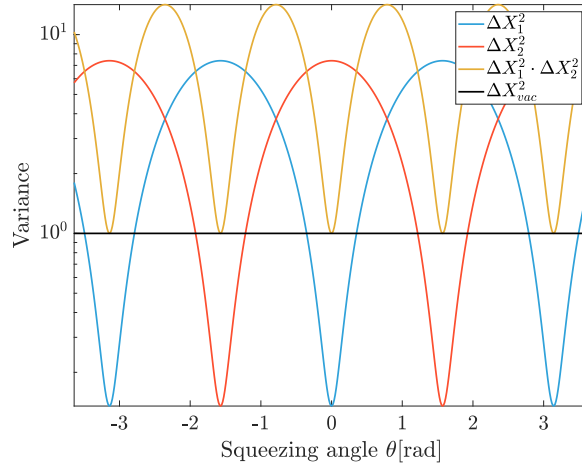


Figure 2.2: Variances of the two quadratures of a squeezed states with $r = 1$ as a function of the squeezing angle θ and setting the quadrature angle to zero. When a quadrature has a variance less than the one of the vacuum state (squeezing), the orthogonal quadrature is above the one of the vacuum state (anti-squeezing). When the squeezing angle is a multiple of $\pi/2$, the state is a minimum uncertainty state as shown in the product of the two quadratures variances (yellow)

$$R_+ = \sqrt{\frac{V_+}{V_{vac}}}$$

$$R_- = \sqrt{\frac{V_-}{V_{vac}}} \quad (2.29)$$

$$(2.30)$$

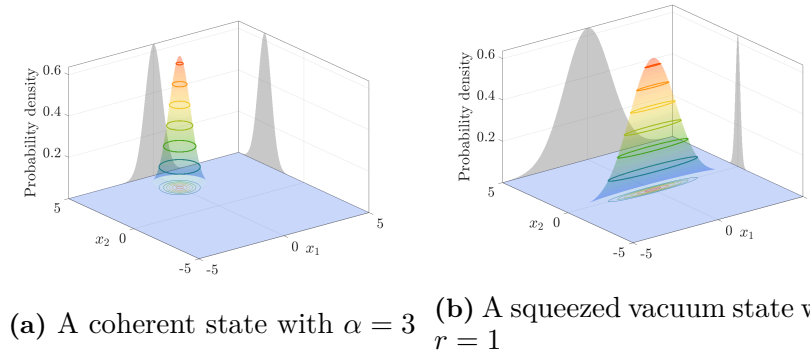
This ratio is often expressed in decibel using

$$\begin{aligned} R_{\pm, dB} &= 20 \log_{10} (R_{\pm}) \text{ [dB]} \\ &= 10 \log_{10} \left(\frac{V_{\pm}}{V_{vac}} \right) \text{ [dB]} \end{aligned} \quad (2.31)$$

Note that the squeezing sign is often omitted (eg 3 dB of squeezing corresponds to a reduction of 3 dB of the variance).

In a similar fashion as for the coherent state, it is possible to expand a squeezed state over the number state [53]. This allows to compute the mean photon number of a bright squeezed state as

$$\langle \alpha, \xi | \hat{n} | \alpha, \xi \rangle = |\alpha|^2 + \sinh^2(r) \quad (2.32)$$



(a) A coherent state with $\alpha = 3$ (b) A squeezed vacuum state with $r = 1$

Figure 2.3: Wigner functions of a coherent state (left) and a squeezed vacuum state (right). The projection of the Wigner function on the two quadrature axes is also represented

Equation 2.32 shows that the squeezed vacuum state (where $|\alpha|^2 = 0$) has its mean photon number not null. And there is thus power in the squeezed vacuum beam. However, this power can be considered negligible in most cases. For instance, the current squeezed vacuum state source used in Advanced Virgo generates squeezed vacuum state with 5.8 photons per second and a power at the order of 1.1 aW. Despite having larger mean photon number than the vacuum state, these states are still called squeezed vacuum states because they do not have coherent amplitude. This fact is important for the representation of the squeezed states as described in the next section.

2.1.4 The quantum states representation

In order to get a more intuitive idea of the various states introduced so far, it is interesting to represent them in a pictorial way.

It has already been introduced that the two quadrature operators correspond to the amplitude and phase quadrature of the electrical field and that a classical electrical field can be fully described by the phasor picture as in figure 2.1. In order to better understand how a coherent state compares to a classical field, it is therefore interesting to describe quantum states in the phasor picture.

The principal difference between the classical and quantum description of a single mode of the electrical field is due to the Heisenberg uncertainty principle that implies quantum fluctuations in the amplitude and phase quadratures. This means that for any measurement, neither the amplitude nor phase quadrature values can be measured with arbitrary precision. There is rather, an uncertainty on the measurement which can be described by probability distribution.

To describe this probability, it is useful to introduce the Wigner function [56]. Indeed, the Wigner function is a quasi-probability distribution that can be used to derive the probability distributions of two non-commuting quadratures (quasi-probability distribution as it can take negative values). For instance, its projection onto each quadrature gives the

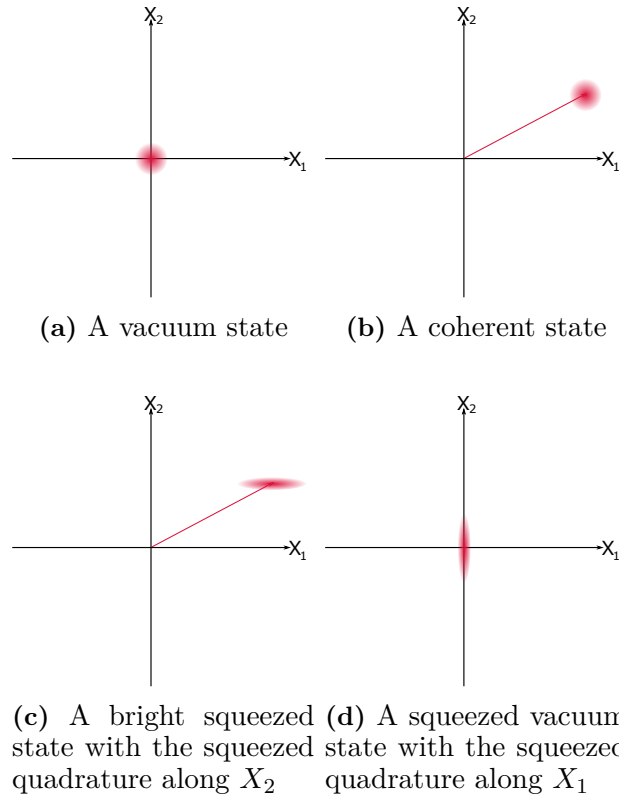


Figure 2.4: The phasor representations of the quantum states introduced so far

probability distribution P of measuring a certain amplitude x_1 of the quadrature \hat{X}_2 :

$$P(x_1) = \int_{-\infty}^{\infty} W(x_1, x_2) dx_2 \quad (2.33)$$

For instance, the Wigner function of a coherent state $|\alpha\rangle$ and a squeezed vacuum state along the \hat{X}_1 quadrature are [53]:

$$W(x_1, x_2) = \frac{2}{\pi} \exp \left[-2(x_1 + \Re(\alpha))^2 - 2(x_2 - \Im(\alpha))^2 \right] \quad (2.34)$$

$$W(x_1, x_2) = \frac{2}{\pi} \exp \left[-2x_1^2 e^{2r} - 2x_2^2 e^{-2r} \right] \quad (2.35)$$

The Wigner functions of a coherent state with $\alpha = 3$ and a squeezed vacuum state with $r = 1$ are represented in figure 2.3. In the case of a coherent state, this corresponds to two identical Gaussian distributions centered around α . The contours of the Wigner function are given by circles. For a squeezed vacuum state, the Wigner function corresponds also to two Gaussian distribution but this time with its contours being elliptical.

The contour lines presented in figure 2.3 corresponds to the projection of the quantum states into the two quadratures. This representation is similar to the classical phasor that was presented in figure 2.1. It is therefore possible to use the Wigner functions of quantum

states to represent them in the phasor picture. Quantum phasors of the quantum states discussed so far are presented in figure 2.4.

For instance, a coherent state can be represented as in figure 2.4b by an uncertainty circle centered around the coherent excitation α . The comparison of this figure to the phasor of a classical electromagnetic field presented in figure 2.1 further highlights their similarities. However, the quantum fluctuations of the coherent state adds an area of uncertainty that limits the measurement accuracy of its quadrature values. Recalling that the quadratures corresponds to the amplitude and phase of the electromagnetic field, it means that the quantum fluctuations can be assimilated to fluctuations in amplitude or phase of the electromagnetic field.

The squeezed vacuum state is represented as in figure 2.4d by an uncertainty ellipse centered around $\alpha = 0$. This ellipse axes are proportional to the uncertainty of their quadratures. Especially, one quadrature exhibits smaller uncertainty than the one of a coherent state. It means that this quadrature can be measured more accurately than the one of a coherent state. Since both coherent and squeezed vacuum states are minimum-uncertainty states, the area of their uncertainty ellipses are identical and equal to one : $\Delta x_\theta \Delta x_{\theta+\frac{\pi}{2}} = 1$ where θ is the direction of one of the ellipse axis.

The phasor representation of quantum states allowed to see that the quantum fluctuations can be assimilated to phase or amplitude fluctuations. This allows to describe in another way these quantum states : the sidebands picture. In order to introduce this representation, it is first interesting to go back to the classical electrical field. Fluctuations in amplitude and noise of this field can be considered as modulation of the amplitude and phase respectively where the modulation depth M and the modulation frequency ω_M depends on the nature of the fluctuation.

An amplitude modulated electrical field E_{am} is expressed as

$$\begin{aligned} E_{am}(t) &= E_0 e^{i\omega_0 t} (1 + M \cos(\omega_m t)) \\ &= E_0 e^{i\omega_0 t} \left(1 + \frac{M}{2} e^{i\omega_m t} + \frac{M}{2} e^{-i\omega_m t} \right) \end{aligned} \quad (2.36)$$

The equation 2.36 shows that an amplitude modulation is equivalent to a carrier field with amplitude E_0 and pulsation ω_0 and two sidebands with amplitude $E_0 \frac{M}{2}$ at the pulsation $\omega_0 \pm \omega_m$. In the rotating frame (that is the frame fixed with respect to the carrier field), the sideband with the pulsation $\omega_0 - \omega_m$ rotates clockwise while the sideband with the pulsation $\omega_0 + \omega_m$ rotates anti-clockwise. Finally, the total field can be computed from the sums of these three fields. Because the two sidebands rotates in opposite directions, their sum cancel out and adds at peculiar times. As represented in figure 2.5a, the sidebands represented by the arrows at the frequencies $\pm\omega_m$ adds when they are both real (ie along the amplitude quadrature) and cancel out when they are both imaginary (ie along the phase quadrature). The sum of the carrier and sidebands is represented by the blue arrow. It can be seen that the sum of the two sidebands results indeed in an amplitude modulation of the total field.

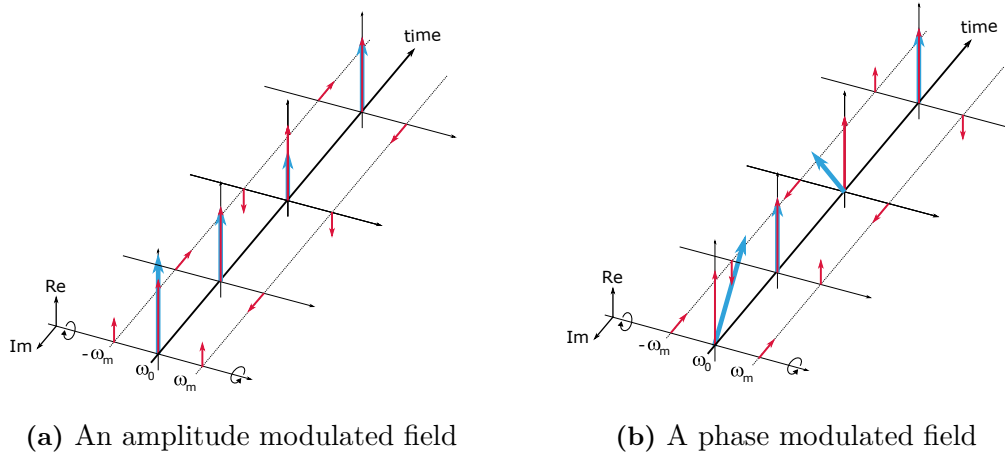


Figure 2.5: The sidebands representation of both an amplitude and phase modulated field. The effect of the modulation can be expressed as the addition of two sidebands around the carrier field represented by the red arrows. Depending on the modulation type, the sidebands cancel in phase (leading to amplitude modulation) or in amplitude (leading to phase modulation). The total field is represented by the blue arrow

A similar analysis of a phase modulated field can be performed.

$$\begin{aligned}
 E_{pm}(t) &= E_0 e^{i\omega_0 t + iM \cos(\omega_m t)} \\
 &\sim E_0 e^{i\omega_0 t} (1 + iM \cos(\omega_m t))
 \end{aligned} \tag{2.37}$$

$$= E_0 e^{i\omega_0 t} \left(1 + i\frac{M}{2} e^{i\omega_m t} + i\frac{M}{2} e^{-i\omega_m t} \right) \tag{2.38}$$

where the approximation holds for small modulation depth.

Equation 2.38 gives a similar description of a phase modulated field into a stationary carrier field with two sidebands with pulsation $\omega_0 \pm \omega_m$. But this time, the sidebands amplitudes are imaginary: $iE_0 \frac{M}{2}$. It is represented in figure 2.5b. This time, the two sidebands cancel out when they are both real and the total field exhibits the expected phase modulation.

Going back to the quantum states, it can be recalled that they possess fluctuations in both amplitude and phase that can also be represented in the sidebands picture. Since the quantum fluctuations are random, it means that at any given time there are both amplitude and phase noise. This can be represented by several several uncorrelated sidebands around the carrier (which length is defined by the number of photons in the field). The amplitude of these sidebands follow a Gaussian distribution. The quantum sideband picture can be obtained by averaging in time the sidebands equally separated around the carrier frequency. Therefore, in a similar manner to the transition between the classical and the quantum phasor picture, the quantum fluctuations can be represented in the sidebands picture as the uncertainty area present at every sidebands around the (possible) carrier.

Applying the squeezing operator to the vacuum states effectively adds photons to the vac-

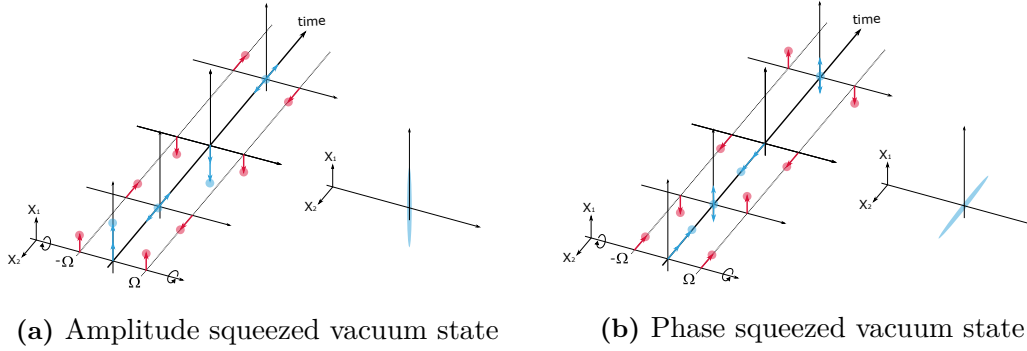


Figure 2.6: The sidebands representation of both an amplitude and a phase squeezed vacuum states. For clarity, only one pair of sidebands is represented. The left figures show the time evolution of the sidebands. The correlated sidebands induced by the squeezing operator are superposed to the uncertainty area. The resulting uncertainty area is represented on the right as an integration over time of the left figures

uum state (see equation 2.32). This means that in addition to the uncertainty area arising because of the quantum fluctuations, deterministic phasors are also present. Recalling that the two photons of a squeezed states are created by pair, these phasors are correlated with the correlation increasing with the squeezing factor. Therefore, the quantum noise sidebands present now correlations at frequencies $\omega \pm \Omega$. For amplitude squeezing, the sidebands are aligned in the phase quadrature but counter-aligned in the amplitude quadrature. The opposite is happening for the phase squeezing. This is represented in figure 2.6.

This description of the quantum states also leads to the two-photons formalism [57] [58]. Indeed, this formalism is especially efficient to describe optical components that act on both sidebands of the field.

The annihilation operator can be expressed as a function of the frequency as

$$\hat{a}(t) = \int_{-\infty}^{+\infty} \frac{d\Omega}{2\pi} \hat{a}(\Omega) e^{i\Omega t} \quad (2.39)$$

and the creation operator is such that : $(\hat{a}(\Omega))^\dagger = \hat{a}^\dagger(-\Omega)$.

The annihilation operators for the upper and lower sideband fields at the frequencies $\omega_0 \pm \Omega$ can be written as

$$\begin{aligned} \hat{a}_+ &= \hat{a}(\omega_0 + \Omega) \\ \hat{a}_- &= \hat{a}(\omega_0 - \Omega) \end{aligned} \quad (2.40)$$

In this formalism, the quadrature operators are redefined as in [57] :

$$a_1 = \frac{a_+ + a_-^*}{\sqrt{2}}$$

$$a_2 = \frac{a_+ - a_-^*}{i\sqrt{2}} \quad (2.41)$$

$$(2.42)$$

The varying part of the electric field is expressed (in SI units) as a function of its sideband components around the frequency ω_0 as in [57] :

$$E(t) = \cos(\omega_0 t) \left[\sqrt{\frac{4\pi\hbar\omega_0}{Ac}} \int_{-\infty}^{\infty} (a_1 e^{-i\Omega t} + a_1^\dagger e^{i\Omega t}) \frac{d\Omega}{2\pi} \right]$$

$$+ \sin(\omega_0 t) \left[\sqrt{\frac{4\pi\hbar\omega_0}{Ac}} \int_{-\infty}^{\infty} (a_2 e^{-i\Omega t} + a_2^\dagger e^{i\Omega t}) \frac{d\Omega}{2\pi} \right] \quad (2.43)$$

with A being the effective cross section area of the field.

Also, it is convenient to regroup the quadratures operator into a single 2×2 matrix $\mathbf{a} = \begin{pmatrix} a_1 \\ a_2 \end{pmatrix}$.

The vacuum state is described by the unity matrix in this formalism.

The action of optical components are expressed by 2×2 matrix \mathbf{T} such that

$$\mathbf{b} = \mathbf{T}\mathbf{a} \quad (2.44)$$

For instance, in the two-photons formalism, the action of the squeezing operator is described by the matrix

$$\mathbf{S}(r, \theta) = R_\theta S_r R_\theta^\dagger = R_\theta S_r R_{-\theta}$$

$$= \begin{pmatrix} \cos(\theta) & -\sin(\theta) \\ \sin(\theta) & \cos(\theta) \end{pmatrix} \begin{pmatrix} e^r & 0 \\ 0 & e^{-r} \end{pmatrix} \begin{pmatrix} \cos(\theta) & \sin(\theta) \\ -\sin(\theta) & \cos(\theta) \end{pmatrix} \quad (2.45)$$

which describes squeezing at θ by the factor e^{-r} and anti-squeezing at $\theta + \pi/2$ by the factor e^r .

Note that it is possible to go from the formalism previously described (or one-photon formalism) to the two-photons formalism by applying the one-photon transfer matrix A_1 [59] :

$$A_1 = \frac{1}{\sqrt{2}} \begin{pmatrix} 1 & 1 \\ -i & i \end{pmatrix} \quad (2.46)$$

Indeed, some optical components that do not mix the two quadratures are often better described by their separate action on each quadrature before being converted into the two-photon formalism transfer matrix.

2.2 The quantum states in experiments

The three quantum states useful to describe a gravitational wave interferometric detector have been introduced in the previous section. This section presents how these quantum states interact with common optical components. Especially, the generation and detection of a squeezed vacuum states that present quantum fluctuations below the one of a vacuum state are presented.

2.2.1 The squeezed states generation

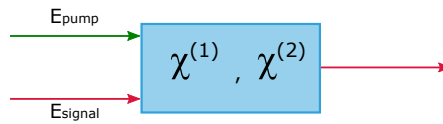


Figure 2.7: Schematic representation of a down-conversion mechanism inside a non-linear medium

The description of the squeezed states exhibited one of their important properties : The squeezing can be described as the generation of correlated sidebands that amplify or deamplify the vacuum fluctuations depending on their phase. It means that the generation of squeezed vacuum state requires an optical component that is able to achieve this effect.

Such behavior can be generated using non-linear interactions. For instance, the first generation of squeezed vacuum states was based on four-wave mixing [60]. Nowadays, the highest squeezing factor are achieved using parametric down-conversion inside a non-linear crystal [61].

The response P of a medium to an electrical field E_{inc} is described by the optical susceptibility of the medium χ as

$$P(t) = \epsilon_0 \left(\chi^{(1)} E_{inc}(t) + \chi^{(2)} E_{inc}^2(t) + \dots \right) \quad (2.47)$$

where χ is decomposed over different orders (for instance $\chi^{(2)}$ is the component of χ that interacts with the square of the electrical field).

A medium is said to be linear when $\chi^{(>1)} = 0$ and thus a medium is said to be non-linear when $\chi^{(>1)} \neq 0$. Usually, the susceptibility with order larger than one has a really small value. Therefore, it is often required to use a strong (so-called) pump field to enhance the non-linear effects.

The squeezed vacuum states presented in this section is based on the degenerate down conversion where some components of the field at the output of the non-linear medium are at the frequency difference of the input fields and the degenerate name comes from the fact that one input beam is at twice the frequency of the other one : two fields are incident on a non-linear medium described by $\chi^{(1)} \neq 0$, $\chi^{(2)} \neq 0$: the signal field $E_{signal} = E_s \sin(\omega t + \phi)$ and the pump field $E_{pump} = E_p \sin(2\omega t)$ where ϕ is the phase corresponds to the phase between these two fields. Combining these two fields with the equation 2.47 while keeping only the components at the frequency ω leads to

$$P_\omega(t) = \epsilon_0 \chi^{(1)} E_s \sin(\omega t + \phi) + \epsilon_0 \chi^{(2)} E_s E_p \sin\left(\omega t - \phi + \frac{\pi}{2}\right) \quad (2.48)$$

The equation 2.48 shows that the signal field interacts with the field generated by the frequency difference process. This interaction corresponds to parametric amplification. Indeed, depending on the value of ϕ it is possible to see that the maximum of the field at the medium output is larger or smaller than the maximal value without the pump field. It can also be noted that the strength of the amplification and the deamplification depends on the interaction non-linear interaction between the pump and signal fields. Therefore, this non-linear medium is often installed inside an optical cavity forming a so-called Opto-Parametric Oscillator (OPO). This classical description of the parametric down conversion hints that this phenomenon could be able to generate squeezed vacuum states.

The quantum description of this phenomenon is based on the Hamiltonian of the interaction between a vacuum field and a pump field inside an OPO. It is defined by their respective annihilation operators \hat{a} and \hat{b} and respective frequencies ω and ω_p is given by [62]

$$\hat{\mathcal{H}} = \hbar\omega \hat{a}^\dagger \hat{a} + \hbar\omega_p \hat{b}^\dagger \hat{b} + i\hbar\chi \left(\hat{a}^2 \hat{b}^\dagger - \hat{a}^{\dagger 2} \hat{b} \right) \quad (2.49)$$

where χ is proportional to χ_2 .

The following equations are based on the degenerate case where a pump photon at frequency $\omega_p = 2\omega$ is converted into two photons at the same frequency ω . If the pump field is a strong coherent field and not depleted during its interaction with the non-linear medium, its annihilation operator becomes $\hat{b} \rightarrow \beta e^{i2\omega t}$. The time evolution of \hat{a} is given by $\hat{a}(t) \rightarrow \hat{a} e^{-i\omega t}$. In the interaction picture, the Hamiltonian can be expressed as

$$\hat{\mathcal{H}}_I = i\hbar\chi \left(\beta e^{i2\omega t} \left(\hat{a} e^{-i\omega t} \right)^2 + \beta^* e^{-i2\omega t} \left(\hat{a} e^{i\omega t} \right)^{\dagger 2} \right) \quad (2.50)$$

And the time evolution operator can be computed as

$$\hat{U}_I(t) = \exp\left(-i \frac{\hat{\mathcal{H}}_I}{\hbar} t\right) = \exp\left(\chi \beta^* \hat{a}^2 t - \chi \beta \hat{a}^{\dagger 2} t\right) \quad (2.51)$$

This has a similar form to the squeezing operator presented equation 2.24 by assimilating $\xi \rightarrow 2\chi\beta t$: the effect of the OPO corresponds to a phase-sensitive amplification or deamplification of the quantum fluctuations of an incident field.

The output squeezing and anti-squeezing levels of an OPO can be expressed as

$$R_{\pm}(P_{\text{pump}}) = \left(\frac{1 \pm \sqrt{P_{\text{pump}}/P_{\text{thresh}}}}{1 \mp \sqrt{P_{\text{pump}}/P_{\text{thresh}}}} \right)^2 \quad (2.52)$$

where P_{pump} is the pump power and P_{thresh} characterizes an OPO cavity performance and depends for example on the OPO non linear gain or its internal losses.

The equation 2.52 shows that the level of squeezing increases with the pump power. Also, for a given level of green pump power, a lower threshold power decreases the level of squeezing.

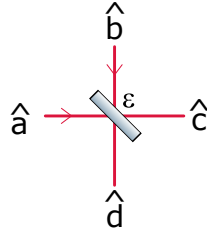


Figure 2.8: Schematic representation of the interaction between quantum states and a beam-splitter described by its reflectivity ϵ

2.2.2 The beam-splitter model

It is then interesting to describe how quantum states interact with a beam-splitter or a mirror as these components are essential in an interferometer. They can both be modeled as a mirror having a power reflectivity ϵ .

The relationship between the two input fields a and b with the output fields c and d is given by the energy conservation as represented in figure 2.8. Assuming that all fields have the same frequency, it can be written as

$$\begin{pmatrix} \hat{c} \\ \hat{d} \end{pmatrix} = \begin{pmatrix} \sqrt{\epsilon} & -\sqrt{1-\epsilon} \\ \sqrt{1-\epsilon} & \sqrt{\epsilon} \end{pmatrix} \begin{pmatrix} \hat{a} \\ \hat{b} \end{pmatrix} \quad (2.53)$$

From this general equation, it is possible to describe a lossless mirror using $\epsilon = 1$ and a lossless beam-splitter using $\epsilon = 0.5$.

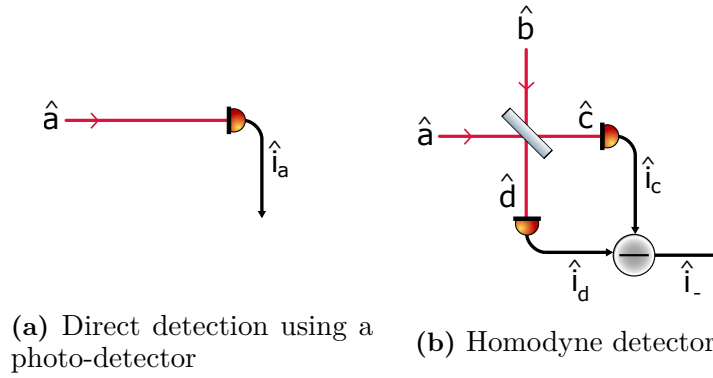


Figure 2.9: Two detection schemes either with a single photo-detector (left) or with a homodyne detector (right) where the squeezed state \hat{a} is combined with a strong coherent state \hat{b}

2.2.3 The squeezing detection

Finally, it is important to describe how quantum states, especially squeezed vacuum states, can be detected. Photo-detectors are sensitive to the power of light which is proportional to the number of photons in the field

$$P_{opt} = \hbar\omega\bar{n} \quad (2.54)$$

Considering a bright squeezed state \hat{a} incident on the photo-detector, the photon number can be derived as

$$\bar{n} = \alpha^2 + \alpha(\delta\alpha + \delta\alpha^\dagger) + \delta\alpha\delta\alpha^\dagger \sim \alpha^2 + \alpha\delta X_1 \quad (2.55)$$

where the approximation arises from neglecting the second order fluctuations.

This means that a single photodiode is only sensitive to the fluctuations of the amplitude quadrature of the field.

In order to characterize a quantum state in more than the amplitude quadrature, the detection scheme can be changed for a balanced homodyne detector. This scheme is represented in figure 2.9.

In this scheme, the quantum field to be measured is combined with a strong coherent field (called the local oscillator) using a 50:50 beam-splitter (if the beam-splitter ratio is changed, the detection scheme is called unbalanced homodyne detector). The fields at the outputs of the beam-splitter are expressed as

$$\begin{pmatrix} \hat{c} \\ \hat{d} \end{pmatrix} = \frac{1}{\sqrt{2}} \begin{pmatrix} 1 & -1 \\ 1 & 1 \end{pmatrix} \begin{pmatrix} \hat{a} \\ \hat{b} \end{pmatrix} \quad (2.56)$$

The two output ports of the beam-splitter are each incident on a photo-detector. Finally,

the output signal of the homodyne detector is the difference of the signals detected by the two photo-detectors. The mean of this signal is

$$\langle \hat{i}_- \rangle \propto \langle \hat{n}_c \rangle - \langle \hat{n}_d \rangle = \langle \hat{c}^\dagger \hat{c} - \hat{d}^\dagger \hat{d} \rangle = \langle \hat{a}^\dagger \hat{b} + \hat{b}^\dagger \hat{a} \rangle \quad (2.57)$$

The strong coherent field can be written as $\hat{b} = \beta e^{i\phi}$ with ϕ the phase between the two input fields. The signal becomes

$$\langle \hat{i}_- \rangle \propto |\beta| \langle \hat{a}^\dagger e^{i\phi} + \hat{a} e^{-i\phi} \rangle = 2|\beta| \langle \hat{X}_{a,\phi} \rangle \quad (2.58)$$

where $\langle \hat{X}_{a,\phi} \rangle$ is the quadrature operator of mode \hat{a} with an orientation given by the Local Oscillator phase ϕ .

This equation shows that by setting the phase ϕ , it is possible to scan both quadratures of the field. Furthermore, the variance of the signal is given by

$$(\Delta (\langle \hat{n}_c \rangle - \langle \hat{n}_d \rangle))^2 = 2|\beta|^2 (\Delta \langle \hat{X}_{a,\phi} \rangle)^2 \quad (2.59)$$

which is increased by the amplitude of the local oscillator field. These two properties of the homodyne detector allows to detect any quadrature of the squeezed states.

2.2.4 The squeezing degradation

Squeezed states are defined by having one quadrature with variance lower than the one of a coherent state, any process that increase the variance of the squeezed quadrature are spoiling the performances of the squeezing. This section discusses the mechanisms that affect the squeezing.

The optical losses

It can be seen from the equation 2.53 that the beam-splitter describes power loss. Since optical losses consist of lost power, the beam-splitter model can therefore be used to describe optical losses. In this model, a power loss L is described by a beam-splitter with a reflectivity L . The quadrature variance are

$$\Delta \hat{X}^L = (1 - L) \Delta \hat{X}_{in} + L \Delta \hat{X}_{vac} = (1 - L) \Delta \hat{X}_{in} + L \quad (2.60)$$

where $\Delta \hat{X}_{vac} = 1$ is the variance of a vacuum state.

The effect of optical losses on a squeezed state with initial variance V_\pm is therefore

$$V_\pm^L = (1 - L) V_\pm + L \quad (2.61)$$

which leads to a degradation of the squeezing ratio given by

$$R_{\pm}^L = (1 - L) R_{\pm} + L \quad (2.62)$$

Several sources of losses can be combined using the product of their respective efficiency $\eta = 1 - L$ and $\eta_{tot} = \prod_k \eta_k$

The effect of optical losses on the squeezing and anti-squeezing level is represented in figure 2.10.

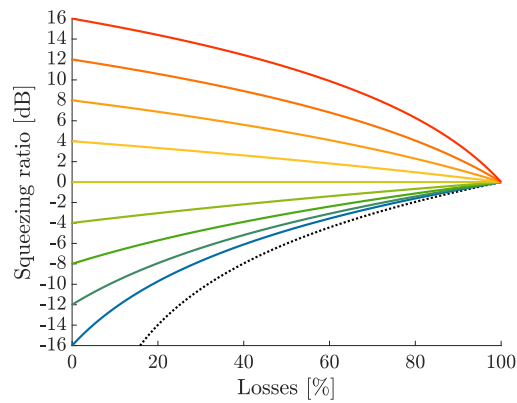


Figure 2.10: Squeezing level as a function of the optical losses. Each plain line shows the evolution of a squeezing (or anti-squeezing) level as the optical losses increase. Each curve corresponds to a different level of initial squeezing given by losses = 0%. The black dotted line indicates the effect of optical losses on infinite level of squeezing

The classical noise

In addition to the optical losses, there might be technical noises. These technical noises can for instance induce noise in the carrier field or additional non-squeezed shot noise. This means that both the squeezed variance V_- and the vacuum variance V_{vac} are affected by the classical noises variance that can be described by their variance V_{class} .

Therefore the variance detected by the photo-detector V^{det} is the sum of these two variances :

$$V_{\pm}^{det} = V_{\pm} + V_{class} \quad (2.63)$$

Since the squeezing level is measured from the detected variance at the photo-detector, the technical noise can limit the measured level of squeezing. The measured level of squeezing

expresses as [55]

$$\begin{aligned}
R_{\pm}^{det} &= \frac{V_{\pm}^{det}}{V_{vac}} \\
&= \frac{V_{\pm} + V_{class}}{V_{vac} + V_{class}} \\
&= \left(1 - \frac{V_{class}}{V_{vac} + V_{class}}\right) \frac{V_{\pm}}{V_{vac}} + \frac{V_{class}}{V_{vac} + V_{class}} \\
&= \left(1 - \frac{V_{class}}{V_{vac}^{det}}\right) R_{\pm} + \frac{V_{class}}{V_{vac}^{det}}
\end{aligned} \tag{2.64}$$

Equation 2.64 is similar to equation 2.62. It means that the effect of classical noises is similar to optical losses for the squeezed variance. The equivalent losses are described by $L_{eq} = V_{class}/V_{vac}^{det}$ [63]. This results holds for the anti-squeezed quadrature but the effect of classical noises is far lower. Indeed, the level of the anti-squeezed variance is above the vacuum one that should in principle be above the classical noises one (eg for Virgo the shot-noise defined the high-frequency sensitivity and technical noises should be less than a tenth of the shot-noise level).

The phase noise

The squeezing level is usually measured using a homodyne detector where the measured quadrature is defined by the phase between the local oscillator and the measured field. This means that the fluctuations of this phase results in a mixing of the measured quadrature with the 90° rotated quadrature. This is particularly troublesome for the squeezing measurement as the squeezed quadrature mixes with the anti-squeezed quadrature. It is therefore crucial to have phase controls to reduce this noise (for instance see section 3.4.2).

With the phase control, the average of the phase is null. However, there might be residual fluctuations that will cause phase noise. These fluctuations can be modeled as normally distributed around a null average value with the root-mean square deviation $\tilde{\theta}$.

The squeezing level with phase noise can be expressed as

$$V_{\pm}^{\tilde{\theta}} \sim V_{\pm} \cos^2(\tilde{\theta}) + V_{\mp} \sin^2(\tilde{\theta}) \tag{2.65}$$

where the approximation holds for small $\tilde{\theta}$.

Therefore, the effect of phase noise increases with the level of initial squeezing and anti-squeezing. This means that phase noise places a limit on the maximum reachable level of squeezing.

The effect of phase noise on the level of squeezing and anti-squeezing is represented in figure 2.11. The black dotted curve shows the maximal level of squeezing reachable for any

given level of phase noise. It can be seen that from few tens of milliradians of phase noise, the level of squeezing is greatly reduced while it does almost not affect the anti-squeezing.

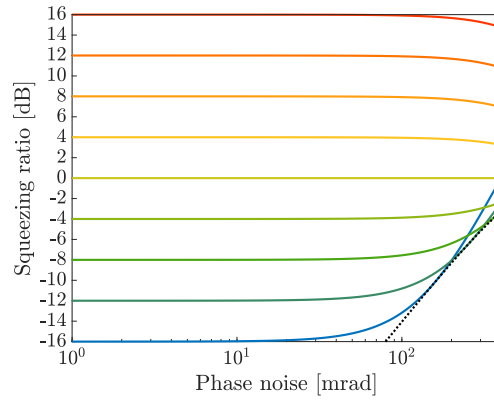


Figure 2.11: Squeezing level as a function of the rms phase noise. Higher level of phase noise mixes strongly the squeezing with the anti-squeezing. Also, this effect increases with the initial level of squeezing. Each curve corresponds to a different level of initial squeezing. The black dotted line indicates the highest level of squeezing for a given level of phase noise

Several sources of phase noise are described in [64] and [65]. It can also be shown that the scattered light has an effect similar to phase noise [55].

The combined degradations

In experiments, the squeezing propagation is affected by a combination of optical losses, classical noises and phase noise. All these sources of degradation for the squeezing can be combined as

$$R_{\pm}^{L, \tilde{\theta}} = (1 - L) \left(R_{\pm} \cos^2(\tilde{\theta}) + R_{\mp} \sin^2(\tilde{\theta}) \right) + L \quad (2.66)$$

Figure 2.12 shows the maximum reachable level of squeezing as a function of optical losses and phase noise. All squeezing experiments aim therefore at lowering optical losses and phase noise in order to reach high level of squeezing.

A last effect that has to be taken into account is that the value of the OPO threshold power influences the achievable level of squeezing. Therefore, any uncertainty in this threshold power directly translates into uncertainties in optical losses or phase noise estimation. To remove this effect, it is also useful to express the squeezing as a function of the anti-squeezing. It allows to remove the effect of the threshold power while being able to compute the effects of optical losses and phase noise. The levels of squeezing as a function of the level of anti-squeezing while varying optical losses or phase noise is represented in figure 2.13. On one hand, it can be seen in figure 2.13a that the optical losses affect more the squeezing than the anti-squeezing. On the other hand, it can be seen in figure 2.13b that the phase noise can limit the reachable level of squeezing. Furthermore, the optical losses affect mainly the low levels of squeezing or anti-squeezing while phase noise affects mainly high levels of squeezing or anti-squeezing.

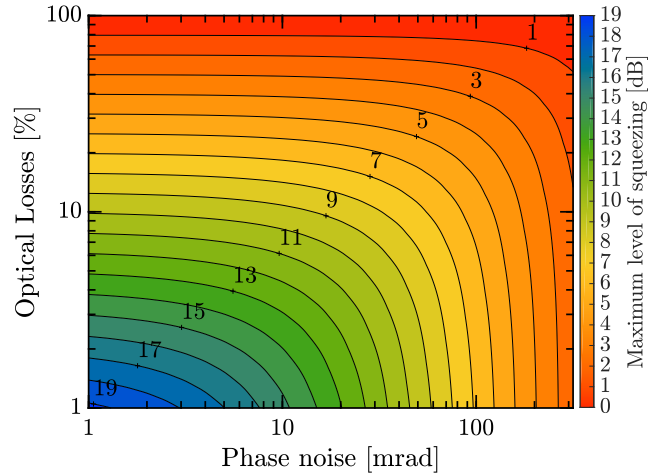


Figure 2.12: Maximal measurable level of squeezing as a function of optical losses (vertical axis) and phase noise (horizontal axis)

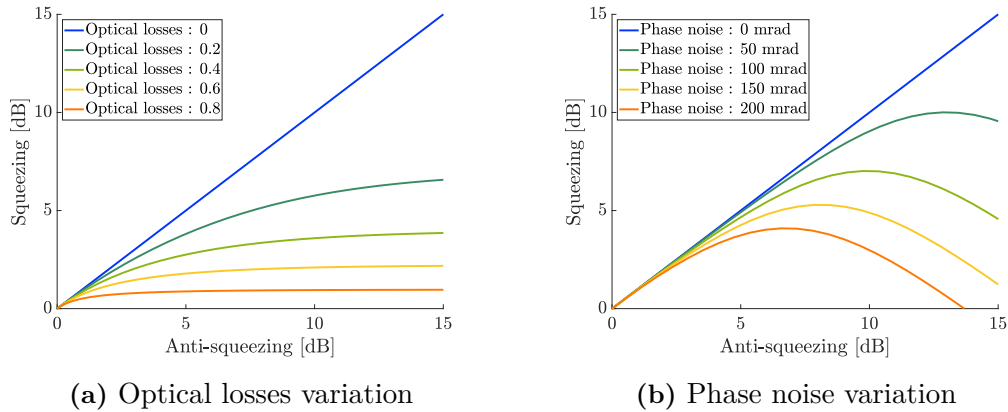


Figure 2.13: Squeezing as a function of anti-squeezing while varying optical losses or phase noise

2.3 The interferometer quantum noise

The previous sections have presented the description of light fields and optical components in quantum mechanics. It is now possible to combine them to compute the interferometer quantum noise.

2.3.1 Michelson

As in section 1.3.2, the Michelson interferometer quantum noise is first derived. This derivation is based on [66] [67].

The fields that propagate in the interferometer are represented in figure 2.14

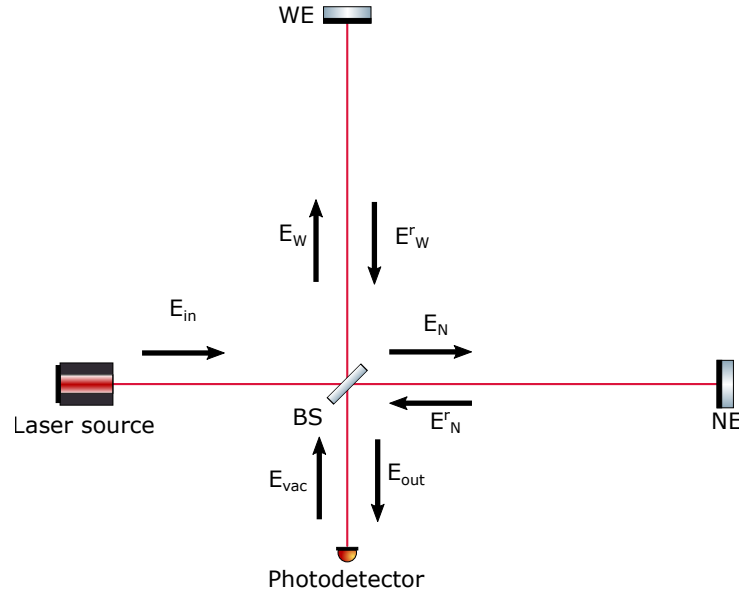


Figure 2.14: Quantum fields propagating in a Michelson interferometer

The laser field is described as a strong coherent field :

$$E_{in} = E_0 \cos(\omega_0 t) + \delta E \quad (2.67)$$

where δE represents the classical and quantum fluctuations of the field and $E_0 = \sqrt{4\pi I_0/Ac}$ with I_0 being the power of the field and A the effective area of the field.

Because the interferometer is operated in dark-fringe, there is no coherent amplitude on the interferometer output port. This also means that the fluctuating part of the input field also interfere destructively. Thus they are neglected in the following computation with $\delta E = 0$.

Another consequence of the dark-fringe operation of the interferometer is that no laser fields are present at the interferometer output. However, it has been shown that this is represented by the vacuum state that has quantum fluctuations. This field is expressed as a function of its quadrature operator as in section 2.1.4

$$E_{vac}(t) = \cos(\omega_0 t) \left[\sqrt{\frac{4\pi\hbar\omega_0}{Ac}} \int_{-\infty}^{\infty} (a_1 e^{-i\Omega t} + a_1^\dagger e^{i\Omega t}) \frac{d\Omega}{2\pi} \right] + \sin(\omega_0 t) \left[\sqrt{\frac{4\pi\hbar\omega_0}{Ac}} \int_{-\infty}^{\infty} (a_2 e^{-i\Omega t} + a_2^\dagger e^{i\Omega t}) \frac{d\Omega}{2\pi} \right] \quad (2.68)$$

The fields after the 50:50 beam-splitter are given by

$$\begin{aligned}
E_N(t) &= \frac{1}{\sqrt{2}} [E_{in}(t) + E_{vac}(t)] \\
E_W(t) &= \frac{1}{\sqrt{2}} [E_{in}(t) - E_{vac}(t)]
\end{aligned} \tag{2.69}$$

Note that the propagation phase of the sidebands are neglected for simplicity.

Any motions of the test-masses x_N or x_W generate a phase shift on the reflected beam so that

$$\begin{aligned}
E_N^r(t) &= \frac{1}{\sqrt{2}} \left[E_{in} \left(t - \frac{2x_N(t)}{c} \right) + E_{vac} \left(t - \frac{2x_N(t)}{c} \right) \right] \\
E_W^r(t) &= \frac{1}{\sqrt{2}} \left[E_{in} \left(t - \frac{2x_W(t)}{c} \right) - E_{vac} \left(t - \frac{2x_W(t)}{c} \right) \right]
\end{aligned} \tag{2.70}$$

Because of the interferometer controls, we can assume that the test-masses motions are small compared to $\lambda/2$. In this case,

$$\cos \left(\omega_0 \left(t - \frac{2x_N(t)}{c} \right) \right) \sim \cos(\omega_0 t) - \sin(\omega_0 t) \frac{2x_N(t) \omega_0}{c} \tag{2.71}$$

and similar expression for the west test-masses.

With this approximation and assuming for simplicity that $\omega_0 L/c$ is a multiple of 2π , the equations 2.70 becomes

$$\begin{aligned}
E_N^r(t) &= \frac{1}{\sqrt{2}} \left[E_0 \cos(\omega_0 t) - E_0 \sin(\omega_0 t) \frac{2x_N(t) \omega_0}{c} + E_{vac} \right] \\
E_W^r(t) &= \frac{1}{\sqrt{2}} \left[E_0 \cos(\omega_0 t) - E_0 \sin(\omega_0 t) \frac{2x_W(t) \omega_0}{c} - E_{vac} \right]
\end{aligned} \tag{2.72}$$

Finally, the beam at the interferometer output is

$$E_{out}(t) = E_{vac}(t) + E_0 \sin(\omega_0 t) \frac{\omega_0 [x_W(t) - x_N(t)]}{c} \tag{2.73}$$

And the output field depends on the differential motion of the test-masses $x_W(t) - x_N(t)$.

As first noted by Carlton M. Caves [68], E_{vac} is responsible for a fluctuating radiation pressure force on the test-masses. The radiation pressure force applied on the test-mass is written as

$$F = \frac{2P}{c} \tag{2.74}$$

The power of the field is

$$P(t) = \hbar \omega_0 (E_N(t))^\dagger E_N(t) = \hbar \omega_0 a_1 \tag{2.75}$$

In the frequency domain,

$$\delta P(\Omega) = \sqrt{P_{in}\hbar\omega_0}a_1(\Omega) \quad (2.76)$$

The Fourier components of the test-mass motion are thus

$$\frac{2\delta\hat{P}_N(\Omega)\chi(\Omega)}{c} \quad (2.77)$$

with $\chi(\Omega) = M\Omega^2$ is the mechanical susceptibility of the test-mass in the free mass limit and M the test-mass mass. Similar result is obtained for the west test-mass but with an opposite sign because of equation 2.70.

Another contribution to the differential motion of the test-masses is the gravitational wave signal h . Assuming a + polarized gravitational wave, the differential motion of the test-masses is Lh .

Finally, the total differential motion of the test-masses is given by

$$x_W - x_N = \frac{4\sqrt{4P_{in}\hbar\omega_0}}{M\Omega^2}a_1 + Lh \quad (2.78)$$

The interferometer output field can be expressed as a function of the quadrature operator b_1 and b_2 as

$$E_{out}(t) = \cos(\omega_0 t) \left[\sqrt{\frac{4\pi\hbar\omega_0}{Ac}} \int_{-\infty}^{\infty} (b_1 e^{-i\Omega t} + b_1^\dagger e^{i\Omega t}) \frac{d\Omega}{2\pi} \right] + \sin(\omega_0 t) \left[\sqrt{\frac{4\pi\hbar\omega_0}{Ac}} \int_{-\infty}^{\infty} (b_2 e^{-i\Omega t} + b_2^\dagger e^{i\Omega t}) \frac{d\Omega}{2\pi} \right] \quad (2.79)$$

The quadrature operator of the output field are extracted by comparing equation 2.79 and equations 2.73 and 2.78. This gives:

$$\begin{aligned} b_1 &= a_1 \\ b_2 &= a_2 - \kappa(\Omega)a_1 - \sqrt{\frac{P_{in}\omega_0}{\hbar c^2}}Lh \end{aligned} \quad (2.80)$$

with $\kappa = \frac{4P_{in}\omega_0}{c^2 M\Omega^2}$ the opto-mechanical coupling of the interferometer.

Equation 2.80 shows that the gravitational wave signal is given by the output field phase quadrature. Furthermore, this output quadrature depends on the amplitude and phase quadrature of the vacuum state entering the interferometer from the output port. Especially, the vacuum field amplitude quadrature couples to output phase quadrature through the factor κ that represents the opto-mechanical coupling of the interferometer.

Finally, the strain sensitivity is

$$S_{qn} = \left(\frac{1}{\kappa} + \kappa \right) \frac{h_{sql}^2}{2} \quad (2.81)$$



where $h_{sql} = \sqrt{\frac{4\hbar}{M\Omega^2 L^2}}$.

This is the quantum noise of a Michelson interferometer with $S_{rpn} = \kappa \frac{h_{sql}^2}{2}$ corresponds to the radiation pressure noise PSD and $S_{sn} = \frac{1}{\kappa} \frac{h_{sql}^2}{2}$ corresponds to the shot noise PSD.

Note that in the two-photons formalism, equation 2.80 is equivalent to

$$\begin{pmatrix} b_1 \\ b_2 \end{pmatrix} = \begin{pmatrix} 1 & 0 \\ -\kappa & 1 \end{pmatrix} \begin{pmatrix} a_1 \\ a_2 \end{pmatrix} = \mathbf{T}_{itf} \begin{pmatrix} a_1 \\ a_2 \end{pmatrix} \quad (2.82)$$

where \mathbf{T}_{itf} describes the effect of the interferometer on quantum fields;

2.3.2 The Advanced Virgo quantum noise

Advanced Virgo is a power recycled Michelson interferometer with Fabry-Perot arm cavities. It can be shown that this improved configuration changes P_{in} , κ and h_{sql} as [67] :

$$\begin{aligned} P_{in} &\rightarrow G_{PR} P_{in} \\ \kappa &\rightarrow K = \frac{2\gamma G_{PR} P_{in}}{\Omega^2 (\Omega^2 + \gamma^2)} \\ h_{sql} &\rightarrow \frac{8\hbar}{M\Omega^2 L^2} \end{aligned} \quad (2.83)$$

with $\gamma = T_{in}c/(4L)$ being the Fabry-Perot arm cavity bandwidth.

Furthermore, in equation 2.80 the output phase quadrature which contains the gravitational wave signal depends on the amplitude and phase quadrature of the vacuum state entering from the output port of the interferometer. Therefore, replacing this vacuum field by a squeezed vacuum field can reduce the fluctuations that can mask the gravitational wave signal [67].

This can be expressed in the two-photons formalism by combining equations 2.45 with 2.82 :

$$\begin{aligned} \begin{pmatrix} b_1 \\ b_2 \end{pmatrix} &= \mathbf{T}_{itf} \mathbf{R}_\theta \mathbf{S}_r \mathbf{R}_\theta^\dagger \begin{pmatrix} a_1 \\ a_2 \end{pmatrix} \\ &= \begin{pmatrix} 1 & 0 \\ -K & 1 \end{pmatrix} \begin{pmatrix} \cos^2(\theta)e^r + \sin^2(\theta)e^{-r} & \cos(\theta)\sin(\theta)(e^r - e^{-r}) \\ \cos(\theta)\sin(\theta)(e^r - e^{-r}) & \sin^2(\theta)e^r + \cos^2(\theta)e^{-r} \end{pmatrix} \begin{pmatrix} a_1 \\ a_2 \end{pmatrix} \end{aligned} \quad (2.84)$$

As first pointed by Carlton M. Caves [69], if the squeezed vacuum states has a constant angle $\theta = \frac{\pi}{2}$, the quantum noise spectral density rewrites

$$\begin{aligned}
S_{qn}^{r,\theta=\pi/2} &= \left(\frac{1}{K} e^{-2r} + K e^{2r} \right) \frac{h_{sq}^2}{2} \\
&= S_{sn} e^{-2r} + S_{rpn} e^{2r}
\end{aligned} \tag{2.85}$$

Thus the shot noise is reduced while the radiation pressure noise is increased. Note that this is similar to an increase of the input power. However, it does not have the drawback of introducing complex thermal effects.

Because most of the current detectors are mostly limited by shot noise (for instance in figure 1.7), this allows to improve the detector sensitivity.

The injection of squeezed vacuum states with constant squeezing angle $\theta = \pi/2$ is called frequency-independent squeezing injection.

On the other hand, for $\theta = 0$ the radiation pressure noise is reduced while the shot noise is increased.

It can be recalled that the radiation pressure noise and the shot noise are respectively dominating the low and high frequency part of the quantum noise. This means that if the squeezing angle could vary in frequency such that $\theta = 0$ at low frequency and $\theta = \pi/2$ at high frequency, the quantum noise would be decreased over the entire detection spectrum of the detector.

This broadband reduction of quantum noise can be achieved if the squeezed states has the frequency dependent angle $\theta = -\text{arccot}(K(\Omega))$ [67]. The resulting quantum noise PSD is reduced by e^{-2r} :

$$S_{qn}^{sqz} = e^{-2r} \left(\frac{1}{K} + K \right) \frac{h_{sq}^2}{2} \tag{2.86}$$

Such squeezed vacuum states are called frequency-dependent squeezed vacuum states.

2.3.3 The frequency dependent squeezing generation

It was first shown in [67] that a high finesse Fabry-Perot cavity near resonance, so called Filter Cavity could be used to generate frequency dependent squeezing. In that case, frequency-independent squeezed vacuum are first generated by an OPO. Then, before their injection into the interferometer, they are reflected by the Filter Cavity.

A Filter Cavity is conveniently described in the one-photon formalism by its complex reflectivity described in equation 1.18. In order to combine the action of the Filter Cavity with the one of the interferometer and the squeezed states, it is useful to express the Filter



Cavity reflectivity in the two-photons formalism [59]

$$\mathbf{T}_{FC} = \mathbf{A}_2 \begin{pmatrix} r_+ & 0 \\ r_-^* & 0 \end{pmatrix} \mathbf{A}_2^{-1} = \frac{1}{2} \begin{pmatrix} r_+ + r_-^* & i(r_+ - r_-^*) \\ -i(r_+ - r_-^*) & r_+ + r_-^* \end{pmatrix} \quad (2.87)$$

where r_+ and r_- are the complex reflectivities for the upper and lower sidebands.

These reflectivities can be expressed with their respective phasor as

$$\begin{aligned} r_+ &= \rho_+ e^{i\alpha_+} \\ r_- &= \rho_- e^{i\alpha_-} \end{aligned} \quad (2.88)$$

In order to get a better understanding of the action of the Filter Cavity, it is interesting to introduce the sum and difference of the reflectivities magnitude and phase as

$$\begin{aligned} \rho_m^p &= \frac{\rho_+ \pm \rho_-}{2} \\ \alpha_m^p &= \frac{\alpha_+ \pm \alpha_-}{2} \end{aligned} \quad (2.89)$$

The reflectivity of the Filter Cavity can be recalled from equation 1.18 :

$$\begin{aligned} r_{FC} &= r_1 - \frac{r_2 t_1^2 e^{-2ikL}}{1 - r_1 r_2 e^{-2ikL}} \\ &= r_1 - \frac{r_2 t_1^2 e^{-i\Phi}}{1 - r_1 r_2 e^{-i\Phi}} \end{aligned} \quad (2.90)$$

where the Filter Cavity phase $\Phi(\Omega) = 2kL(\Omega - \delta\omega_{FC})$ that depends on the Filter Cavity detuning $\delta\omega_{FC}$ has been introduced.

As the Filter Cavity is near resonance with a high finesse, this gives the respective approximations

$$\begin{aligned} e^{-i\Phi} &\sim 1 - i\Phi \\ r_1 r_2 &\sim 1 - \frac{t_1^2}{2} \end{aligned} \quad (2.91)$$

Combining equations 1.18 and 2.91 yields

$$r_{\pm} = \frac{-1 + i\xi(\pm\Omega)}{1 + i\xi(\pm\Omega)} \quad (2.92)$$

where $\xi(\pm\Omega) = \Phi(\pm\Omega)/t_1^2$.

For a high finesse cavity near resonance $r_+ = r_-$. It means that $\rho_p = \rho_m$.

With these approximations, equation 2.87 becomes

$$\mathbf{T}_{FC} = \rho_p e^{i\alpha_m} \begin{pmatrix} \frac{e^{i\alpha_p} + e^{-i\alpha_p}}{2} & \frac{e^{i\alpha_p} - e^{-i\alpha_p}}{2i} \\ \frac{e^{i\alpha_p} - e^{-i\alpha_p}}{2i} & \frac{e^{i\alpha_p} + e^{-i\alpha_p}}{2} \end{pmatrix} = \rho_p e^{i\alpha_m} \mathbf{R}_{\alpha_p} \quad (2.93)$$

It shows that the action of a Filter Cavity corresponds in the two-photons formalism to a rotation with a frequency dependency α_p . This shows that the reflection of a Filter Cavity can indeed transform frequency-independent squeezed vacuum states into frequency-dependent squeezed vacuum states. Note that this derivation holds for lossless Filter Cavity. The case of realistic Filter Cavity is studied in more details in section sec:realFC.

2.4 Conclusion

This chapter has derived a quantum model of the interferometer. This description allowed to see that the interferometer quantum noise is due to the vacuum fluctuations in phase and in amplitude quadrature of the vacuum states entering by the output port of the interferometer. Finally, replacing this vacuum states by frequency-independent squeezed vacuum states with the proper squeezing angle improves the shot-noise while spoiling the radiation pressure noise. But injecting frequency-dependent squeezed vacuum states achieved a broadband reduction of the quantum noise.



3

Frequency Independent Squeezing commissioning for O3

Contents

3.1	Introduction	59
3.2	The External Squeezer Bench	60
3.2.1	The Squeezer	60
3.2.2	The injection optics	62
3.3	Alignment and mode-matching	65
3.4	The squeezer controls	70
3.4.1	The Phase Locked Loops	70
3.4.2	Phase control	72
3.4.3	The Alignment Controls	77
3.5	Conclusion	82

3.1 Introduction

The previous chapters have presented how to generate squeezed vacuum states and how the injection of such states through the detection port of an interferometer could improve its sensitivity by decreasing the level of shot-noise.

Frequency-independent vacuum squeezed states have been injected for the first time in interferometric gravitational-wave detector at GEO600 in 2010 [70] and later on also



demonstrated at the LIGO Hanford detector [71] improving the sensitivity above few hundreds Hertz. Furthermore, the demonstration of long term injection [72] proved that this technique was mature enough to be considered as an important upgrade for all interferometric gravitational-wave detectors.

In Virgo, the injection of frequency-independent squeezed vacuum states has been planned for the O3 run. This section will present the components and commissioning activities required to integrate the squeezer and its controls within the Advanced Virgo detector.

3.2 The External Squeezer Bench

In January 2018, a squeezer [40] assembled at the AEI has been installed in Virgo detection laboratory as presented in figure 3.1. This squeezer is contained inside a 1 m by 1.2 m box and has been installed on an in-air optical board, namely the External Squeezing Bench (ESQB). The ESQB is hosted itself inside an acoustic enclosure useful to decrease environmental noises.

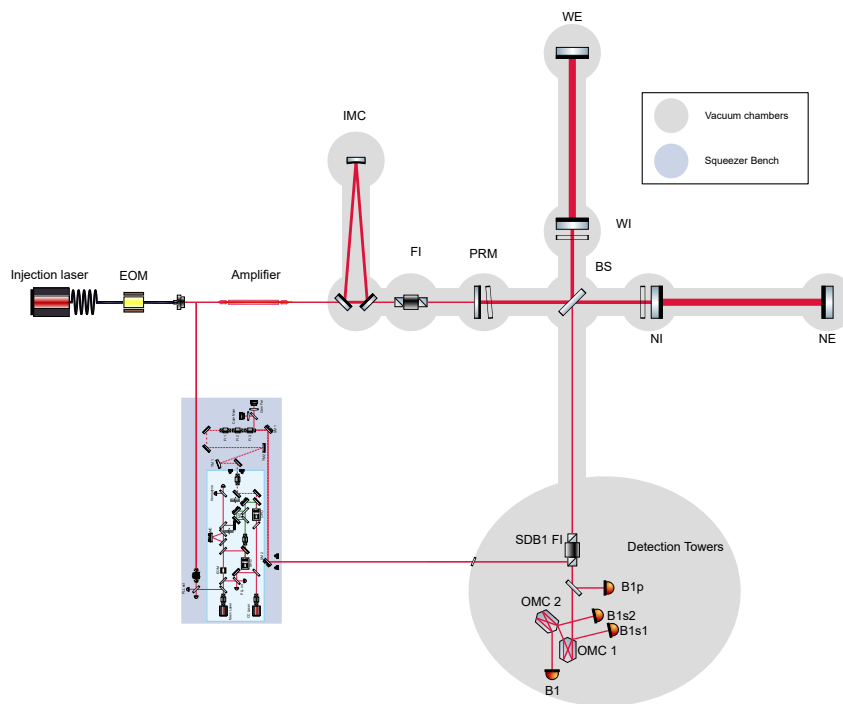


Figure 3.1: Simplified optical layout of the the Advanced Virgo detector

3.2.1 The Squeezer

The squeezer uses a doubly resonant OPO to generate frequency-independent squeezed vacuum states through parametric down-conversion.

Figure 3.2 shows a simplified optical layout of the ESQB (dark blue) hosting the AEI squeezer (light blue).

The squeezer components can be divided in different parts:

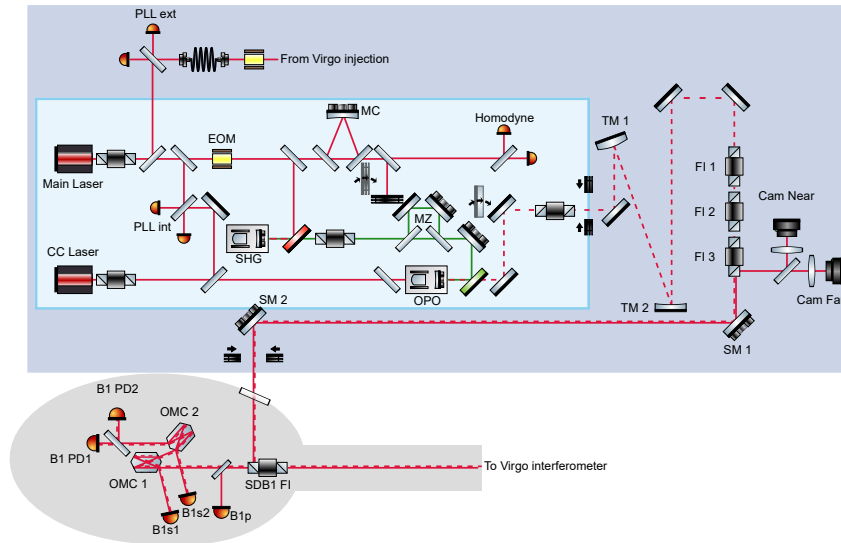


Figure 3.2: Simplified optical layout of the ESQB hosting the AEI squeezer. The red and green solid lines represent respectively the IR and green laser beams. The red dashed line represent the squeezed beam

- Two infrared lasers labeled main laser and coherent control laser. The main laser is phase-locked to Virgo master laser using a Phase-Locked Loop (PLL) (PLL ext). In a similar fashion, the coherent control laser is phase-locked to the master laser with an offset frequency of 7 MHz using the PLL int. These controls will be presented later in this chapter (section 3.4.1).
- A pick-off of the main laser is injected into a Second Harmonic Generator (SHG) which produces a green field. Its power is stabilized using a Mach-Zehnder interferometer (MZ). Indeed, the MZ output power is directly dependent on its two arm length difference. Therefore, by acting on the MZ arm length control it is possible to stabilize the MZ output power.
- An EOM is used to imprint one phase modulation to the IR beam so to obtain the error signals required for the length control of the squeezer optical cavities, namely the infra-red Mode Cleaner (MC), the SHG and the OPO. All cavities are locked using the Pound-Drever Hall (PDH) technique.
- The green field is used to pump the OPO which produces the squeezed vacuum field.
- The frequency shifted coherent control laser is used as a Coherent Control field for the produced squeezed field [73] and co-propagates with it.
- The squeezed beam passes a Faraday isolator and can then be injected to the ESQB or to a characterization Homodyne detector depending on the position of a flipping steering mirror. The Local Oscillator (LO) of this Homodyne detector is a pick-off of the squeezer main laser spatially cleaned by the infra-red MC.



As represented by the arrows in figure 3.2, there are two flipping optics inside the squeezer: a beam dump after the MC and a mirror before the Faraday isolator. This allows the squeezer to be operated in three different modes :

- If the beam dump and the flipping mirror are on the beam paths (as shown on the scheme 3.2), the squeezer produces frequency-independent squeezed vacuum states which is sent to the ESQB.
- If the beam dump is moved out of the path, an infrared beam is sent to the OPO. The OPO cavity can be locked to generate a bright unsqueezed beam (which consists of the incident infrared beam (de-)amplified) that shares identical geometrical parameters with the squeezed beam. Therefore, it can be used to align and mode-match the squeezed vacuum field to the interferometer. Thus the name Bright Alignment Beam (BAB).
- If the steering mirror is moved out of the path, the squeezed vacuum field is sent to the Homodyne detector. This allows the characterization of the produced squeezed vacuum field.

After the installation of the AEI squeezer on Virgo site, the squeezer performances have been characterized by sending the squeezed vacuum field to the Homodyne detector. A similar level as the one measured in AEI [40] has been obtained : up to 14 dB of produced squeezing in the audio-band with phase noise level of 3mrad and optical losses of 5.3 %.

3.2.2 The injection optics

Once frequency-independent squeezed vacuum states are generated, it is required to inject them from Virgo detection port with proper geometrical properties (ie beam waist size and location common between the squeezed beam and the interferometer beam). This requires to add optical components on the ESQB to obtain and control these properties represented on the dark blue part of figure 3.2. These optical components are presented starting from the squeezer box to the detection towers.

The injection Telescope

As mode-mismatch will spoil the level of squeezing at the interferometer output, an injection matching telescope is required to mode-match the squeezed beam to the interferometer beam. The squeezed vacuum field is injected into the interferometer by one polarizer of the SDB1 Faraday isolator. This means that the squeezed beam has to be mode-matched to the interferometer beam at that position. The nominal geometrical parameters of both beams are given in table 3.1

In order to match these two beams, a reflective telescope has been designed. Indeed, this allows to reproduce the slight astigmatism of the interferometer beam and does not introduce losses due to scattering or absorption losses. This telescope is composed of two

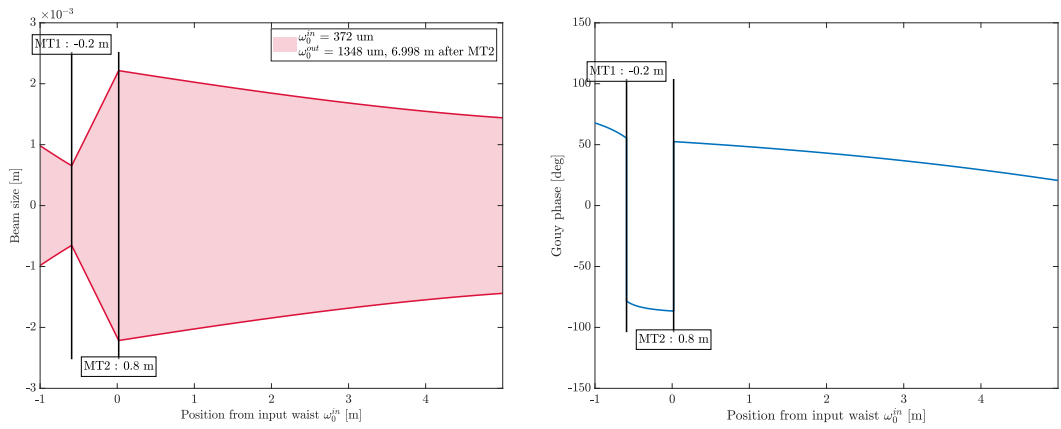
Parameter	Interferometer main beam	Squeezer BAB
Sagittal waist size [mm]	1.351	0.372
Distance to the squeezer box [m]	7.291	1.02
Tangential waist size [mm]	1.346	0.372
Distance to the squeezer box [m]	7.344	1.02

Table 3.1: Geometrical parameters of the squeezer BAB and the interferometer main beam to match measured on the ESQB between the MT2 and the SDB1

mirrors TM1 and TM2 in figure 3.2 with respective equivalent focal length $f_{MT1} = -200$ mm and $f_{MT2} = 800$ mm separated by $L = 610$ mm with MT1 installed 591 mm before the squeezer beam waist. The goal is to have the beam waist located 7.017 m after MT2.

As shown in figure 3.3a, this telescope reproduces the interferometer beam geometrical parameters.

However, as shown in figure 3.3b, any steering optics after this telescope will have Gouy phase difference quite smaller than 90° . This means that any actuation matrix used for these steering optics will not be diagonal and tilt and shift of the beam will be coupled.



(a) Beam size evolution during the propagation through the telescope (b) Gouy phase evolution during the propagation through the telescope

Figure 3.3: Design telescope effects on the squeezer beam size and Gouy phase

The Faraday isolators

Following the injection telescope and two steering mirrors, there is a chain of three Faraday isolators. The purpose of these Faraday isolators is to reduce the amount of light back-scattered from the squeezer optics into the interferometer. The back-scattered light has been and is still troublesome for interferometric gravitational waves detectors as it can spoil the detectors sensitivity spectrum below few hundreds Hertz where most binary



black-hole and binary neutron stars gravitational wave signals are expected [74].

In case of the squeezing injection, the addition of several optics corresponds also to the addition of possible back-scattered light sources. Using GWINC [75], the effects of back-scattered light from the squeezer optics into the interferometer have been simulated [76]. From this study, the main source of back-scattered light within the squeezer was the OPO itself. In order to reduce this effect by more than a factor 10 below the O3 sensitivity (which is a requirement on technical noises level), three Faraday isolators, each with throughput losses below 2% and isolation factor above 40 dB were required. For this purpose, EGO developed low-losses Faraday isolators both vacuum and in-air compatible [77]. Their respective throughput have been measured at the level of 99% and isolation factor above 40 dB.

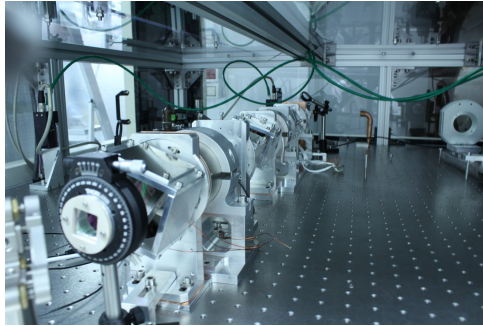


Figure 3.4: Picture of the three Faraday isolators installed on the ESQB

The alignment optics

Following the Faraday isolators, the optics required to align the squeezed beam and the coherent control beam are installed. The two mirrors labeled SM1 and SM2 in figure 3.2 are used to steer the alignment of the squeezed beam and the co-propagating coherent control beam with the interferometer beam. They consist of two 1 inch super-polished optics equipped with piezo-electrical actuators. These actuators allow to control the angular position of the steering optics over 20 mrad. These piezo-actuators accept up to 10V at their input and their angular motions are linear over this range.

A spurious beam is coming from the SDB1 to the ESQB. This beam arises from spurious p-polarization of the beam on the SDB1 that is directed toward the ESQB by the SDB1 Faraday isolator. This beam is sensing the relative motions between the ESQB and the interferometer and can therefore be used to control the alignment of the squeezed beam into the interferometer. This beam is extracted at the level of the polarizer of the last Faraday isolator on the ESQB (FI3 in figure 3.2) and directed to two cameras. A lens is located before each camera which allows to sensing both the near field and far field of the spurious interferometer beam. As will be presented in a later section, this allows to sense and control the squeezed beam alignment.

The SDB1 modifications

In order to inject the squeezed beam and the co-propagating coherent control beam, the SDB1 tower had to be modified.

First, the modification of the SDB1 tower north wall in order to install a flange supporting a window through which these beams could be injected. This window has been coated at LMA with anti-reflective coating.

Furthermore, the SDB1 Faraday isolator has been replaced with a new one developed at EGO [77] with reduced optical losses and better isolation ratio. Its output polarizer by which the squeezed beam is injected reflects the light downwards so an additional steering mirror has been installed (but is not represented in figure 3.2).

Finally, the B1 photodiodes have also been replaced with higher quantum efficiency ones in order to reduce optical losses.

All the values of optical losses of optical components encountered by the squeezed beam are summarized in table **tab:optLoss** in the next chapter.

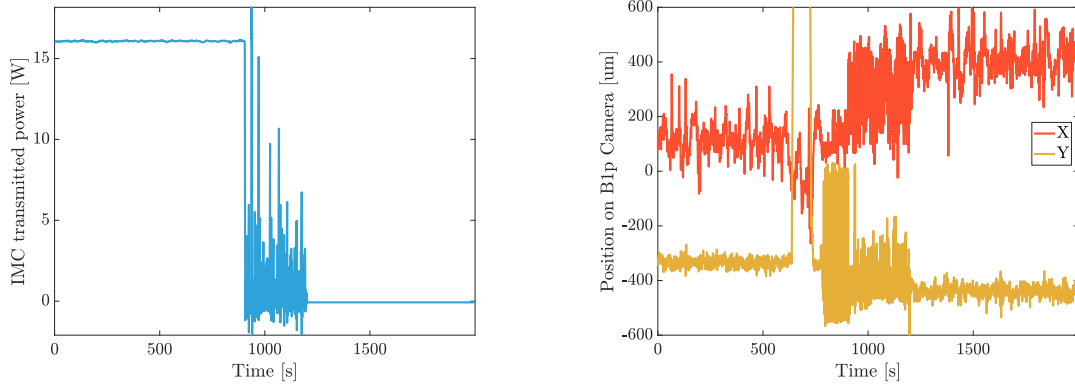
3.3 Alignment and mode-matching

In order to align and mode-match the squeezed beam with the Virgo main laser beam, we used the BAB as a marker of the squeezed beam geometrical properties.

When working on the squeezed beam alignment and mode-matching, and in a similar fashion as for the OMC, Virgo is set to Single Bounce mode meaning that only the NI mirror is kept aligned such that the beam reaching SDB1 and ESQB is the Virgo main laser beam after reflection on the NI.

In order to overlap the BAB and the interferometer beam, two diaphragms were put on the ESQB separated by 2.5 m. By moving the folding mirror under SDB1 Faraday isolator, as well as the mirrors SM1 and SM2, it was possible to overlap these two beams within the approximate 3 mm aperture of the diaphragms. This alignment procedure was checked by looking at the B1p camera which is located at the same position as the B1p photodiode and sensing the Virgo main laser beam incident on the OMC1 . The power reaching this camera from the interferometer being greatly superior to the BAB power, the interferometer Input Mode-Cleaner was unlocked around $t = 900$ s in figure 3.5a to compare the center position of these two beams. Figure 3.5b shows that this technique allowed to superpose the two beams within $300 \mu\text{m}$ after their propagation inside the interferometer. This rough alignment allowed to look for the BAB in reflection and transmission of OMC1.





(a) IMC transmitted power with an unlock at $t = 900$ s (b) Interferometer beam position on B1p followed by the BAB position after the IMC unlock. X and Y indicates the horizontal and vertical position respectively

Figure 3.5: Positions of the interferometer beam and the BAB on B1p camera

The goal of the alignment was from now on to align the BAB to the OMC1. This should translate to good alignment inside the interferometer as the OMC1 itself is well aligned with the interferometer beam. Indeed the losses induced by the misalignment of the interferometer main beam and the OMC1 has been measured at the order of 1% and even less with good alignment.

From that point, the geometrical parameters of interferometer beam and BAB have been measured on ESQB between SM1 and SM2.

Figure 3.6 shows the power transmitted by the OMC1 (B1s2) during a scan of its temperature. Indeed, the OMC length changes with its temperature meaning that different modes of the incident laser field will resonate inside the OMC1. Using camera that looks at the beam at the level of B1s2, it is possible to extract which mode is resonating inside the OMC1. In this figure, the time scale of the two scans have been set such that the fundamental mode is resonating at $t = 0$ s. Then, the second and third peaks correspond respectively to the first and second modes, which can also be associated to misalignment and mode-mismatch of the beam. Indeed, when the incident laser beam is properly aligned, most of the power is within these three modes.

As shown in figure 3.6, before the tuning of the matching telescope length several higher-order modes were resonating inside the OMC1 representing more than 40% of the resonating power. After the tuning of the length of the matching telescope, most of the power was in the fundamental-mode.

To improve this alignment, piezo-actuators on SM1 and SM2 were used to imprint an angular modulation on the BAB pointing into the interferometer.

Indeed as shown in figure 3.7, the power transmitted by the OMC1 brings information on the alignment quality. For instance, the black curve represent the power transmitted by the OMC in function of the incident beam angular position (where the angular position 0 au corresponds to perfect alignment).

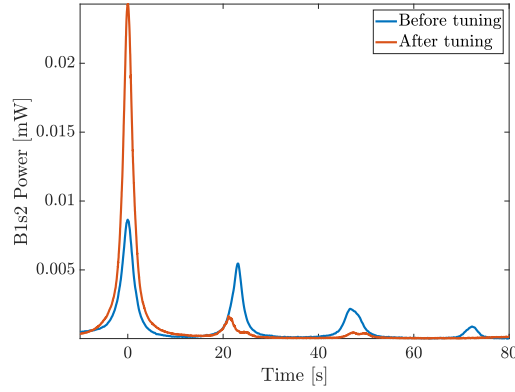


Figure 3.6: Power transmitted by the first OMC cavity (B1s2 beam) during a scan of its temperature before and after the matching telescope length tuning. Time scale has been changed to have modes of both signals overlapped

On one hand, if the BAB is badly aligned into the OMC1, a modulation of its angular position at the frequency f_{mod} will result in a modulation of the power transmitted by the OMC1 at the same frequency f_{mod} . This is represented by the red arrow in figure 3.7. On the other hand, a good alignment corresponds to the case where all the BAB power is transmitted by the OMC1. In this case, modulating the BAB angular position at the frequency f_{mod} results in a modulation of the transmitted power at $2f_{mod}$. Therefore, the goodness of the BAB alignment into the OMC1 can be judged by looking at the strength of the signal at $2f_{mod}$ in the transmitted power.

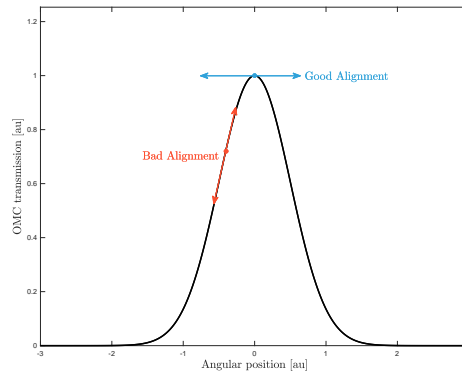


Figure 3.7: OMC transmission as a function of the angular position of an incident beam. The arrows represent angular modulations for two angular positions : bad and good alignment

For every degree of freedom, an angular modulation was applied to one mirror while the angular position of the other mirror was moved to reach symmetrical fluctuations of the transmitted and reflected power of the OMC1. Figure 3.8 shows the evolution of the B1s2 power while performing this operation. Note that SM1 and SM2 being mounted in opposite manners, both SM2X and SM1Y corresponds to vertical angular motions of the BAB as seen on SDB1.

While applying the angular modulation to SM1Y, the angular set-point of SM2X was



moved by small steps. At first almost only the angular modulation frequency is visible on the B1s2 power (OMC1 transmission) meaning that the BAB was almost not passing by the optimal alignment to the OMC1. Moving the SM2X set-points made the frequency at double the angular modulation frequency appear clearer up to the point where the amplitude of each angular scan was symmetrical, meaning that the BAB vertical alignment to the OMC1 was almost centered to the optimal alignment.

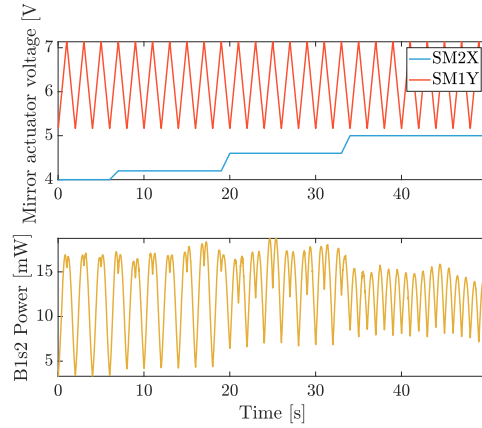


Figure 3.8: Evolution of B1s2 power using angular modulation to the BAB. Note that during this measurement SM2X and SM1Y corresponded to the same degree of freedom

The OMC substrates were characterized in Laboratoire d’Anney de Physique des Particules (France) (LAPP) showing an astigmatism of OMC1 input RoC with an horizontal RoC of 2217 ± 194 mm and a vertical RoC of 1653 ± 115 mm as seen by the OMC1 fundamental mode [39]. This slight astigmatism means that the resonance temperature of the horizontal and vertical modes are slightly separated.

In order to check the alignment improvement with the dithering technique, a temperature scan of OMC1 was performed to compare the power in the OMC1 fundamental mode and first-order mode. Figure 3.9b shows the B1s2 power (ie OMC1 transmitted power) during this scan. The effect of RoC astigmatism is slightly visible in high-order mode resonances positions. This showed that at this time the vertical misalignment was dominating.

In order to evaluate the level of misalignment, the first-order modes power has to be compared with the fundamental mode one. As shown in figure 3.10, the fundamental mode has been fitted by an Airy function to subtract the contribution of the fundamental mode power to the first-order power as well as to estimate the power in the fundamental mode. The finesse resulting from the fit was equal to 124 in good agreement with the one measured at LAPP (126 ± 6) [39]. From the power in the first and second higher-order modes, the misalignment and mode-mismatch induced losses have then been estimated to be respectively 1.54% and 1.14%.

Because the squeezer is installed on an in-air not suspended optical board, any motions of suspended SDB1 following the interferometer beam will affect the matching of the squeezed beam to the interferometer.

The SDB1 follows the angular motions of the interferometer main laser in TX and TY which correspond to pitch and yaw (or equivalently to an angular motion of the optical

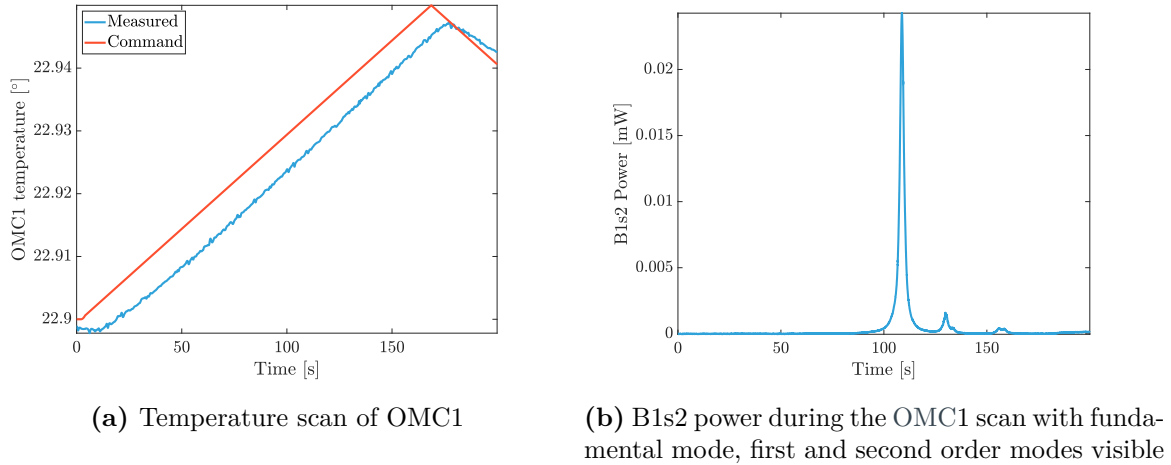


Figure 3.9: B1s2 power during a temperature scan of OMC1

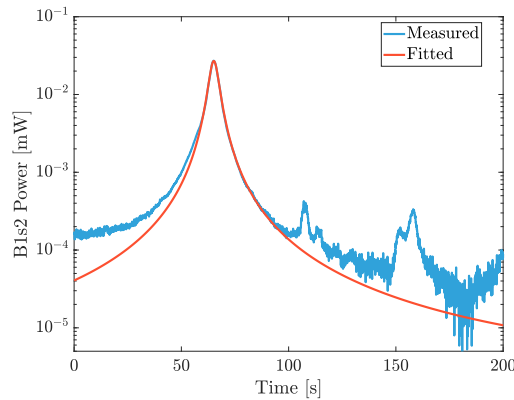


Figure 3.10: Fit of B1s2 power by an Airy function. The measured data are identical to figure fig:somcP after the tuning of the matching-telescope

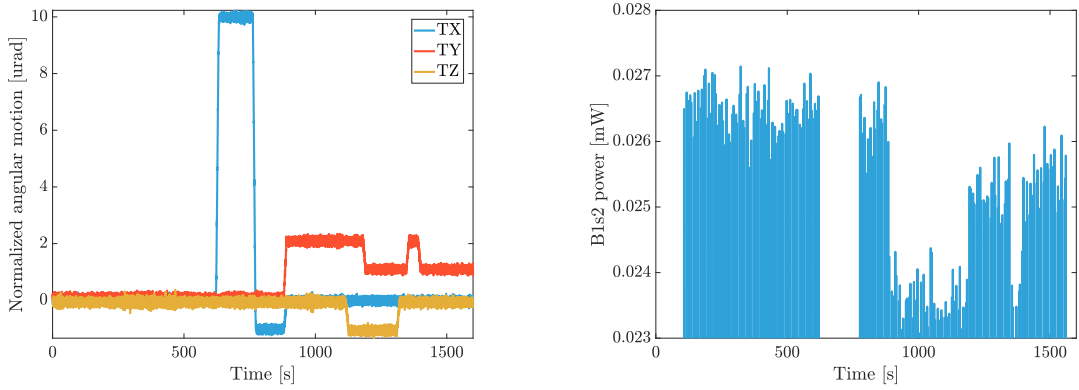
axis). The TZ degree of freedom corresponding to roll of the beam (ie angular motion around the laser optical axis) is stabilized at a fixed position. Indeed, the angular motions of the SDB1 around the interferometer beam optical axis do not affect the propagation of the interferometer laser beam inside the detection towers.

However, the squeezed beam is injected orthogonally to the interferometer beam meaning that it should be insensitive to TX motions of SDB1 but sensitive to TZ and TY motions.

To test this effect, the squeezer laser frequency has been scanned to see the power in OMC1 fundamental-mode on B1s2 while shifting the angular positions of SDB1. This frequency scan of the squeezer main laser frequency is equivalent to a scan the OMC1 temperature but faster. As shown in figure 3.11, it is possible to estimate the effect of SDB1 angular motions by comparing the mean power on the OMC1 fundamental mode during these motions with respect to the nominal position. It has to be normalized with the SDB1 angular motion to express the losses in unit of $\frac{\%}{\text{urad}}$.

The results are summarized in table 3.2





(a) Angular motions of the SDB1. The starting position has been normalized to 0 μrad (b) B1s2 power measured during the angular motions of the SDB1

Figure 3.11: B1s2 power during a frequency scan of the squeezer main laser

Motions	TX	TY	TZ
Mode-mismatch losses[%/urad]	0.26	2.33	1.55

Table 3.2: Losses induced by SDB1 angular motions on the squeezer alignment

It can be seen that TY and TZ angular motions of SDB1 have an important effect on the squeezer alignment quality. Therefore an alignment control system is required to keep the optimal alignment conditions of the squeezer with the interferometer to minimize the losses these motions induce.

3.4 The squeezer controls

Following the installation and tuning of the ESQB optical components, the frequency-independent squeezing could be injected. However, in order to maintain optical performances of this injection during the one-year long O3 run, several controls loop were also required. This section will describe these controls loops.

3.4.1 The Phase Locked Loops

Two frequency control loops are implemented using the PLL [78] that allows to stabilize the frequency difference between two lasers by comparing the beat-note of these two lasers detected on a photodiode with a local oscillator field oscillating at the frequency difference that we want to achieve.

The first one, labeled PLL ext, is used to stabilize the frequency of the squeezer main laser to the frequency of the Virgo main laser. Indeed, this will ensure to have a constant

phase offset between the squeezer main laser and Virgo laser, therefore avoiding phase noise coming from relative phase fluctuations between the squeezed beam and the Virgo main laser.

In order to generate a detectable beat-note between these two lasers, the Virgo main laser is shifted by 80 MHz and their frequency difference is stabilized at 80 MHz.

The second one, labeled PLL int, is used to stabilize the coherent control laser frequency with a 7 MHz offset from the squeezer main laser frequency. This 7 MHz shift is then used to generate the required control signals for the Coherent Control that will be presented later on.

These two PLLs represented in figure 3.12 work in a similar fashion :

First, the two lasers are superposed with a beam-splitter and matching optics not represented on the scheme. They are then incident on a photodiode whose output contains signal at the difference of the frequency between the two lasers (the second photodiode is used as an out-of-loop monitor). This beat-note frequency is then compared with a Local Oscillator (a 80 MHz Voltage Controlled Oscillator for the PLL ext and of a MHz clock for the PLL int).

Two correction signals are then generated from the comparison of these two signals. The first one acts on the laser PZT actuator. While it can provide a fast actuation, it doesn't have a range large enough for long term stability. Therefore, another correction signal is acting on the laser Peltier cell and allows a long term control of the system. These frequency stabilization loops have bandwidth at the order of 40 kHz.

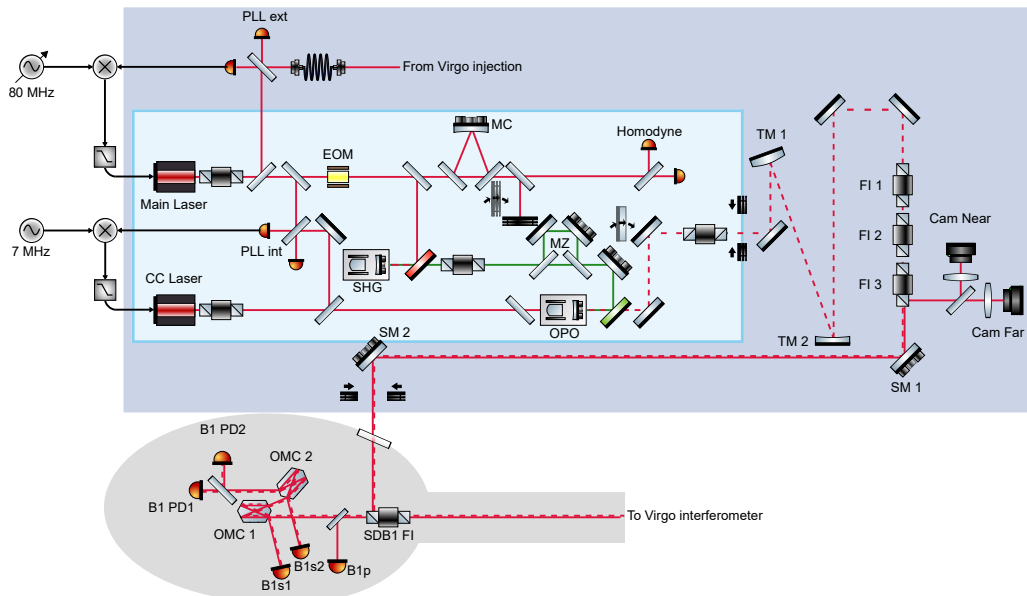


Figure 3.12: Simplified scheme of the two PLL controls. The matching optics are not represented

Because PLL ext is stabilizing the squeezer main laser to the Virgo laser frequency, it is



required to wait to have the Virgo main laser stabilized in frequency. This means that PLL ext. can be locked following the lock of the Virgo injection system. On the other hand, the lock of PLL int. can be performed independently of the state of Virgo. This lock is performed as soon as both squeezer main and CC lasers are available.

The residual phase noise due to the PLL can be estimated by using a spectrum analyzer and results are presented in figure 3.13. This measurement gives 23.94 mrad and 16.32 mrad of residual phase noise for respectively the PLL ext. and the PLL int.

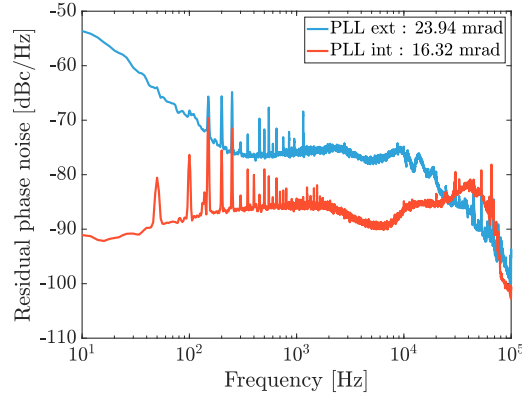


Figure 3.13: Phase noise of PLL ext and PLL int

3.4.2 Phase control

The squeezed quadrature has to be aligned with the interferometer signal in order to fully benefit from the squeezing injection by keeping phase noise as low as possible. This means that the phase between the squeezed beam and the interferometer laser on the interferometer main photodiode (B1) has to be stabilized.

This phase is stabilized using coherent control and quantum-noise locking techniques.

The overall phase control scheme is presented in figure 3.14.

The coherent control

In order to benefit from the squeezing injection, it is required to control the vacuum squeezed quadrature to the proper phase with respect to the interferometer readout quadrature. This is challenging as injecting a weak phase-modulated field is enough to introduce technical noises that can prevent the low frequency squeezing generation[79].

The coherent control first proposed by *Chelkowski et al.* [73] and demonstrated by *Vahlbruch et al.* [80] is able to control the squeezer field phase with respect to the interferometer readout phase without degrading the generated squeezed vacuum state. The name coherent control comes from the use of optical fields coherent with the squeezed vacuum field but that do not interact with it.

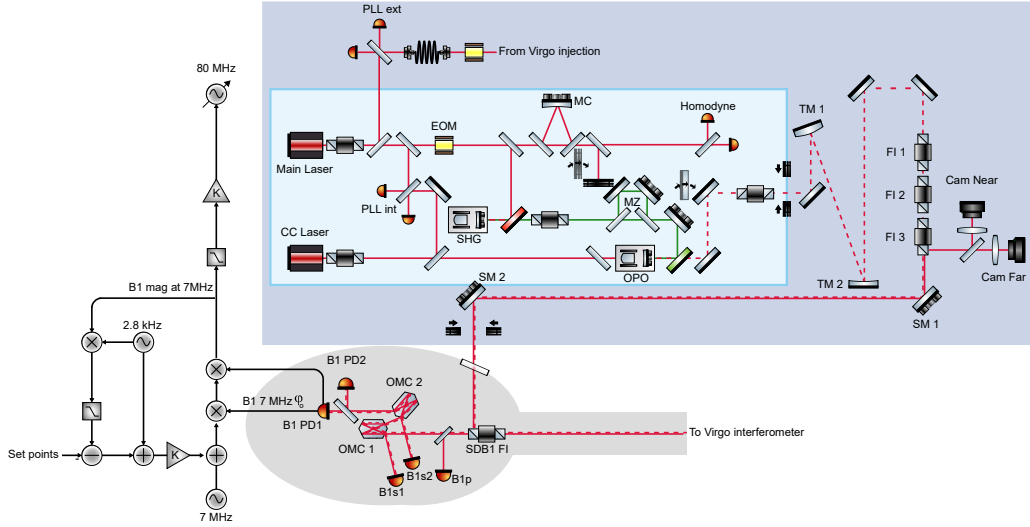


Figure 3.14: Scheme of the two phase controls used during O3

First, the OPO length has to be controlled, as this will define the frequency at which the squeezed vacuum states will be generated. The sidebands present on the green pump beam can be used to extract the PDH signal to lock the OPO length. Then, the OPO temperature is tuned to achieve simultaneous resonance of the green and infrared beams inside the OPO.

Then, the phase between the squeezed field and the interferometer readout has to be controlled. The coherent control working principle can be understood by the fact that a field coherent with the squeezed vacuum state (hence the name) is used as a phase reference with both the squeezed vacuum field and the interferometer readout field.

First, a frequency-shifted (to avoid interaction with the squeezed field) and RF phase-modulated field at $\Omega_{cc} = 7$ MHz is injected into the OPO. This frequency was chosen because it is transmitted by the OMC therefore insuring its detection at the B1 photodiode. This coherent control field can be expressed as

$$E_{cc}^{in} = \alpha \cos(\omega_0 t + \Omega_{cc} t) \quad (3.1)$$

where ω_0 is the carrier frequency and α the amplitude of the coherent control field.

This field interacts with the OPO and the green pump field E_{pump} is defined as

$$E_{pump} = \beta \cos(2\omega_0 t + \phi) \quad (3.2)$$

where ϕ is the green pump field phase with respect to the coherent control field and β the amplitude of the pump field.

The non-linear interaction of these two fields with the OPO generates a second sideband



at $-\Omega_{cc}$ so that the coherent control at the OPO output is expressed as in [73] :

$$E_{cc}^{out} \propto (1 + g) \cdot \cos(\omega_0 t + \Omega_{cc} t + 2\phi) - (1 - g) \cdot \cos(\omega_0 t - \Omega_{cc} t - 2\phi) \quad (3.3)$$

with g being the OPO non-linear gain.

This field is then used to generate two error signals to control the squeezing phase with the coherent control field and to control the coherent control field phase with the interferometer readout field at the B1 photodiode.

The first error signal is extracted from the beating of the two sidebands Ω_{cc} demodulated at $2\Omega_{cc}$ and applying a low-pass filter :

$$I_1^{cc} \propto \frac{(-1 + g^2) \cdot \sin^2(2\Phi)}{4g} \quad (3.4)$$

The zero-crossing of this signal forces the phase between the green pump power and the coherent control sidebands ϕ to be constant, allowing to use the coherent control sidebands as a marker of the squeezing phase at the interferometer readout. This is performed by acting on a phase shifter on the green pump beam path.

What remains now is to control the phase between the coherent control field and the interferometer readout field Φ to control the squeezing phase with respect to the interferometer readout.

The coherent control field co-propagates with the squeezed vacuum field up to the interferometer readout system (B1 photodiode) where it produces a beat-note with the interferometer readout field ($\propto \cos(\omega_0 t)$). The goal of this control loop is to control the phase Φ between the coherent control field and the interferometer readout field. This beat-note can be expressed as :

$$B(t) \propto \cos(\Omega_{cc}) \left[(1 + g) \cos(\phi) - (1 - g) \cos(\phi - 2\Phi) \right] + \quad (3.5)$$

$$\sin(\Omega_{cc}) \left[-(1 + g) \sin(\phi) - (1 - g) \sin(\phi - 2\Phi) \right] \quad (3.6)$$

By demodulating this beat-note at Ω_{cc} and low-pass filtering it, it is possible to extract the second error signal for the coherent control :

$$I_2^{cc} \propto (-1 + g) \sin(\phi + 2\Phi) \quad (3.7)$$

As ϕ is already controlled with the first coherent control loop, this signal allows to control Φ .

Finally, acting on the 80 MHz voltage controller will change the squeezer main laser phase and therefore the relative phase between the squeezed quadrature and the interferometer readout quadrature.

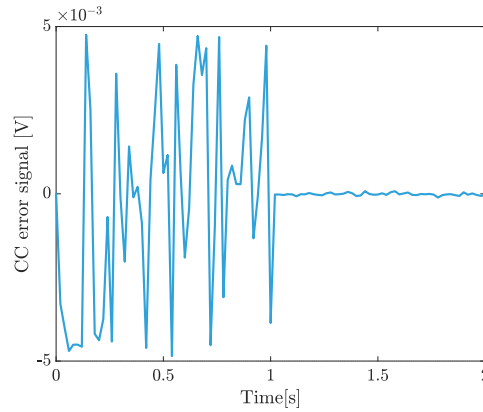


Figure 3.15: Coherent Control error signal evolution during the closing of the Coherent Control (closed at 1 s)

Figure 3.15 shows the coherent control error signal with this loop closed at 1 s. When the coherent control loop is open, the phase between the coherent control field and the B1 phase is free. This means that this phase can cross several fringes. This allows also to extract the coherent control error signal calibration in [V/rad] as the peak-to-peak amplitude corresponds to one fringe of the coherent control demodulation phase (or π rad). From this figure, the PD1 calibration factor is 0.0032 V/rad. This calibration can then be used to estimate the coherent control phase noise in loop. From figure 3.16, we can extract 18 mrad of phase noise rms.

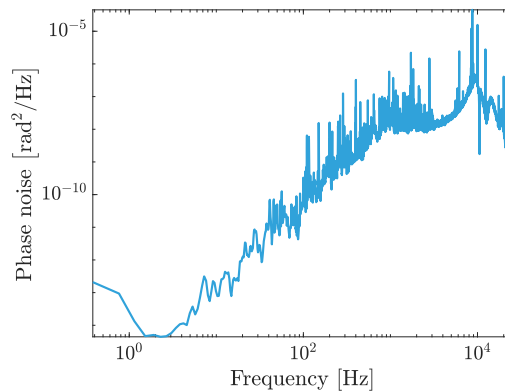


Figure 3.16: Coherent Control in loop phase noise



Dithering based phase control

From equation 3.4.2, it is possible to extract the demodulation phase ϕ_{demod} which corresponds to the coherent control actuation phase.

$$\phi_{cc} = \arctan \frac{-(1+g)\sin(\phi) - (1-g)\sin(\phi - 2\Phi)}{(1+g)\cos(\phi) - (1-g)\cos(\phi - 2\Phi)} \quad (3.8)$$

This equation highlights that the coherent control actuation phase depends non-linearly on the squeezing phase. It is represented in figure 3.17. Especially, if $\Phi \neq 0$ (as represented in this figure where $\Phi = 0.3$ rad), the demodulation phase that minimizes the squeezing level is not equal to zero. It is therefore needed to implement a second phase control loop to insure to stabilize the squeezing phase at the maximum squeezing level.

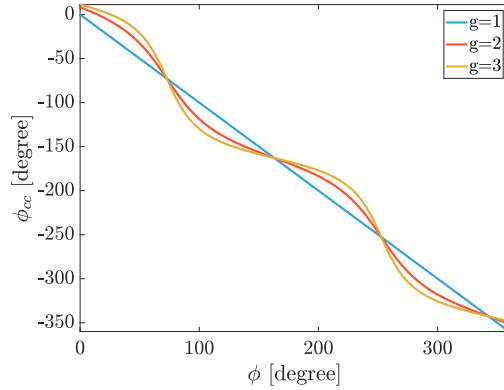


Figure 3.17: Evolution of the coherent control demodulation phase as a function of the squeezing phase for 3 values of OPO non-linear gain ($g=1$: no squeezing). Here, $\Phi=0.3$ rad

Figure 3.18 shows the evolution of the B1 magnitude demodulated at 7 MHz and the squeezing level when linearly varying the coherent control demodulation phase ϕ_{cc} . In later section, this is named a phase scan.

First, it can be seen that the squeezing level minimum is broader than its maximum while the opposite behavior is expected. This arises because of the non-linear relationship between ϕ_{cc} and ϕ . Furthermore, it can also be seen that the B1 magnitude demodulated at $\Omega_{cc}=7$ MHz is sensitive to the variations of ϕ_{cc} and therefore on the squeezing phase. Moreover, there is an offset between the coherent control phase that minimizes the B1 magnitude demodulated at 7 MHz and the phase that minimizes the squeezing level. This means that it is required to implement a second phase control loop in order to insure to stabilize the squeezing at the phase that minimize its level. The B1 magnitude demodulated at 7 MHz can be used to performed this control loop. By modulating ϕ_{cc} around the phase that minimizes the squeezing, the squeezing level can be stabilized to its minimum.

This second phase control loop induces negligible levels of phase noise.

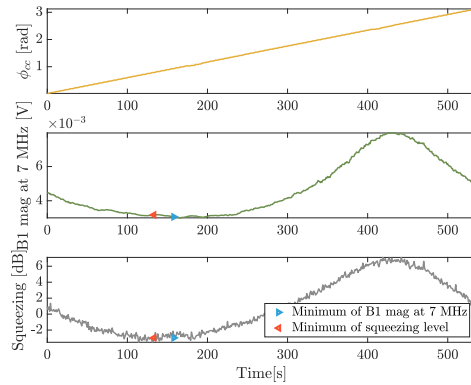


Figure 3.18: Evolution of the B1 magnitude demodulated at 7 MHz and the squeezing level when varying the coherent control demodulation phase ϕ_{cc}

3.4.3 The Alignment Controls

As SDB1 is following the interferometer beam motions, it is important that the squeezed beam also follows these motions to keep an optimal matching and thus low optical losses. As shown in figure 3.11, TY and TZ angular motions are likely to impact the squeezer matching to the interferometer.

Two different alignment control loops have been implemented and are presented in figure 3.19.

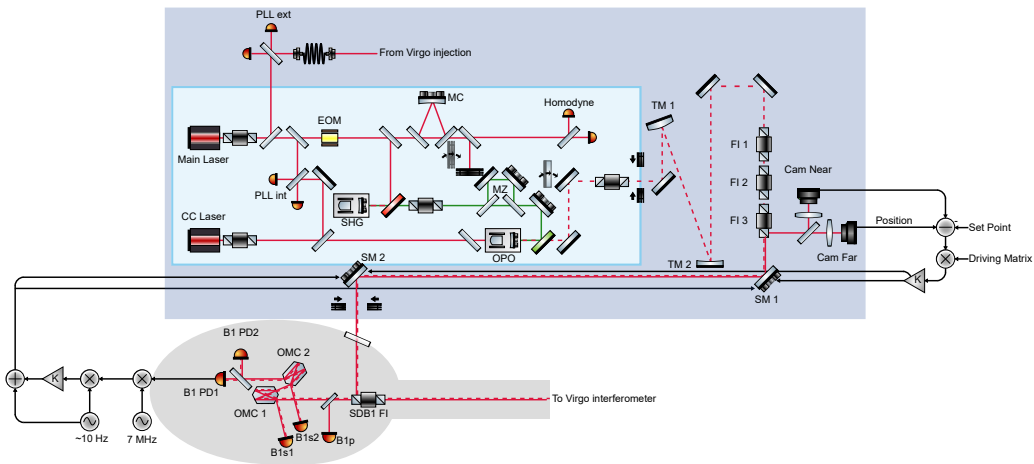


Figure 3.19: Scheme of the two alignment controls used during O3

Cameras

The first alignment control loop is based on signals from the two cameras (Cam Far and Cam Near). These two cameras are sensing the spurious interferometer beam from the SDB1 Faraday Isolator reflected by the last Faraday Isolator on the ESQB (FI3) and can therefore be used independently of the squeezed beam injection. However, this requires to have a stable interferometer beam meaning having the interferometer locked in dark-fringe



with the mirrors well aligned.

The goal of this loop is to keep this beam position around the camera set points that optimize the alignment, by acting on SM1 and SM2 PZT actuators. This control loop implementation is presented in figure 3.19.

First, the error signals are constructed by computing the difference between the beam positions on the cameras with a reference position or set points that optimize the alignment. This set point position is corrected if the interferometer alignment changes drastically. As the error signals are computed from camera signals, they are limited by the 1 Hz sampling rate of the cameras and can therefore only be used for slow alignment control.

The correction signals are then computed by multiplying the error signals by a non-diagonal driving matrix due to the Gouy phase of the steering mirrors as discussed earlier (section 3.2.2).

The correction signals values are then clipped at ± 0.15 V. While this value is large enough to allow the alignment control in normal conditions, it can be useful when large misalignment between the interferometer and the squeezed beam occur. Indeed, if for example the interferometer unlocks, there will be a transient during which the slow alignment loop will try to keep a spurious beam on the camera. It means that there will be large corrections sent to the steering mirrors actuators which can move the alignment far from the optimal one. As the alignment loop is slow, it will require a long time to go back on the optimal alignment during the next lock. The clipping allows to keep the correction low enough to keep the steering mirrors positions close to the optimal one.

Finally, it can be seen in figure 3.20 that the engagement of this loop triggers actuation on SM1 and SM2 which effectively brings the interferometer beam on both Cam Near and Cam Far to their set point positions.

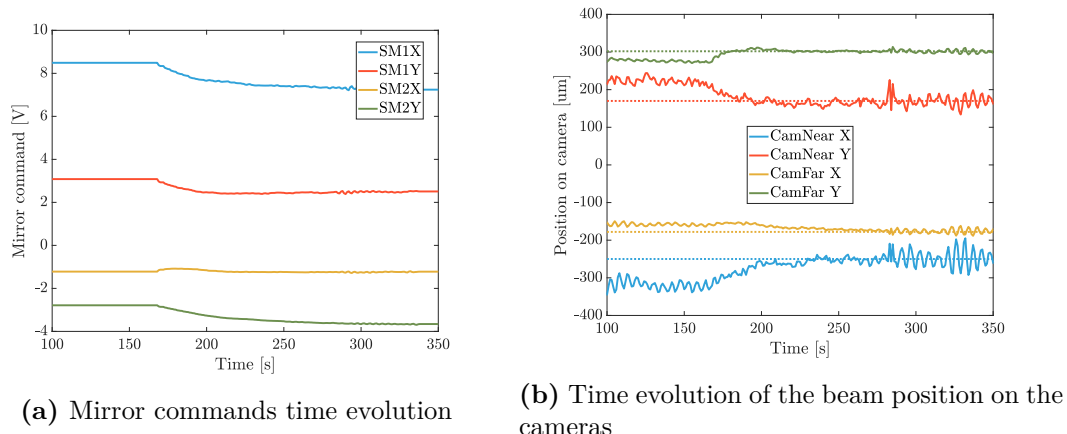


Figure 3.20: Slow Auto-Alignment loop engagement

Kick and degaussing Another motivation for the implementation of the clipping of the correction signals appeared during the commissioning of the squeezer alignment. If a too high command (or kick) is sent to a steering mirror PZT actuator, it might move the

PZT actuator position along its hysteresis curve because this kick can induce a remanent magnetic field of the PZT. For the alignment, this remanent magnetic field means that the position of the

This effect can be seen in figure 3.21 when a kick occurred on SM1X. Despite all actuators command values going back to their initial values, the position of the beam changed on the cameras.

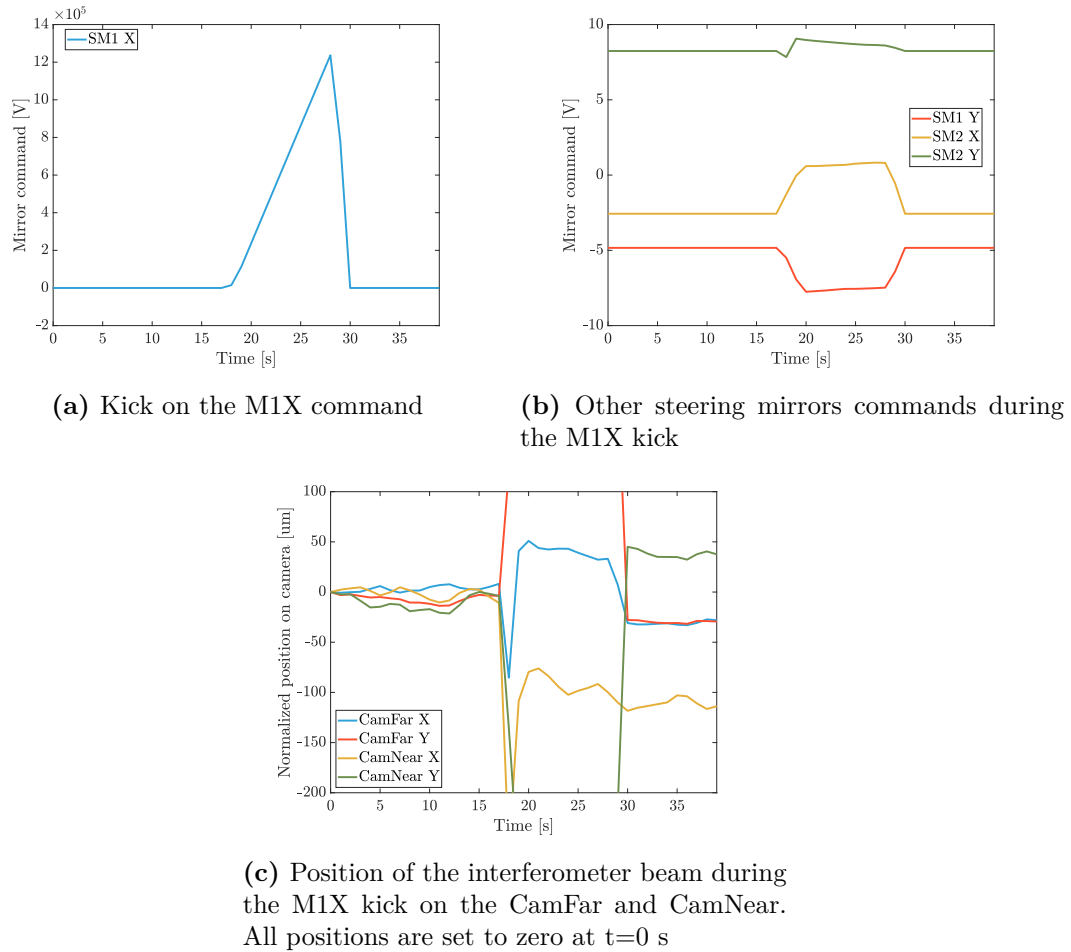
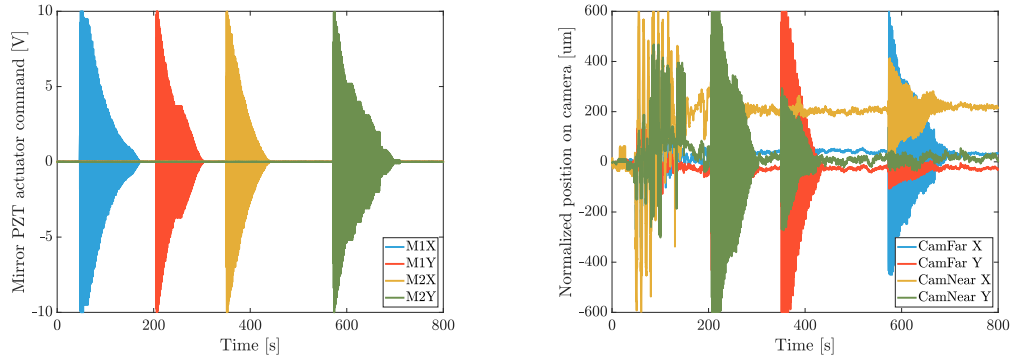


Figure 3.21: Effect of a kick on M1X on the interferometer beam position on the alignment cameras (CamFar and CamNear)

In order to remove this magnetic field, the degaussing operation was performed which consists in applying to each PZT actuator a ramp with slowly decreasing amplitude from -10 V and 10 V to 0 V as presented in figure 3.22

It can be seen that the degaussing operation allows indeed to remove the spurious polarization as the position of the beam on each camera changed following this operation. As the main change on the beam position is with the degaussing performed on M1X, it indicates that this actuator moved the most on its hysteresis curve.





(a) Degaussing of all steering mirrors PZT ac- (b) Interferometer beam position on the cam-
tuators eras (CamFar and CamNear) during the de-
gaussing technique

Figure 3.22: Degaussing performed on all mirrors PZT actuators and resulting effects on the normalized beam position on the cameras

Angular dither lines

The relative alignment between the squeezer and the interferometer is subject to drift. Indeed, as the interferometer optics are suspended but not the squeezer ones, it is possible that the overall interferometer moves with respect to the ESQB. It could be due for example from a different alignment condition of the injection system followed by the entire interferometer motions. At the level of the SDB1, it means that the bench could be moved to a different location and therefore the spurious beam sent to the two camera might move as well. It could be also possible that the squeezer beam is misaligned before SM1 and SM2 (for example due to thermal or humidity transient) and the two cameras are not able to sense this misalignment.

This means that the set points used for the camera based automatic alignment might not represent the optimal alignment conditions over long period of time where relative motions of the ESQB with respect to the interferometer suspended optics can occur.

Therefore another automatic alignment control loop has been implemented so to accurately keep track of the optimal alignment positions.

Because the Coherent Control beam co-propagates with the squeezed beam, it will suffer the same misalignment as the squeezed beam. And because it is detected up to the B1 photodiodes, this beam will precisely sense the overall misalignment. Indeed, as presented in figure 3.23 which shows the B1 signal demodulated at $\Omega_{cc} = 7$ MHz and the SDB1 TY angular motions, it is possible to see that the B1 signal demodulated at $\Omega_{cc} = 7$ MHz is highly sensitive to the alignment conditions. With poor alignment, the SDB1 TY motions are imprinted on the B1 signal while almost not present with good alignment conditions.

As already presented in figure 3.7, a dithering of the angular position of a beam can provide useful signal to monitor and correct its alignment. Therefore, 8 Hz, 11 Hz, 15 Hz and 17 Hz dithering lines with 100 nrad amplitude have been applied to SM1 and

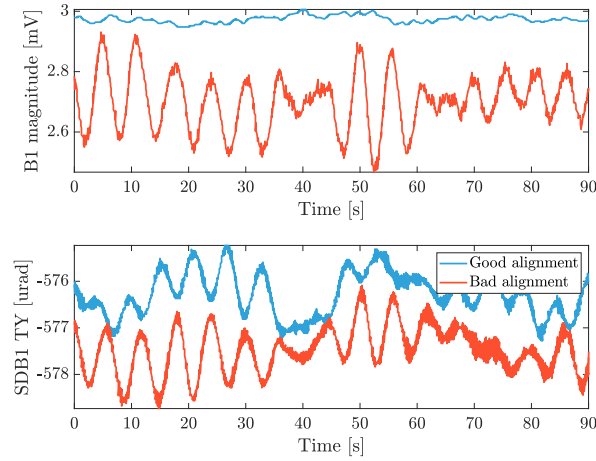


Figure 3.23: Magnitude of the B1 signal demodulated at 7 MHz with good or poor alignment. Bottom figures shows the SDB1 TY motions which are the SDB1 angular motions that affect the most the squeezer alignment

SM2 respective PZT actuators so to generate a dithering of the angular position of the squeezed and the Coherent Control beams for each degree of freedom.

These frequencies will be visible on the B1 magnitude demodulated at 7 MHz. And by demodulating this signal at the dithering frequency, it is possible to extract an error signal for this alignment. Indeed, a good alignment corresponds to the zero-crossing of the B1 magnitude demodulated at 7 MHz and at the dithering frequencies. This error signal is finally used to act on the SM1 and SM2 PZT actuator.

Because this signal requires the Coherent Control beam, this dithering alignment can only be used after that the Coherent Control beam is injected. This technique can therefore be complementary of the camera based alignment.

First, the camera based alignment control is used to pre-align the squeezed beam within the interferometer. Then, from the lock of the Coherent Control, the dithering based alignment is used as it provides a better sensing of the squeezed beam alignment.

This dithering will also induce a beam jitter that can be responsible for optical loss. This loss, estimated at the beam waist is described as :

$$\Lambda_{jitter} = \left(\frac{\delta x}{\omega_0} \right)^2 + \left(\frac{\delta \theta}{\theta_{div}} \right)^2 \quad (3.9)$$

where δx and $\delta \theta$ are the lateral and angular shifts of the beam, ω_0 and θ_{div} the beam waist and divergence.

The dithering technique is responsible for 1 % of optical loss and is not a limiting source of losses for the O3 run.



3.5 Conclusion

This chapter has presented the optical components required to generate and inject frequency-independent squeezed vacuum states at Virgo. The commissioning activities focused on the alignment and mode-matching of these frequency-independent squeezed vacuum states with the Virgo interferometer beam have also been presented. Finally, the alignment and phase controls loops required for the long term injection of frequency-independent squeezed vacuum states have been described.

All these activities allowed to inject for the first time frequency-independent squeezed vacuum states at Virgo as will be described in the next chapter.

4

Frequency Independent Squeezing during O3

Contents

4.1	Introduction	83
4.2	The stray light mitigation	84
4.2.1	First squeezed light injection and scattered-light	84
4.2.2	Mechanical resonances and Virgo sensitivity	97
4.3	The shot-noise decrease	99
4.3.1	Characterization of the squeezing performances	100
4.3.2	Degradation budget	101
4.3.3	Conclusion	112
4.4	The radiation-pressure increase	112
4.4.1	Virgo quantum noise model	112
4.4.2	Experimental results	115
4.4.3	Conclusion	118
4.5	The O3 performances	118
4.5.1	Median squeezing level	118
4.5.2	Duty cycle	121
4.6	Conclusion	123

4.1 Introduction

Following the integration of the squeezer optics and control within Virgo, it was possible to inject for the first time frequency-independent squeezed vacuum states from the Virgo



detection port. This chapter will present the effects of this injection on the Virgo sensitivity from the first frequency-independent squeezed vacuum states injection in November 2018 to the end of the O3 run in March 2020.

4.2 The stray light mitigation

4.2.1 First squeezed light injection and scattered-light

During the commissioning activities presented in last chapter, the frequency-independent squeezed vacuum states have been injected into the Virgo detector. Figure 4.1 shows one of the first injection of the squeezed beam. It compares the Virgo sensitivities with and without a beam dump installed at the output of the ESQB. This corresponds equivalently to check the effects of the coherent control beam as well as the spurious beam coming from the interferometer and optical components required to inject the squeezed beam on the Virgo sensitivity. Especially, this beam dump allows to check if any of these beams can be back-reflected into the interferometer.

Because the alignment and controls were not optimized at that point, optical losses and phase noise degraded too much the squeezing quality to see any improvement of the Virgo sensitivity at high-frequency.

However, a broadband degradation at low-frequency, from about 10 Hz to 80 Hz as well as a few peaks (eg. around 45 Hz and 60 Hz) are visible in the sensitivity. These two effects are symptomatic of scattered light recombining with the Virgo main laser beam and being detected at the B1 photodiodes. This figure particularly highlights the threat of scattered light for interferometric gravitational waves detectors [81] [44] as it affects their sensitivity below a few hundred Hertz where most of the BNS and BBH signals are expected.

Few mechanisms could be responsible for such light :

- First, the OPO reflectivity and the residual reflections on anti-reflective coatings of the squeezer optical components (located on the light blue part of figure 3.2) can be sources of back-reflected light into the interferometer.

It has been computed that the OPO is the main source of back-scattered light inside the squeezer box [76]. However, the installation of three Faraday isolators, with each an isolation factor of 40dB, between the squeezer box and the Virgo interferometer was enough to reduce the level of back-scattered light by more than a factor ten below Virgo sensitivity. This factor ten being the standard tolerated level of technical noises at Virgo.

- Dust particles located on optical components and hit by the beam will be source of scattered light. Therefore the squeezer components were installed inside a closed box.

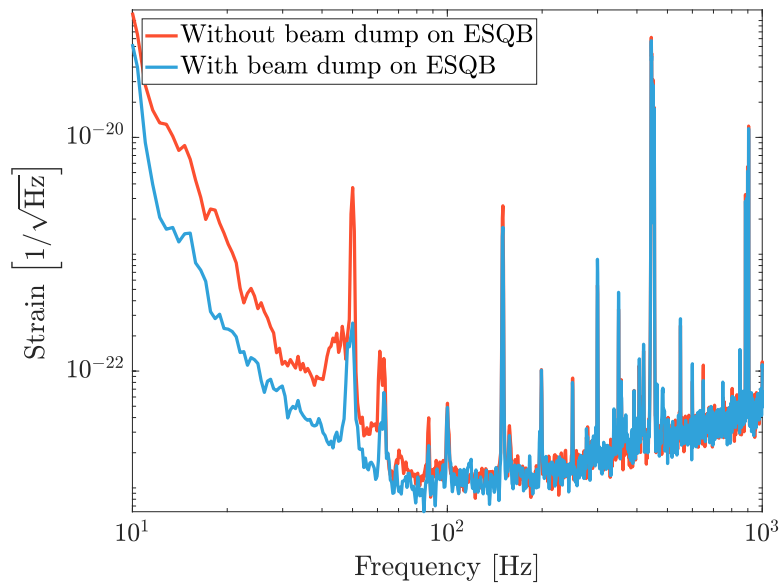


Figure 4.1: Virgo sensitivity with and without a beam dump on the ESQB with a poor squeezer alignment and controls not optimized

However, optical components required for the squeezed light injection were also likely to be affected by dust particles. It has been found out during commissioning activities that a lot of dust was present both on optical components as well as on the viewport installed at the vacuum interface between the SDB1 and the ESQB.

After a careful cleaning of these components, a Plexiglas enclosure has been installed above the ESQB to prevent dust particles. In addition, an airflow was used during each commissioning activities requiring to open this Plexiglas enclosure such that dust particles would be pushed outside this enclosure.

The careful cleaning and Plexiglas enclosure should mitigate back-scattered light due to this effect.

- Another possible source of back-scattered light into the interferometer is a misaligned beam hitting optical mounts. Again, since the three Faraday isolators are installed on the ESQB, it can be expected that only components between the FI3 and the SDB1 might induce such spurious light. This include both Cam Far and Cam Near, crystal and polarizer of FI3, SM1 and SM2 and the SDB1 viewport.

If a beam hits one of these components mounts, any mechanical resonance of this component mount can imprint an excess of noise at the component mechanical resonance frequency. To limit this effect, ESQB has been installed inside an acoustic enclosure which should isolate the ESQB and the components installed on it from the acoustic noise. Furthermore, the ESQB optical bench is installed on a rigid steel frame mounted on elastomer pads to limit the seismic motions that could excite mechanical resonances.

The last item from this list, namely scattered light due to optical component mechanical resonance, was particularly troublesome. The next sections will present the activities



performed to mitigate its effect on the Virgo sensitivity.

Shaking and tapping tests measurement

Figure 4.1 highlighted some possible effects that can be induced by scattered light from the squeezer optics. The peaks present in this figure might be due to a spurious beam hitting an optical component which mechanical resonance couples to an optical path difference. Therefore, this effect can be mitigated by finding the mechanical resonance frequency of optical components on the squeezed beam path.

Because in normal conditions the ground seismic activities are too low to excite all the ESQB mechanical resonances, shaking and tapping of the ESQB optical bench and components have been performed. This allows indeed to excite these mechanical resonances and ease their detections.

The ESQB optical breadboard was shaken by hand in its short and long directions. Three ultra low frequency seismic accelerometers *Wilcoxon Research model 731-207* have been installed on ESQB which sense acceleration noise in every degree of freedom. They are labeled in the following '*X axis*' which senses acceleration noise in the short direction of ESQB (ie parallel to the Faraday isolators chain), '*Y axis*' for the vertical direction and '*Z axis*' for the long direction of ESQB.

The ESQB optical components mechanical resonances have been excited using the *ICP Impulse Force Test Hammer model 086C01*. This hammer provides a broadband nearly-constant force and was used in every degrees of freedom close to the tested optical component.

The *ICP mini accelerometer model 352C68* was mounted on each tested component. Since it weights only two grams, it should not affect the weight distribution of the tested component and therefore allows to not distort its mechanical resonance frequencies. It will be named '*Mini Acc*' in the following sections.

The ESQB mechanical resonances analysis

First, the ESQB mechanical resonances have been measured.

Figure 4.2 shows the resulting acceleration noises sensed by X, Y and Z accelerometers from top to bottom plots while applying excitations along the X and Z directions. On each plot, the gray curve represent the quiet reference spectrum, the blue curve the X excitation spectrum and red curve the Z excitation spectrum between 1 and 1000 Hz. The FFT used to compute these spectra has a 0.15Hz precision.

From this figure, several peaks that are not present in the quiet reference spectrum appear. They correspond to mechanical resonances of the ESQB that are excited by the shaking of the bench.

It can also be seen that for some frequencies, peaks are present both in reference spectrum

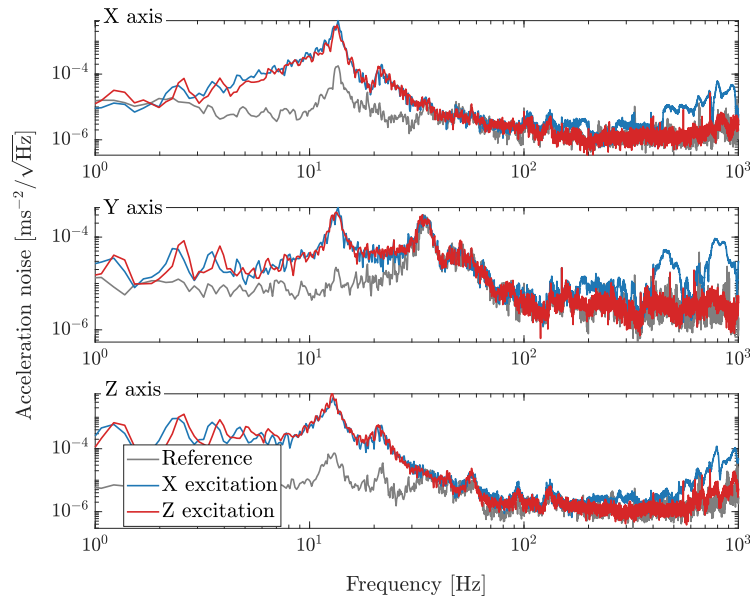


Figure 4.2: Shaking tests performed on the ESQB

and excited spectrum. This means that the excitation has no impact on the acceleration noise at this particular frequency. This could be due to another source of excitation (eg the airflow which is always turned on during commissioning activities in the detection lab) or another component mechanical resonance.

In order to extract the mechanical resonances of the ESQB, the mean spectrum of all sensor for each excitation has been computed.

First, the peaks due to the 50Hz of the power grid and its harmonics may appear on some spectra and spoil the analysis. Therefore, for all frequencies close to 50 Hz and its harmonics (where the 'closeness' is estimated using modulo of the frequency with respect to 50 Hz, eg. between 49.59 Hz and 50.35Hz for the 50Hz line), the spectrum values have been replaced by constant value. This frequency window to remove the 50 Hz harmonics was empirically chosen in order to remove all the harmonics. The constant value replacing the 50 Hz harmonics is taken at the last frequency which has a non-null modulo with respect to the lowest frequency of the frequency window (eg 49.43Hz for the 50Hz case).

Then, a sliding mean filter has been applied to the reference and excitations spectra. In order to keep low-frequency information while smoothing the high-frequency data, the number of points used in the mean computation depends on the frequency f as $\frac{f}{11}$ and $\frac{f}{1}$ for the excited and reference spectra respectively. The reference spectrum is smoother than the excited one in order to remove spurious excitations present in it. For example, as the commissioning activities require to use an airflow, a permanent excitation is present even in the reference spectrum. Finally, the smoothing is performed three times to avoid discontinuities in the smoothed spectra.

The smoothed reference spectrum defines hereafter the background spectrum. Although



this procedure distorts the peak height, it will not change the peak location, and can therefore be used to extract each peak frequency. Then, the peak heights in the excitation spectra are compared to the background level to extract a SNR of each peak. As the smoothing is distorting the peak height, the non-smoothed spectrum levels at each peak frequency are used to estimate this SNR. Finally, only peaks with SNR above 9 are kept.

This analysis is presented in figure 4.3. The reference, X and Z excitation spectra are respectively the gray, blue and red semi-transparent curves. The plain curves represent the smoothed spectra. Each black dot represent a mechanical resonance with SNR above 9. While their frequencies correspond to the frequencies of the mechanical resonances, their heights correspond to the smoothed spectra for better visualization

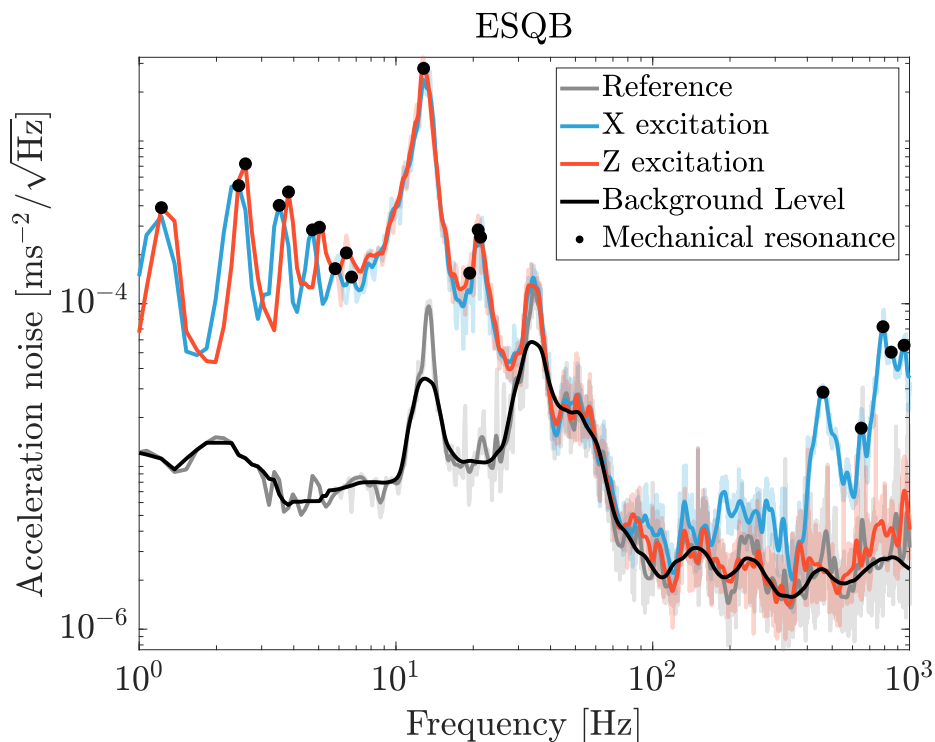


Figure 4.3: Shaking tests on ESQB. Each black dot represents a mechanical resonance

Finally, all mechanical resonances frequencies and SNR are summarized table 4.1.

At low frequency, several mechanical resonances appear to have been detected. But many of them correspond to harmonics of lower frequency mechanical resonances. The 2.44, 3.51, 3.81, 4.73 and 5.95 Hz are harmonics of the 1.22Hz within the 0.15Hz precision of the FFT. This 1.22 Hz was expected to appear from the design of the ESQB optical table and corresponds to a mechanical resonance of this table along the Z directions. The fact that the mechanical resonance is also detected on the X directions could hint that the hand-made excitation along each direction was in practice exciting a combination of both the short and long directions of the ESQB.

The ESQB optical components analysis

In the following, the tapping and shaking tests results of other ESQB optical components are presented. The same analysis as for the ESQB. However, another accelerometer labelled '*Mini Acc*' was also installed on each tested optical element such that it senses acceleration noise in the direction parallel to the incident beam direction of the tested component.

The SDB1 viewport pipe

The SDB1 viewport pipe by which the squeezed beam is injected into the interferometer has also been tested with an X excitation which is parallel to the incident beam direction. The frequency window for the smoothing is $\frac{f}{12}$. As the SDB1 viewport pipe reference spectrum exhibits several peaks, the background level was estimated by using a sliding median filter with a window of $\frac{f}{2}$. This allows to extract a background level less sensitive to peaks with respect to a mean filter.

Here, the subtraction of all 50Hz lines is also quite visible when comparing the raw and smoothed data.

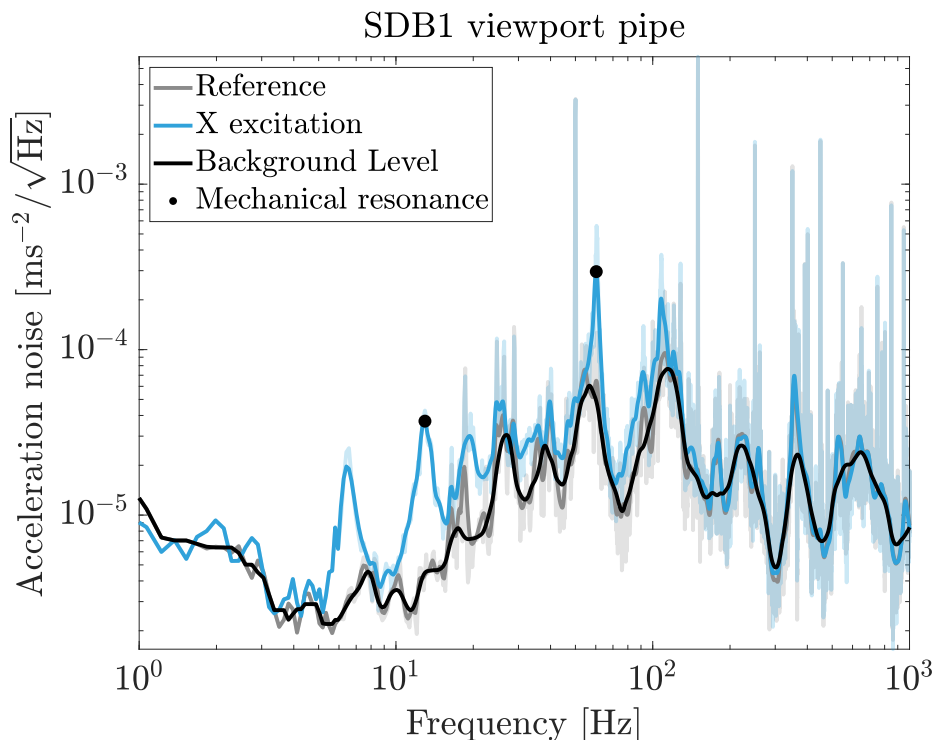


Figure 4.4: Tapping tests on SDB1 viewport pipe. Each black dot represent a mechanical resonance

As can be seen in figure 4.4, only two mechanical resonances with q SNR above 9 have been found.



The steering mirrors

SM1 and SM2 are installed on identical mount so it can be expected that they share the same mechanical resonances. On the other hand, their holders or mounts might have been installed differently which could lead to some distortions of their mechanical resonances. However, there was not enough space to perform the measurement on the SM1. Therefore only one steering mirror has been tested. This is a critical test to do as stray-light is highly sensitive to these steering mirrors motions. This test consisted of excitations along the X, Y and Z directions (similar to the following components).

SM2 being the last component on the ESQB, it is the most affected by the SDB1 motions relative to the ESQB. Indeed, a misalignment between the interferometer and the ESQB leads directly to a motion of the interferometer beam on the SM2. Since the SM2 is used to steer the beam position, the beam should always be on the same position on the SM1 (but might have a different incidence angle that is corrected by the SM1). Furthermore both SM1 and SM2 are 1" optics installed on mount with 23mm clear aperture with beams incident at 45° on both of them. These two effects could make the SM2 a critical source of back-scattered light into the interferometer.

As can be seen in figure 4.5, two broadband excitations are present in the excited spectrum. In order to well represent these excitations, a median filter with small windows has been applied. They are respectively $\frac{f}{32}$ and $\frac{f}{6}$ for the excited and reference spectra. Indeed these smaller windows allow to detect peak on the shoulder of these two main excitations.

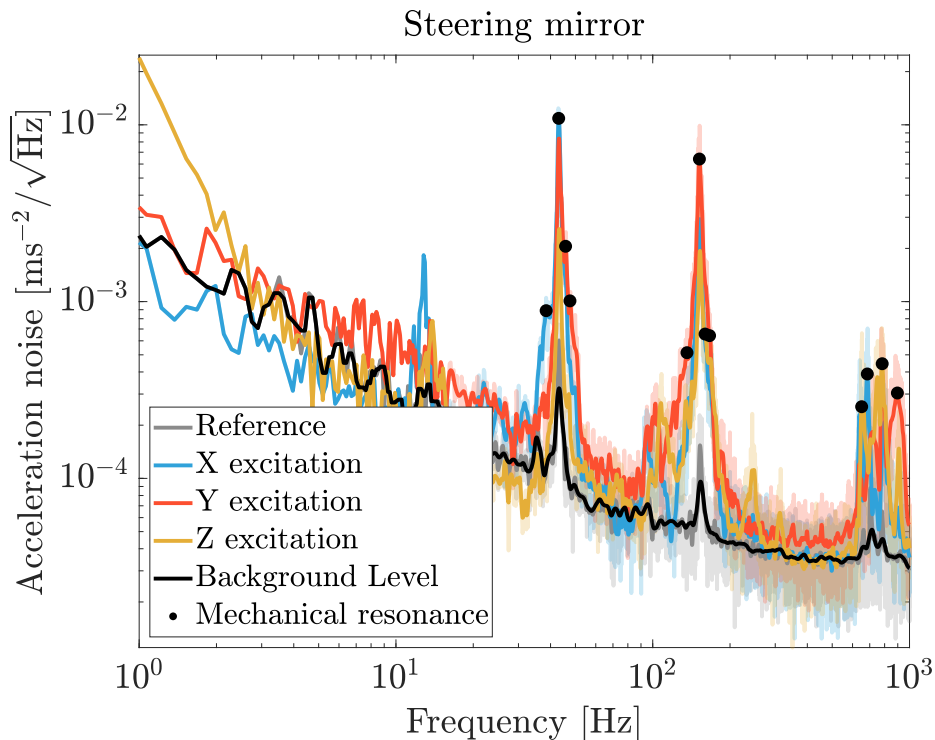


Figure 4.5: Tapping tests on SM mount. Each black dot represents a mechanical resonance

The Faraday isolator

The Faraday isolators chain should prevent scattered light from the squeezer box to be injected back into the interferometer. However FI3, which is the first Faraday isolator that the interferometer beam will encounter, can itself be a source of back-scattered light into the interferometer. The amount of spurious light coming from the interferometer can be reduced by properly tuning the SDB1 Faraday isolator wave-plate leading to approximately $500\mu\text{W}$ on the ESQB. The FI3 is constituted by several components that have been tested independently. The results are presented below.

The polarizer mount The FI3 polarizer is the first element of the FI3 hit by the interferometer spurious beam. It has a size of $25\text{mm} \times 55\text{mm}$ with a 10mm thickness.

In a similar fashion to the steering mirrors analysis, a median filter with a small smoothing windows has been chosen. The windows are respectively $\frac{f}{40}$ and $\frac{f}{3}$ for the excited and reference spectra. The results are presented in figure 4.6. The polarizer mount main mechanical resonances are located around 45, 70 and 300 Hertz.

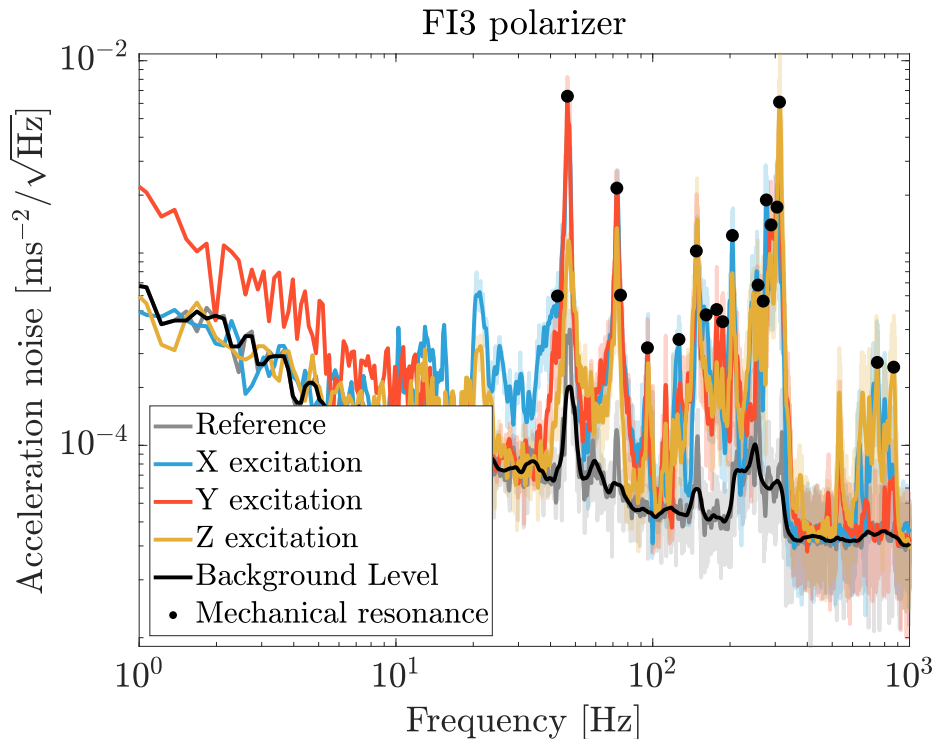


Figure 4.6: Tapping tests on FI3 polarizer mount. Each black dot represents a mechanical resonance

The polarizer mount base The FI3 polarizer mount base has been also tested and the results are presented in figure 4.7. Due to space constraints, only an X excitation could be performed.

The excited spectrum used a $\frac{f}{12}$ window and the background a $\frac{f}{2}$ window to apply



a median filter. The polarizer mount base exhibits only few mechanical resonances around 300 Hertz compared to the other components.

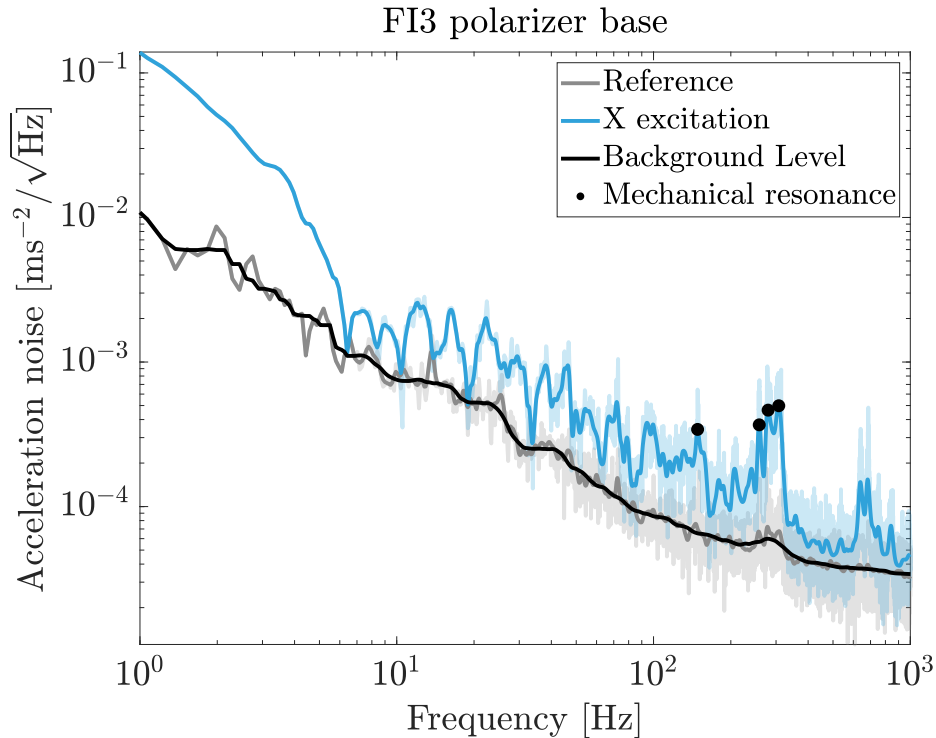


Figure 4.7: Tapping tests on FI3 polarizer mount base. Each black dot represents a mechanical resonance

The crystal mount Finally the FI3 crystal mount has been tested with results presented in figure 4.8. The crystal is a cylinders of 13mm diameter and 18mm thickness.

A median filter with window of respectively $\frac{f}{26}$ and $\frac{f}{4}$ were applied for the excited and reference spectra. The crystal mount exhibits the most mechanical resonances with and SNR above 9 in all the tested components. These mechanical resonances are especially located between 40 and 70 Hertz as well as between 80 and 300 Hertz.

The Cameras

The two cameras Cam Far and Cam Near can also be a source of stray-light for the interferometer as they sense the interferometer beam reflection from FI3.

Similar to the Steering Mirrors, they are identical and installed in identical mounts. Therefore, data of tapping tests performed on both cameras have been analyzed together.

Many 50Hz are visible in the raw signals and removed before the analysis as previously presented. A median filter with respective windows $\frac{f}{20}$ and $\frac{f}{5}$ for the excited and reference spectra was applied.

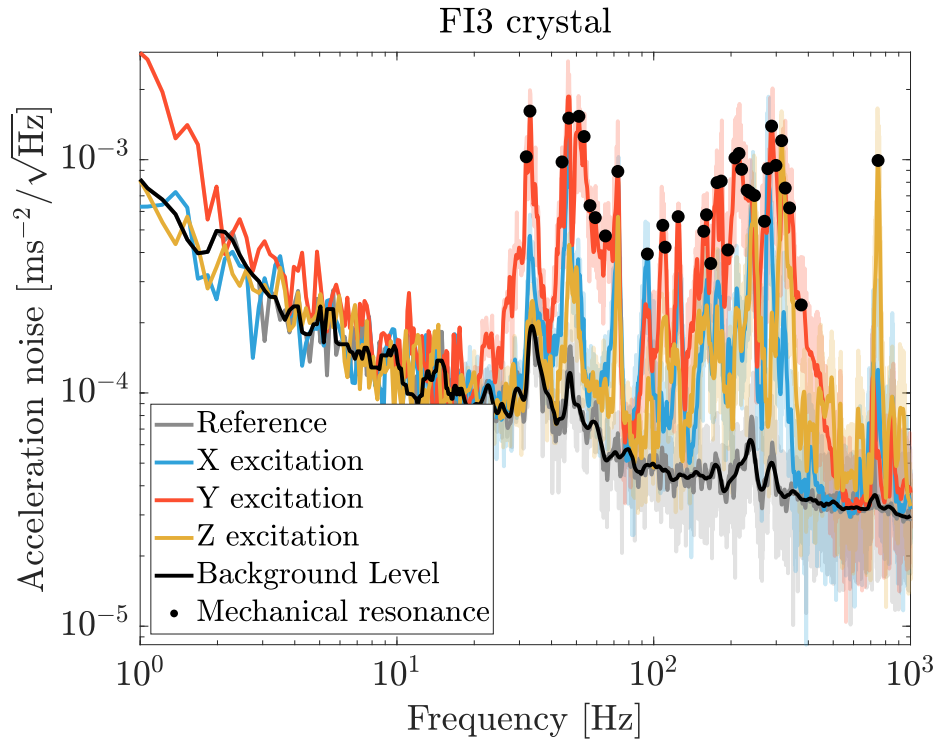


Figure 4.8: Tapping tests on FI3 crystal mount. Each black dot represents a mechanical resonance

It can be seen in figure 4.9, that 2 mechanical resonances are detected around 27Hz. As the frequency difference is so small between the peaks due to different mechanical excitations, it can be assumed that they actually correspond to the same mechanical resonance. This brings a limit to the precision with which the mechanical resonance frequency is estimated at the order of $\pm 0.8\text{Hz}$. This precision is given by the two mechanical resonance frequencies difference. The frequency of this mechanical resonance has then been estimated as the mean of these frequencies.

All results of the tapping tests are summarized in table 4.1. We can recall here that the excited spectra were less smoothed than the background spectrum to insure that spurious excitations present even in the reference spectrum are not introducing bias in the measurement. A possible important source of excitation is the airflow turned on during the measurement.

Frequency [Hz]	SNR	Component
1.2	35.50	ESQB
2.4	42.79	ESQB
2.6	62.94	ESQB
3.5	55.38	ESQB

Continued on Next Page



Frequency [Hz]	SNR	Component
3.8	76.18	ESQB
4.7	43.66	ESQB
5.0	44.59	ESQB
5.8	25.88	ESQB
6.4	35.66	ESQB
6.7	24.16	ESQB
8.5	29.34	ESQB
12.8	76.38	ESQB
13.0	9.56	SDB1 viewport pipe
20.9	29.28	ESQB
21.4	19.53	ESQB
27.2	16.81	Camera
31.9	10.90	FI3 Crystal
33.0	10.90	FI3 Crystal
38.5	9.31	Steering Mirror
42.6	9.14	FI3 Polarizer
43.0	38.25	Steering Mirror
44.0	14.36	FI3 Crystal
45.8	17.38	Steering Mirror
46.5	42.06	FI3 Polarizer
46.7	16.19	FI3 Crystal
47.6	11.75	Steering Mirror
51.0	21.53	FI3 Crystal
53.4	15.70	FI3 Crystal
56.5	9.58	FI3 Crystal
59.2	10.00	FI3 Crystal
60.3	9.55	SDB1 viewport pipe
63.6	21.67	Camera
64.8	11.40	FI3 Crystal

Continued on Next Page

Frequency [Hz]	SNR	Component
66.5	28.01	Camera
72.3	23.14	FI3 Crystal
72.5	41.86	FI3 Polarizer
73.5	57.86	Camera
74.9	10.72	FI3 Polarizer
92.8	18.59	Camera
95.4	10.04	FI3 Polarizer
108.5	12.89	FI3 Crystal
122.7	9.08	Camera
124.5	11.07	FI3 Crystal
126.5	10.57	FI3 Polarizer
136.0	11.06	Steering Mirror
137.6	12.01	Camera
144.3	12.86	Camera
147.9	30.41	FI3 Polarizer
148.5	9.88	FI3 Polarizer Base
152.0	75.47	Steering Mirror
156.3	10.10	FI3 Crystal
159.9	10.25	Steering Mirror
160.2	11.53	FI3 Crystal
161.4	13.09	FI3 Polarizer
166.5	14.32	Steering Mirror
176.1	22.61	FI3 Crystal
177.5	16.51	FI3 Polarizer
182.9	19.70	FI3 Crystal
187.2	11.78	FI3 Polarizer
204.3	26.55	FI3 Polarizer
207.8	25.61	FI3 Crystal
214.5	19.75	FI3 Crystal

Continued on Next Page



Frequency [Hz]	SNR	Component
230.4	13.34	FI3 Crystal
236.8	10.82	FI3 Crystal
242.3	12.04	FI3 Crystal
257.1	13.89	FI3 Polarizer
258.0	10.38	FI3 Polarizer Base
269.3	15.11	FI3 Polarizer
269.9	16.17	FI3 Crystal
276.9	34.75	FI3 Polarizer
278.3	32.73	FI3 Crystal
279.4	11.42	FI3 Polarizer Base
287.9	32.14	FI3 Crystal
289.0	36.21	FI3 Polarizer
291.3	13.11	Camera
304.9	40.46	FI3 Polarizer
307.5	12.29	FI3 Polarizer Base
311.7	112.99	FI3 Polarizer
314.9	37.54	FI3 Crystal
341.6	21.10	FI3 Crystal
341.8	10.44	Camera
363.0	9.65	FI3 Crystal
403.1	12.70	Camera
432.0	29.23	Camera
460.4	10.71	ESQB
548.7	9.80	Camera
651.1	9.03	Steering Mirror
685.0	14.20	Steering Mirror
747.1	38.74	FI3 Crystal
748.9	13.26	Camera
749.4	10.81	FI3 Polarizer

Continued on Next Page

Frequency [Hz]	SNR	Component
782.8	12.55	Steering Mirror
788.4	25.05	ESQB
846.6	15.27	ESQB
867.9	9.08	FI3 Polarizer
897.1	9.15	Steering Mirror
950.6	15.85	ESQB

Table 4.1: Mechanical resonances of the ESQB components with a SNR above 9 with respect to a quiet reference spectrum. The frequency precision is $\pm 0.45\text{Hz}$

4.2.2 Mechanical resonances and Virgo sensitivity

Following these tests, the airflow has been accidentally been left on inside the squeezer enclosure causing a broadband excitation of its mechanical resonances. This had a clear effect on the sensitivity as presented in figure 4.10.

However, by comparing the excitations in this figure to the mechanical resonances of the ESQB components, these data can be used to find which of the previously found mechanical resonances are critical for the sensitivity. For instance, it can be seen that several are matching the FI3 Crystal mechanical resonances, polarizer and steering mirrors. Indeed, using an infra-red viewer, the beam was found out to be hitting the mounts of SM1 and FI3 polarizer while a spurious beam was hitting Cam Near mount. After a careful realignment, making sure that the beam was well centered on all optics and that no spurious beam was present, the degradation of the interferometer sensitivity due to back-scattered light on ESQB disappeared.

Later on, during the O3 run, some suspect structures appeared again in the sensitivity spectrum. By comparing these structures peak frequencies to the ESQB mechanical resonances frequencies of table 4.1, it was again possible to incriminate the same components. This highlighted the fact that the scattered light coming from the ESQB is highly sensitive to the relative alignment between the ESQB and the interferometer.

For the O4 run, it is foreseen to replace the steering mirrors SM1 and SM2 by 2 inches aperture optics. Also, the FI3 crystal and polarizer might be replaced by larger aperture ones. However, the Faraday isolators will be installed on suspended optical benches under vacuum which will decrease the coupling between environmental noises and mechanical resonances.



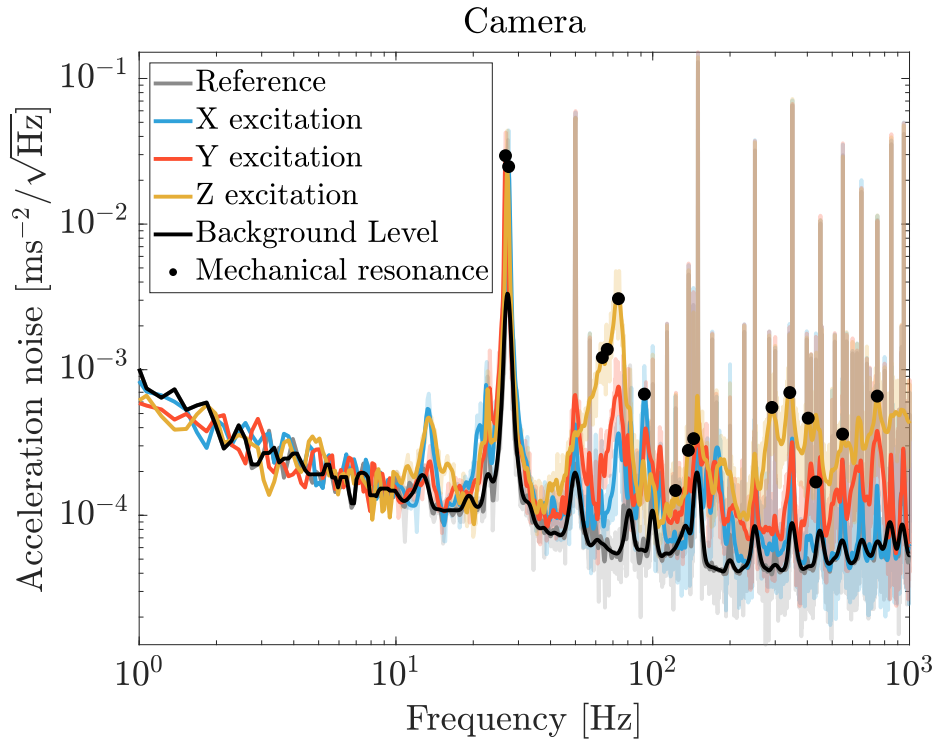


Figure 4.9: Tapping tests on both Cam Far and Cam Near mounts. Each black dot represents a mechanical resonance

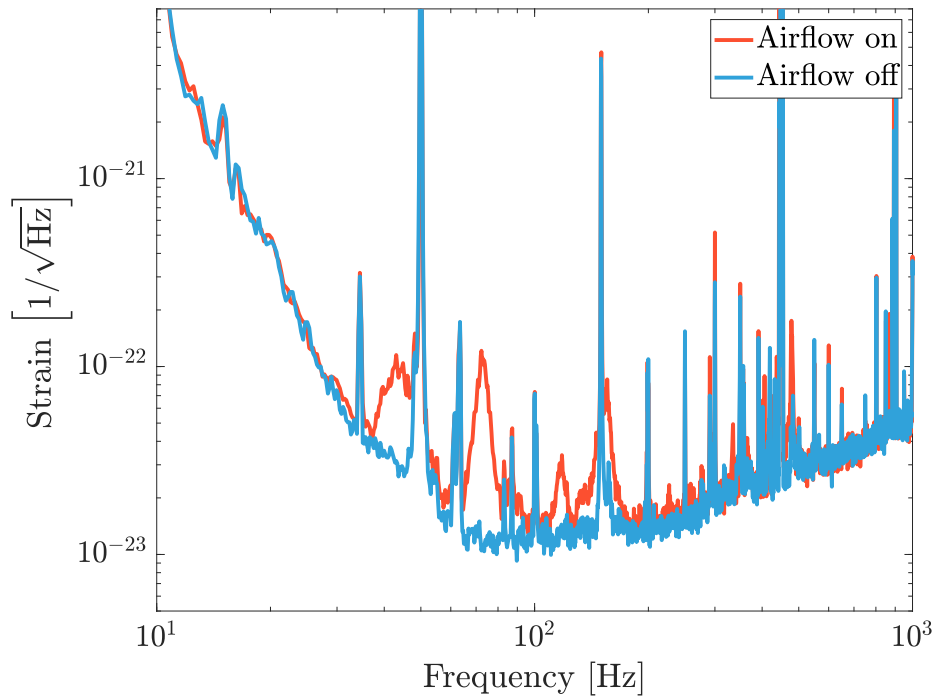


Figure 4.10: Effects of airflow inside the squeezer enclosure on the interferometer sensitivity with poor squeezer alignment conditions

4.3 The shot-noise decrease

This section presents the improvement of the Virgo sensitivity when injecting frequency-independent squeezed vacuum states.

As already presented before, it is possible to accurately control the phase between the squeezed vacuum quadrature and the interferometer readout quadrature. This means that it is possible to inject squeezing and anti-squeezing by tuning this phase. For the O3 run, the shot-noise limits the high frequency sensitivity while the radiation-pressure noise is hidden under technical noises, the goal of the squeezing injection is to reduce the shot-noise level while limiting the radiation-pressure noise increase in order to not spoil the low-frequency sensitivity.

Following the scattered light mitigation activities, it was possible to observe the improvement on the interferometer sensitivity thanks to the squeezing injection accompanied by a BNS range improvement. This improvement has been summarized in [82].

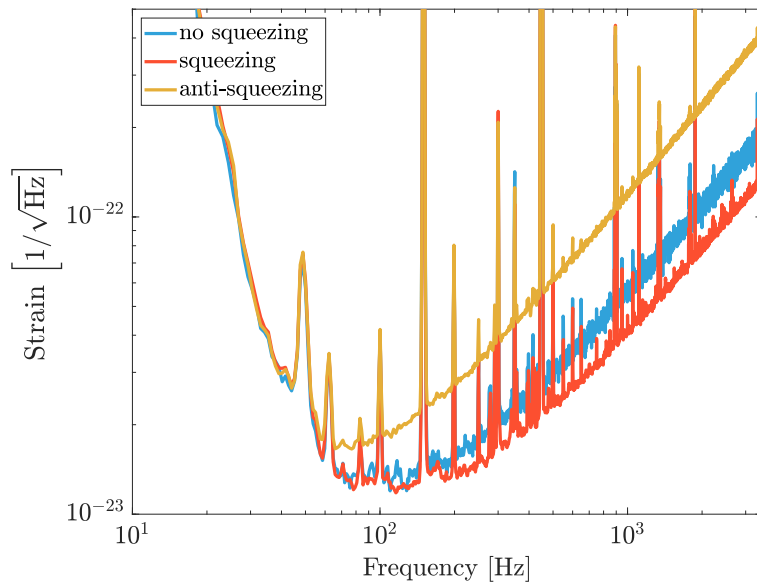


Figure 4.11: Virgo sensitivity without squeezing (blue), with squeezing (red) and anti-squeezing (yellow) injected from the detection port. This measurement was performed with 4.4 mW of OPO green pump power in February 2019

By comparing the sensitivities with and without the squeezing injection which correspond respectively to the red and blue traces in figure 4.11, it is possible to see an improvement of the sensitivity down to ~ 80 Hz. This observation is coherent with the Standard Quantum Limit frequency (f_{SQL}) of the Virgo interferometer which is given by :

$$f_{SQL} = \frac{1}{2\pi} \frac{8}{c} \sqrt{\frac{P_{arm}}{m} \frac{\omega_0}{T_{IM}}} = 72Hz \quad (4.1)$$

using parameters in the table ??.



Parameter	Symbol	Value
Arm circulating power	P_{arm}	95 kW \pm 5kW
Arm mirror mass	m	42 kg
Input Mirror Transmittance	T_{IM}	1.37 %
Carrier frequency	ω_0	1.77 10^{15} rad/s

On the other hand, comparing the anti-squeezing injected sensitivity with no squeezing sensitivity, the degradation of the shot-noise is clearly visible at high-frequency. As expected, no improvement of the sensitivity at low-frequency due to the radiation-pressure noise reduction is visible.

From such figure, it is also possible to estimate the improvement on the BNS and BBH ranges.

Using a GWINC [75] built-in function which computes the BNS and BBH ranges as described in [83], it is possible to compute the range improvement. From figure 4.11, we get an improvement on the BNS range of 1Mpc and an improvement on the BBH range of 12Mpc. At the time of the measurement, the BNS and BBH ranges without squeezing injection were respectively 42 Mpc and 435 Mpc or equivalently to an improvement of 8% and 9% for respectively the BNS and BBH detection rates.

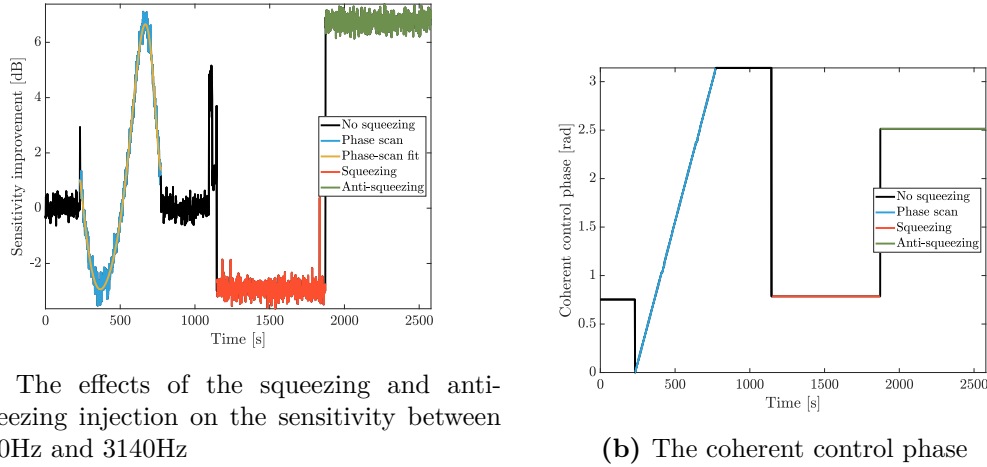
This level of improvement was obtained with 4.4 mW of OPO green pump power. However, in the case of frequency-independent squeezing injection, there is an optimal level of OPO green pump power.

On one hand, too low green pump power will lead to a minor improvement of the shot-noise and therefore the detector sensitivity. On the other hand, too high green pump power will lead to a deterioration of the radiation-pressure noise up to the point where there is a broadband degradation of Virgo sensitivity below hundred Hertz. As this is the range where most of the BBH and BNS signals happen, this will badly affect both their detection rates.

This is one of the reason why various levels of green pump power were tested to find the optimum configuration. This test also allows to extract many useful informations for the squeezing system integration at Virgo as it will be presented in the next sections.

4.3.1 Characterization of the squeezing performances

In order to measure the level of squeezing and anti-squeezing, the Band Root Mean Square (BRMS) of the sensitivity between 2650 Hz and 3140 Hz has been used. This frequency range is used for two reasons. First it is at high enough frequency to be only limited by shot-noise. This means that any changes in this frequency range is mainly due to effects on the shot-noise. Finally, this frequency range presents also the advantage to not contain any frequency lines used to calibrate the detector. This avoids any distortion on the BRMS value.



(a) The effects of the squeezing and anti-squeezing injection on the sensitivity between 2640Hz and 3140Hz

(b) The coherent control phase

Figure 4.12: Squeezing and anti-squeezing effects on the sensitivity between 2640Hz and 3140Hz while changing the coherent control phase. This measurement was performed with 4.4 mW of OPO green pump power

Following the usual convention, the squeezing level can be expressed in decibels as

$$R_{\pm}^{L, \tilde{\theta}} [\text{dB}] = 10 \log_{10} \left(\frac{BRMS_{V_{\pm}}}{BRMS_{NOSQZ}} \right) \quad (4.2)$$

Figure 4.12 presents the effect of variations of the coherent control demodulation phase on the level of this high-frequency BRMS expressed in dB :

First, a reference level is obtained by taking data with the squeezer shutter closed (or equivalently without the squeezing injection) as represented by the black line. This level acts as the normalization level to estimate the (anti-)squeezing effect in dB. This reference level is used to compute the sensitivity without squeezing (blue curve) of figure 4.11.

Then, a scan of the coherent control demodulation phase is performed (green window). Note the shape of the squeezing exhibits the behavior described in section 3.4.2. By fitting the effect on the BRMS, it is possible to extract the highest and lowest levels which corresponds respectively to the measured anti-squeezing and squeezing. In this figure, there was 6.7dB and -2.9dB of respectively measured anti-squeezing and squeezing. From the fit, it is also possible to extract the Coherent Control (CC) demodulation phase which corresponds to (anti-)squeezing.

Finally, data are acquired for these phases and it is possible to extract (anti-)squeezing data. For instance, the red curve of figure 4.11) corresponds to the squeezing injection represented by the red curve in figure 4.12.

4.3.2 Degradation budget

The previous two sections presented how to estimate the (anti-)squeezing level from its effect on the sensitivity.

As presented in figure 2.12, optical losses and phase noise degrade the measured level



of (anti-)squeezing¹ However, it is possible to disentangle these two mechanisms since their effects change with the level of injected (anti-)squeezing. In particular optical losses limit especially low-level of injected (anti-)squeezing while phase noise limits especially high-level of injected (anti-)squeezing. This is expressed in equation 2.66.

First we can see that by varying the OPO pump power P_{pump} , it is possible to change the level of injected (anti-)squeezing. This means that if we measure the levels of squeezing and anti-squeezing at the output of the interferometer we can probe the optical losses and phase noise. However, the level of injected (anti-) squeezing is also dependent on the OPO threshold power P_{thr} which adds an uncertainty on the estimation of optical losses and phase noise.

In order to more precisely estimate the optical losses and phase noise, it is then preferable to compute the measured squeezing as a function of measured anti-squeezing. This will remove the dependency on the OPO threshold power.

This measurement has been performed twice in February and May 2019. Indeed, in between these two dates, many commissioning activities have been performed to improve the Virgo sensitivity for the O3 run. Related to the squeezing, the main effect was the change of B1 photodiodes for higher quantum efficiency ones, which should translates into lower optical losses.

These two measurements are presented in figure 4.13. Experimental data correspond to the dotted points. They corresponds to the measured levels of squeezing and anti-squeezing at the interferometer output for a given level of green pump power into the OPO. The error-bars correspond to the standard deviation of the measurement.

The fitting uncertainties were estimated using a one sigma confidence interval.

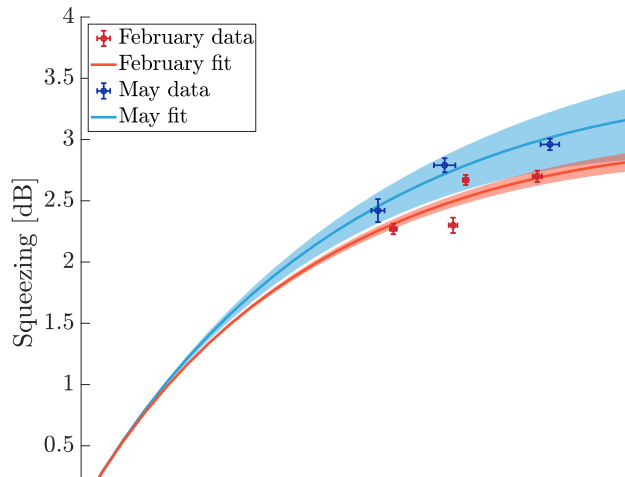


Figure 4.13: Fitting of squeezing as a function of anti-squeezing for February and May 2019 scan of the OPO green pump power. The shaded areas correspond to the one sigma uncertainties on the fit

For the February measurement (45 ± 1)% of optical losses and (55 ± 7) mrad of phase noise is found. While for the May measurement (40 ± 2)% of optical losses and (52 ± 30)

¹Note that the classical phase noise also participate to the optical losses through their equivalent losses

mrاد of phase noise is measured.

The main difference between these two measurements comes from the improvement of the optical losses.

For the May measurement, it was not possible to inject the highest OPO green pump power as in February. As a consequence, the phase noise is far less constrained in the fit (as its effect increases with the level of produced squeezing).

To better quantify these differences, optical losses and phase noise possible origins have been studied.

The optical losses

Optical losses have been grouped into two categories depending on their location with respect to the interferometer :

- all optical losses between the squeezer and the interferometer are called injection losses.
- all optical losses between the interferometer and the B1 photodiodes are called readout losses.

This distinction is useful when trying to estimate their levels as the detection losses will affect the shot-noise even without the squeezing injection.

The optical losses estimation is presented in table 4.2. From this table we can see that there are various origins for optical losses.

First, non-perfect highly-reflective or anti-reflective coatings can be a source of losses. The corresponding values in the table are either coming from measurements for critical components (eg telescope lenses on the SDB1, optical window,...) or an estimate of the value was used (eg steering mirrors on the ESQB have a good polishing quality so a conservative value of 100 ppm of losses per reflection on such mirror was used).

Then, the non-perfect matching between either the squeezed beam or the OMC with the interferometer is inducing losses. They have been measured with only the NI mirror aligned. This is called the cold state as there is no power in the arm cavities. However, during the steady state operation $\sim 100\text{kW}$ is circulating inside the arm cavities. This creates thermal deformation of both the arm mirrors thickness and surface curvature meaning that the arm mirrors effective radius of curvature is changed. This means that the interferometer beam parameters are different between the matching measurements and the steady state operation.

A measurement of the matching between the OMC and the interferometer has been performed with the interferometer in nominal condition which showed an increase of 1% of the matching losses due to the thermal effects inside the arm cavities.

Table 4.2 shows the squeezing injection and detection losses estimated as the product of the efficiency of each component interacting with the squeezed beam. As precised on the reference column, some of the optical components have been characterized at LMA while other have been measured on the detector or on other experiments. The interferometer



losses have been estimated from the GWINC model of the detector by computing the degradation of high frequency squeezing without injection or readout optical losses and without phase noise. The interferometer losses are mainly coming from the BS losses (1510 ppm).

By comparing the optical losses derived from the optical properties of the component seen by the squeezed beam from table 4.2 and the optical losses derived from the OPO green pump power scan (extracted from figure 4.13), we can see that there are still 26 % of unknown optical losses.

A part of this unknown losses could come from the fact that this table refers to the best measured (or estimated) values of losses. Especially, the mode-matching between the squeezed beam and the OMC is estimated in single bounce meaning that it could differ in normal interferometer conditions. It has been estimated that the losses in this normal conditions could rise to 8%. Also, the various Faraday isolators losses are estimated from [77] where thermal control was present. Without such thermal control, as it is the case for the O3 run, the Faraday isolators losses could rise to 2.5%.

Taking into account these degradations leads to 27.6% of optical losses. Despite this change, there is still an important part of the optical losses which origin is not described. As presented in the next section, a possible explanation could be technical noises that induces equivalent shot noise at the B1 photodiodes while not being decreased by the squeezing injection.

The technical noises

From the previous sections, it can be seen that the level of optical losses directly measured with the injection of squeezing or anti-squeezing is larger than the level of optical losses deduced from the optical properties of components encountered by the squeezed beam. The difference between the two values could be explained by technical noises below the shot-noise. They can indeed limit the shot-noise improvement when injecting squeezing which can mimic the effect of optical losses for the squeezing injection.

To estimate this effect, a high-frequency noise budget for the February and May 2019 measurements has been computed. This has been performed using GWINC [75] and applying the following steps :

First, the interferometer parameters that affect the shot-noise have been tuned to reproduce the conditions of the two measurements. Most of these parameters were extracted from the GWINC configuration file for the nominal Virgo operation during the O3 run

The input power

The input power has been set to 18.4 ± 1 W as measured during the each measurement. The input power uncertainty is coming from uncertainty on the various coating reflectivities and photodiode quantum efficiency uncertainties.

The round-trip losses

The arm cavity round-trip losses has been set to 80 ppm so that the interferometer PR gain is similar to the measured one (36 ± 0.2). This PR gain can be measured

Source	Value	Reference
OPO escape efficiency	0.99	[40]
Squeezer box Faraday isolator	0.98	[40]
ESQB Faraday isolator [3 passes]	0.9269	[77]
Squeezer and interferometer matching	0.95	[82]
Alignment jitter	0.99	[82]
SDB1 Faraday isolator	0.975	[77]
All lenses on the path	0.9998	Mesured at LMA
All mirrors on the path	0.9999	Mesured at LMA
SDB1 viewport window	0.9999	Mesured at LMA
Injection efficiency	0.8325	
Injection Losses	0.1675	
OMC coupling	0.975	[39]
OMC intra-cavity	0.98	[39]
OMC and interferometer coupling	0.97	[82]
SDB1 pick-off	0.985	[82]
SDB1 Faraday isolator	0.992	[77]
B1 quantum efficiency	0.99	[61]
All mirrors on path	0.999	Conservative estimation
SDB1-SDB2 Window	0.9992	Mesured at LMA
All lenses on path	0.9982	Mesured at LMA
Readout efficiency	0.8794	
Readout losses	0.1206	
Interferometer efficiency	0.989	
Interferometer losses	0.011	
Total efficiency	0.7241	
Total losses	0.2759	

Table 4.2: Optical efficiencies and losses for components seen by the squeezed beam from measurements. Best values are indicated. The interferometer losses are extracted from GWINC modelisation



by comparing the arm circulating power with the PR cavity aligned and locked or with the PR cavity misaligned and not locked. The PR gain corresponds to the ratio of these two powers. The PR gain is measured with a good precision as it can be deduced from a relative measurement of the arm circulating power; thus removing the systematical uncertainty of the measurement system.

The finesse

The arm cavity finesse has been set to 465 ± 5 as measured during the calibration measurements.

The shot noise is then only dependent on the detection efficiency. As the high-frequency sensitivity is the quadratic sum of shot-noise and technical noises, it means that by estimating the level of technical noises it is possible to estimate the detection efficiency.

There are several noises that affect the high-frequency sensitivity :

The B1 photodiodes dark noise

The dark noise refers to the noise induced by the current flowing inside the photodiodes even when no light hits it (hence the name). This current implies that part of the signal detected by the B1 photodiodes is independent from the shot noise and therefore can not be reduced by the squeezing injection. The dark noise can therefore be considered equivalent to optical losses. It can be computed by looking at the high-frequency spectrum of the B1 photodiodes with their shutters closed. It was measured to be $11 \cdot 10^{-9} \text{mW}/\sqrt{\text{Hz}}$ in February and $7 \cdot 10^{-9} \text{mW}/\sqrt{\text{Hz}}$ in May 2019.

The B1 photodiodes flicker noise

Another noise arising from the B1 photodiodes is the flicker noise. This noise was estimated by computing the spectrum of the difference between the two B1 photodiodes which is expected to contain only non common noises (electronic noise and shot noise). In addition to the dark noise and shot noise exhibiting a white spectrum, a noise with a $\frac{1}{f}$ dependency appeared in the noise PSD. This frequency behavior is typical of the flicker noise. This measurement allowed to extract its values : it was measured to be $\frac{37}{\sqrt{f/40}} \cdot 10^{-9} \text{mW}/\sqrt{\text{Hz}}$ in May (ie with the high quantum efficiency B1 photodiodes) and a third of it in February. This noise was removed in January 2020 by changing the B1 photodiodes pre-amplifiers.

The contrast defect

If there is a mismatch in geometrical properties of the two beams recombining at the BS (eg due to asymmetry of the two arms reflectivity or arm test-masses RoC), a spurious beam arises from the non-perfect destructive interferences. This effect (introduced in section 1.3.2) is called Contrast Defect (CD) and induces on the interferometer readout a

field that is responsible for part of the shot noise. This spurious shot noise is not reduced by the squeezing injection (as it does not arise from the vacuum fluctuations entering from the interferometer dark port) and therefore is equivalent to optical losses for the squeezing injection. By varying the dark-fringe offset, it is possible to extract the contrast defect power which was estimated as $(\pm 30) \mu\text{W}$ during the O3a run (ie with 18 W of input power) and $(260 \pm 60) \mu\text{W}$ during the O3b run (ie with 26 W of input power).

All these technical noises can then be converted into equivalent strain and compared to the shot noise level.

All the technical noises previously introduced, namely the levels of B1 dark noise, flicker noise and contrast defect can be expressed in strain using the simple pole approximation of the transfer function of the differential arm motions. As the arm cavities optical gain (OG) is computed from the $B1_DC$ channel which is half of the power on the B1 photodiodes, the optical gain used in this transfer function has to be multiplied by two.

This gives the transfer function between the B1 power and the strain displacement as

$$h = \frac{2OG}{L} \cdot \frac{1}{1 + (\frac{f}{f_p})^2} \quad (4.3)$$

where f is the frequency, L the arm cavity length and f_p is the arm cavities pole.

In additions to these technical noises, there are two other important technical noises at high-frequency to take into account :

The 56 MHz Relative Intensity Noise (RIN) and the frequency noise

The Virgo main laser frequency noise and 56MHz sideband RIN are two noises that are subtracted when computing the interferometer strain sensitivity. These noises can indeed be measured by two monitoring photodiodes, respectively the quadrature in-phase of the B2 signal demodulated at 8 MHz and the B1s1 signal demodulated at 56 MHz.

The subtraction of these noises is performed using the coherence between theses signals and the strain sensitivity. For the frequencies where the coherence is larger than 0.4, the corresponding noise is subtracted from the strain sensitivity. This also implies that the residual contributions of these noises to the strain sensitivity can be computed using their coherences. Especially, the square-root of the coherence $\langle PD, H_{REC} \rangle$ between the photodiode channel (PD) used to subtract these noises with the reconstructed gravitational wave amplitude H_{REC} during the detector calibration gives directly their contribution to the sensitivity h_n as

$$h_n = \sqrt{\langle PD, H_{REC} \rangle} \cdot H_{REC} \quad (4.4)$$

These coherences have been measured during both the February and May measurements.

The combination of technical noises



Finally, all the technical noises from the above list have been represented in figure 4.14 by the thin lines with their quadratic sum represented by the thick blue curve. For both the February and May measurements, the measured high frequency strain sensitivity should match the estimated strain sensitivity which is the quadratic sum of the quantum and technical noises. Any remaining discrepancy should arise from the interferometer detection efficiency, meaning that overlapping the estimated and measured high frequency strain sensitivity will provide a measurement of it. This method gives $\eta_F = (0.65 \pm 0.11)$ and $\eta_M = (0.7 \pm 0.12)$ for respectively February and May. The uncertainty is driven by the error on the parameters and from the H_{REC} amplitude uncertainty .

As already stated, the main change between February and May for the detection system was the change of the B1 photodiodes for high quantum efficiency ones. From the estimated change on this quantum efficiency, a 1.1 factor of improvement on the detection efficiency can be expected between the two measurements. This is in good agreement with the estimated improvement : $\eta_M/\eta_F = 1.08$.

The effects of the technical noises on the measurement of the squeezing level can be converted into equivalent optical losses L_{eq} as described in section ?? . Indeed, the SNR between the technical noises and the shot noise ² gives directly access to the level of equivalent losses as [55][84]

$$L_{eq} = \left(\frac{1}{SNR} \right)^2 \quad (4.5)$$

This gives 13 % and 15 % of equivalent optical losses (or 87% and 85% of efficiency) for February and May 2019 respectively. As the May 2019 corresponds to the interferometer condition used for the O3 run, the May 2019 measurement are used by default in the following.

Computing the product of the efficiency from table 4.2 to the one coming from technical noises gives a total losses of 34.7 % and 38.2 % for the best measured and estimated degraded parameters respectively.

This is in good agreement with the 40 % total losses extracted from the squeezing and anti-squeezing injection presented in figure 4.13.

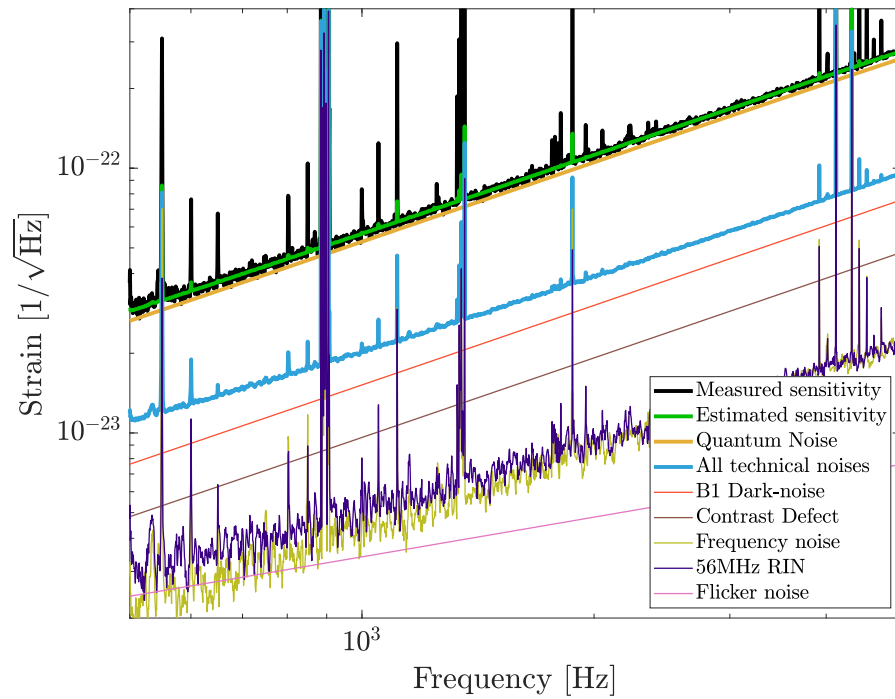
The phase noise

As presented in figure 2.11, phase noise can spoil the squeezing injection by mixing squeezing with anti-squeezing.

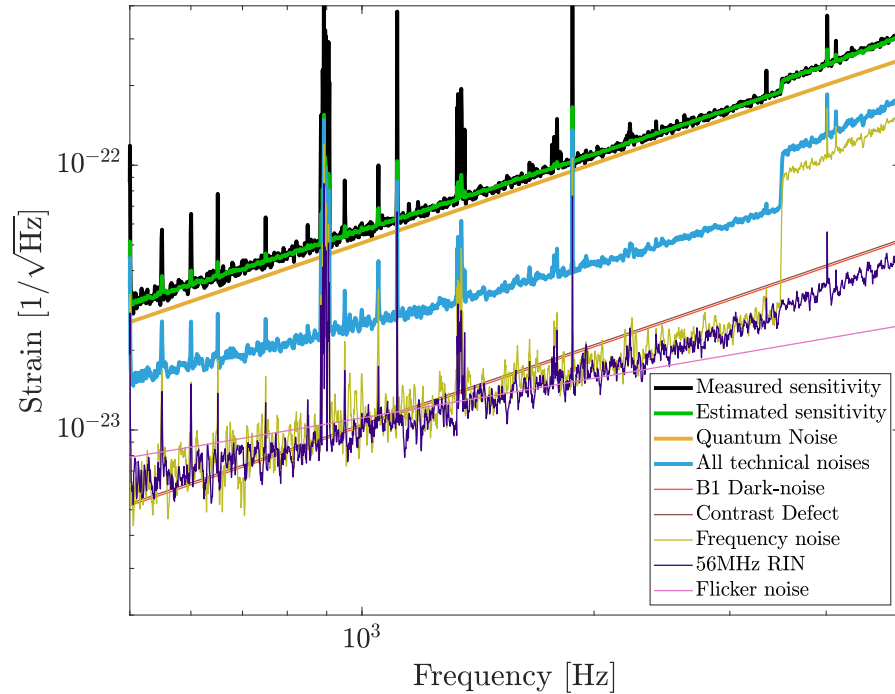
There are three main sources of phase noise.

- First, the OPO can add phase noise to the produced squeezing. For example variations of the OPO crystal length or temperature as well as a frequency shift of the OPO green pump power can shift the frequency of the generated squeezing causing frequency noise.

²here the SNR is computed from the amplitude spectral density of these noises



(a) February 2019



(b) May 2019

Figure 4.14: The high-frequency noise budget without squeezing injected during the February and May 2019 measurements



The AEI squeezer has been characterized following its installation in Virgo giving 3.5mrad of residual phase noise [40].

- Another source of phase noise is the residual phase from the control scheme. This level has already been presented in sections 3.4.1 and 3.4.2. Note that part of the PLL phase noise is attenuated by the coherent control. As this section used the PLL phase noise, it means that the resulting phase noise is an upper limit of its actual value.
- Finally, the phase noise of the interferometer output field might introduce phase noise for the squeezing. Indeed, the interferometer output field, E_{B1} , is used as a Local Oscillator for the squeezing measurement. This field is composed of the interferometer main field as well as fields due to the interferometer contrast defect or control sidebands. An amplitude modulations of these two last fields that could arise from any length fluctuations along their optical paths can translate into phase modulation.

In order to understand how the combination of these fields can induce phase noise, it is useful to use the phasor picture that was introduced in section sec:phasor.

First, the principal field at the interferometer output is the one due to the dark fringe offset and contain the gravitational wave signal. It is labeled E_{DF} and is used as the reference for the rotating frame.

In addition to this field, and as introduced in section 1.3.2, the interferometer contrast defect is responsible for a field E_{CD} that is in opposition of phase with the interferometer main field. This means that any amplitude fluctuations of E_{CD} is equivalent to phase fluctuations on the interferometer output field E_{B1} .

Furthermore, the interferometer control sidebands fields E_{SB} , that are in phase with the interferometer main field as they are circulating inside the arm cavities generates similar effects.

The origin of this phase noise is graphically represented in figure 4.15 where the interferometer output field E_{B1} is decomposed over its components. This representation can be used to understand the phase noise sources affecting E_{B1} . Indeed, the phase noise of this field can be understood as fluctuations affecting this field orthogonally to the direction of the vector E_{B1} .

The phase noise $\tilde{\theta}$ due to these two effects can be expressed as in [65] and [64]:

$$\tilde{\theta} = \sqrt{\frac{P_{SB}P_{CD}}{P_{DF}^2} + \frac{dP_{SB}^2}{8P_{SB}P_{DF}}} \quad (4.6)$$

with P_{SB} the average power in each sideband, dP_{SB} the power difference between sidebands, P_{CD} the contrast defect power and P_{DF} the dark-fringe offset power (where all the power are measured at the B1 photodiodes). Also, as only one 56 MHz sideband is transmitted by the OMCs, there is a factor 2 difference with [65].

The table 4.3 summarizes the various known sources of phase noise and the phase fluctuations rms they induce. The total phase fluctuations rms is extracted by performing the

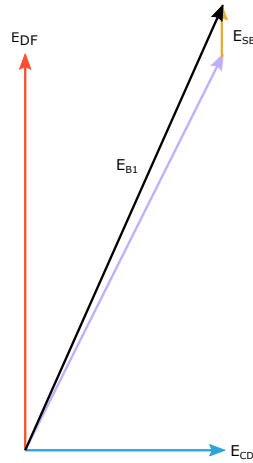


Figure 4.15: Graphical representation of the interferometer output field detected at the B1 photodiodes. Inspired from [64] where more details are available

Noise source	Phase fluctuations rms [mrad]
Squeezer	5
PLL int	23.94
PLL ext	16.32
Coherent control	18
Interferometer output field	20
Total phase noise	40

Table 4.3: Known sources of residual phase noise

quadratic sums of all known phase fluctuations rms leading to 40 mrad of phase fluctuations rms. Note that this value corresponds to an upper limit of the actual phase noise level as the phase noise introduced at low frequency by the two PLL is suppressed by the Coherent Control.

This is coherent with the phase noise extracted from the squeezing and anti-squeezing measurement while varying the OPO green pump power. However, due to limitations of the reachable level of green pump power, there is a large uncertainty on this measurement (52 ± 30) mrad. In February 2019, larger amount of phase noise with smaller uncertainty were measured (55 ± 7) mrad as larger pump power level were injected. The discrepancy between this measurement and the total presented in this section might arise from the residual phase noise at higher frequency than could be measured (limited due to the spectrum analyzer bandwidth).

Reducing the residual levels of phase noise due to the phase control loops is a promising way to reduce the overall phase noise.



4.3.3 Conclusion

This section has presented the effect of the squeezing injection at the Virgo detector. This leads to an improvement of the sensitivity of up to 2 Mpc on the BNS range corresponding of up to 15 % improvement on the BNS event detection rate.

The measurement campaigns of February and May 2019 also allowed to characterize the squeezing total optical losses and phase noise. For the O3 run, the optical losses were (40 ± 2) % and phase noise (52 ± 30) mrad.

They are in good agreement with the expected values of optical losses and phase noise.

4.4 The radiation-pressure increase

During both February and May 2019 measurements, higher levels of green pump powers have been injected into the OPO compared to the nominal situation during O3. Therefore it was also possible to inject high-level of anti-squeezing. This section reports the first measurement of radiation pressure noise increase at Virgo [85] which was also observed at a similar time at the LIGO detectors [86].

This measurement is of particular interest for gravitational waves detectors as it demonstrates the two aspects of quantum noise due to both the amplitude and phase quantum fluctuations of the vacuum states entering from the interferometer dark port [87] [68] [69].

While shot noise and the effect of squeezing on it has been observed from more than a decade ago, the radiation pressure noise due to amplitude fluctuations of the vacuum state entering from an interferometer dark port has been more elusive. This is because, at low-frequency where the radiation-pressure noise is dominating the quantum noise, several other noises (Brownian thermal noise, scattered light and various technical noises) are present and hide this radiation pressure noise.

In a more general manner, it was the first time that this effect has been observed on 40 kg-scale objects. Indeed, the radiation pressure noise is competing with the Brownian thermal noise of the tested object. So far, the radiation pressure noise could only be studied with light mass object used (to enhance the radiation pressure noise effect) in cryogenic environment (to decrease the Brownian thermal noise). The first demonstration was performed using ng-scale object cooled down to mK regime [88].

Since the interferometric gravitational wave detectors have been designed to be sensitive to BNS and BBH gravitational wave signals, their peak sensitivity is below a few hundreds Hertz. They are particularly suited to detect effects from radiation-pressure noise as they are sensitive to atto-metter differential arm motions.

4.4.1 Virgo quantum noise model

During February and May 2019 measurements, it was possible to see an increase of the Virgo sensitivity at low-frequency. The goal of the analysis presented in this section is to find if this increase was due to the enhancement of the vacuum state amplitude fluctuations

and therefore if the increase of the Virgo sensitivity at low-frequency corresponds to an increase of the radiation pressure noise.

During the February 2019 measurements, there was a high seismic activity which increased a lot the scattered-light noise. Figure 4.16 shows the typical scattered-light arches on the Virgo sensitivity spectrum. The data used for this plot span over roughly 12 h (corresponding to the data taking time of the February measurements). In this figure, no squeezing was injected meaning that the scattered light originated from another part of the Virgo detector. However, this was particularly troublesome as the low-frequency spectrum could not be used in the analysis and the Virgo sensitivity spectrum worsening due to scattered-light could mimic an increase due to the anti-squeezing injection.

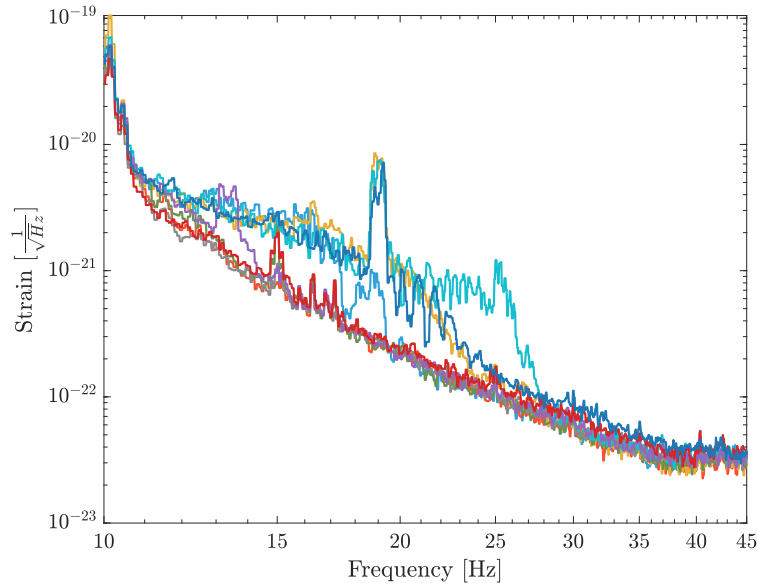


Figure 4.16: Evolution of the Virgo low-frequency sensitivity spectrum during the 12 h duration of the February 2019 measurement. The typical arches due to scattered light are visible

In order to disentangle the effects of the squeezing injection from the effects of classical noises (eg the scattered-light noise) on the sensitivity, it is first required to build a quantum noise model that can accurately describe the action of the squeezing injection on the Virgo sensitivity $S_h = S_q + S_{class}$ where S_q and S_{class} are respectively the quantum noise and classical noises PSD.

While the section 2.3 described the effect of the frequency independent squeezing injection on the quantum noise of an ideal interferometer (ie no losses arising inside the interferometer), we need now to include these losses. Indeed, such losses might affect differently the squeezing or the anti squeezing performances.

The quantum noise without frequency independent squeezing injection and interferometer losses can be described as [67]³:

$$S_q^{nosqz} = \frac{h_{sql}^2}{2} \left[\frac{\tilde{\epsilon} + \epsilon_{det}}{K} + \frac{\epsilon}{2}K + \left(1 - \frac{\tilde{\epsilon}}{2}\right) \right] \cdot \left[K + \frac{1}{K} \right] \quad (4.7)$$

³here ϵ_{det} corresponds to the ϵ_{OT} of [67] to keep the same notations throughout this manuscript



Symbol	Parameter	Value
P_{in}	Laser input power	18.4 ± 1 W
G_{pr}	Power recycling cavity gain	36 ± 0.2
M	Mirror mass	42 kg
L	Arm length	3000 m
\mathcal{F}	Arm cavity finesse	465 ± 5
λ	Carrier wavelength	1064 nm
η_d	Detection efficiency	$0.65 \pm 0.12 \rightarrow 0.7 \pm 0.12$
η_{sqz}	Squeezing path total efficiency	$0.55 \pm 0.01 \rightarrow 0.60 \pm 0.02$

Table 4.4: Virgo quantum noise parameters during February and May measurements. The improvement on the two efficiencies comes mainly from the change of the B1 photodiodes for higher-quantum efficiency ones

where K and h_{sqt}^2 were derived in chapter 3 and ϵ is the arm cavity losses that depends on the arm cavity round-trip losses ϵ_{rt} and the arm transmission T_{itm} as :

$$\epsilon = \frac{2\epsilon_{rt}}{T_{itm}} \quad (4.8)$$

$$\tilde{\epsilon} = \frac{2\epsilon}{1 + \left(\frac{f}{f_p}\right)^2} = 2\epsilon \cdot g \quad (4.9)$$

where g is the optical response of the interferometer.

Using $\alpha_r = 1 + \epsilon \left(\frac{1}{2} - g\right)$ and $\alpha_s = \frac{\tilde{\epsilon}}{2} + 1 + \epsilon_{det} \sim \epsilon g + \frac{1}{\eta_{det}}$, equation 4.7 can be rewritten as

$$S_q^{nosqz} = \frac{h_{sqt}^2}{2} \cdot \left[\alpha_r K + \frac{\alpha_s}{K} \right] = \alpha_s S_{SN} + \alpha_r S_{RPN} \quad (4.10)$$

The shot noise (SN) and radiation pressure noise (RPN) terms can be computed from table 4.4 using

$$\begin{aligned} S_{SN}(f) &= \frac{1}{(4\mathcal{F})^2} \cdot \frac{\pi \hbar \lambda c}{P_{in} G_{PR}} \cdot \frac{1}{g(f)}; \\ S_{RPN}(f) &= \left(\frac{4\mathcal{F}}{M}\right)^2 \cdot \frac{\hbar P_{in} G_{PR}}{\pi^5 \lambda c} \cdot \frac{g(f)}{f^4} \end{aligned} \quad (4.11)$$

4

⁴One can note that in the high frequency limit, $K, g \rightarrow 0$ and equation 4.7 becomes $:S_q^{nosqz} \sim \frac{h_{sqt}^2}{2\eta_d} \cdot \frac{1}{K} = \frac{S_{SN}}{\eta_d}$ which is the shot noise in presence of detection losses

The quantum noise with losses and squeezing injection is expressed as [67] :

$$S_q(f, R, \theta) = S_q^{nosqz} \cdot \left[\cosh 2R - \cos 2(\Phi - \theta) \sinh 2R \right] \quad (4.12)$$

where the squeezing injection efficiency η_{inj} influences the squeezing with :

$$e^{\pm 2R} = 1 \pm \eta_{inj} \frac{4x}{(1 \mp x)^2} \quad (4.13)$$

and R and θ are respectively the squeezing factor and angle, x is the OPO non-linear gain and $\Phi = \text{arccot}(K)$

Following some trigonometrical transformations gives :

$$\begin{aligned} S_q(f, \theta, x) = & \alpha_S(f) S_{SN}(f) \left\{ 1 + \frac{\beta(f)}{\alpha_S(f)} [\mathcal{A}_\theta(x) - 1] \right\} + \\ & + \alpha_R(f) S_{RPN}(f) \left\{ 1 + \frac{\beta(f)}{\alpha_R(f)} [\mathcal{A}_\theta(x + \pi/2) - 1] \right\} + \\ & + \beta(f) [\mathcal{A}_{\theta-\pi/4}(x) - \mathcal{A}_{\theta+\pi/4}(x)] \sqrt{S_{SN}(f) S_{RPN}(f)} \end{aligned} \quad (4.14)$$

where \mathcal{A}_θ is the squeezing enhancement factor defined as :

$$\mathcal{A}_\theta(x) = 1 - 4x \left(\frac{\langle \cos^2 \theta \rangle}{(1+x)^2} - \frac{\langle \sin^2 \theta \rangle}{(1-x)^2} \right) \quad (4.15)$$

with the bracket indicating averages over the squeezing angle fluctuations and $\beta = [1 - \epsilon g] \eta_i$

This model allows a generic description of the quantum noise as it covers squeezing injection with any phase between the vacuum squeezed quadrature and the interferometer readout quadrature as well as no squeezing injection in presence of losses.

4.4.2 Experimental results

Assuming that all noises are time-stationary, the difference between Virgo sensitivity PSD with squeezing injected and without squeezing injected $S_{\text{diff}}(f, \theta, x)$ is expressed as :

$$\begin{aligned} S_{\text{diff}}(f, \theta, x) = & (S_q(f, \theta, x) + S_{class}) - (S_q(f, 0, 0) + S_{class}) = \\ = & \beta(f) \{ S_{SN}(f) [\mathcal{A}_\theta(x) - 1] + S_{RPN}(f) [\mathcal{A}_{\theta+\pi/2}(x) - 1] \} \end{aligned} \quad (4.16)$$

where the cross-correlation term, i.e. the third line of equation (4.14), has been omitted for simplicity, as it is not relevant if the squeezing angle is a multiple of $\pi/2$.



Equation 4.16 shows that $S_{\text{diff}}(f, \theta, x)$ depends only on the quantum noise and the squeezing enhancement factor as long as the classical noises can be assumed to be constant over the two measurements and not affected by the squeezing injection. Note that following figure 4.16, the time-stationarity can only be assumed over ~ 30 Hz. The high level of optical isolation with the three Faraday isolators chain satisfies the second condition. Therefore, this equation can be used to probe quantum effects on the sensitivity.

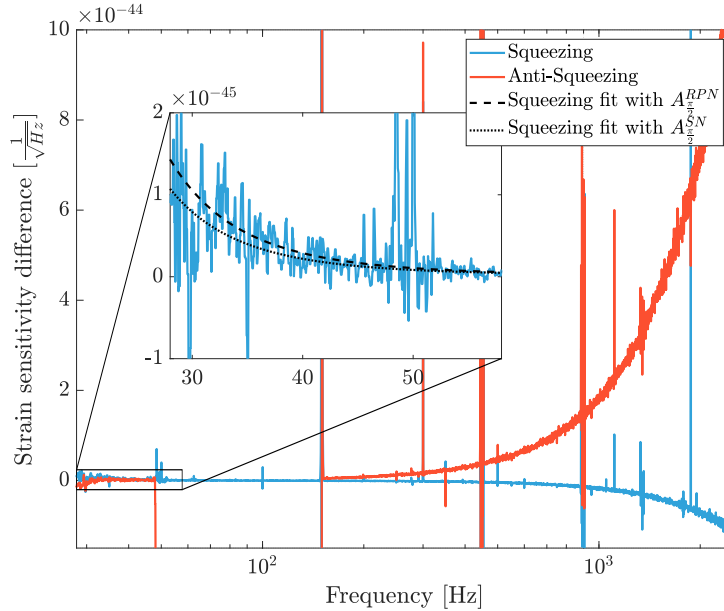


Figure 4.17: Fits used to estimate the squeezing enhancement factor $\mathcal{A}_{\frac{\pi}{2}}$. The blue and red curves correspond respectively to $S_{\text{diff}}^{\text{asqz}}$ and $S_{\text{diff}}^{\text{sqz}}$. The dotted black line and dashed black line corresponds to low-frequency fit of S_{diff} with phase squeezing injection using respectively $\mathcal{A}_{\frac{\pi}{2}}^{\text{RPN}}$ and $\mathcal{A}_{\frac{\pi}{2}}^{\text{SN}}$

The phase squeezing and amplitude squeezing corresponds respectively to a squeezing angle of $\theta = \frac{\pi}{2}$ and $\theta = 0$. The effect of both squeezing and anti-squeezing injection depends only on the same enhancement factors $\mathcal{A}_0(x)$ and $\mathcal{A}_{\frac{\pi}{2}}(x)$. Furthermore, the increase of the low-frequency sensitivity when injecting squeezing is equal to the high-frequency sensitivity increase when injecting anti-squeezing. This relationship has been checked for every level of OPO non-linear strength x .

The analysis of the anti-squeezing injection will be presented before the (similar) analysis of the squeezing injection.

To estimate if $\mathcal{A}_{\frac{\pi}{2}}^{\text{SN}}(x) = \mathcal{A}_{\frac{\pi}{2}}(x)$, a fit of $S_{\text{diff}}(f, \theta = \frac{\pi}{2}, x)$ has been performed between 1 kHz and 3.5 kHz. This threshold of 1 kHz allows to use data at high enough frequency to not be affected by the radiation-pressure noise nor by the $\mathcal{A}_0(x)$ value. In order to remove too large peaks present in the sensitivity, a one-sigma threshold between adjacent points has been applied to these data.

The fit output corresponds to the dotted black curve. Using this $\mathcal{A}_{\frac{\pi}{2}}^{\text{SN}}(x)$ parameter, it is also possible to fit the low-frequency spectrum of $S_{\text{diff}}(f, \theta = 0, x)$.

An identical analysis was performed when injecting squeezing but this time looking at

the low-frequency sensitivity spectrum. The frequency window was chosen to be between 33 Hz and 48 Hz for the February 2019 measurement and between 28 Hz and 48 Hz for the May 2019 measurement. The difference between the low-frequency threshold for the February and May 2019 measurements is due to the scattered light present in February that spoiled too low frequency (as shown in figure 4.16). This fit output gives the parameter $\mathcal{A}_{\frac{\pi}{2}}^{RPN}(x)$ as represented by the dashed black curve.

This analysis have been repeated for February and May 2019 measurements allowing to compare the values of $\mathcal{A}_{\frac{\pi}{2}}^{SN}(x)$ and $\mathcal{A}_{\frac{\pi}{2}}^{RPN}(x)$ from an OPO green power of 2.3 mW to 9 mW.

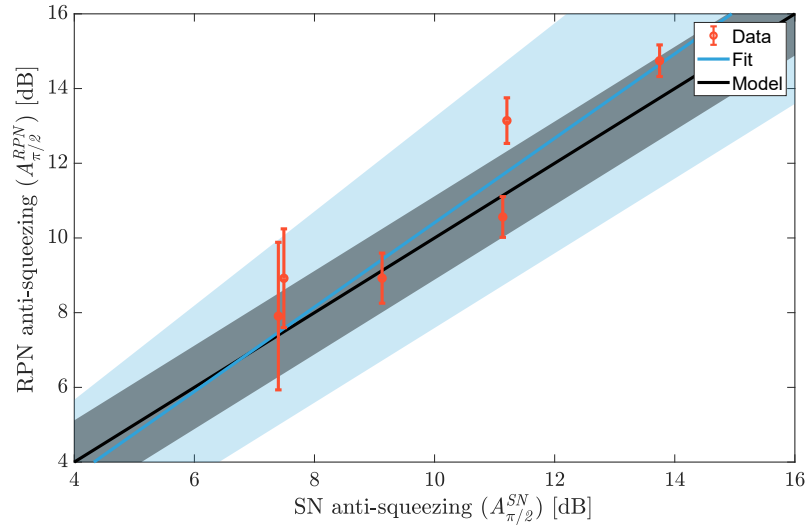


Figure 4.18: Linear fit of $\mathcal{A}_{\frac{\pi}{2}}^{RPN}$ versus $\mathcal{A}_{\frac{\pi}{2}}^{SN}$. The dark curve corresponds to the squeezing enhancement model and the blue curve to the linear fit of the data

This is represented in figure 4.18. Each red point corresponds to a different value of OPO non-linear strength. Their error bars come from the one-sigma uncertainty in the fit output represented by the black curves presented in figure 4.17. The highest data point corresponds to the highest level of injected squeezing (more than 13.7 dB). Removing the effects of high-frequency technical noises, it was possible to infer more than 5.5 dB of squeezing level which is the highest level of inferred squeezing observed at Virgo output. The dark curve shows the expected dependency between $\mathcal{A}_{\frac{\pi}{2}}^{SN}(x)$ and $\mathcal{A}_{\frac{\pi}{2}}^{RPN}(x)$ which is expected to be linear. The dark shaded area comes from the quantum noise model uncertainty. This gives a prediction of :

$$\mathcal{A}_{\frac{\pi}{2}}^{RPN} = 1.0 \cdot \mathcal{A}_{\frac{\pi}{2}}^{SN} \pm 0.2 \quad (4.17)$$

Fitting $\mathcal{A}_{\frac{\pi}{2}}^{RPN}$ against $\mathcal{A}_{\frac{\pi}{2}}^{SN}$ using a first-order polynomial gives

$$\mathcal{A}_{\frac{\pi}{2}}^{LF} = (1.1 \pm 0.1) \cdot \mathcal{A}_{\frac{\pi}{2}}^{HF} - (0.9 \pm 1.5) \quad (4.18)$$

As we can see, the fit of $\mathcal{A}_{\frac{\pi}{2}}^{RPN}$ against $\mathcal{A}_{\frac{\pi}{2}}^{SN}$ is consistent with the quantum noise uncer-

tainty. The reduced χ^2 of this linear fit is 2.8 but drops to 1.4 when adding to $\mathcal{A}_{\frac{x}{2}}^{RPN}$ the variance of the un-squeezed reference spectrum in the 30-70 Hz range (which is slightly affected by the non time-stationnarity of low-frequency technical noises).

This measurement confirms the observation of radiation-pressure noise enhancement with the squeezing injection.

4.4.3 Conclusion

This section showed the first measurement of radiation-pressure noise enhancement when injecting squeezing in a gravitational wave detector and more generally for kg-scale objects. This exhibits the need for frequency-dependent squeezing to further reduce the quantum noise.

Furthermore, during this measurement, we injected up to 13.7 dB of squeezing into Virgo interferometer. Removing the effects of high-frequency technical noises, it was also possible to infer more than 5.5 dB of squeezing at Virgo readout.

4.5 The O3 performances

Frequency-independent squeezing has been injected into the Virgo interferometer during the one-year long O3 run. This section will present the performances of the squeezing system throughout the O3 run.

After six months of observation LIGO and Virgo collaboration agreed to perform a month-long break in October 2019. At Virgo, this time was spent by increasing the input laser power from 18 W to 26 W, reducing the effects of scattered light, investigating the infamous flat noise. In practice, this divided the O3 run into the O3a and O3b runs.

Relative to the squeezing system, the increase of the input power affects the quantum noise. It means that the O3a and O3b runs had to be studied separately.

4.5.1 Median squeezing level

Since the squeezing level is estimated by comparing the 2650-3140 Hz strain sensitivity BRMS level with and without squeezing, it means that it is not possible to directly this value during O3a as squeezing was always injected and therefore no data without squeezing injection were available.

In order to extract a reference level representative of the shot-noise level without squeezing, one can use the fact that the arm cavities optical gain level is proportional to the shot-noise level. Fitting the BRMS value as a function of the arm cavities optical gain will therefore give a way to estimate the shot-noise level without squeezing as a function of the BRMS value.

This estimation has been performed using all of the O3a data with various conditions to only use reasonable data (ie only using data with the interferometer in good operation).

These conditions are :

- The interferometer is in nominal observing conditions without squeezing being injected.
- The interferometer is in science, calibration or locked mode with the calibration down or in states where it doesn't affect the high-frequency sensitivity. It is interesting to add the calibration period as, since September 2019, 15 minutes of data were acquired during the weekly calibration of the interferometer with the interferometer in nominal conditions without squeezing injected.
- Since the laser frequency is stabilized on the arm cavities common mode, the fluctuations of this common mode induce laser frequency noise. The laser frequency noise is mainly affecting the high-frequency sensitivity which can spoil the quantum noise measurement. It is therefore required to select period when this common mode fluctuations is not too high. The coupling of the common mode to the laser frequency is characterized by the Common Mode Rejection Factor (CMRF). Empirically, the periods with CMRF below $2.3 \cdot 10^{-5}$ have been selected.
- The BNS range is over 60 % of the maximal BNS range during the period studied. This is especially useful to only keep commissioning period with good interferometer conditions.

The selected data are presented in figure 4.19 with their linear fit which gives the reference level as a function of the arm cavities optical gain OG as

$$reference = -1,822.10^{-30}.OG + 7,093.10^{-21} \quad (4.19)$$

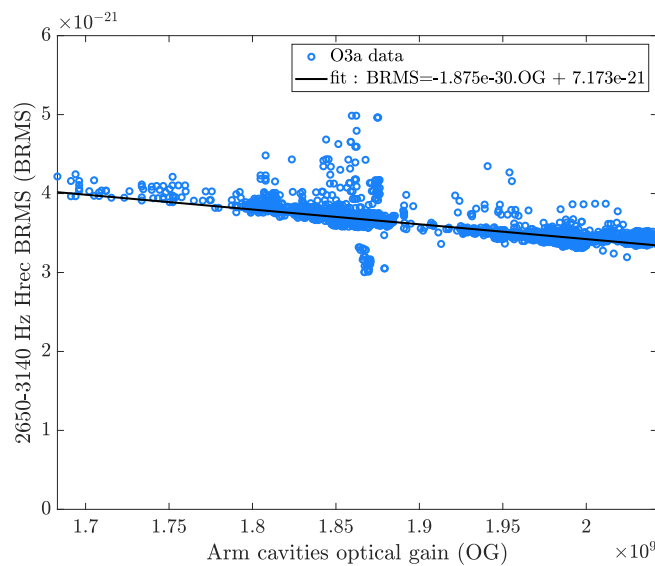


Figure 4.19: 2650-3140 Hz BRMS as a function of the arm cavities optical gain during O3a. The data were selected during period with the interferometer locked with a good CMRF

The squeezing level can then be estimated as :

$$R_{-}[dB] = 10 \cdot \log_{10} \left(\frac{BRMS}{reference} \right) \quad (4.20)$$

where *BRMS* corresponds to the 2650-3140 Hz Hrec BRMS.

As already stated, the O3b run was performed with the increase of Virgo input laser power from 18 W to 26 W. This means that the calibration of the reference shot-noise level used to estimate the level of squeezing throughout the O3b run had to be performed again.

Furthermore, the DARM offset has been reduced from 2 mW per B1 photodiodes to 1 mW in December 6th 2019 in order to reduce the effects of B1 photodiodes flicker noise. This lowered DARM offset has been kept until the change of B1 photodiodes in January 28th 2020 that removed their flicker noise. These activities impacted the squeezing reference level and required to be analyzed separately.

These new reference levels are presented in figure 4.20. They allow to compute the level of squeezing during the entire O3b run.

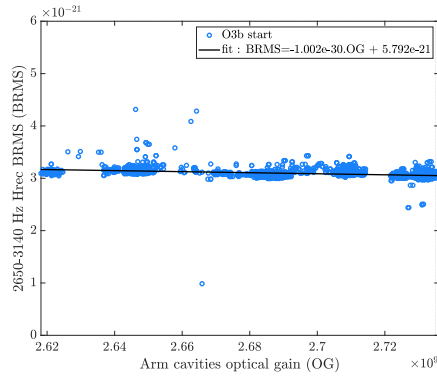
The median level of squeezing averaged every hour is represented by the black trace in figure 4.21.

In this figure we can see that on average less squeezing was injected during O3b than during O3a.

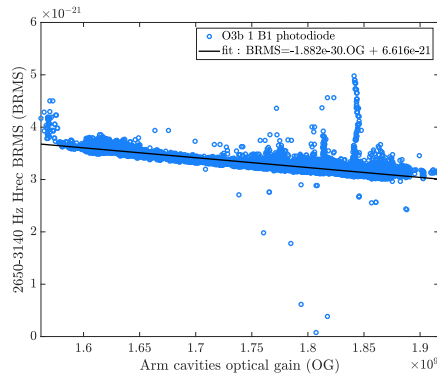
This behavior can be explained by looking at the squeezer performances, meaning looking at the level of squeezing produced by the squeezer.

During the O3 run, phase scans have been performed allowing to extract squeezing and anti-squeezing levels. As the anti-squeezing is far less sensitive to optical losses or phase noise than the squeezing, the anti-squeezing can be used as a marker for the squeezer performances. The results of the phase scans performed during the O3 run are presented in figure 4.22. It can be seen that the anti-squeezing (blue dot) are slowly decreasing throughout the O3 run. This indicates a possible degradation of the squeezer due to this one-year long operation. Similar behavior was also observed at the GEO600 detector requiring to replace the OPO crystal.

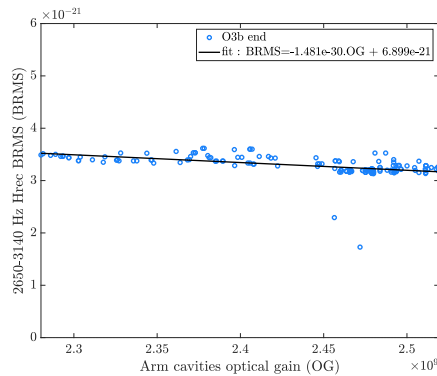
Another possible explanation comes from the increase of the Virgo input laser power. Indeed, this increase leads to a decrease of the shot noise. Therefore, the shot-noise level is getting closer to other noises that are independent of the input laser power. Regarding the squeezing injection, the increase of the input laser power is equivalent to an increase of the level of technical noises (that are independent from the input laser power). This appears in figure 4.21 where the squeezing level decrease after the October commissioning break.



(a) Reference level from the beginning of O3b to the decrease of the DARM offset.



(b) Reference level from the decrease of the DARM offset to the change of the B1 photodiodes.



(c) Reference level from the change of the B1 photodiodes to the end of O3b.

Figure 4.20: 2650-3140 Hz BRMS as a function of the arm cavities optical gain during O3b. The data were selected during period with the interferometer in nominal conditions without squeezing injected, a good CMRF and a good BNS range

4.5.2 Duty cycle

We can compare how much of the science time was spent with the squeezing injected. During O3a, 98.6 % of the science time was spent with squeezing injected. This duty cycle



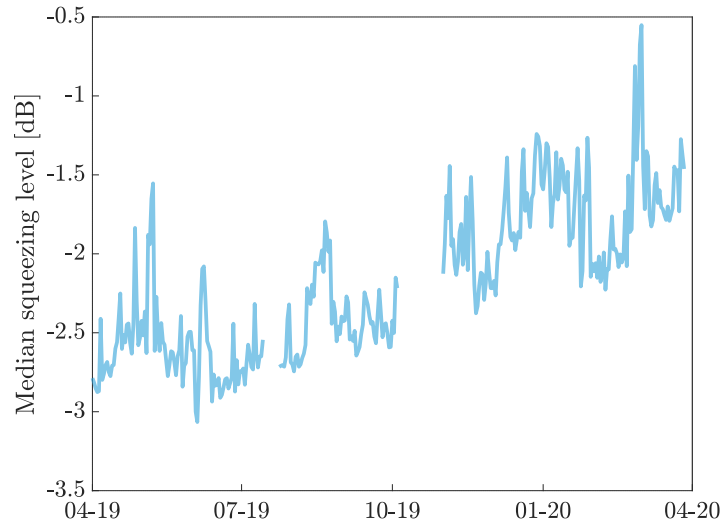


Figure 4.21: Median level of frequency-independent squeezing detected at the Advanced Virgo detector readout. The squeezing level has been averaged every hour. No data of the October commissioning break separating O3a and O3b are represented. Also, the period without data in O3a corresponds to the period with only one B1 photodiode

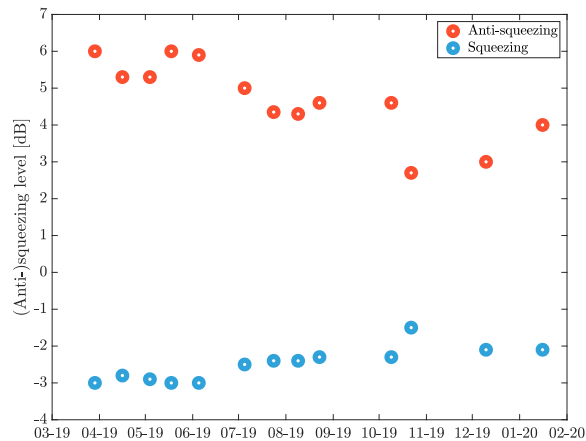


Figure 4.22: Squeezing and anti-squeezing measured while performing several phase scans during the O3 run

gives information about the squeezing performances in science (or observation) mode. This duty cycle might be slightly overestimated as it might hide some breaking of the science operation due to the squeezer itself.

Another estimation of the squeezing duty cycle could be to compare the time spent with the interferometer in nominal condition and squeezing injected and the O3a duration. Virgo was in normal operation with squeezing injected during 74 % of the O3a duration. This duty cycle gives information about the overall Virgo performances as well as the duration over which the squeezer was used.

During O3b, 96.2 % of the science time was spent with squeezing injected. The squeezing was injected during a slightly shorter duration in O3b with respect to O3a. This might be because during winter time, the higher seismic activities caused several misalignment of the squeezer with respect to the Advanced Virgo detector. Furthermore there had been troubles with the humidity control of the detection lab where the squeezer is installed inducing issues with the squeezer internal alignment and forcing to turning it off.

Virgo was in normal operation with squeezing injected during 73 % of the O3b duration.

4.6 Conclusion

This chapter presented the impact of the frequency-independent squeezing injection to Virgo sensitivity and therefore its BNS and BBH ranges. The performances of this injection have also been characterized before and during the O3 run.

Measurements performed before the O3 run allowed to measure the highest level of injected squeezing into the Virgo detector, the highest level of inferred squeezing at Virgo readout as well as the first observation of radiation-pressure enhancement at Virgo.

This observation highlights the need for the frequency-dependent squeezing injection to improve Virgo sensitivity across its entire spectrum.



5

Filter Cavity design

Contents

5.1	Introduction	125
5.2	From Advanced Virgo to Advanced Virgo+	126
5.2.1	The phase I : lowering the quantum noise	126
5.2.2	The phase II : lowering the thermal noise	130
5.2.3	Other upgrades	130
5.3	The Filter Cavity degradation mechanisms	131
5.3.1	The Filter Cavity round-trip losses	131
5.3.2	The optimal rotation	131
5.3.3	The degradation mechanisms	135
5.3.4	The Filter Cavity length	143
5.4	The impact of frequency-dependent squeezing on the sensitivity	144
5.5	The Filter Cavity length and the Advanced Virgo+ ranges	147
5.6	Conclusion	148

5.1 Introduction

The previous chapters have presented how the frequency-independent squeezing has been injected at Virgo during the O3 run. During these activities, the first observation of the radiation-pressure noise increase due to the frequency-independent squeezing injection has also been observed. This demonstrated the need for frequency-dependent squeezing to further improve Virgo sensitivity.



This chapter presents the sensitivity improvement of the Advanced Virgo + detector when injecting frequency-dependent squeezing. Especially, the performances of a realistic Filter Cavity are derived. And this allows to derive the Filter Cavity length choice.

5.2 From Advanced Virgo to Advanced Virgo+

From the end of the O3 run, the Advanced Virgo detector has entered in an important phase of upgrade towards the Advanced Virgo+ detector. These upgrades planned up to the O5 run should bring the Advanced Virgo+ sensitivity close to the maximal one allowed by the site infrastructure.

These upgrades are divided into two phases Advanced Virgo+ phase I up to the O4 run (around mid 2022 to mid 2023) and Advanced Virgo+ phase II from the end of the O4 run to the O5 run (around mid 2025 to mid 2026). Indeed, the aim of the transition from Advanced Virgo to Advanced Virgo+ consists of a broadband reduction of the quantum noise (Advanced Virgo+ phase I) before a thermal noise reduction (Advanced Virgo+ phase II).

The simulations presented in this chapter are using the Matlab GWINC code [75] which requires as input the interferometer parameters. These simulations assumed for both O4 and O5 runs a pessimistic and optimistic scenario that, later on, are respectively labeled high and low (corresponding to high and low strain sensitivity).

5.2.1 The phase I : lowering the quantum noise

During the O3 run, the Advanced Virgo detector reached a BNS range of 60 Mpc with frequency-independent squeezing injected during the entire O3 run duration. This injection of frequency-independent squeezing allowed to decrease the shot-noise by up to 2.7 dB (meaning that the radiation-pressure noise increased by the same amount).

From the O4 run, the so-called Advanced Virgo+ Phase I, several upgrades are planned to reshape and reduce the quantum noise.

Input power increase

In order to further decrease the shot-noise, the Advanced Virgo+ detector input power will increase to 40 W for the O4 run. Note that this input power is similar to the ones in the LIGO detectors during the O3 run (LIGO Hanford : 35 W and LIGO Livingston : 40 W). This power increase was anticipated during the O3 commissioning break of October 2019 when the Advanced Virgo detector input power was increased from 18 W to 26 W.

Going from 26 W to 40 W means that there will a reduction of 24% of the shot-noise (and similar increase of the radiation-pressure noise).

As presented in figure 5.1, the increase of the interferometer input power decreases the shot-noise while increasing the radiation pressure noise proportionally to the square root of the input power.

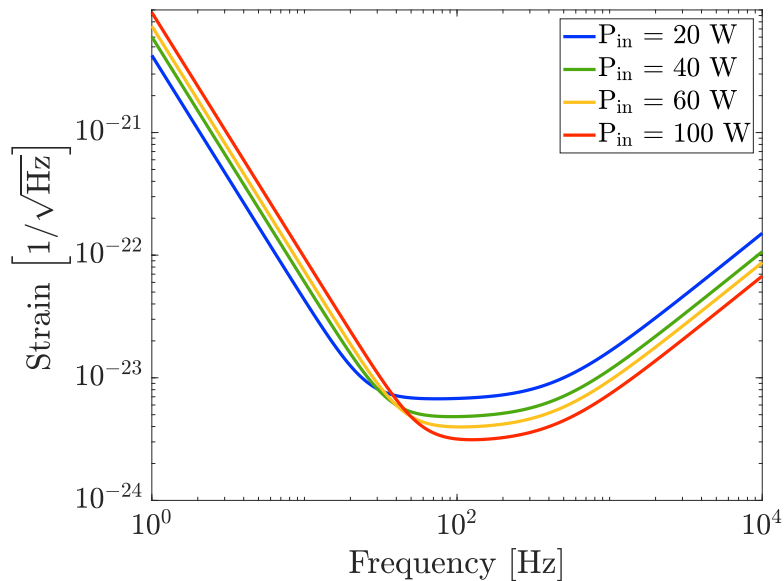


Figure 5.1: Virgo quantum noise while varying its input power

Since the radiation pressure noise is not yet limiting the low-frequency sensitivity, the increase of the input power will improve Virgo BNS range.

The Advanced Virgo+ detector input power choice was driven by technical considerations. Especially, it has been decided to not go to higher input laser power in order to decrease the commissioning time required to control a high input power interferometer. For instance, further increasing the input power means both higher probability of parametric instabilities and more thermal deformations of the test-masses that make the interferometer lock acquisition more complex.

For the O5 run, it is foreseen to further increase the input power to 60 W. The input laser power foreseen for the O4 and O5 low and high scenarii are presented in table 5.1.

Scenario	O3	O4	O5 high	O5 low
Input power [W]	18 → 26	40	60	80

Table 5.1: Virgo main laser input power

The Signal Recycling mirror installation

Initially planned during the Advanced Virgo period, the SR mirror will be installed during the Advanced Virgo+ phase I.

As already presented in section 1.3.3 the addition of the SR mirror to the Advanced Virgo+ detector reshapes the quantum noise as shown in figure 5.2. It can be seen that there is a trade-off in the SR transmittance choice between a better sensitivity around 100 Hz where most of the BNS SNR is expected versus a broader sensitivity.

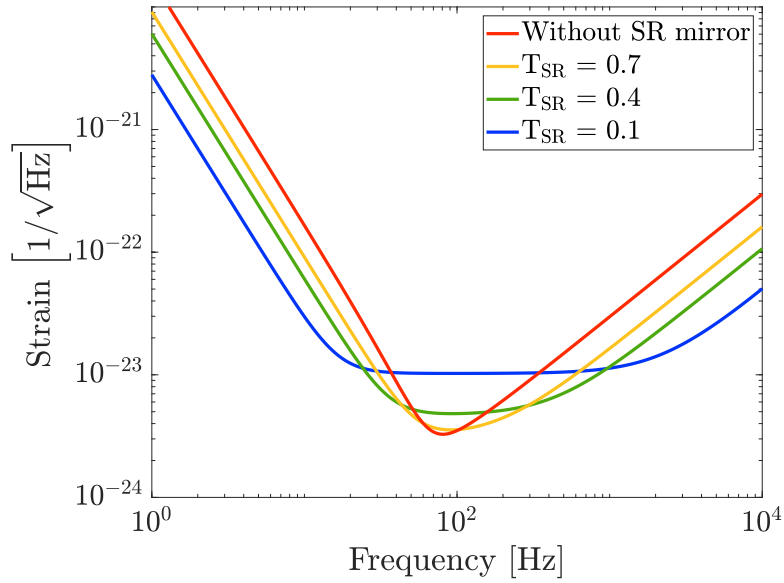


Figure 5.2: Virgo quantum noise while varying the SR mirror transmittance

Since the beam size inside the arm cavity will change between the O4 and O5 runs (see next section for more details), the SR mirror will also have to be changed between these two runs. The SR transmittance has therefore been optimized for the O4 run (ie phase I).

The choice of the SR transmittance was driven by the BBH, BNS and supernovae [89] ranges. Indeed, the combination of these three figures of merit allows to probe the entire sensitivity spectrum of Advanced Virgo+.

Also, this choice has been made using both frequency-independent (corresponding to the O4 high scenario) and frequency-dependent squeezing injection (corresponding to the O4 low scenario). As the low frequency technical noise could hide the benefit from the SR installation, it has also been taken into account in the choice of the SR transmission.

Finally, a SR transmittance of 0.4 ensures to reach more than 98% of the maximal BNS range for both frequency-independent squeezing and frequency-dependent squeezing with and without low-frequency technical noise while not decreasing too much the supernovae range. The low-frequency technical noise level were estimated from its value during the O3 run. This noise is modeled as $\alpha \cdot f^\beta$ with f being the frequency. The α and β values for the O4 and O5 high and low scenarii are presented table 5.2.

The frequency-dependent squeezing injection

Another upgrade planned for the Advanced Virgo+ phase I is the injection of frequency-dependent squeezed vacuum states through the detector dark-port instead of the frequency-independent squeezed vacuum states injected during the O3 run.

Indeed, the performances of the frequency-independent squeezing are limited by the degradation of the radiation pressure noise : Since most of the BNS and BBH signals are located at low-frequencies, the increase of the radiation pressure noise affects more these ranges

Scenario	O3	O4 high	O4 low and O5 high	O5 low
α	$\sqrt{2} \cdot 3.1 \cdot 10^{-17}$	$3.1 \cdot 10^{-17}$	$1.4 \cdot 10^{-17}$	0
β			-4	

Table 5.2: Virgo low-frequency technical noise estimation for the O3 run as well as the estimation for the O4 and O5 high and low scenarii. The noise is expressed in equivalent strain as $\alpha \cdot f^\beta$

than the shot noise decrease.

However, as already introduced in section 2.3, the injection of frequency-dependent squeezing is able to reduce the quantum noise over the entire sensitivity of gravitational wave interferometer. Figure 5.3 compares the quantum noise without squeezing, with frequency-independent squeezing injection and with frequency-dependent squeezing injection. Last chapter already presented how optical losses and phase noise affected the squeezing injection during the O3 run.

As a reminder, despite the fact that the squeezer is able to generate up to 13.7 dB of squeezing (as measured in February 2019), only 6 dB to 8 dB of squeezing were generated for the O3 run in order to improve the BNS and BBH ranges [82].

Section 5.3.3 will present the performances of a realistic Filter Cavity.

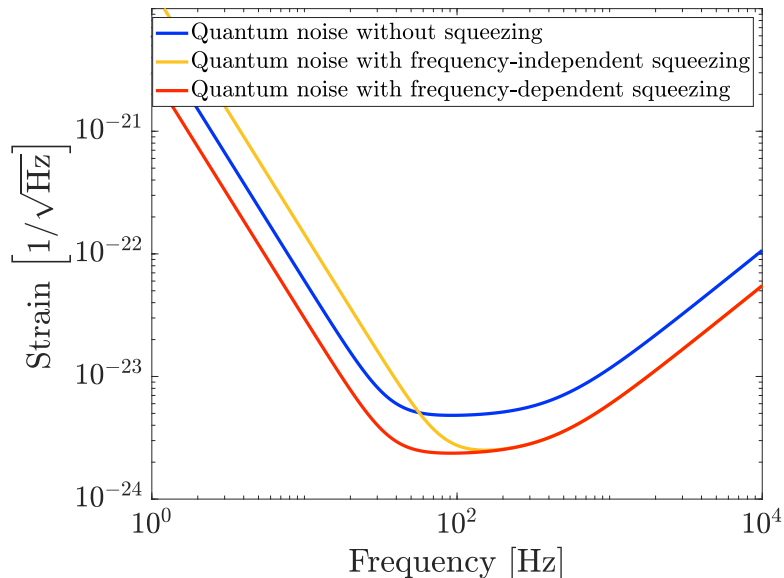


Figure 5.3: Virgo quantum noise with no squeezing, frequency-independent squeezing and frequency-dependent squeezing injections without optical losses compared to the mirror coating thermal noise

5.2.2 The phase II : lowering the thermal noise

The mirror thermal noise is one of the limiting noise of the Advanced Virgo detector sensitivity around 100 Hertz. Due to the broadband reduction of the quantum noise during the Advanced Virgo+ phase I, the part of the sensitivity spectrum where the thermal noise is limiting will also increase.

In order to reduce the thermal noise, the end test-masses will be changed for larger ones. The end test-masses diameter becomes 55 cm, their thickness 20 cm and mass 105 kg.

Larger end-test masses allow for larger beams circulating inside the arm cavities. Therefore, the coating Brownian noise of the test-masses will be reduced. Furthermore, the suspension thermal noise is also reduced with heavier test-masses. This is also beneficial for the radiation pressure noise that decreases with the mirror mass.

These two effects are represented in figure 5.4 where the coating noise and the quantum noise are representing going from phase I to phase II arm cavity mirrors with other interferometer parameters kept constant. During the phase II only the arm cavity end mirror is larger and heavier. This is the chosen scenario for the O5 run in order to avoid to deal with larger beam outside the arm cavities.

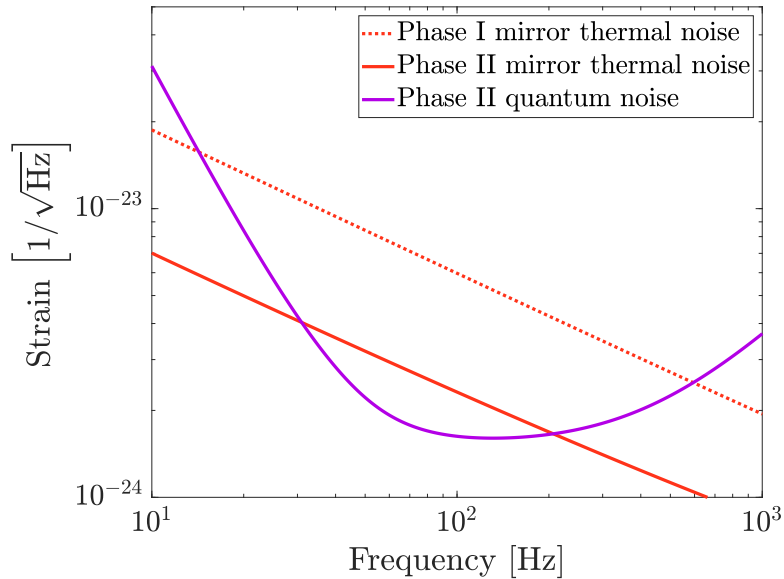


Figure 5.4: The Advanced Virgo+ coating thermal noise and quantum noise with phase I and phase II arm cavity mirrors

5.2.3 Other upgrades

While the two previous sections presented the most important upgrades for the Advanced Virgo+ detector, there will be also other upgrades that will improve the detector sensitivity.

- The Newtonian noise will become a limiting noise source at low-frequencies. In Virgo, this noise arises mainly from the local seismic and acoustic fields.

The acoustic field can be reduced by decreasing the environmental noises such as the vacuum system pump or the air conditioning system ventilation. The seismic field can be reduced offline if one is able to estimate the seismic field fluctuations. Using a 140 seismometers array inside Virgo main buildings, it is possible to measure the seismic field and estimate its fluctuations.

Combining these two fields reduction, it should then be possible to decrease the Newtonian noise by a factor 3 for the phase I and a factor 5 for the phase II with respect to the O3 level [36].

- The detection systems will also undergo upgrades throughout these phases.

Related to the squeezing injection, the OMC will be changed from two cavities of finesse 121 to one with finesse 1000. This will remove the optical losses due to the second cavity. However, this means that the 7 MHz sidebands used for the coherent control will be greatly attenuated by this new design. Therefore, the coherent control is planned by either lowering the sidebands frequency to 4 MHz or to use the B1p photodiode as a sensor for the coherent control error signal.

Furthermore, the B1 photodiode dark noise will be reduced to represent less than 1% of equivalent optical losses (compared to the 4% during the O3 run).

5.3 The Filter Cavity degradation mechanisms

As presented in section 2.2.4, optical losses and phase noise affect the performances of the squeezing. This section describes the effects of optical losses and phase noise on the frequency-dependent squeezing. This section is based on the model developed by Kwee *et al.* [59].

5.3.1 The Filter Cavity round-trip losses

The frequency-dependent squeezing can be generated using a high-finesse detuned Fabry-Perot cavity named a Filter Cavity.

Because of its high finesse and because squeezed vacuum states are highly sensitive to optical losses, the Filter Cavity losses are playing a crucial role in the frequency-dependent squeezing performances.

5.3.2 The optimal rotation

In section 2.3.3, it has been shown that a broadband reduction of the quantum noise is achieved if

$$\alpha_p(\Omega) = \arctan(K(\Omega)) \quad (5.1)$$

This condition means that in order to achieve a broadband reduction of the quantum noise, the squeezing rotation $\alpha_p(\Omega)$ has to counter-act the opto-mechanical coupling of the interferometer given by $\arctan(K(\Omega))$.

For a dual recycled interferometer with Fabry-Perot arm cavities, the opto-mechanical coupling of the interferometer K can be approximated at low frequencies (where the Filter Cavity is acting) by

$$K \sim \left(\frac{\Omega_{sql}}{\Omega} \right)^2 \quad \text{with} \quad \Omega_{sql} = \frac{t_{SR}}{1 - r_{SR}} \frac{8}{c} \sqrt{\frac{P_{arm}\omega_0}{MT_{arm}}} = 2\pi \cdot 43.6 \text{ Hz} \quad (5.2)$$

where t_{SR} and r_{SR} are the SR transmissivity and reflectivity, P_{arm} is the circulating power inside the arm cavities, T_{arm} the arm cavity input mirror power transmissivity, ω_0 the carrier field angular frequency and M the mirror mass. The value of the standard quantum limit frequency is computed for the Advanced Virgo+ detector parameters presented in table 5.3. As already presented, for the phase II the arm cavity end mirror are changed for heavier ones. In that case, the mirror mass is computed as the mean of the mass of the arm cavity input and end mirror : $M = (m_1 + m_2) / 2$.

Parameter	Symbol	Value
Wavelength of the carrier field	λ	1064 nm
Arm cavity length	L	2998 m
Signal recycling cavity length	L_{SR}	24 m
Arm cavity half-width	γ_{arm}	$2\pi \cdot 143.32$ Hz
Arm cavity input mirror power transmissivity	T_{arm}	0.0145
Signal recycling mirror power transmissivity	t_{SR}^2	0.4
Arm circulating power	P_{arm}	190 kW [O4low] 390kW [O5low]
Mass of arm cavity input mirror	m1	42 kg
Mass of arm cavity end mirror	m2	42 kg [O4] 105kg [O5]

Table 5.3: Advanced Virgo parameters for O4 low and O5 low scenarii

Since the Filter Cavity has a high-finesse, the Filter Cavity Round-Trip Losses (RTL) plays an important role when computing the squeezing angle rotation. Indeed, the RTL represent the power lost at each round-trip of light inside the Filter Cavity. As the number of round-trip increases with the Filter Cavity finesse, a high-finesse cavity is very sensitive to RTL.

In this section, the optimal squeezing angle rotation is computed when taking into account the Filter Cavity RTL.

Because the RTL are similar to a reduction of the Filter Cavity input mirror, both the Filter Cavity bandwidth and detuning are changed. In presence of the round-trip losses, they are expressed as

$$\gamma_{FC} = \sqrt{\frac{2}{(2-\epsilon)\sqrt{1-\epsilon}}} \cdot \frac{\Omega_{sql}}{\sqrt{2}} \quad (5.3)$$

$$(5.4)$$

$$\Delta\omega_{FC} = \gamma_{FC} \cdot \sqrt{1-\epsilon} \quad (5.5)$$

Finally, ϵ is expressed as a function of Λ_{rt}^2 and the Filter Cavity free spectral range $f_{FSR} = \frac{c}{2L_{FC}}$ as [59]

$$\epsilon = \frac{4}{2 + \sqrt{2 + 2\sqrt{1 + \left(\frac{2\Omega_{sql}}{f_{FSR}\Lambda_{rt}^2}\right)^4}}} \quad (5.6)$$

Note that the lossless case can be computed by setting $\epsilon = 0$.

It is then possible to explicitly compute α_p which defines the squeezing rotation from equation 5.10 in presence of Filter Cavity RTL [59] :

$$\begin{aligned} \alpha_p &= \arctan(K) \\ &\sim \arctan\left(\frac{(2-\epsilon)\gamma_{FC}\Delta\omega_{FC}}{(1-\epsilon)\gamma_{FC}^2 - \Delta\omega_{FC}^2 + \Omega^2}\right) \end{aligned} \quad (5.7)$$

where the approximation holds for low losses Filter Cavity.

This shows that to achieve a broadband reduction of the quantum noise of an interferometer described by its opto-mechanical coupling K , it is required to use a the Filter Cavity with a peculiar length L_{FC} and finesse F_{FC} . Their relationship is dependent on the Filter Cavity RTL Λ_{rt}^2 . This implies that for a given level of RTL, there is an optimal relationship between the Filter Cavity finesse and length given by

$$F_{FC} = \frac{\pi c}{2L_{FC}} \frac{1}{\gamma_{FC}} = \frac{\pi c}{2L_{FC}} \sqrt{\frac{(2-\epsilon)\sqrt{1-\epsilon}}{2}} \frac{\sqrt{2}}{\Omega_{sql}} \quad (5.8)$$

This relationship is presented in figure 5.5 where the Filter Cavity RTL were supposed to be 20 and 60 ppm. It is calculated for the phase I and phase II scenarii.

This figure shows that the Filter Cavity finesse decreases with its length with a linear dependency above few hundred meters length. This is of particular interest as lower finesse optical cavities are easier to realize and to operate than higher finesse one.

Another point is that with longer Filter Cavity, the influence of Filter Cavity RTL on the optimal Filter Cavity finesse decreases. This is also of particular interest as a cavity RTL can be easily spoiled by dust during its installation and commissioning.

Also, if the Filter Cavity RTL increase to the point where they reach the same order of magnitude than the Filter Cavity input mirror transmission, they start to be the main contributor to the Filter Cavity finesse value. This can be seen from the dashed lines in figure 5.5 that corresponds to 60 ppm of Filter Cavity RTL : For Filter Cavity length at

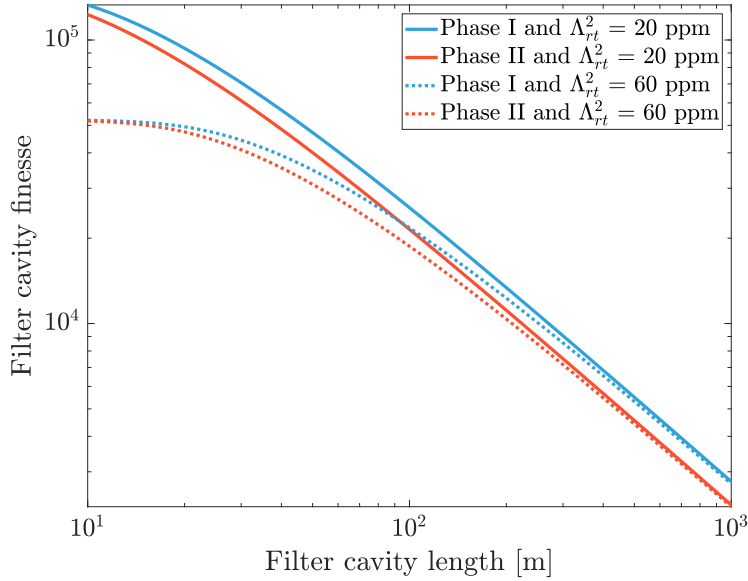


Figure 5.5: Relationship between Filter Cavity finesse and length for the phase I and phase II test-masses and assuming two values of Filter Cavity round-trip losses

the order of 10m that requires finesse at the order of 100 000 (without losses), the Filter Cavity RTL are larger than the Filter Cavity input mirror transmissivity. This explains the apparition of the plateau for small Filter Cavity length in figure 5.5.

The Filter Cavity transfer matrix with round-trip losses

The RTL can be assimilated by a decreased reflectivity of the input mirror. In that case the approximated reflectivity of the input mirror given by equation 2.91 is changed to account for the RTL by adding the Filter Cavity RTL to its input mirror transmissivity as

$$r_1 r_2 \sim r_1 \sim 1 - \frac{t_1^2 + \Lambda_{rt}^2}{2} \quad (5.9)$$

The Filter Cavity reflectivity is also changed as [59]

$$r_{FC}(\Omega) = 1 - \frac{2 - \epsilon}{1 + i\xi(\Omega)} \quad (5.10)$$

where ϵ is a function of the round-trip losses

$$\epsilon = \frac{2\Lambda_{rt}^2}{t_+^2 \Lambda_{rt}^2} = \frac{c\Lambda_{rt}^2}{2L_{FC}\gamma_{FC}} = \frac{f_{FSR}}{\gamma_{FC}} \Lambda_{rt}^2 \quad (5.11)$$

where γ_{FC} is the Filter Cavity bandwidth, f_{FSR} the Filter Cavity free spectral range and L_{FC} the Filter Cavity length.

The actions of the Filter Cavity can be again derived following section 2.3.3. However, because of the round-trip losses $\rho_m \neq 0$.

The Filter Cavity transfer function is expressed as in 2.3.3

$$\mathbf{T}_{FC} = \frac{1}{2} \begin{pmatrix} r_+ + r_-^* & i(r_+ - r_-^*) \\ -i(r_+ - r_-^*) & r_+ + r_-^* \end{pmatrix} \quad (5.12)$$

with

$$r_{\pm} = (\rho_p \pm \rho_m) e^{i(\alpha_p \pm \alpha_m)} \quad (5.13)$$

Combining these two equations gives

$$\begin{aligned} \mathbf{T}_{FC} &= e^{i\alpha_m} \begin{pmatrix} \rho_p \cos(\alpha_p) + \rho_m \sin(\alpha_p) & \rho_p \sin(\alpha_p) + i\rho_m \cos(\alpha_p) \\ -\rho_p \sin(\alpha_p) - i\rho_m \cos(\alpha_p) & \rho_p \cos(\alpha_p) + \rho_m \sin(\alpha_p) \end{pmatrix} \\ &= e^{i\alpha_m} \mathbf{R}_{\alpha_p} (\rho_p \mathbf{I} - i\rho_m \mathbf{R}_{\pi/2}) \end{aligned} \quad (5.14)$$

This shows that round-trip losses induces unbalanced reflectivities of the sidebands which in turn combines squeezing with anti-squeezing.

5.3.3 The degradation mechanisms

In order to generate frequency-dependent squeezed vacuum states, the frequency-independent squeezed vacuum states have to be propagated up to the Filter Cavity before reaching the interferometer. This requires several optical components which can be source of losses for the squeezed vacuum states that can each be modeled in the two-photons formalism by their 2×2 transfer matrix. Furthermore, the presence of optical losses can be assimilated to the introduction of vacuum states that can co-propagate with the squeezed state.

It means that the performances of the frequency-dependent squeezing injection can be understood by propagating several vacuum states through several optical components up to the homodyne detector. This is represented in figure 5.6 where the vacuum states propagate from the squeezer on the left to the photo-detector on the right. The photo-detector uses the homodyne detector scheme described section 2.2.3. The local oscillator beam corresponds to the interferometer readout beam.

There are three main vacuum fields to consider when dealing with losses. First, the vacuum field ν_1 incident on the squeezer that propagates to the Filter Cavity before being injected into the Advanced Virgo+ interferometer and detected at its output. Then a vacuum field ν_2 that is injected by the injection losses η_{inj} and propagates towards the interferometer and is detected at the interferometer output. Finally, a vacuum field ν_3 that is injected by the detection losses η_{det} and is detected at the photo-detector.

First, the vacuum field ν_1 interacts with the squeezer described in section 2.1.4 by

$$\mathbf{T}_{SQZ} = \mathbf{R}_{\phi} \cdot \mathbf{S}_{\sigma} \cdot \mathbf{R}_{\phi}^{\dagger} \quad (5.15)$$

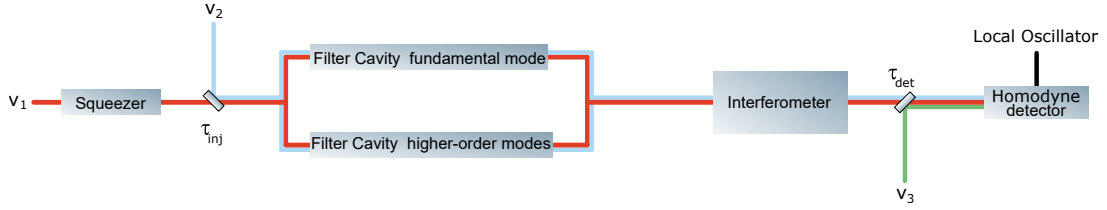


Figure 5.6: Model of the implementation of the frequency-dependent squeezing for the Advanced Virgo+ detector. Three vacuum fields propagate toward the photo-detector. The field ν_1 (red) passes through the squeezer and corresponds therefore to the squeezed field. The field ν_2 (blue) is introduced because of the injection optical losses. The field ν_3 (green) is introduced because of the readout losses. The gray boxes represent the main optical components used to inject frequency-dependent squeezing into an interferometer as well as the homodyne detector at its output required for the frequency-dependent squeezing measurement

For the O4 run, it is planned to use the AEI squeezer used during the O3 run that is able to generate up to 14 dB of squeezing.

Several optical components, mainly steering mirrors, matching optics and Faraday isolators, are required to inject this squeezed vacuum field into the Filter Cavity and the interferometer. As there are no non-linear components and as their optical losses can be considered frequency-independent, their action on the squeezed field can be expressed by a single scalar Λ_{inj}^2 that regroups all the optical losses between the squeezer and the interferometer at the exception of the Filter Cavity. By defining the injection efficiency $\tau_{inj} = \sqrt{1 - \Lambda_{inj}^2}$, they can be combined with the squeezer transfer matrix as :

$$\mathbf{T}_{inj} = \tau_{inj} \cdot \mathbf{T}_{sqz} = \tau_{inj} \cdot \mathbf{R}_\phi \cdot \mathbf{S}_\sigma \cdot \mathbf{R}_\phi^\dagger \quad (5.16)$$

All the sources of injection losses are presented in table 5.4.

There are several changes planned between O3 and O5 runs. The squeezer box Faraday isolator is replaced by a lower losses one [77]. 14 new mirrors are required to propagate the squeezed beam to the Filter Cavity and back to the interferometer. Their respective losses were estimated at the conservative level of 100 ppm. The biggest unknown concerns the value of mode-matching between the squeezed field and the interferometer. But an improvement can be expected for the O4 run with the installation of the new mode-matching telescope. For the O5 run, an active control of the mode-matching should be implemented. This technique is based on the sensing of Laguerre-Gauss higher-order modes that contains informations about the mode-mismatch. For the O5 run, an adaptative wave-front correction system might be also implemented [90].

A realistic Filter Cavity will affect the incident squeezed field with three additional mechanisms with respect to a loss-less Filter Cavity.

As already discussed, the Filter Cavity RTL modify the Filter Cavity transfer matrix as described by equation 5.14.

Another parameter that can affect the performances of the Filter Cavity is the mode-matching between the squeezed beam and the Filter Cavity. Indeed, due to the high finesse of the Filter Cavity, only the part of the squeezed beam that is on the Filter Cavity fundamental mode has its phase modified by the Filter Cavity as described by

Parameter	O3 and O4 high	O4 low	O5
OPO escape efficiency	0.99	0.99	0.99
Squeezer box Faraday isolator	0.98	0.992	0.992
ESQB FI [3]	0.927	0.976	0.976
infra-red pick-off for sub-carrier	-	0.994	0.994
All mirrors on the path	0.9988	0.998	0.998
SDB1 Faraday isolator	0.975	0.992	0.992
ESQB-SDB1 window	0.9958	0.9958	0.9958
Squeezer/Interferometer matching	0.95	0.97	0.99
All lenses on the path	0.9974	0.9974	0.9974
Injection efficiency	0.833	0.92	0.939
Injection Losses	0.167	0.08	0.061

Table 5.4: Injection optical losses from the O3 run to the O5 run. They are computed from the product of the efficiency of the optical components from the squeezing source to the main interferometer

equation 5.14. The part of the squeezed beam that is not coupled on the Filter Cavity fundamental mode sees the cavity as a simple mirror and therefore bypasses the Filter Cavity.

The detection of squeezed states is performed by a homodyne detector (presented in section 2.2.3) where the squeezed beam beats with a local oscillator beam. It means that the mode-mismatch between the squeezed beam and the local oscillator is also affecting the squeezing performances.

The effect of these two sources of mode-mismatch can be described by expressing the squeezed beam and the local oscillator beam in the orthogonal basis of spatial modes U_n such that

$$U_{sqz} = \sum_{n=0}^{\infty} a_n U_n$$

$$U_{lo} = \sum_{n=0}^{\infty} b_n U_n \tag{5.17}$$

$$\tag{5.18}$$

where a_n and b_n are complex coefficients. It is convenient to use the basis where U_0 corresponds to the Filter Cavity fundamental mode. The part of the squeezed beam and local oscillator beam that are coupled to the Filter Cavity fundamental mode are

expressed as

$$\begin{aligned} a_0 &= \sqrt{1 - \sum_{n=1}^{\infty} |a_n|^2} \\ b_0 &= \sqrt{1 - \sum_{n=1}^{\infty} |b_n|^2} \end{aligned} \quad (5.19)$$

The squeezed beam reflected by the Filter Cavity is therefore given by

$$U_{FC}^r = r_{FC}(\Omega) a_0 U_0 + \sum_{n=1}^{\infty} a_n U_n \quad (5.20)$$

Finally, the field detected by the homodyne detector corresponds to the overlap between the squeezed beam reflected by the Filter Cavity with the local oscillator beam. This is given by

$$\langle U_{lo} | U_{FC}^r \rangle = a_0 b_0^* + \sum_{n=1}^{\infty} a_n b_n^* = t_{00} r_{FC}(\Omega) + t_{mn} \quad (5.21)$$

In this equation, the complex parameter t_{mn} describes the part of the squeezed beam that is not matched to the Filter Cavity nor to the local oscillator beam or equivalently the overlap between the mismatched part of the squeezed beam with the mismatched part of the local oscillator beam.

This complex parameter t_{mn} can be expressed as a phasor using $t_{mn} = |t_{mn}| \exp(i \arg(t_{mn}))$. In a similar fashion to the description of the Filter Cavity, the action of the mismatch is described in the two-photons formalism by a rotation matrix

$$\mathbf{T}_{mn} = |t_{mn}| \mathbf{R}_{\arg(t_{mn})} \quad (5.22)$$

This means that the mismatch is generating a frequency-dependent rotation of the squeezed beam. Therefore, the mismatch is a source of frequency-dependent degradation for the frequency-dependent squeezing generation.

From equation 5.19, the magnitude of the overlap between these two mismatched beams is constrained by

$$|t_{mn}| \leq \sqrt{(1 - a_0^2)(1 - b_0^2)} \leq 1 - t_{00} \quad (5.23)$$

In practice, the mode-matching between the squeezed beam and the Filter Cavity a_0^2 can be easily measured. For instance this can be performed by using the BAB that is sensing the squeezed beam geometrical properties as performed during the O3 run. On the other hand, the mode-matching between the local oscillator beam and the Filter Cavity is not easily measured. Indeed, the local oscillator beam is the interferometer beam that does not interact with the Filter Cavity. However, it is easy to measure the mode-matching c_0^2 between the squeezed beam and the local oscillator at the photo-detector level. This

allows to express the mode-matching between the local oscillator beam and the Filter Cavity as [59]

$$b_0 = a_0 c_0 + \sqrt{(1 - a_0^2)(1 - c_0^2)} \exp(i \arg(t_{mn})) \quad (5.24)$$

As the mode-matching is estimated using the power in the overlapped part of two beams, the phase $\arg(t_{mn})$ is hard to estimate. In the following simulations, the conservative choice of using $\arg(t_{mn}) = \pi/2$ (that corresponds to the maximum of equation 5.24) is made.

Finally :

$$\begin{aligned} t_{mm} &= c_0 - t_{00} \\ t_{00} &= a_0 \cdot b_0^* \end{aligned} \quad (5.25)$$

The action of a realistic Filter Cavity with RTL and non-perfect mode-matching is described by

$$t_{00} \mathbf{T}_{FC} + \mathbf{T}_{mn} \quad (5.26)$$

This vacuum field is injected into the interferometer which is described by the equation 2.82. Note that in this chapter, the interferometer is considered loss-less. This is valid as the interferometer losses are small compared to the injection and readout losses.

Finally, the vacuum field is affected by the detection losses. The detection losses can be treated in a similar manner to the injection losses. They can be gathered together using their efficiency $\tau_{det} = \sqrt{1 - \Lambda_{det}^2}$.

Table 5.5 presents the estimated readout losses from the O3 run to the O5 run. As in table 5.4, the O4 high scenario corresponds to a pessimistic case where optical losses are higher than for the O4 low scenario where optical losses are lower. Compared to the previous chapter, the B1 photodiodes dark-noise has been taken into account as equivalent optical losses. The upgrades between these two scenarii have been described in section 5.2.3. Note that the effects of injection and detection losses has to be separated as they are separated by components that mix the two quadrature of the propagating vacuum fields.

The propagation of this vacuum field from the squeezed to the homodyne detector is therefore described by the following transfer matrix :

$$\mathbf{T}_1 = \tau_{det} \cdot \mathbf{T}_{ITF} \cdot (t_{00} \cdot \mathbf{T}_{FC} + \mathbf{T}_{mm}) \cdot \mathbf{T}_{inj} \quad (5.27)$$

A second vacuum field ν_2 is introduced by the injection losses before the Filter Cavity but after the squeezer. Its interaction with the Filter Cavity is described by the sidebands transmission coefficient defined in equation 5.21. The losses for this field can be described in the two-photon formalism as the average of the lower and upper sidebands [59]. This means that the propagation of this vacuum field is described by the transfer matrix :

$$\mathbf{T}_2 = \tau_{ro} \cdot \mathbf{T}_{ITF} \cdot \Lambda_2 \quad (5.28)$$

Parameter	O3 and O4 high	O4low and O5
All lenses on path	0.997	0.997
SDB1 pick-off	0.985	0.9925
SDB1 Faraday isolator	0.975	0.992
All mirrors on path	0.999	0.999
OMC coupling	0.975	1
OMC intra-cavity	0.98	0.99
OMC-interferometer matching	0.97	0.985
SDB1-SDB2 window	0.99958	0.99958
Alignment jitter	0.99	0.99
B1 photodiode efficiency	0.99	0.99
Detection efficiency	0.880	0.927
Detection losses	0.120	0.073

Table 5.5: Detection losses foreseen for the O4 and O5 runs. They are computed from the product of the efficiency of each component between the SR mirror and the B1 photodiode. The optical losses of each mirror is based on a conservative estimate that each mirror has 100 ppm of losses

where Λ_2 depends on the sidebands transmissivity as

$$\Lambda_2 = \sqrt{1 - \frac{|\tau_2(\Omega)|^2 + |\tau_2(-\Omega)|^2}{2}} \quad (5.29)$$

The last vacuum field ν_3 is introduced through the detection losses. The propagation of this vacuum field is described by

$$\mathbf{T}_3 = \tau_{det} \quad (5.30)$$

These three vacuum fields are incident on the homodyne detector. The quantum noise detected by the homodyne detector is given by the beating between the vacuum fields and the local oscillator beam which is defined by $\mathbf{b}_\zeta = A_{lo} (\sin \zeta, \cos \zeta)$. The single sided PSD is then

$$N(\zeta) = \sum_{i=1}^3 |\mathbf{b}_\zeta \cdot \mathbf{T}_i \cdot \nu_i|^2 \quad (5.31)$$

In equation 5.31, ζ represents the quadrature angle that is detected. As discussed in section 2.2.4, the phase noise is a source of degradation for the squeezing performances.

The phase noise is taken into account by assuming fluctuations of the homodyne angle. For low level of phase noise following a Gaussian distribution with a variance $\delta\zeta$, it is possible to express its effect as :

$$\delta N_\zeta = \frac{N(\zeta + \delta\zeta) + N(\zeta - \delta\zeta)}{2} \quad (5.32)$$

This equation describes the effect of frequency-independent phase noise similar to the phase noise measured during the O3 run. It has been estimated at the level of 55 mrad.

In addition to this frequency-independent phase noise, the Filter Cavity length fluctuation δL induces a frequency-dependent phase noise. Indeed, this length fluctuation will also affect the Filter Cavity detuning which defines the squeezing angle frequency-dependent rotation. This is expressed as :

$$\delta\Delta\omega_{FC} = \frac{\omega_0}{L_{FC}} \delta L_{FC} \quad (5.33)$$

Finally, the squeezing level measured at the interferometer output can be computed by normalizing it with the interferometer quantum noise without squeezing. This corresponds to the equation 2.30.

The effects of these three vacuum fields on the frequency-dependent squeezing performances can be decomposed through the five degradation mechanisms presented above. Namely, the injection and detection losses, the Filter Cavity round-trip losses and length fluctuations, the mode-mismatch between the squeezed field and the Filter Cavity, the mode-mismatch between the squeezed field and the interferometer and the phase noise.

Parameter	O3	O4 high	O4 low	O5 high	O5 low
Produced squeezing [dB]	8	8	12	12	12
Injection losses	0.167	0.167	0.08	0.06	0.06
Readout losses	0.12	0.12	0.07	0.07	0.07
Squeezed field-Filter Cavity mode-mismatch	-	-	0.03	0.01	0.01
Squeezed field-local oscillator mode-mismatch	-	-	0.03	0.01	0.01
Filter Cavity round-trip losses [ppm]	-	-	40	40	20
Filter Cavity length fluctuations [rms pm]	-	-	0.3	0.3	0.3
Frequency-independent phase-noise [rms mrad]	55	55	40	40	30

Table 5.6: Foreseen degradation parameters value for the O4 and O5 runs compared with the values obtained from the frequency-independent squeezing injection during the O3 run. Both the O3 and O4 high scenarii are using frequency-independent squeezing

In a similar manner to the observing scenarios for the O4 and O5 runs [50], the values of the parameters responsible for frequency-dependent squeezing degradation have been estimated for each run in a high and low configuration.

Table 5.6 shows the expected values of the parameters that affects the frequency-dependent squeezing injection in the Advanced Virgo+ detector. This table allows to compute the frequency-dependent squeezing degradation budget which corresponds to the level of squeezing measured at the interferometer output. The injection and readout losses and the frequency-independent phase noise are estimated from their measured level in the O3 run. The values of mode-mismatch, Filter Cavity round-trip losses and length fluctuations are justified in the next chapters.

Note that the technical noises do not appear in the table 5.6. Therefore in all the following simulations, the level of squeezing is larger that what will be measured during the O4 and O5 runs. The levels of squeezing presented in this table should be extracted from the data by applying the method presented in section 4.4.

An example of the frequency-dependent squeezing degradation budget is presented in figure 5.7 where the O4 low level of losses and a 300 m long Filter Cavity are assumed.

As expected, the high-frequency squeezing is mostly limited by the injection and readout losses as the Filter Cavity acts as a simple mirror on this frequency region.

At lower frequencies were the Filter Cavity is interacting with the squeezed field, the Filter Cavity round-trip losses and the mode-mismatch between the Filter Cavity and the squeezed field are limiting the frequency-dependent squeezing performances.

However, one can see that with such parameters, the Advanced Virgo+ quantum noise is improved by at least 2.5 dB over its entire sensitivity spectrum.

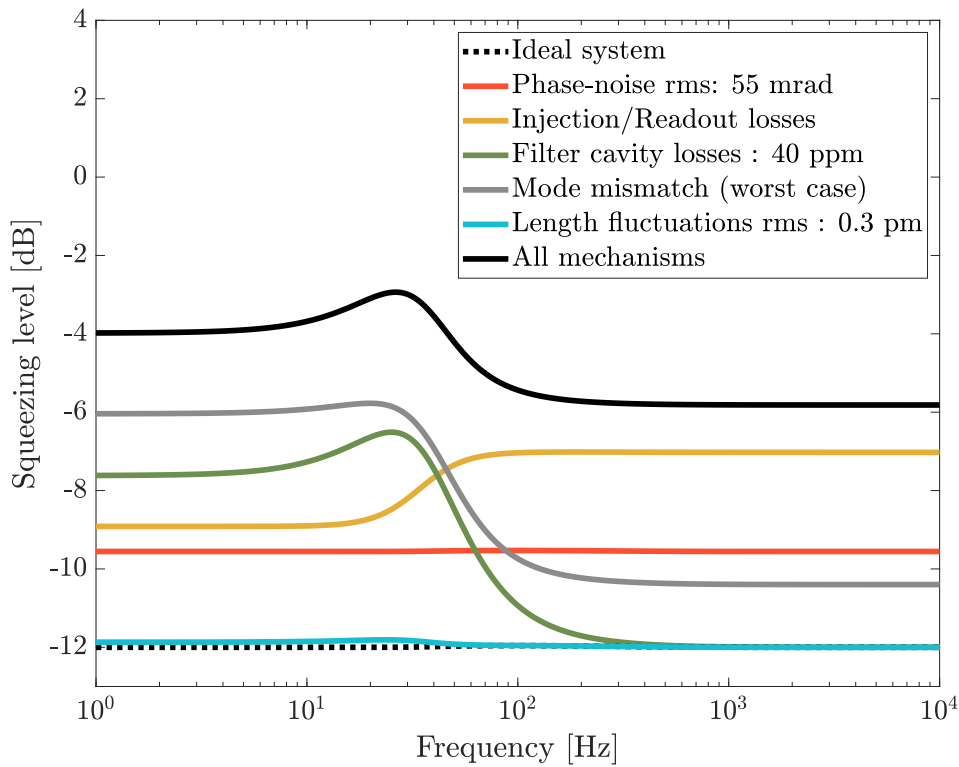


Figure 5.7: The frequency-dependent squeezing degradation budget for the O4 low scenario and assuming a 300m long Filter Cavity

5.3.4 The Filter Cavity length

With the model presented in the last section, it is possible to see that two out of the 5 frequency dependent squeezing degradation mechanisms are dependent on the Filter Cavity length, namely the Filter Cavity RTL and the Filter Cavity length fluctuations.

It means that the Filter Cavity length can be optimized to avoid having these noises limiting the frequency-dependent squeezing low-frequency performances.

The effect of the Filter Cavity length on the frequency-dependent squeezing performances are presented in figure 5.8 where the Filter Cavity length is varying from 30 m to 1 km and assuming again the O4 low scenario. It can be seen that the Filter Cavity RTL and length fluctuations induced degradations from limiting the frequency-dependent squeezing performances to a negligible level.

In particular, while the Filter Cavity round-trip losses are limiting the low-frequency performances of the frequency dependent squeezing for a Filter Cavity length of 30 m (figure 5.8a) and 100 m (figure 5.8b), these losses are reduced below the injection/readout losses and the mode-mismatch losses for a Filter Cavity length of 300 m (figure 5.8c) and 1000 m (figure 5.8d).

This indicates that by increasing the Filter Cavity length, it is possible to improve the low-frequency performances of the frequency-dependent squeezing. However, there is no

need for excessively long Filter Cavity as other losses are then limiting its performances.

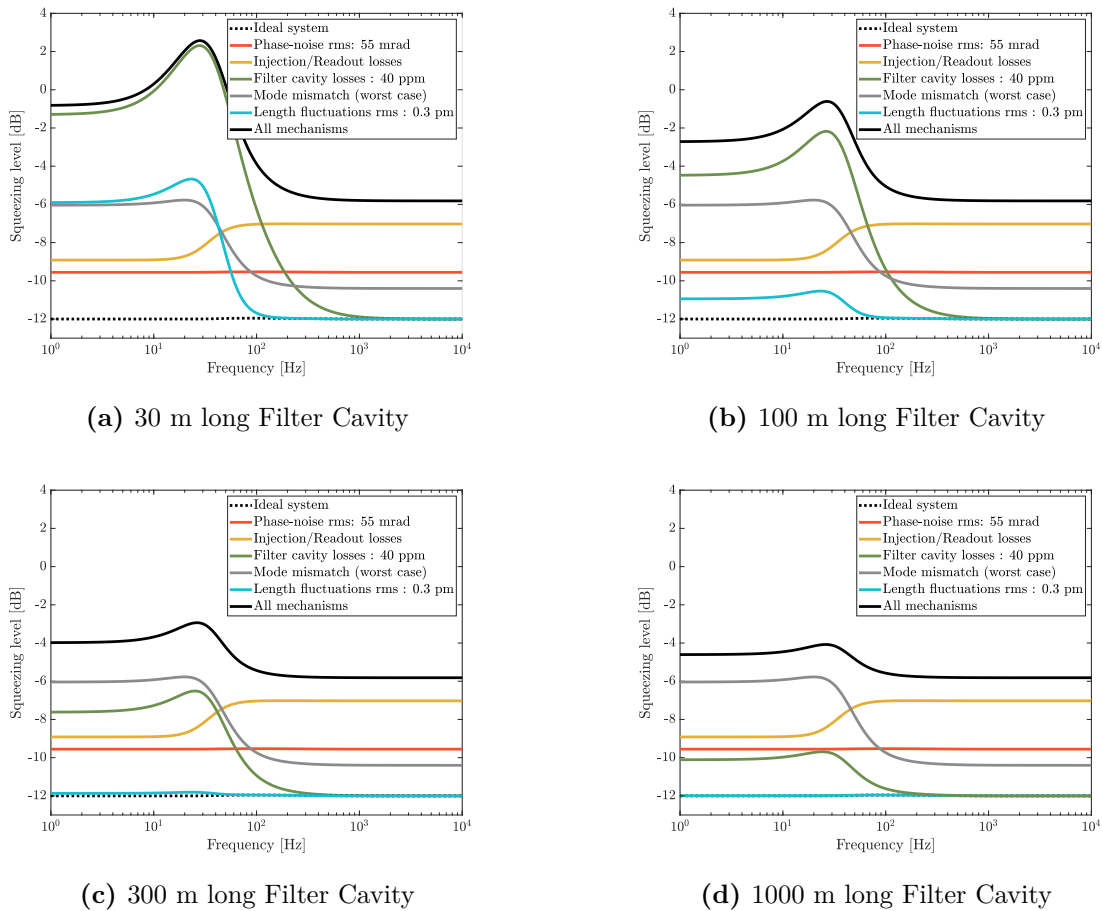


Figure 5.8: The frequency-dependent squeezing degradation budget for the O4 low scenario while varying the Filter Cavity length from 30m to 1000m

5.4 The impact of frequency-dependent squeezing on the sensitivity

While figure 5.8 allows to compute the frequency-dependent squeezing performances, it has to be remembered that this is only improving the quantum noise. However, for the Advanced Virgo+ detector, the quantum noise is not limiting the entire sensitivity spectrum. Especially at low and intermediate frequencies where suspension technical noises or thermal noise are present.

In order to combine this frequency-dependent squeezing budget into the Advanced Virgo+ sensitivity, the model described in the previous section has been combined with the GWINC program.

The quantum noise and the sensitivity

As four different configurations of the Advanced Virgo+ detector have been taken into account in these simulations, it is useful to compare for each of them the quantum noise with frequency-dependent squeezing and the other noises inferred for these configurations. While the respective *low* and *high* configurations corresponds roughly to the same interferometer configuration with increased losses for the *high* scenario, the phase I (O4) and phase II (O5) will see drastic changes in the configurations meaning that the relative strength of the quantum noise with respect to other noises will also change a lot.

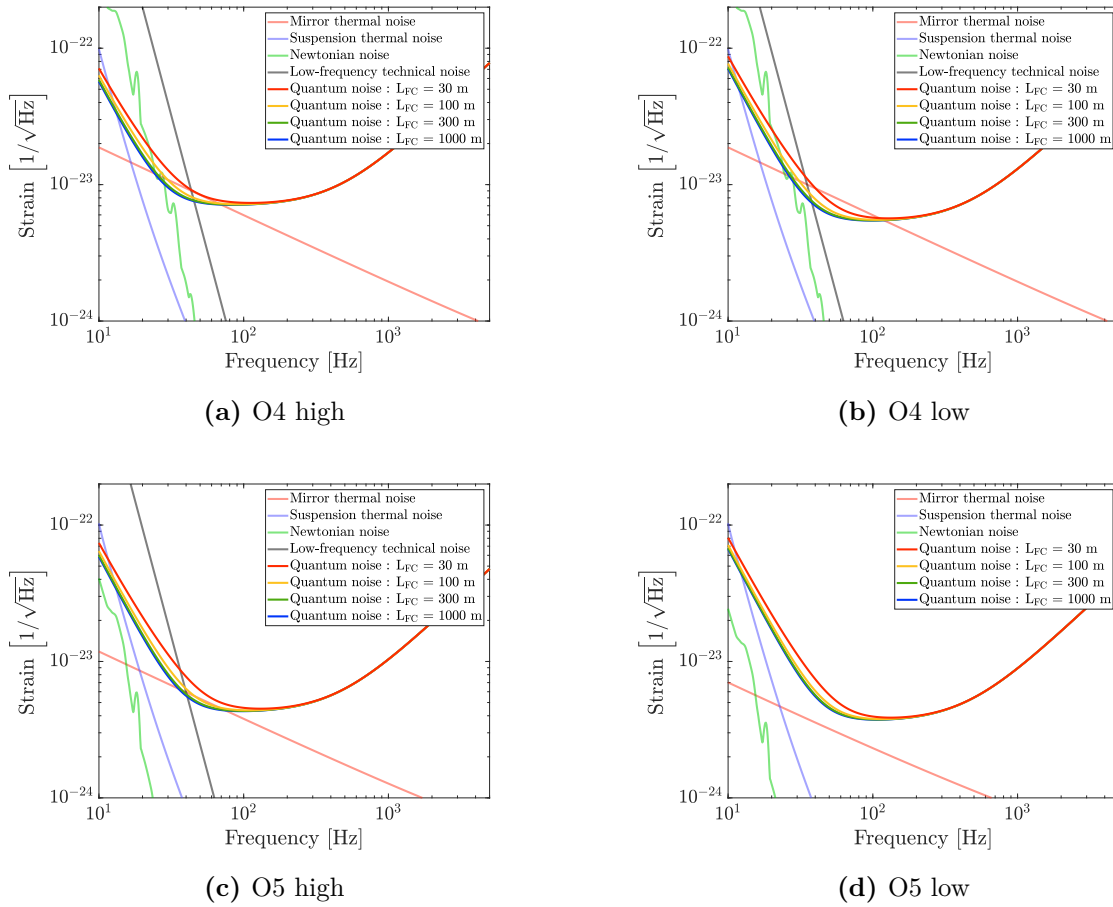


Figure 5.9: Advanced Virgo+ limiting noises for the O4 and O5 runs. The quantum noise is computed for 4 different Filter Cavity length : 30 m, 100 m, 300 m and 1000 m

Figure 5.9 compares the quantum noise with various Filter Cavity length to the others limiting noises for the O4 and O5 run.

While we can see a clear improvement on the quantum noise by going from a 30 m long Filter Cavity to a 100 m long one, going from 300 m to 1000 m does not bring significant improvement. Furthermore, the suspension technical noise and the Newtonian noise are limiting the low frequency sensitivity. Nevertheless as the Filter Cavity installation requires heavy infrastructural work, its design should be made for all these configurations.

Comparing only the various quantum noises, these figures indicate already that there is

no need to go for a Filter Cavity length above 300 m as the improvement on the low-frequency quantum noise is not significant on a region where it is already not the limiting noise.

On the other hand, if the suspension technical noise was removed from these figures (as in figure 5.9d), one can see that by going from a 30 m long Filter Cavity to a 300 m long Filter Cavity drastically reduces the spectrum region where the quantum noise is the limiting noise. This means that there is a clear gain to aim for a few 100 m-scale Filter Cavity.

All these noises can be summed together to compute the Advanced Virgo+ sensitivity for these various scenarios. This allows to quantify more precisely the effect of the Filter Cavity length on the Advanced Virgo+ sensitivity.

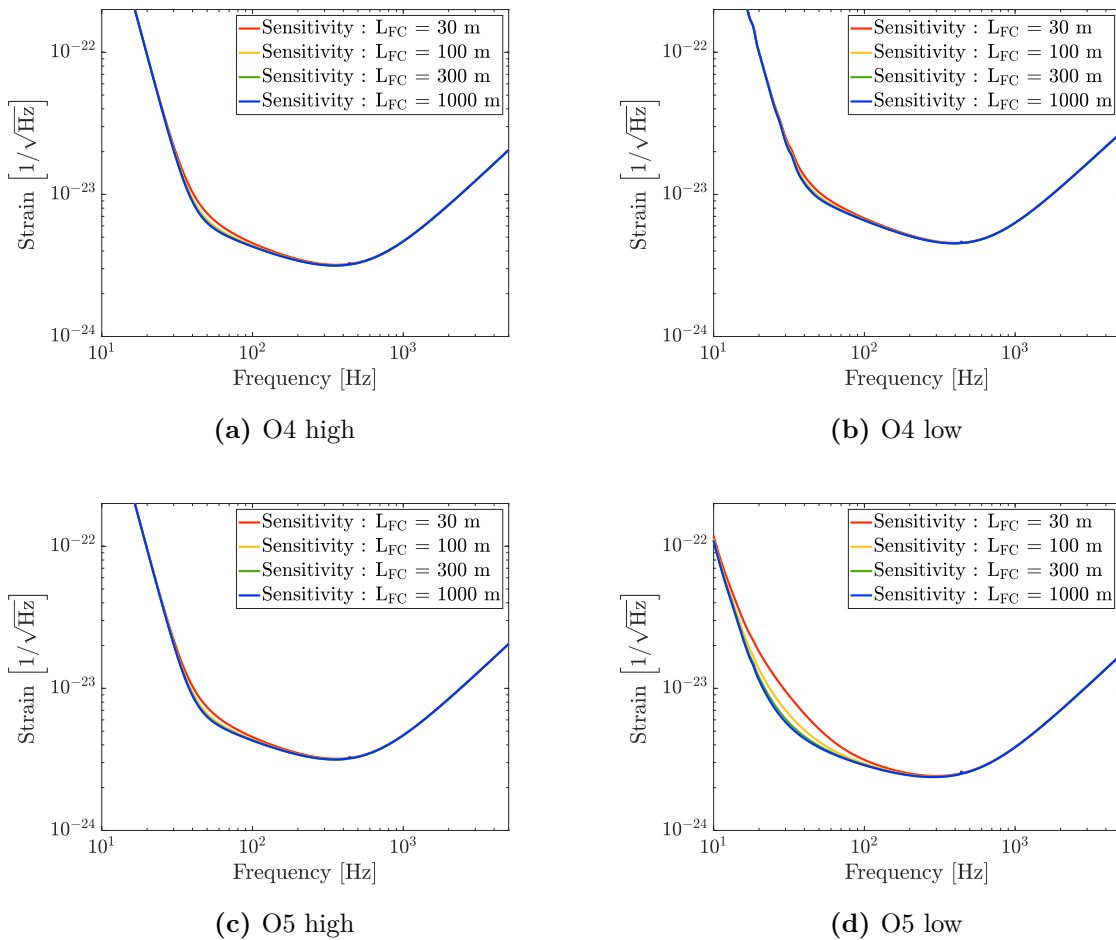


Figure 5.10: Advanced Virgo+ sensitivity for the O4 and O5 runs. The quantum noise is computed for 4 different Filter Cavity length : 30 m, 100 m, 300 m and 1000 m

Figure 5.10 presents the sensitivity for the 4 scenarios and with various Filter Cavity lengths. These figures highlight the fact that there is no improvement on the sensitivity by going from a 300 m Filter Cavity to a 1000 m one. Indeed, only in figure 5.10d, the sensitivities with 300 m or 1000 m long Filter Cavity are slightly distinguishable. Therefore, there is a hint that a few 100 m-scale Filter Cavity is a good compromise between frequency-dependent squeezing performances and excessively long Filter Cavity.

5.5 The Filter Cavity length and the Advanced Virgo+ ranges

While comparing the effects of the Filter Cavity length on the quantum noise or on the sensitivity allows to obtain a qualitative guess of the optimal Filter Cavity length, it is now useful to look at the BNS and BBH ranges [91] to get more quantitative estimates. Here the supernova range is not used as the Filter Cavity acts only at low frequencies.

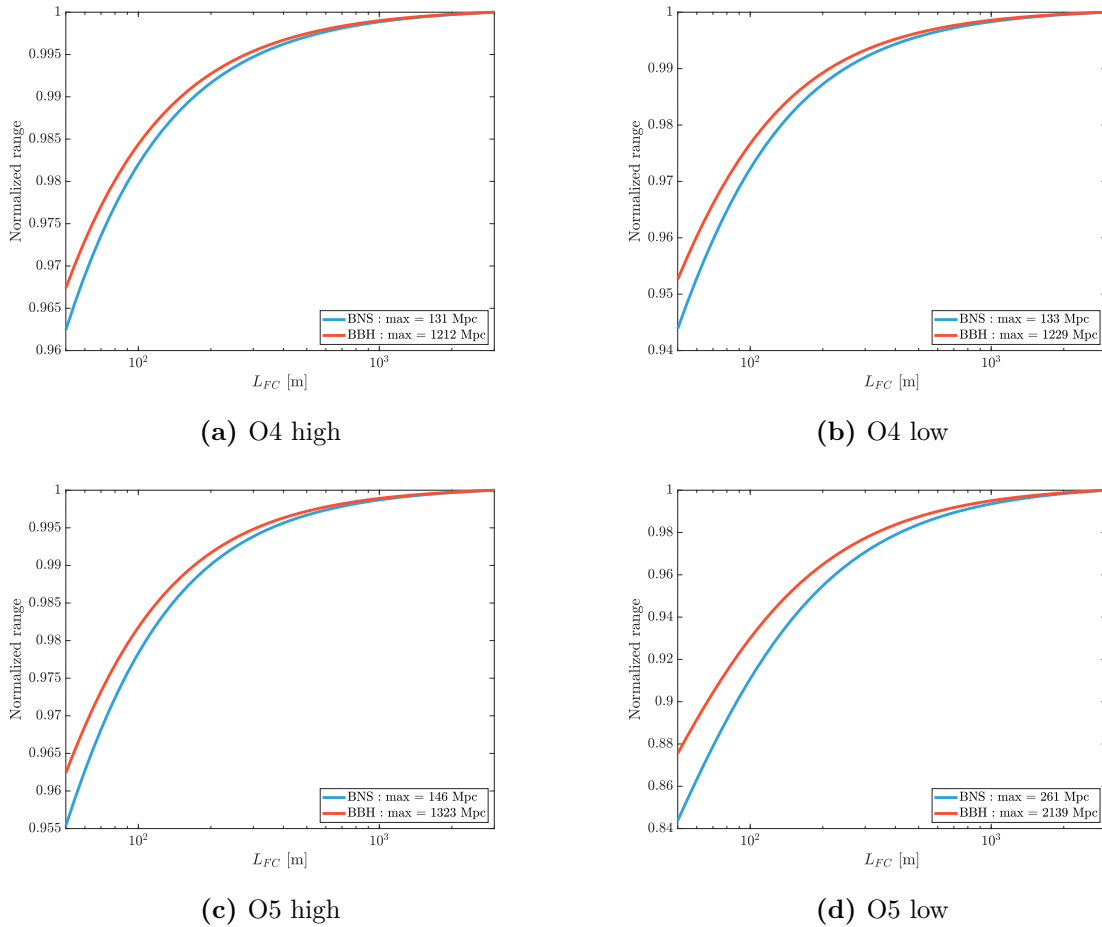


Figure 5.11: Advanced Virgo+ BNS and BBH ranges normalized with their respective maximum for the O4 and O5 runs as a function of the Filter Cavity length

For each scenario, the BNS and BBH ranges have been computed varying the Filter Cavity length from 30 m to 3 km which is the longest possible Filter Cavity within the Virgo infrastructure.

Figure 5.11 presents the BNS and BBH ranges for each scenario normalized by their respective maximum. As we could already see by looking at the quantum noise figure 5.9 or the Advanced Virgo+ sensitivity in figure 5.10, the improvement in the BNS and BBH ranges is not linear with the Filter Cavity length independently on the scenario considered : a significant improvement of the BNS and BBH ranges up to 100 m-scale Filter Cavity followed by a slower increased up to km-scale Filter Cavity where the ranges almost do

not change with the Filter Cavity.

From this figure, we can see that the inflection region where the ranges improvement slow is around few 100 m for every scenario.

In more details, for every scenario where the suspension technical noise is present (meaning O4 high to O5 high in figures 5.11a, 5.11b and 5.11c), more than 99 % of the maximum ranges is achieved for a 300 m long Filter Cavity. For the O5 low scenario figure 5.11d where no suspension technical noise are present and a factor 5 reduction of the Newtonian noise is expected, a 300 m long Filter Cavity leads to 97 % of the maximum BNS range and almost 98 % of the maximum BBH range.

However, reaching 99 % of the maximum ranges for this scenario requires to build a 1 km long Filter Cavity. It does not seem realistic to quasi triple the Filter Cavity length and therefore complicate the infrastructure work for such a little improvement. Also, a longer Filter Cavity requires larger optics and more complicated alignment system.

Furthermore, the frequency-dependent squeezing degradation budget of a 1 km long Filter Cavity presented in figure 5.8d shows that for these length range, the Filter Cavity length induced degradation mechanisms are far below other degradation mechanisms. It means that it should be more useful to further decrease the injection and optical losses or improve the mode-matching and phase noise rather than aiming for excessively long Filter Cavity.

Therefore, it has been decided to use a 300 m scale Filter Cavity for the Advanced Virgo+ detector.

5.6 Conclusion

This chapter has derived a frequency-dependent squeezing noise budget using realistic losses for the O4 and O5 runs. This degradation budget shows that the Filter Cavity length have an important effect due to the Filter Cavity RTL and length fluctuations. By looking at the Filter Cavity length effect on the foreseen BNS and BBH ranges, it could be seen that a 300 m scale Filter Cavity reaches almost similar performances to a 3 km long Filter Cavity while bringing less constraints on optics sizes or control schemes. Therefore, the Advanced Virgo+ Filter Cavity will be a 300 m scale Filter Cavity.

As will be presented in the next chapter, due to infrastructural constraints, the Advanced Virgo+ Filter Cavity length has been set to 285 m.

The performances of such a Filter Cavity on the Advanced Virgo+ radiation pressure noise and shot noise are presented in the table 5.7.

This allows to compute the planned BNS ranges for the Advanced Virgo+ detector for the O4 and O5 runs presented in the observing scenario [50]. Note that in this document, the O4 high scenario used a frequency-independent squeezing injection instead of a frequency-dependent squeezing injection. However, losses are similar to the ones presented in this chapter (meaning that high frequency performances should be similar).

	O4 high	O4 low	O5 high	O5 low
Shot noise reduction [dB]	4.3	5.8	6.8	6.9
Radiation pressure noise reduction [dB]	3.4	3.6	5.3	5.5

Table 5.7: Foreseen reduction of the quantum noise at low-frequency (radiation pressure noise) and high frequency (shot noise) using the parameters of table 5.6 combined to a 285 m long Filter Cavity. The improvement of the radiation pressure noise is estimated around 10 Hz and the one of the shot noise around 5 kHz to be far from the squeezing rotation frequency

6

The Filter Cavity optical design

Contents

6.1	Introduction	151
6.2	The Filter Cavity optical configuration	152
6.2.1	The beam size	152
6.2.2	The alignment	153
6.3	The mirrors maps characterization	157
6.3.1	The surface defects	157
6.3.2	Realistic mirror maps	159
6.4	Single Round-Trip simulation	161
6.4.1	Fabry-Perot round-trip losses	161
6.5	The Filter Cavity degeneracy	166
6.6	The etalon effect	171
6.7	Conclusion and Mirror specifications	172

6.1 Introduction

With the Filter Cavity length chosen, it is now possible to derive the optical properties of the Filter Cavity. This concerns mainly the design of the Filter Cavity mirrors to reach the performances presented in the last chapter. In particular, this chapter will compute the Filter Cavity round-trip losses from its mirror quality. This allows to derive the requirements on the Filter Cavity optical design to allow a broadband reduction of the Advanced Virgo+ Quantum Noise.



These requirements are driven by the frequency of the rotation of the squeezing ellipse and by the level of the Filter Cavity optical losses. The simulations performed to define these requirements use the four scenarii of the squeezing degradation budget presented in table 5.6 for both O4 and O5 runs.

6.2 The Filter Cavity optical configuration

The previous chapter has shown that the frequency-dependent squeezing angle rotation can be achieved by reflecting a frequency-independent squeezed state on a high-finesse detuned optical cavity.

In this section, we will study two Filter Cavity optical configurations : a plane-curved cavity (PC) and a curved-curved cavity with identical RoC on both mirrors (CC).

6.2.1 The beam size

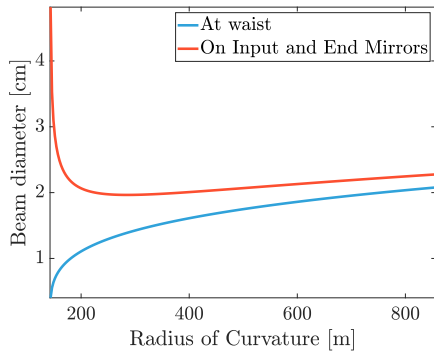
As the waist is not located at the same position for these two configurations (on the Input Mirror Filter Cavity (IMFC) reflective surface for the PC configuration and at the cavity center for the CC configuration) [92], the beam size on the mirrors will also be different. The beam diameter on the Filter Cavity mirrors for each configuration is represented in figure 6.1. The beam size on the Filter Cavity mirrors plays an important role in the Filter Cavity losses. Especially, if the beam starts to reach size similar to the mirror one, part of the beam power is lost outside the mirror. This is known as the clipping losses.

A point to notice is that for the CC configuration, the beam size will be the same on both mirrors, therefore making the effects of the mirrors identical for both IMFC and End Mirror Filter Cavity (EMFC).

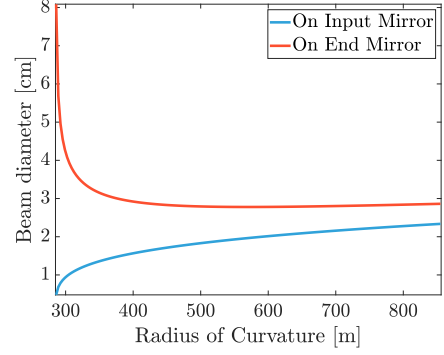
For the PC configuration, as the waist is located on the IMFC, the beam size on IMFC will be smaller than for the CC configuration while being larger on the EMFC. Having a smaller beam on the IMFC could be helpful for the Filter Cavity telescope design as a smaller beam size magnification means that the telescope is less sensitive to astigmatism.

However, to have a really smaller beam on the IMFC, one needs to have a quite small EMFC RoC, therefore close to the cavity instability. For instance, in order to have a beam diameter of 1 cm on the IMFC (which is two times smaller that what can be achieved with a CC configuration), it is required to have the EMFC RoC at the order of 300 m. This gives a stability condition of $(1 - L/R_{IM})(1 - L/R_{EM}) = 0.05$. This is really close to the instability which is given by $(1 - L/R_{IM})(1 - L/R_{EM}) = 0$ or 1. Here the RoC of the IMFC and EMFC have been introduced respectively as R_{IM} and R_{EM} .

Furthermore, a larger beam on the EMFC means that the cavity will be more sensitive to the clipping losses. A larger beam on the EMFC will also increase the optical losses due to mirror surface flatness defects on larger scales.



(a) Beam diameter on mirrors for the CC configuration. In this configuration, the beam diameter on the two mirrors can be kept in the range of 2 cm.



(b) Beam diameter on mirrors for the PC configuration. In this configuration, the beam diameter on the IMFC can be reduced to 1 cm. But in this case the beam diameter on the EMFC becomes very large.

Figure 6.1: The beam diameter on mirrors. The CC configuration is a curve-curve cavity with the same RoC for both mirrors. The PC configuration has its IMFC flat.

6.2.2 The alignment

Another parameter directly linked to the Filter Cavity optical configuration is the alignment sensitivity to mirror tilts. Indeed, as shown in figure 6.2, a tilt of a cavity mirror can shift and/or tilt the cavity optical axis. It means that the overlap between an input beam and the cavity will not be perfect anymore and couplings with the cavity first HOM will appear [93].

For the O4 low scenario, the mode-mismatch losses between the squeezer and the Filter Cavity should be of the order of 1 %. We can therefore compare for the PC and CC configurations, how such level of alignment is constraining the tilt of one of its mirror.

Using the fact that the cavity optical axis go through the centers of curvature of both mirrors while being orthogonal to the mirror surfaces, one can define the relationship between the cavity optical axis tilt α and shift a at the level of the cavity waist, and the IMFC and EMFC tilts, respectively θ_1 and θ_2 as :

$$\begin{pmatrix} \alpha^{CC} \\ a^{CC} \end{pmatrix} = \begin{pmatrix} \frac{R}{2R-L} & \frac{R}{2R-L} \\ \frac{R}{2} & -\frac{R}{2} \end{pmatrix} \times \begin{pmatrix} \theta_1 \\ \theta_2 \end{pmatrix} \quad (6.1)$$

$$\begin{pmatrix} \alpha^{PC} \\ a^{PC} \end{pmatrix} = \begin{pmatrix} 1 & 0 \\ R-L & -R \end{pmatrix} \times \begin{pmatrix} \theta_1 \\ \theta_2 \end{pmatrix} \quad (6.2)$$

where CC and PC subscripts indicate the optical configuration considered, R indicates the RoC of both mirrors for the CC configuration or the EMFC for the PC configuration.

The power lost due to such misalignment, namely the part of the light which couples to the Filter Cavity first order mode and therefore is lost for squeezing application, is defined

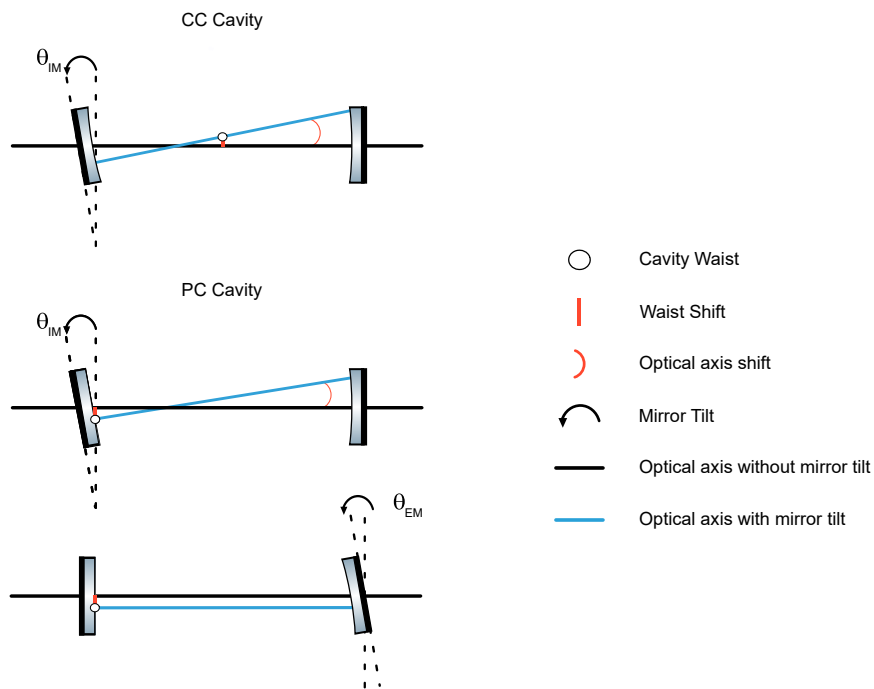


Figure 6.2: The effect of mirror tilt on the optical axis position is presented for a cavity with two curved mirrors with the same RoC [CC] and a cavity with the IMFC plane and the EMFC curved [PC]. Positive angles are given by the direction of the black arrow. An optical axis (blue) shift above the optical axis without mirror tilt (black) gives a positive shift. In the case of the CC configuration, a tilt of the EMFC will shift and tilt the optical axis in the opposite direction to an IMFC tilt.

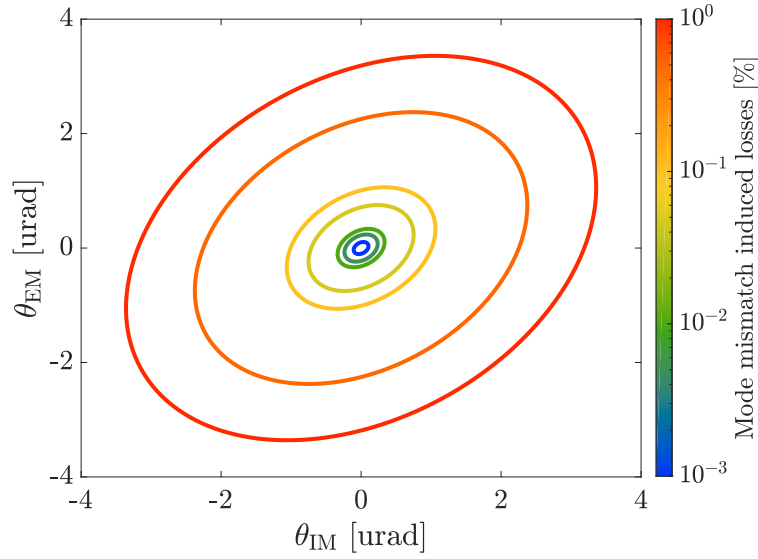


Figure 6.3: Misalignment losses induced by angular motions of the IMFC θ_1 and angular motions of the EMFC θ_2 . This figure corresponds to a CC configuration with $R = 385$ m

as

$$\left(\frac{\alpha^{xx}}{\theta_{div}}\right)^2 + \left(\frac{a^{xx}}{\omega_0}\right)^2 = mm \quad (6.3)$$

with mm the part of the light coupled to the first order cavity mode, ω_0 the cavity waist size, $\theta_{div} = \lambda / (2\pi\omega_0)$ with $\lambda = 1064$ nm and the subscript xx represent either the CC or PC configuration.

It means that for a fixed R and L there is maximum values of θ_1 and θ_2 such that the misalignment losses will reach the level noted mm .

This relationship represented in figure 6.3 exhibits an elliptical shape. But because each Filter Cavity mirror angular motions will be controlled with similar system, in order to reach a certain misalignment we need to limit each mirror angular motion below this ellipse semi-minor axis. Therefore, this represents the maximal allowed mirror angular motion for any mm value. This is represented in figure 6.4.

One could notice that in figure 6.4a exhibits a discontinuity for $R = L = 285$ m. This appears because at this value the ellipse is a circle and therefore the semi-minor axis and semi-major axis are exchanged as presented in figure 6.5.

Figure 6.4 shows that the misalignment sensitivity on mirror tilts is similar for the PC and the CC configuration. However, an automatic alignment system can provide a mirror angular motions below $0.1 \mu\text{m}$. It means that for any cavity optical configuration the angular motions of the mirrors are responsible for less than 0.1% of lost power on the Filter Cavity fundamental mode. This level is far below the mode-mismatch requirement of 1% for the O4 low and O5 scenarii (see for instance table 5.6).

This section studied the differences of the CC and PC configuration on beam size and

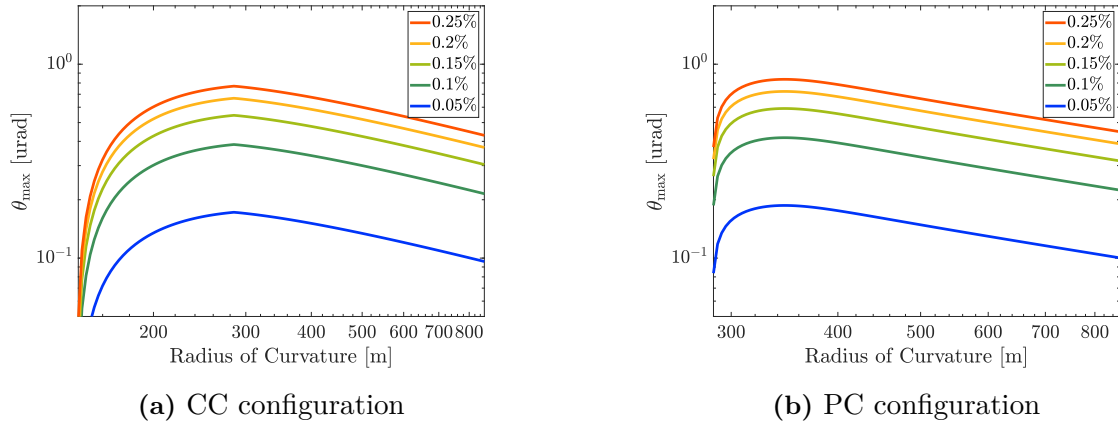


Figure 6.4: Maximal mirror angular motions for two optical configurations as a function of the mirror RoC and of the targeted misalignment losses. The Filter Cavity length is $L = 285$ m

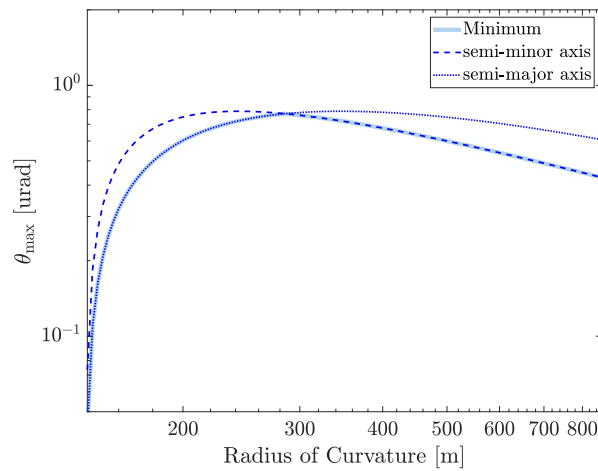


Figure 6.5: The maximum angle for a CC configuration and a 2 % misalignment. The dotted lines present arbitrary named semi-minor axis (big dots) and semi-major axis (small dots) which are equal for $R = L = 285$ m where the discontinuity happens.

misalignment. There is no clear advantages in misalignment between these two configurations. Therefore, the following sections will study these two configurations. Especially, the effects of the configuration on the Filter Cavity RTL will be presented.

6.3 The mirrors maps characterization

This section presents the characterization of realistic mirrors. Especially, the surface defects that corresponds to the non-perfectly spherical surface of the mirrors are introduced and characterized.

6.3.1 The surface defects

The surface of an ideal mirror describes a sphere that defines the RoC of this mirror. However, it is in practice impossible to make mirrors whose surface perfectly describes a sphere. The surface of a realistic mirror can thus be described by adding deviations of its surface from this sphere. These deviations are called surface defects and allow to judge the surface quality of the mirrors.

The mirror defects are represented by the mirror map, which is a $n \times n$ matrix with $n = D_{mirror}/dx$ with D_{mirror} and dx are respectively the mirror diameter and the resolution of the map. Each matrix element contains the measure of the height h of the mirror surface with respect to the perfectly spherical one.

A first way to judge the quality of the surface of a mirror is to use the peak-to-valley (PV) value of the mirror map. Indeed, this value indicates what is the largest surface deviation from a perfect sphere. The problem with this value is that its influence is strongly related to its position on the mirror. For instance, if the surface defect that causes the PV value is located outside the beam hitting the mirror, it will have no influence on the beam.

Therefore, it is interesting to introduce a second way to judge the quality of a mirror independent of the position of the surface defects on the mirror surface : the root mean square (RMS) of the mirror surface that allows to characterize the global fluctuations of the whole mirror surface. This RMS value σ_{RMS} is expressed as

$$\sigma_{RMS} = \sqrt{\frac{1}{n} \sum_{i=1}^n (h_i - \bar{h})^2} \quad \text{with} \quad \bar{h} = \frac{1}{n} \sum_{i=1}^n h_i \quad (6.4)$$

where each h_i describes the height of the i^{th} element of the mirror map and \bar{h} is the mirror map mean height.

The PV and RMS values of a mirror map allow both to judge the quality of this mirror surface. However, they do not allow to judge the effects of surface defects on an incident beam. To simulate these effects, it is interesting to study the mirror map in the spatial frequency domain. This passage in the frequency domain is realized by applying a 2D Fourier transform to the mirror map. This Fourier transform is defined for frequencies between a minimum frequency $f_{min} = 1/D_{mirror}$ which corresponds to the inverse of

the mirror diameter and a maximum frequency $f_{max} = 1/(2dx)$ which depends on the resolution of the map. It is then possible to introduce a 1D PSD depending on the mirror map expressed in the spatial frequency domain. Finally, this PSD is connected to the RMS of the mirror surface by

$$\sigma_{RMS}^2 = \int_{f_{min}}^{f_{max}} PSD(f) df \quad (6.5)$$

The surface defects with low frequency (typically below 10^3 /m) contribute to the so-called mirror flatness while the surface defects with higher frequency contribute to the so-called mirror roughness. This distinction only arises because of different measurement techniques used for low and high frequency surface defects [94].

A beam hitting a realistic mirror is scattered by the mirror spatial defects. The scattering angle θ for a beam at normal incidence on the mirror surface is related to the light wavelength λ and the spatial frequency of the surface defect f as in [95]

$$\theta = \lambda \cdot f \quad (6.6)$$

This equation means that a fraction of the light incident on a mirror with surface defects is not reflected at normal incidence. The amount of light not reflected at normal incidence is given by

$$\left(\frac{4\pi\sigma(f)}{\lambda} \right)^2 \quad (6.7)$$

with σ is the amplitude of a spatial defect with spatial frequency f . As the mirrors have a finite size, there is a scattering angle limit above which the light will directly exit the cavity given by

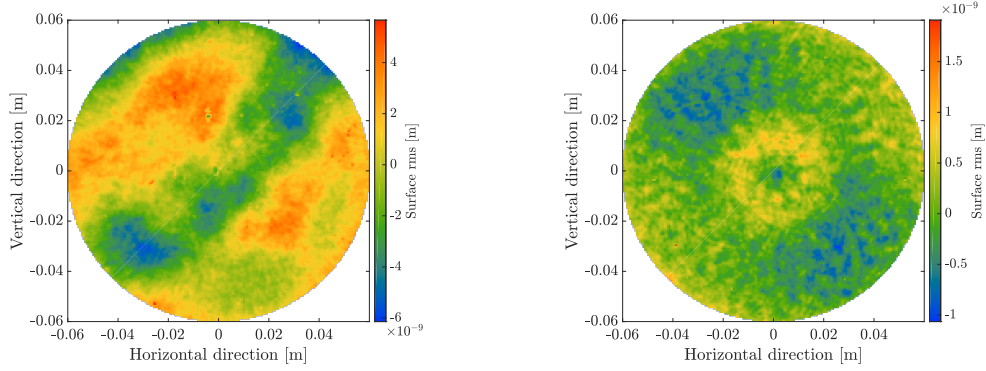
$$\theta_{lim} = \frac{D_{mirror}}{2L_{FC}} \quad (6.8)$$

Combining equations 6.6 and 6.8 means that there is a limit to the spatial frequency above which the light will directly exit the cavity given by

$$f_{lim} = \frac{D_{mirror}}{2L_{FC} \lambda} \quad (6.9)$$

For a 285m long Filter Cavity with mirror diameter of 13cm, this gives $f_{lim} = 214 \text{ m}^{-1}$. The Filter Cavity mirror diameters are related to the use of ring heaters which are introduced in section 6.5.

Combining the equations 6.7 and 6.9, it is possible to estimate the fraction of power that is directly reflected outside the Filter Cavity because of mirror surface defects with spatial



(a) VIM06 surface as measured at LMA (b) EM03 surface as measured at LMA

Figure 6.6: The two mirror maps used in the following simulations. EM03 is Advanced Virgo-like quality while VIM06 is Initial Virgo-like quality.

frequency above f_{lim} as

$$\text{losses}(f > f_{lim}) = \left(\frac{4\pi\sigma(f > f_{LIM})}{\lambda} \right)^2 \quad (6.10)$$

with $\sigma(f > f_{lim})$ the RMS for frequencies higher than f_{LIM} .

We can therefore obtain directly from the mirror surface RMS an estimate of the light that will be directly scattered outside of the cavity. This light directly scattered outside of the Filter Cavity consists of losses for the squeezing application.

6.3.2 Realistic mirror maps

Two mirror maps have been studied : VIM06 of Initial Virgo-like quality and EM03 of Advanced Virgo-like quality. The difference between these two mirrors arise from the polishing technique used for each mirror. For instance, the VIM06 was polished using standard polishing technique while the EM03 mirror was polished using the ion beam polishing technique.

These two mirror maps have been measured at LMA and the results of this measurement is represented in figure 6.6. In this figure, the piston, tilt and focus of the mirror maps have been subtracted over 5 cm. Indeed, this study focuses on the power lost due to surface defects. Furthermore, the effects of the piston, tilt and focus of the mirror can be compensated by changing the macroscopic position of the mirror.

Note that in this figure that the color-scale that represents the surface height is different for the two mirrors maps. For instance, the color-scale of the VIM06 map is going from -6 nm to 5 nm while the color-scale of the EM03 map is going from -1 nm to 2 nm.

The surface quality of these two mirrors is summarized in table 6.1 using the parameters introduced in the previous section.

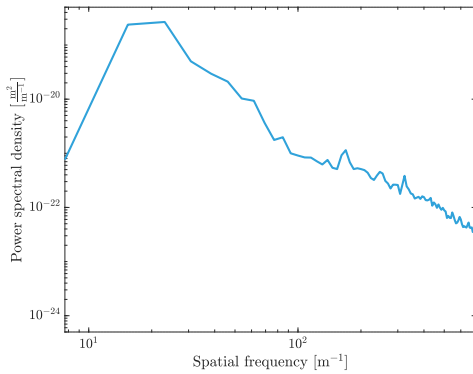
On the EM03, the PV value arises from a small area on the bottom left part of the mirror surface which is visible as a red dot pixel on a blue background in figure 6.6b. The

Parameters	VIM06	EM03
PV value [nm]	14.0	2.5
RMS value [nm]	2.3	0.4
Losses [ppm]	9.9	1.4

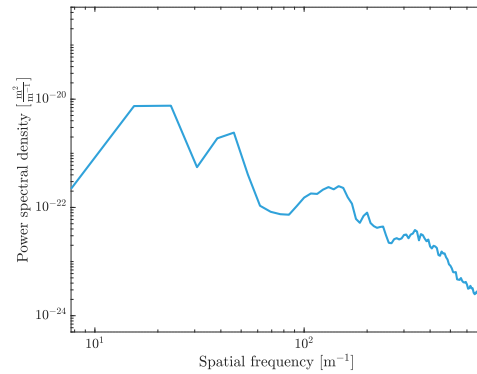
Table 6.1: PV and RMS values for the VIM06 and EM03 mirror maps used in this chapter. The losses corresponds to the amount of light directly scattered outside the Filter Cavity and are computed using the equation 6.10

remaining part of this mirror appears to have its height varying between -1 nm and 1 nm. This is not the case for the VIM06 where larger parts of the mirror surface seem to exhibit large PV value. For instance in figure 6.6a, almost one third of the surface seems to have negative height at the order of -2 nm while the other two-third seem to have positive height above 2 nm. This difference appears more clearly in the mirror surface RMS value.

The PSD of these two mirror maps are presented in figure 6.7. As expected from their RMS values, the EM03 PSD is lower than the one of the VIM06 PSD for all the spatial frequencies.



(a) VIM 06 surfacePSD



(b) EM03 surfacePSD

Figure 6.7: The 1D PSD associated to the mirror maps VIM 06 (initial Virgo-like quality) and EM03 (Advanced Virgo-like quality)

It is also possible to extract the amount of loss due to surface defects with too high spatial frequencies as described in equation 6.10. This gives 1.14 ppm of losses for the EM03 map and 9.9 ppm of losses for the VIM06 map. It can be noted that the ratio of losses for these two mirrors follows the ratio of their RMS values.

6.4 Single Round-Trip simulation

The previous section has presented how the mirror surface quality can induce Filter Cavity losses. However, this estimation of the Filter Cavity losses was independent on the Filter Cavity optical configuration. This section presents how the Filter Cavity optical configuration can impact the Filter Cavity losses.

6.4.1 Fabry-Perot round-trip losses

The RTL of a Fabry-Perot cavity can be obtained via different methods. The simulations performed in this section follow the description of [96] which compares different ways to calculate the cavity RTL.

Because of energy conservation, the RTL of a Fabry-Perot cavity are defined as

$$\Lambda_{rt}^2 = \frac{P_{in} - P_r - P_t}{P_{circ}} \quad (6.11)$$

with respectively P_{in} , P_r , P_t and P_{circ} the input, reflected, transmitted and circulating powers. Furthermore, we suppose the input power to be on the fundamental mode.

However, in the case of a Frequency-Dependent Squeezed states generation, any part of the squeezed beam that is not in the Filter Cavity fundamental mode will degrade the produced Frequency-Dependent Squeezed states as presented in figure 5.7. Therefore, any part of the circulating or reflected beam that is not in the Filter Cavity fundamental mode is also a source of cavity losses. Following equation 6.11, we can define the losses on the fundamental mode as

$$\Lambda_1^2 = \frac{P_{in} - P_r^{00} - P_t^{00}}{P_{circ}^{00}} \quad (6.12)$$

where P_x^{00} indicates the power that is on the Filter Cavity fundamental mode for either the reflected, transmitted or circulating beam.

It is useful to make this distinction because the light directly scattered outside the cavity will be a loss for both the fundamental mode and all modes. It therefore represents the lowest RTL value achievable. On the other hand, losses that are present on the fundamental mode and not on all modes are due to a cavity degeneracy as presented in the following section.

As presented in the previous section, the mirror defects with spatial frequency higher than f_{lim} scatter a fraction of the incident beam directly outside of the Filter Cavity. Their induced losses have been computed in table 6.1.

In order to combine the effects of the mirror surface defects with the Filter Cavity optical configuration, a single round-trip simulation has been performed. The apparatus of this simulation is represented in figure 6.8.

A beam (on the Filter Cavity fundamental mode) is reflected by the cavity EMFC upon

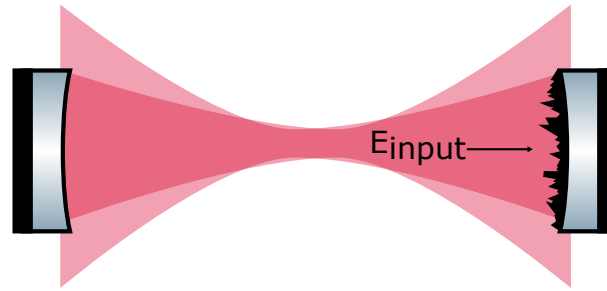


Figure 6.8: An input beam is reflected of the cavity EMFC where a non-perfect mirror map is applied. Fields are calculated at the levels of each mirrors as well as the part directly scattered outside the mirrors and during the beam propagation.

which a map (ie surface defects) is applied. The beam is then propagated for $L_{FC} = 285$ m towards the IMFC. At the level of the IMFC, the fraction of the beam that is scattered outside the IMFC is computed by applying a circular mask on the mirror with the same diameter as the foreseen coating (13 cm). The beam is then reflected by the perfect IMFC and propagated towards the EMFC. At this level, the fraction of the beam directly scattered outside this mirror is computed in a similar fashion as for the IMFC. The power lost during the propagation of the beam between these two mirrors is also computed by comparing the power reflected by a mirror with the power of the beam after its propagation over L_{FC} .

This simulation is performed using the Matlab based code OSCAR [97]. OSCAR is a Fast Fourier Transform (FFT) code that can in particular propagate electromagnetic fields inside a Fabry-Perot with non-perfect mirror surfaces. In the following simulations, the electromagnetic fields are computed over a square matrix with 512 points that is representing a physical size of 18 cm. The 18 cm size is chosen with respect to the effective mirror diameter (13 cm) in order to properly propagate the various beams inside the Filter Cavity. Furthermore, the mirror maps piston, tilt and focus are subtracted over the beam diameter on the mirror as they can be corrected by moving the mirror.

The results of this simulation for the CC configuration are presented figures 6.9 and 6.11 when applying respectively the VIM06 and the EM03 map on the EMFC. On this simulation the RoC of both the IMFC and EMFC was equal to 550 m.

The results of this simulation for the PC configuration are presented figures 6.10 and 6.12 when applying respectively the VIM06 and the EM03 map on the EMFC. The color-scale is identical for all these figures. As presented in figure 6.1, the main difference between the CC and the PC configuration is that the PC configuration allows to different beam sizes on the IMFC and the EMFC. Therefore, the simulation for the PC configuration are performed using an EMFC RoC equal to 340 m. Indeed, for this RoC, the beam diameter on the IMFC is 1.5 cm which is smaller than what can be achieved for the CC configuration and the beam diameter on the EMFC is 3.2 cm which is larger than what can be achieved for a stable CC configuration.

The table 6.2 summarizes the power lost due to scattering outside the Filter Cavity mirrors when mirrors maps are applied to the EMFC.

Table 6.2 allows to compare the effect of the mirror surface quality for a given configuration

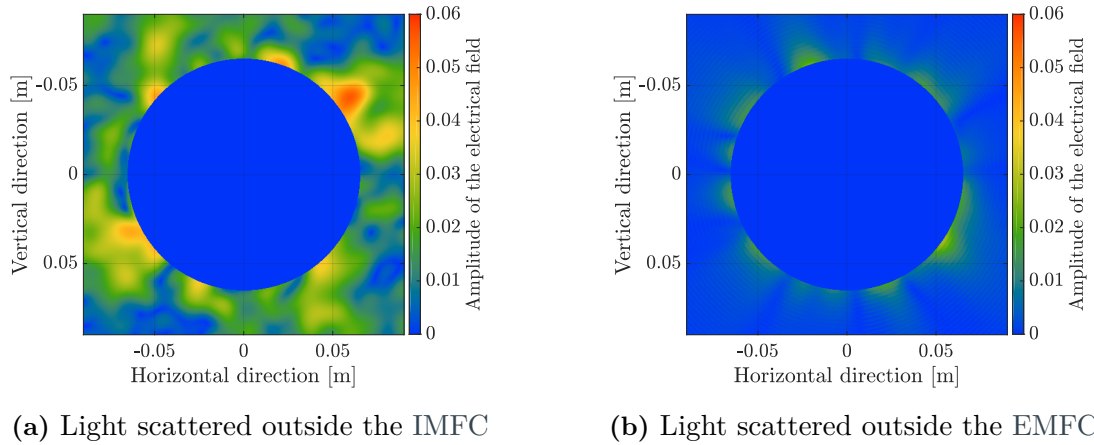


Figure 6.9: Light directly scattered outside Filter Cavity mirrors for the CC configuration where the VIM06 map is applied on the EMFC..

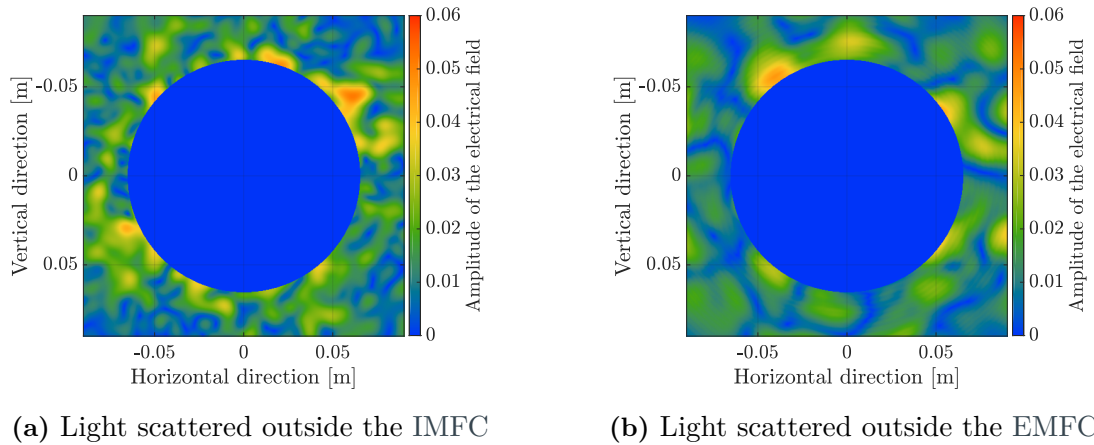


Figure 6.10: Light directly scattered outside Filter Cavity mirrors for the PC configuration where the VIM06 map is applied on the EMFC.

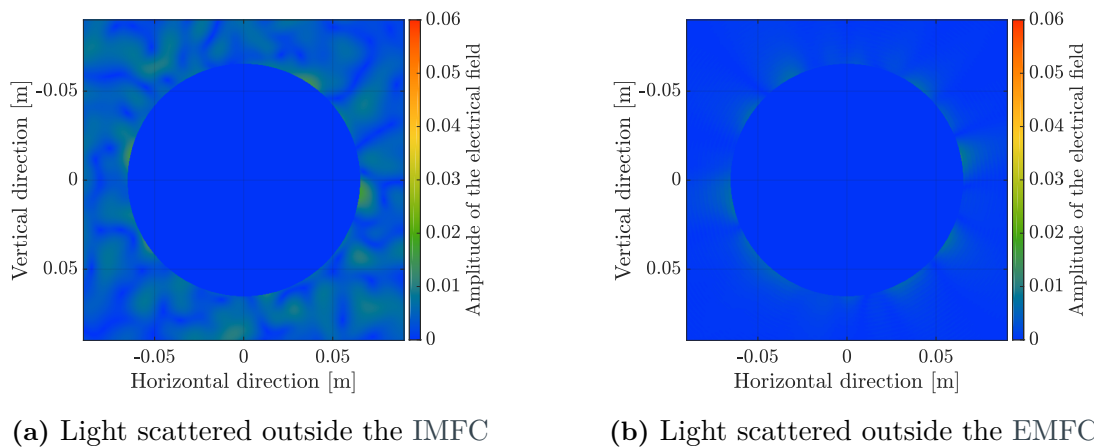


Figure 6.11: Light directly scattered outside Filter Cavity mirrors for the CC configuration where the EM03 map is applied on the EMFC.



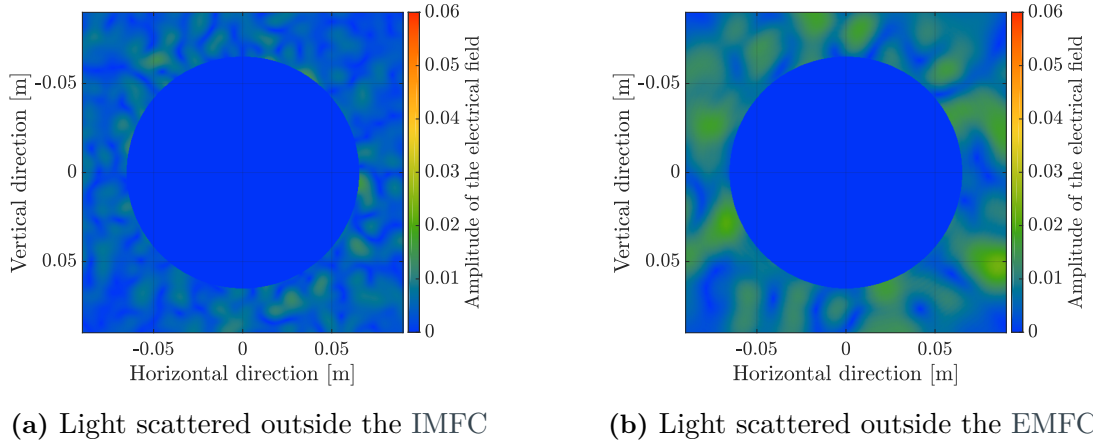


Figure 6.12: Light directly scattered outside Filter Cavity mirrors for the PC configuration where the EM03 map is applied on the EMFC.

Mirror Map	VIM06		EM03	
	CC	PC	CC	PC
Configuration				
Losses at the IMFC [ppm]	6.72	5.14	0.48	0.48
Losses during propagation [ppm]	7.68	9.64	0.57	1.63
Losses at the EMFC [ppm]	0.44	4.53	0.04	1.67
RTL [ppm]	14.85	19.31	1.10	3.79

Table 6.2: Losses due to direct scattering outside mirrors for the CC and PC configurations where the VIM06 and the EM03 maps were applied to the EMFC with $R^{CC} = 550$ m and $R^{PC} = 340$ m. Piston, tilt and focus have been subtracted over the beam diameter on the mirror.

and to compare the effect of the optical configuration on the Filter Cavity losses.

As expected, the Filter Cavity losses increase for lower surface mirror quality. It also appears that the PC configuration is suffering higher losses than the CC configuration. From table 6.2, it can be seen that the Filter Cavity losses difference arises mainly from the losses at the EMFC. This is due to the fact that the beam is larger on the EMFC which further participates to the scattering of the circulating beam outside of the Filter Cavity.

All these simulations were performed with only one map applied to the EMFC. For the CC configuration, as both mirrors are identical, we expect similar results by applying the map either to the IMFC or the EMFC. The total amount of RTL, the one with two realistic mirrors, should therefore be twice the amount of RTL with only one map applied [98].

However, for the PC configuration, as the beam size is different on the IMFC and the EMFC, the total amount of losses is the sum of the losses with map applied to each of these mirrors. Therefore, the single round-trip simulations have been performed a second

time for the PC configuration and applying the mirror maps to the IMFC. This time, the input beam is injected toward the IMFC. The results of these simulations are presented in figures 6.13 and 6.14. The losses are then computed in similar fashion to the previous simulations.

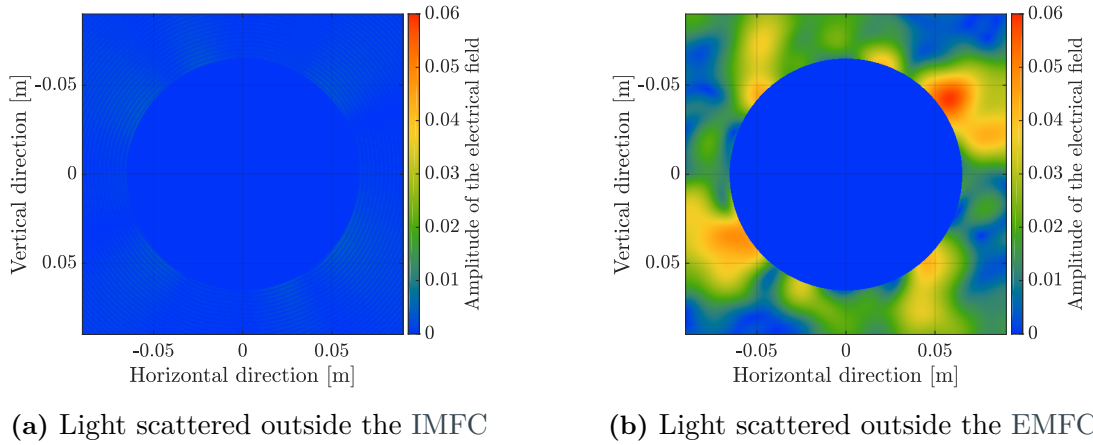


Figure 6.13: Light directly scattered outside Filter Cavity mirrors for the PC configuration where the VIM06 map is applied on the IMFC.

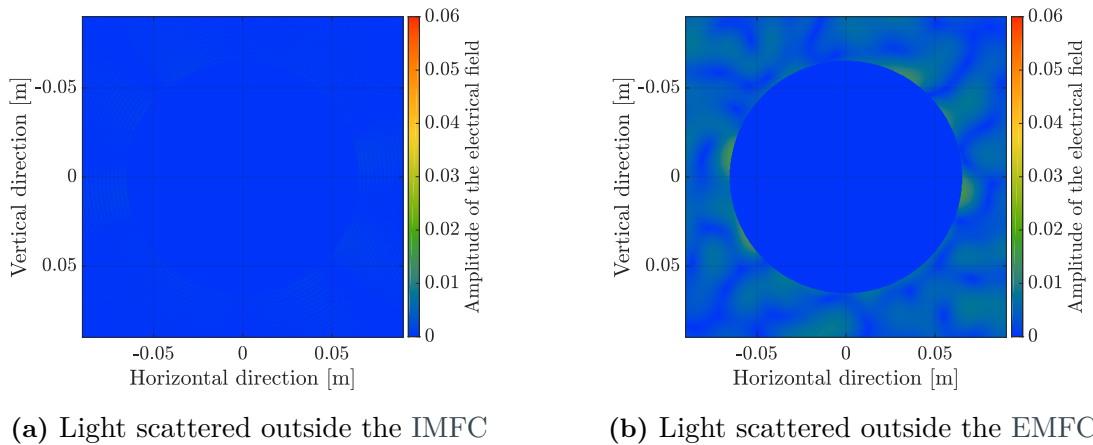


Figure 6.14: Light directly scattered outside Filter Cavity mirrors for the PC configuration where the EM03 map is applied on the IMFC.

The total amount of light scattered outside the Filter Cavity due to the mirror surface defects is presented in table 6.3.

The total RTL in the table 6.3 represents therefore the RTL that can be expected for a cavity with both realistic mirrors.

However, as we will see in the next section, the low frequency spatial defects have also to be taken into account.



Mirror Map	VIM06		EM03	
	CC	PC	CC	PC
Configuration				
Losses with the mirror map applied to the IMFC [ppm]	14.85	26.79	1.10	1.03
Losses with the mirror map applied to the EMFC [ppm]	14.85	19.31	1.10	3.79
RTL [ppm]	29.70	46.10	2.20	4.82

Table 6.3: Losses due to direct scattering outside mirrors for the CC and PC configurations using the VIM06 and the EM03 maps. For the CC configuration, the RTL consist of twice the losses obtained when applying the mirror map on the EMFC. For the PC configuration, the RTL consist of the sum of the losses obtained when applying the mirror map on the EMFC and the one with the map applied to the IMFC.

6.5 The Filter Cavity degeneracy

While the spatial defects with frequency higher than f_{lim} scatter light directly outside the Filter Cavity, the lower frequency spatial defects also contributes to the Filter Cavity losses. As presented in this section, the effect of surface defects with spatial frequency below f_{lim} is to couple an incident beam to the Filter Cavity HOM. The resulting beam might eventually be scattered outside the Filter Cavity.

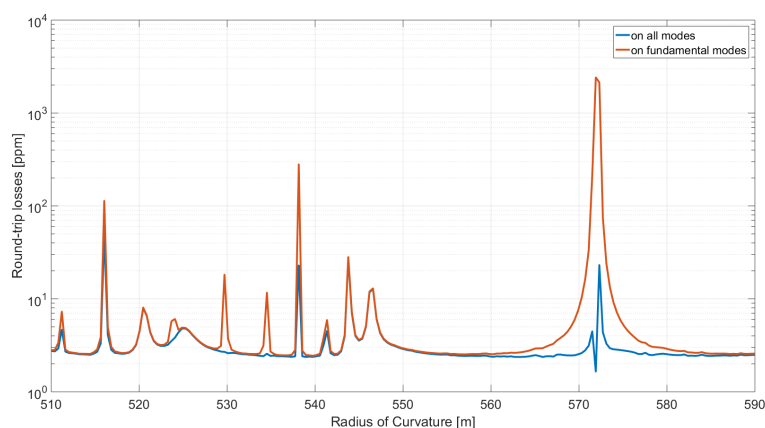
The low-frequency spatial defects of a mirror change the cavity mode shapes [96], therefore spoiling the matching between a beam in the cavity fundamental mode and the cavity with real optics. As represented in figures 6.1a and 6.1b, changing the cavity mirror RoC can lead to important change in the beam size on the mirrors. This means that the beam will sense a larger surface of the mirrors and therefore more surface defects and thus more cavity mode shape changes.

Following the equations 6.11 and 6.12, the RTL for both CC and PC configuration have been computed over a broad range of RoC.

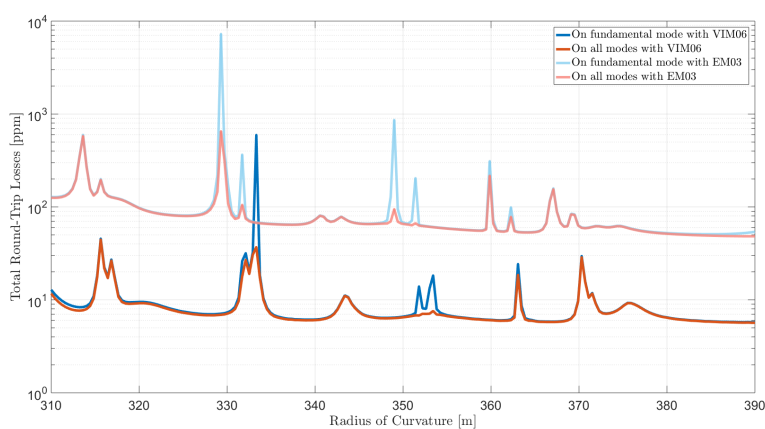
Figure 6.15 shows the evolution of the Filter Cavity RTL as a function of the RoC. It can be seen that the RTL are highly dependent on the RoC. It has therefore been decided to implement an active control of the Filter Cavity mirrors RoC. This can be achieved by installing ring heaters around the Filter Cavity mirrors. They induce a thermal expansion of the mirror therefore allowing to reduce the mirror RoC. The Filter Cavity ring heaters are a scaled down version of the ring heaters used for the Advanced Virgo detector. Their diameter was used to define the Filter Cavity diameter. They can reduced the Filter Cavity mirrors RoC by up to 10 m.

Going back to figure 6.15, the RTL floor level corresponds to the light directly scattered outside the cavity and it is in good agreement with the previous computations.

The discrepancy between RTL on the fundamental mode with the ones on all modes comes from the fact that any fraction of the beam coupled with HOM will not be considered as losses when all modes are taken into account while being losses for the fundamental modes. The RTL floor level being due to direct scattering outside the cavity is therefore



(a) CC configuration with only EM03



(b) PC configuration.

Figure 6.15: Total RTL for CC and PC configuration as a function of the mirror RoC. RTL on all modes refers to equation 6.11 while RTL on fundamental mode refers to equation 6.12.



the same when considering all modes or only the fundamental mode. This shows again that the RTL floor level is higher for the PC configuration than for the CC configuration.

There are certain values of RoC for which this discrepancy is quite important. It corresponds to cavity degeneracy where a HOM will be resonating inside the cavity. For each of these RoC, a modal decomposition of the beam circulating inside the cavity has been performed.

It means that there are RoC for which part of the light circulating inside the cavity will be coupled with cavity HOM. These particular RoC corresponds to the peaks of figures 6.15. As the higher order the HOM, the lower the probability to excite it, a modal decomposition of the HOM on the cavity mode basis has been performed for every peak. Because of the long computation time, only HOM up to order 32 have been taken into account.

As extra losses can be expected, due to absorption or transmission for example, it is needed to roughly add between 5 and 10 ppm of RTL per mirror to the RTL budget [98]. This brings therefore high constraints of PC configuration mirror quality. Another advantage of the CC configuration is that we can order many identical substrates and keep the most efficient pairs as the RoC is the same for the IMFC and the EMFC.

Therefore, the Filter Cavity optical configuration is chosen to be the CC configuration, namely two curved mirrors with identical RoC.

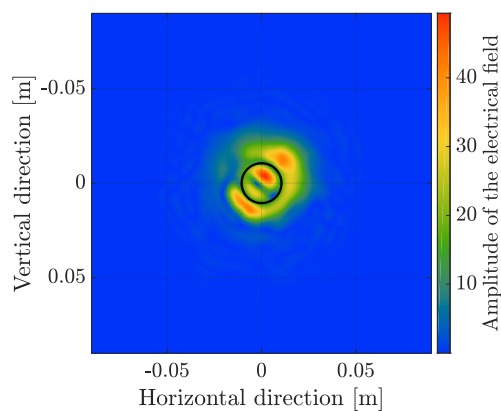
It is of particular interest to have studied an Advanced-Virgo like quality mirror because it is the state of the art for mirror polishing. The study of such mirror map allows to clearly see HOM that are hidden by lower quality map such as VIM06. Therefore the modal decomposition of each cavity degeneracy was performed with the Advanced-Virgo like quality map (EM03).

Figure 6.16a shows the shape of the circulating beam inside a CC cavity with $R = 571.9$ m where the power in the fundamental mode is subtracted in order to better see the HOM shape. One can notice that the beam size is bigger than the fundamental mode one represented by the black circle. It means that HOM sense a larger part of the mirror surface. But as the RoC corresponds to the RoC only over the fundamental mode beam size, it means that a HOM will sense a different RoC. And the higher the mode the stronger the effect on the RoC. Another point is that since the mirror surface quality is different between the 2 maps, different effective RoC appear for every degeneracy. It explains why some peaks seem to be shifted when comparing the VIM06 and the EM03 .

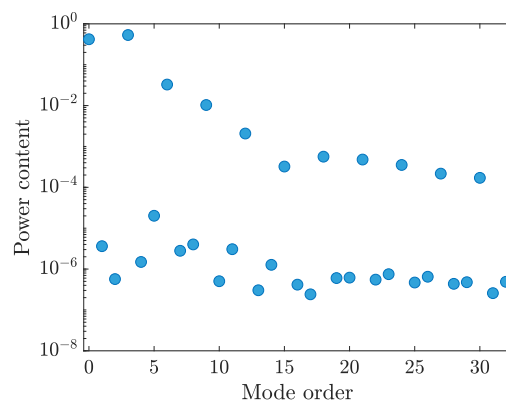
Figure 6.16b shows the modal decomposition of this circulating beam. The beam appears to be mainly in the fundamental mode with the mode 3 and its harmonics resonant as well. It can be deduced that the peak at $R = 571.9$ m is due to the mode 3 resonating inside the Filter Cavity.

All the peaks, each representing the resonance of a particular HOM, have been also decomposed in a similar manner as in figure 6.17. As we want to have Filter Cavity RTL as low as possible, the Filter Cavity mirror RoC have to be chosen in order to avoid Filter Cavity degeneracy. Taking into account that the higher the mode order, the lower its resonance probability, it is possible to define a safe ranges of RoC.

An appealing region is the one between $R = 550$ m and $R = 570$ m, where only orders



(a) Circulating beam shape with the fundamental mode subtracted. The black circle shows the beam size if the Filter Cavity mirrors were perfect.



(b) Modal decomposition over 32 modes.

Figure 6.16: Shape of the circulating beam and its modal decomposition for a CC configuration with $R = 571.9$ m.



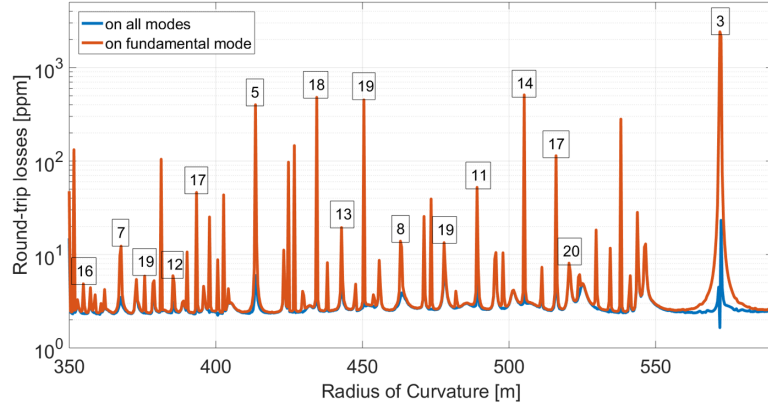


Figure 6.17: Modal expansion of beam resonating inside the Filter Cavity for the CC configuration. The numbers indicate the dominant mode (below the order 32) for each peak.

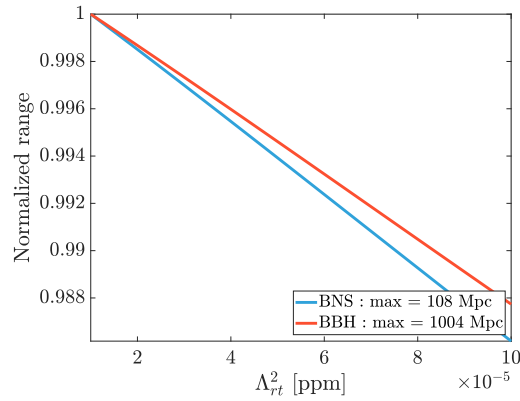


Figure 6.18: Normalized BNS and BBH ranges as a function of the Filter Cavity RTL for the O4 low scenario presented table 5.6

above 17 resonate while having a long enough range to be compliant with usual polishing. Furthermore, the use of Ring Heater could decrease the Filter Cavity mirrors RoC allowing to avoid Filter Cavity degeneracy with a precision at the order of 1 m which is roughly the RoC range where a Filter Cavity degeneracy occurs. Thus this range can allow to not have too stringent constraints on polishing while having total Filter Cavity RTL below 3 ppm.

The study of Advanced-Virgo like quality mirrors was useful to know what HOM can be expected to be resonant inside the Filter Cavity for any given mirror RoC. But such quality is not mandatory to reach the O4 Quantum Noise reduction. As seen in figure 6.18, going from 20 ppm (Advanced Virgo-like quality) to 60 ppm (Initial Virgo-like quality), one loses 2.5% of the BNS range for the O4 low scenario. It means that a good starting point for the mirror surface quality could be to use Initial Virgo-like quality as the delay for Advanced Virgo-like quality could be too long to perform the Filter Cavity commissioning for O4.

Finally, the table 6.4 present the expected Filter Cavity RTL as a function of the mirror surface quality.

Mirror Map	VIM06	EM03
Light scattered outside the Filter Cavity [ppm]	59.4	4.4
Mirror substrate absorption [ppm]	<20	<20
EMFC power transmissivity [ppm]	5	5
Total RTL	74.4	29.4

Table 6.4: Total RTL of the Filter Cavity with the CC configuration. This value is the sum of all sources of RTL

6.6 The etalon effect

Until now, we have studied the Filter Cavity as any Fabry-Perot cavity with the goal of minimizing the RTL and mode-mismatch to be compliant with some scenarii. But this cavity have the particular objective to rotate the Frequency-Independent Squeezing ellipse to generate Advanced Virgo Frequency-Dependent Squeezed states. As shown in the previous chapter, it means that the Filter Cavity finesse should be $F = 10300$.

The finesse of a cavity is directly linked to its IMFC transmissivity t_{in}^2 and RTL with

$$F = \frac{2\pi}{t_{in}^2 + \Lambda_{RTL}^2} \quad (6.13)$$

With $\Lambda_{RTL}^2 = 40$ ppm we should therefore have $t_{in}^2 = 610$ ppm.

During the polishing, we can expect to have 1% error on t_{in}^2 and thus in finesse. This means that the squeezing ellipse will not be rotated exactly at the wanted frequency.

To compensate such effect, one can use the so-called etalon effect of the IMFC. The etalon effect provides indeed a mean to tune the IMFC reflectivity.

If the two surfaces of the IMFC are parallels, the IMFC forms therefore a Fabry-Perot cavity where the input mirror is defined by the anti-reflective surface of the IMFC, the end mirror is defined by the highly-reflective surface of the IMFC and the cavity length is defined by the IMFC thickness. By tilting the IMFC, it is possible to vary the optical path of a beam incident on the IMFC. The reflectivity of a Fabry-Perot cavity has been defined in equation 1.18 which showed that it depends on the optical path inside the cavity.

This makes the IMFC reflectivity vary between r_{min} and r_{max} defined as :

$$r_{min} = \frac{r_{HR} - r_{AR}}{1 - r_{AR}r_{HR}} \quad (6.14)$$

$$r_{max} = \frac{r_{HR} + r_{AR}}{1 + r_{AR}r_{HR}} \quad (6.15)$$



where $r_{HR} = \sqrt{1 - t_{in}^2} = 0.9996$ and $r_{AR} = 0.01$ are respectively the reflectivity of the anti-reflective and highly-reflective surfaces of the IMFC. The etalon effect can therefore provide up to 2% shift of the cavity finesse by controlling the IMFC equivalent reflectivity.

These two effects are presented in figure 6.19 which shows the BNS range as a function of the IMFC transmissivity or equivalently the Filter Cavity finesse.

The error on IMFC transmissivity spoils less than 1% of the BNS range and therefore there is no need to use the etalon effect. In order to avoid possible interactions between the light incident on the Filter Cavity and the light on-going several reflections inside the IMFC, the surface of this mirror outside the Filter Cavity is slightly tilted. This corresponds to the addition of a wedge characterized by this tilt angle.

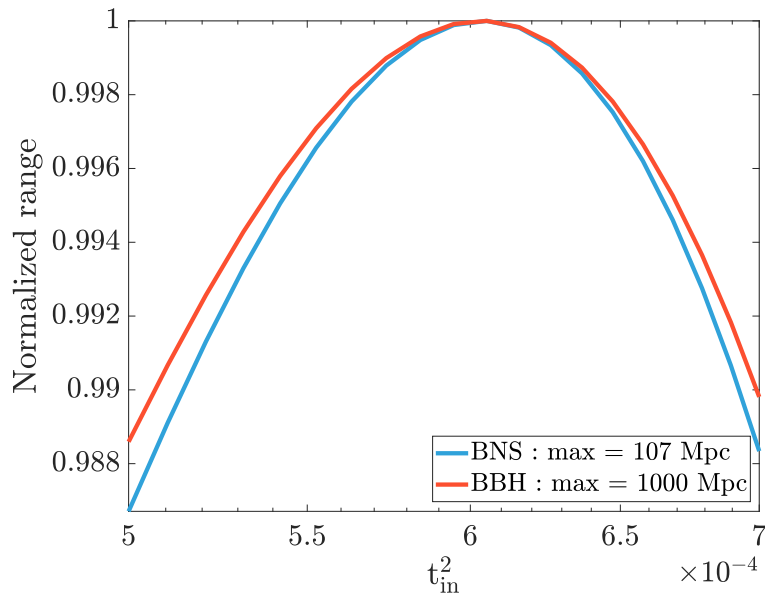


Figure 6.19: Effect of variation of t_{IM}^2 and therefore the finesse on the BNS and BBH ranges normalized with respect to the case without losses for the O4 low scenario presented in table 5.6

6.7 Conclusion and Mirror specifications

In this chapter, the optical configuration of the Filter Cavity and the requirements on the mirror parameters have been studied. These parameters were defined to be compliant with the goal of Quantum Noise reduction foreseen for Advanced Virgo O4 run. Finally, table 6.5 summarizes all the foreseen parameters of the IMFC and the EMFC.

The main conclusions are that the Filter Cavity will be a Fabry-Perot cavity where both mirrors have a RoC of 558 m. The RoC errors could lead to an unacceptable level of RTL. Therefore, the use of Ring Heater is foreseen which fixed the diameter and thickness of the mirrors.

The infra-red transmission of the IMFC is also of particular importance as it will define the Filter Cavity finesse and therefore the frequency of rotation of the squeezing ellipse.

The flatness and roughness of the mirror surfaces have been defined over an area of 50 mm in order to avoid point defects.

However, with usual uncertainty of the IMFC transmissivity, there is no need to use particular control of the IMFC transmissivity. It means that the geometry of the IMFC and the EMFC can be identical : a curved surface inside the Filter Cavity and a plane surface outside the Filter Cavity. The green transmissivity has been chosen so to have enough light to control the Filter Cavity [98].¹

The wedge value is derived in next chapter based on the Filter Cavity implementation inside the Virgo infrastructure.

Because of the IMFC wedge, there are spurious beams that are generated due to the multiple reflections on an incident beam inside the IMFC (more details in the next chapter). These spurious beams might be a source of back-scattering that affect the squeezing performances. In order to avoid too large scattering, the quality of the mirror surface facing outside the Filter Cavity can not be too bad. A good choice could be to have 2 nm roughness for these surfaces as it will not be limiting while not bringing too much constraints on the polishing. Furthermore, in order to decrease the power in the spurious beam, the surface outside of the Filter Cavity of the mirrors have anti-reflective coatings.

As it is also foreseen to use a pick-off of the green light used to generate Frequency-Independent Squeezing to control the Filter Cavity, the Filter Cavity mirrors transmissivity and reflectivity for green have been chosen so to have enough power to perform this control.

The Filter Cavity mirrors are already polished and their coatings should start soon. As the Virgo input power might change a lot for the O5 run, the squeezing rotation angle will change as well. Depending on the input power change, it might be possible to use the same Filter Cavity mirrors for both O4 and O5 runs.

¹The need for this green transmissivity is introduced in the next chapter.



Parameter	IMFC	EMFC
Material	Suprasil	Suprasil
Diameter	15 cm	15 cm
Thickness	9 cm	9 cm
Wedge	220 urad	220 urad
Surface 1 - Face inside of the cavity		
RoC	558 m	558 m
Flatness (over 50 mm)	0.5 nm rms	0.5 nm rms
Roughness (over 50 mm)	<0.1 nm rms	
Transmission - 1064 nm	610 ppm	5 ppm
Transmission - 532 nm	3%	3%
Surface 2 - Face outside of the cavity		
RoC	>100 km	>100 km
Flatness (over 50 mm)	6 nm rms	6 nm rms
Roughness (over 50 mm)	0.2 nm rms	0.2 nm rms
Reflexion - 1064 nm	< 200 ppm	<200 ppm
Reflexion - 532 nm	< 500 ppm	<500 ppm

Table 6.5: Filter Cavity mirrors parameters

7

Frequency dependent squeezing for Advanced Virgo+

Contents

7.1	Introduction	175
7.2	The integration overview	176
7.2.1	The Filter Cavity location	176
7.2.2	The benches overview	177
7.2.3	The optical paths	180
7.3	The matching telescopes	185
7.3.1	The infrastructure and beam parameters	185
7.3.2	The matching telescopes design	189
7.3.3	The matching telescope tolerances	195
7.4	Conclusion	196

7.1 Introduction

The two previous chapters have presented the optical design of the Advanced Virgo+ Filter Cavity. This chapter presents how the frequency dependent squeezing can be injected in the Virgo detector. In particular, the integration of the Filter Cavity and its mode-matching telescope is presented.



7.2 The integration overview

As described in the previous chapter, the Advanced Virgo+ Filter Cavity will be 285 m long. This places constraints on its integration within the Virgo infrastructure. This section presents where the Filter Cavity will be installed and how its location will affect the design of the optical system required for the injection of the squeezed states inside the Filter Cavity and the interferometer.

7.2.1 The Filter Cavity location

As a reminder, figure 7.1 shows a simplified layout of the Virgo vacuum system. The inset which contains the central interferometer vacuum chambers is so called the central building.

It can be recalled that the squeezer source is installed close to the detection tower SDB1. More precisely, the squeezer is installed on the right of the SDB1 labeled *detection tower* in figure 7.1.

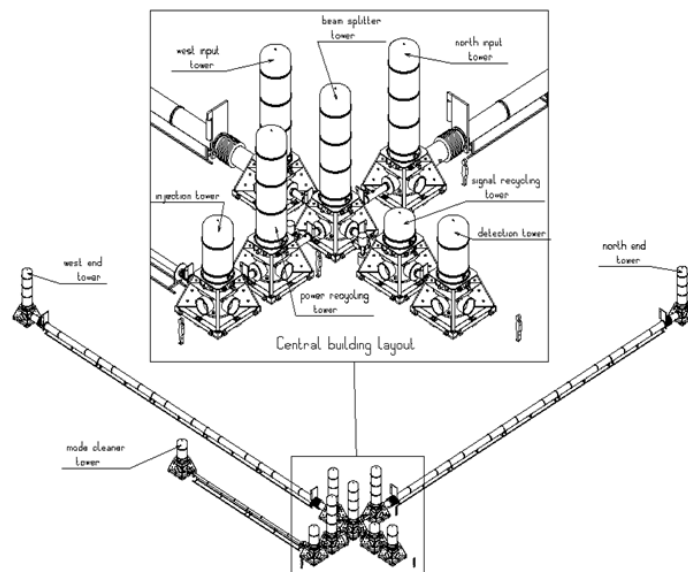


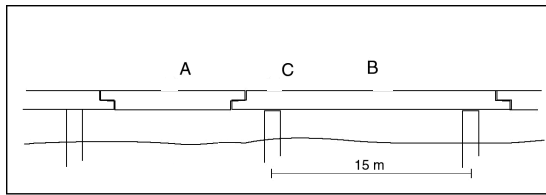
Figure 7.1: Simplified layout of the Virgo vacuum system. Credit : B. Lieunard

The Filter Cavity could be installed along either the north or the west arm in order to benefit from the existing infrastructure. The west arm tunnel seems to be the most convenient location to install the Filter Cavity as it could allow to go in straight line from the squeezer to the Filter Cavity. However, due to the squeezer location, the Filter Cavity would not be inside the west arm tunnel but rather be located close to it. It means that in order to place the Filter Cavity inside the west arm tunnel, at least an additional optical bench located inside the central building would be needed to shift the optical path. Therefore, installing the Filter Cavity inside the west arm tunnel does not bring any advantage for the optical path. The Filter Cavity will be installed along the north tunnel as it is closer to the squeezer and does not require to add vacuum chambers and vacuum pipes inside the central building.

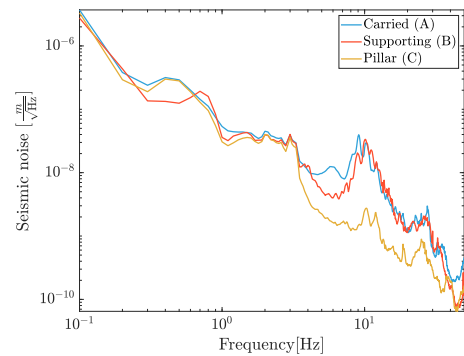
The Virgo north arm is composed of three main structures as shown in figure 7.2a from [99]. The portion labeled *A* corresponds to a short slab of concrete so called carried beam. The portion labeled *B* corresponds to a longer concrete slab named the load-bearing beam. Both of these concrete slabs lay on 18 m deep pillars located every 15 m and labeled *C* in the figure. It means that the coupling between the ground seismic motions and any optics installed inside the arm depends on which arm portion they are installed. Therefore, a seismic survey has been performed on these three different portions on the arm.

The resulting ground motion is presented in figure 7.2b. One can see that both the carried beam (*A*) and the load-bearing beam (*B*) exhibit resonances around 10 Hz. On the other hand, these resonances are reduced above the pillar (*C*).

Following this measurement, it has been decided to install the Filter Cavity input and end mirror on such pillars in order to avoid increased seismic motions of the Filter Cavity mirrors. A 300 m scale length is achieved by installing the Filter Cavity input and end mirror respectively 51.7 m and 336.7 m away from the Advanced Virgo+ beam-splitter leading to the 285 m long Filter Cavity.



(a) Side view sketch of a portion of the 3km long Virgo Tunnel from [99].



(b) Seismic motions of the two concrete slabs and the supporting pillar inside Virgo north arm.

Figure 7.2: Layout of the Virgo tunnel and its associated seismic noise

7.2.2 The benches overview

Because the Filter Cavity position is fixed inside the north arm and the squeezer is located close to the detection tower SDB1, several new optical benches are required to inject the squeezed vacuum states into the Filter Cavity and back to the interferometer.

Also, all the optics that the squeezed beam encounters are placed on suspended optical benches inside vacuum chambers in order to reduce dust contamination as well as acoustic and seismic motions coupling to optical components. This should decrease the effect of scattered light from the squeezing system into the interferometer. This back-scattered light was found out to be particularly sensitive to the squeezing alignment during the O3 run as presented in section 4.2.

These new optical benches are represented in figure 7.3 where one can see that the squeezing system drastically changes from the O3 configuration. Indeed, the squeezed vacuum

states are generated in the in-air External SQueuezing Bench 1 (ESQB1). Then, they propagate on two in-vacuum benches Suspended sQueuezing Bench 1 (SQB1), Suspended sQueuezing Bench 2 (SQB2) before reaching the IMFC and EMFC. In addition, there are also two in-air benches called the External SQueuezing Bench 2 (ESQB2) and the End Mirror Filter Cavity Bench (EMFCB) used to extract control signals. In the following, the functions of these benches are described starting from the ESQB1 hosting the squeezer to the EMFCB located after the Filter Cavity end mirror.

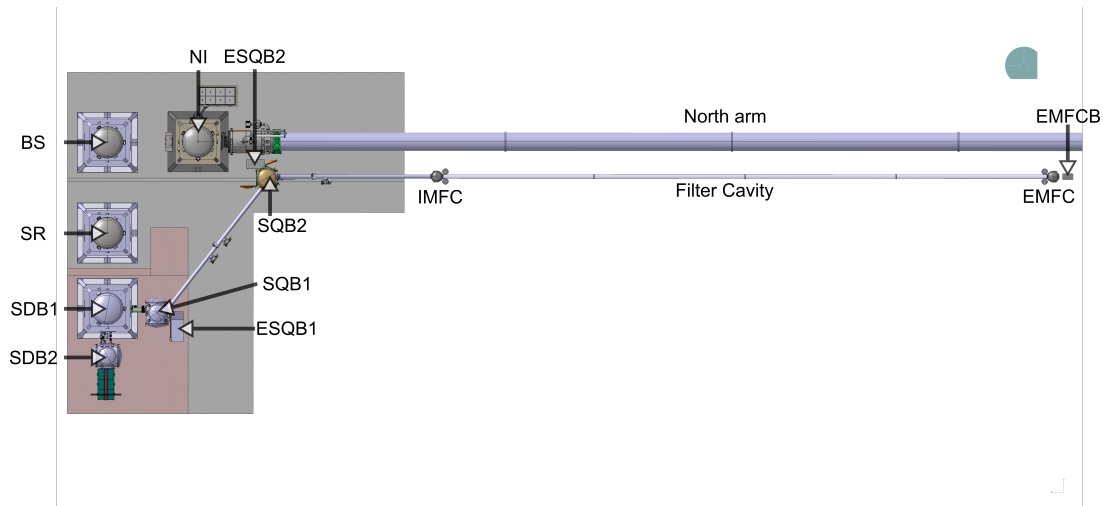


Figure 7.3: CAD drawing of the frequency-dependent squeezing system. Credit : B. Lieunard

The ESQB1

The ESQB1 is an in-air optical bench located nearby the detections towers SDB1 and SDB2. One of the main function of this optical bench is to generate the frequency-independent squeezed beam as well as the required control beams that consist of a green beam produced by the squeezer SHG and a new infra-red laser source (the so-called sub-carrier laser).

As described later in section 7.2.3, the green beam is used for the coarse locking and angular control of the Filter Cavity as well as the relative alignment control of the suspended benches. The sub-carrier field is used for the angular and longitudinal control of the Filter Cavity as well as the alignment and mode-matching of the squeezed beam with respect to the interferometer.

This bench hosts also the PLL to frequency lock the squeezer to the Advanced Virgo+ main laser, the injection Faraday isolator, a diagnostic homodyne detector, photo-detectors sensing the green beam back-reflected from the Filter Cavity and matching and steering optics.

In order to reduce the acoustic noise that can couple to optical components motions, the ESQB1 is installed inside an acoustic enclosure. A similar acoustic enclosure was used during the O3 run to isolate the ESQB which provided a good damping of the high frequency acoustic noise.

The SQB1

The SQB1 is an in-vacuum suspended optical bench located between the ESQB1 and the SDB1. Its main function is to recombine the green control beam with the squeezed beam and IR control beams as well as to inject and mode-match the frequency-dependent squeezing back-reflected from the Filter Cavity with the interferometer. It also hosts one of the two mirrors of the mode-matching telescope between the frequency-independent squeezed beam and the Filter Cavity, the Faraday isolators chain, photo-detectors for the SQB1 alignment and cameras looking at the interferometer spurious beam for the rough alignment of the squeezed beam with the interferometer (as performed during the O3 run). The SQB1 vacuum chamber is represented in figure 7.4.

Both ESQB1 and SQB1 are installed inside a clean room to avoid dust contamination during commissioning activities.

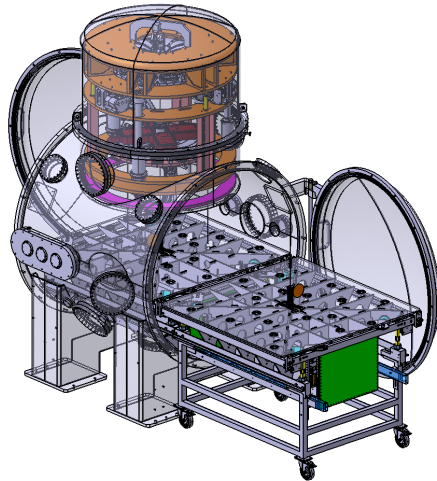


Figure 7.4: CAD scheme of the SQB1 vacuum chamber. Credit : B. Lieunard

The SQB2 and ESQB2

The SQB2 is an in-vacuum suspended optical bench located close to the NI tower based on a similar design to the SQB1. Its main function is to inject and mode-match the frequency-independent squeezed beam (and co-propagating control beams) into the Filter Cavity. Another function is also to extract pick-offs of the control beams. For instance, the green pick-off beam is sent to photo-detector on the SQB2 to control the SQB2 alignment while the infra-red pick-off beam is sent to the ESQB2.

The ESQB2 is an in-air optical bench nearby the SQB2. Its main function is to provide the infra-red photo-detectors required for the longitudinal and alignment control of the Filter Cavity. Its hosting vacuum chamber is represented in figure 7.5.

The IMFC, EMFC and EMFCB

The in-vacuum IMFC and EMFC micro towers are hosting respectively the Filter Cavity input and end mirrors. Both mirrors are suspended using an inverted pendulum. Two



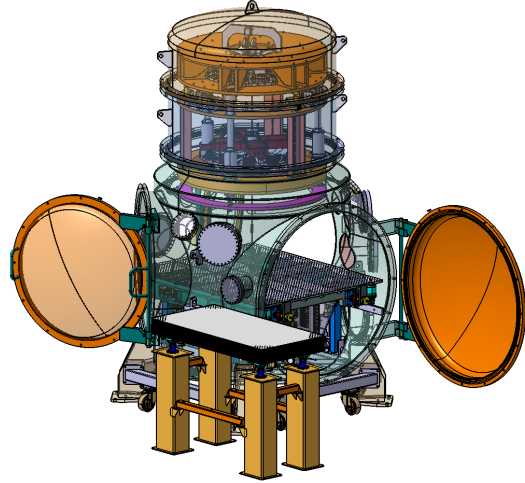


Figure 7.5: CAD scheme of the SQB2 vacuum chamber. Credit : B. Lieunard

windows are mounted on each micro-towers with adjacent optical benches hosting the mirror local controls.

The in-air EMFCB is located in transmission of the EMFC. Its main function is to provide the Filter Cavity transmission signals required to lock and control the Filter Cavity. Figure 7.6 shows the vacuum chamber hosting the EMFC. On its left the smaller EMFCB is also represented and the two optical benches hosting the mirror local controls are also visible.



Figure 7.6: CAD drawing of the Filter Cavity mirrors suspension and picture of the micro-tower hosting them. Credit : A. Bertolini

7.2.3 The optical paths

With the additions of several suspended optical benches and the Filter Cavity itself, the control and relative alignments of these new components is required. It means that in

addition to the new suspended benches, new optical beams are also required. These optical paths are represented on the simplified optical layout in figure 7.7.

The squeezed beam

For the O4 run, it is planned to use the in-air AEI squeezer [40] as for the O3 run. The squeezed beam generated by the squeezer OPO on the SQB1 is represented by the dashed red line in figure 7.7. The squeezer Faraday isolator that was located inside the squeezer itself is changed to a lower losses one based on the EGO design [77] located outside the squeezer. The squeezed beam then propagates toward the Filter Cavity before its injection into the Advanced Virgo+ main interferometer. The mode-matching between the squeezed beam and the Filter Cavity is performed using a two stage mode-matching telescope.

First, the *MM IR* mode-matching telescope ensure that no clipping losses occur at the SQB1 Faraday isolator. Then the two curved mirrors M_4 on the SQB1 and M_2 on the SQB2 form a mode-matching telescope used to match this beam to the Filter Cavity. Finally, using the SQB1 Faraday isolators, this squeezed beam is sent to a mode-matching telescope *MM ITF* that insures that the squeezed beam has the proper geometrical parameters with respect to the interferometer. Finally, the squeezed beam is sent into the main interferometer. In order to decrease optical losses, the squeezed beam is only interacting with super-polished reflective optics (and the low losses Faraday isolators [77]).

It is also possible to rotate a half-waveplate located between the two Faraday isolators (FI1 and FI2) of the SQB1 in order to send the frequency-dependent squeezing to a characterization homodyne detector.

The coherent control beam

In a similar fashion of the O3 run, the coherent control beam is generated inside the squeezer and phase-locked to the squeezer main laser using the PLL int. However, as the Advanced Virgo+ OMC changes from two monolithic cavities with finesse of 121 to a single monolithic cavity with finesse 1000, the 7 MHz sidebands used for the coherent control will not be transmitted by the OMC. It is therefore planned to decrease the sidebands frequency from 7 MHz to 4 MHz. Another solution could have been to use the 7 MHz sidebands and extracting the error signals from the OMC reflection on B1p.

This beam co-propagates with the squeezed beam up to the Advanced Virgo+ readout photodiodes B1 where the coherent control error signal is extracted.



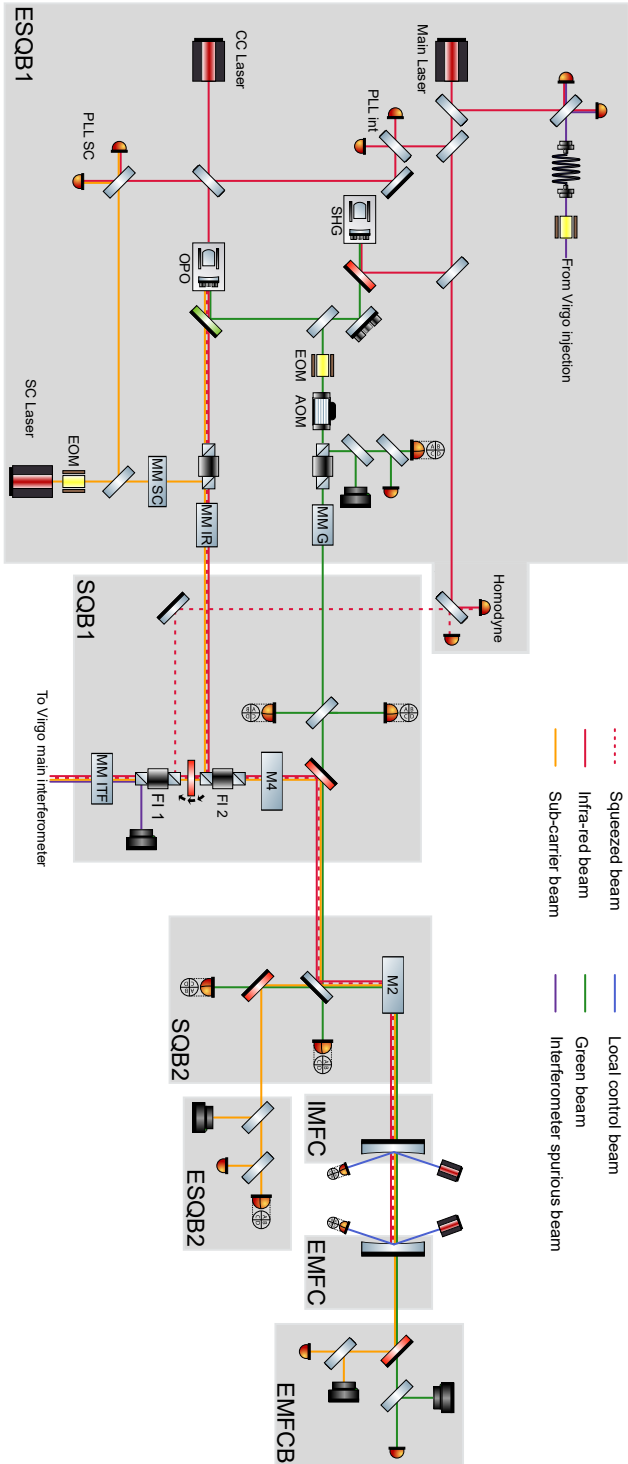


Figure 7.7: Simplified optical layout of all beams required for the frequency-dependent squeezing injection in Advanced Virgo+ interferometer. *MM* holds for mode-matching telescope with steering optics and *M_i* together with *M₂* are the two curved optics forming the Filter Cavity mode-matching telescope. No steering optics nor the squeezer optics (at the exception of the SHG and OPO) are represented on this layout and the cameras and quadrant-photodiodes represent both the far field and near field detectors. The laser beams labeled *IR beam* corresponds to the infra-red beam emitted by the squeezer main laser. A first pick-off of this beam are used to generate the green beam in the SHG. The other pick-off of this infra-red beam are used as local oscillator for the three PLL

The local oscillator beam

The local oscillator beam used for the characterization homodyne detector is, again in a similar fashion of the O3 configuration, a pick-off of the squeezer main laser. Using matching optics and a refractive telescope not represented in figure 7.7, this beam is mode-matched to the frequency-dependent squeezed beam before being combined on the homodyne detector. Despite the higher optical losses of a refractive telescope compared to a reflective telescope, this choice was made to save space on the crowded ESQB1 and because optical losses will not affect drastically the performances of the homodyne detector.

The green beam

A pick-off of the green beam generated by the squeezer SHG is propagated outside the squeezer in order to provide several control signals.

First, as in the TAMA prototype [100], this green beam can be used to control and lock the Filter Cavity. On the ESQB1, the green beam passes through an EOM in order to generate the sidebands required to lock the Filter Cavity using the PDH technique [101]. Furthermore, an Acousto-Optic Modulator (AOM) is used in order to control the Filter Cavity detuning. The green beam is mode-matched to the squeezed beam using the refractive mode-matching telescope $MM\ G$. The green beam is overlapped with the squeezed beam on a dichroic mirror located on the SQB1 using steering optics not represented in the figure.

On the EMFCB, the green transmission of the Filter Cavity is also monitored to extract a trigger for the PDH locking technique.

As this green beam propagates on the suspended SQB1 and SQB2 and because there is no constraint of low optical losses for the green beam, it is possible to extract pick-off of this beam on both SQB1 and SQB2. These pick-off beams can be used to control the relative alignment between these benches.

First, the relative alignment between the ESQB1 and the SQB1 is controlled using a pick-off of the green beam sensed by a pair of quadrant photodiodes. Then, the relative alignment of the SQB1 and SQB2 is controlled using a pair of quadrant photodiodes sensing a pick-off of the green beam incident on the SQB2. The two pairs of quadrants located on the SQB1 and SQB2 that are looking at the green beam reflected by the Filter Cavity are used for a finer alignment of the SQB1 and SQB2.

Finally, the PDH error signal to lock the Filter Cavity is extracted from the green beam reflected by the Filter Cavity with the green Faraday isolator located on the ESQB1.

The sub-carrier beam

The sub-carrier (SC) beam generated on the ESQB1 provides another mean of controlling the Filter Cavity.

This infra-red beam is generated by a low-noise Nd:YAG laser source installed on the ESQB1 and labeled *SC laser* in the figure 7.7. The frequency of this laser is stabilized on



the squeezer main laser frequency using the PLL SC.

This SC laser beam is then mode-matched to the OPO using the *MM SC* refractive telescope. It then propagates to the OPO which means that the squeezed beam geometrical properties are imprinted on the SC beam. Therefore, it can be used as a marker of alignment and mode-matching of the squeezed beam with the Filter Cavity. This beam co-propagates with the squeezed beam up to the SQB2 where a pick-off of this beam is sent to the ESQB2 where a photodiode, quadrants photodiodes and cameras are available to control the Filter Cavity. In order to perform the PDH locking of the Filter Cavity [101], this SC beam is passing through an EOM to imprint sidebands used for this control.

The local control beams

There are two in-air optical benches located nearby both IMFC and EMFC that are hosting a laser source on one side of the micro-tower and position sensor detectors on the other side. This setup can be used to control the position of the mirror with respect to the ground.

The phase control beams

In a similar fashion to the O3 configuration (see section 3.4.1), two PLL are used : one to stabilize the frequency of the squeezer main laser with the Virgo main laser and another one to stabilize the frequency of the squeezer main laser and the squeezer CC laser with the wanted offset to perform the coherent control. As already described, the frequency offset imprinted on the CC laser might be reduced from 7 MHz as in the O3 run to 4 MHz for the O4 run. This reduction of the sidebands frequency allows the sideband to be transmitted by the OMC. The other solution consisting to use the signal in reflection of the OMC.

An additional PLL is also installed on the ESQB1 to stabilize the SC laser frequency with respect to the squeezer main laser one.

Comparison of green beam and sub-carrier locking

Both the green beam and the infra-red SC beam propagate into the Filter Cavity. They can therefore both be used to control the Filter Cavity. This multi-wavelength strategy is indeed useful as each beam brings different advantages.

On one hand, the Filter Cavity green finesse is much lower than the infrared one meaning that it is easier to lock the Filter Cavity using the green beam. On the other hand, it requires to well overlap the green beam with the squeezed beam. This overlap appeared to be difficult to achieve in the 300 m long Filter Cavity of the TAMA experiment [100].

As derived in appendix 7.4, the thermal fluctuations of the IMFC and the EMFC can induce phase fluctuations between two beams at different wavelengths. It means that if the Filter Cavity is locked using the green beam, the squeezed beam will be affected by phase fluctuations. For the squeezed beam, these phase fluctuations correspond effectively to fluctuations of the Filter Cavity length which is a source of degradation for the squeezing performances (for instance see section 5.3.3).

Using the mirror parameters of the TAMA Filter Cavity [100] and an estimated temperature fluctuation of 30 mK¹, the equivalent length fluctuations as a function of the temperature is estimated to be of the order of 0.17pm. This is below the the length fluctuations requirement for the O4 and O5 run (3pm). It means that the thermal fluctuations are not problematic to lock the Filter Cavity with the green beam.

On the other hand, the infra-red SC beam sees a Filter Cavity with a really high finesse. It implies that the Filter Cavity lock using solely the SC beam is difficult to achieve. However, the SC beam is resonating inside the OPO and therefore has the same geometrical properties as the squeezed beam. Therefore, the interaction of the SC beam with the Filter Cavity provides directly the behavior of the squeezed beam with the Filter Cavity.

Finally, an interesting solution to control the Filter Cavity is to first lock the Filter Cavity with the green beam and in a second step lock the Filter Cavity using the SC beam. This multi-wavelength locking technique benefits indeed from the advantages of using the green and the SC beams.

7.3 The matching telescopes

The previous section has presented the Filter Cavity location as well as all the optical benches required to inject frequency-dependent squeezing into the interferometer. This section discusses the parameters of the mode-matching telescope between the Filter Cavity and the interferometer. The design of this telescope is driven by the goal of 1% of mode-mismatch between the squeezed beam and the Filter Cavity and between the squeezed beam and the interferometer.

7.3.1 The infrastructure and beam parameters

The locations of all the required optical benches and the Filter Cavity has been chosen following infrastructural considerations. Here, the impact of the benches location on the geometrical properties of the various beam is discussed.

The benches location and beam sizes

Figure 7.8 shows a view of the vacuum system required for the frequency-dependent squeezing injection up to the Filter Cavity vacuum pipe.

With the location of the IMFC being defined by the north arm seismic properties and the SQB1 location being chosen for its proximity with the SDB1 flange, it remains to define the location of the SQB2.

As can be seen in figure 7.8, the vacuum pipe connecting the SQB1 and the SQB2 has to go through the detection lab walls. Since this wall is made in concrete, heavy infrastructural work is needed to pierce it. The SQB2 location has been chosen in order to minimize this infrastructural work which allows in return to reduce the interferometer downtime.

¹This temperature fluctuation correspond to the main interferometer vacuum chambers over one week.



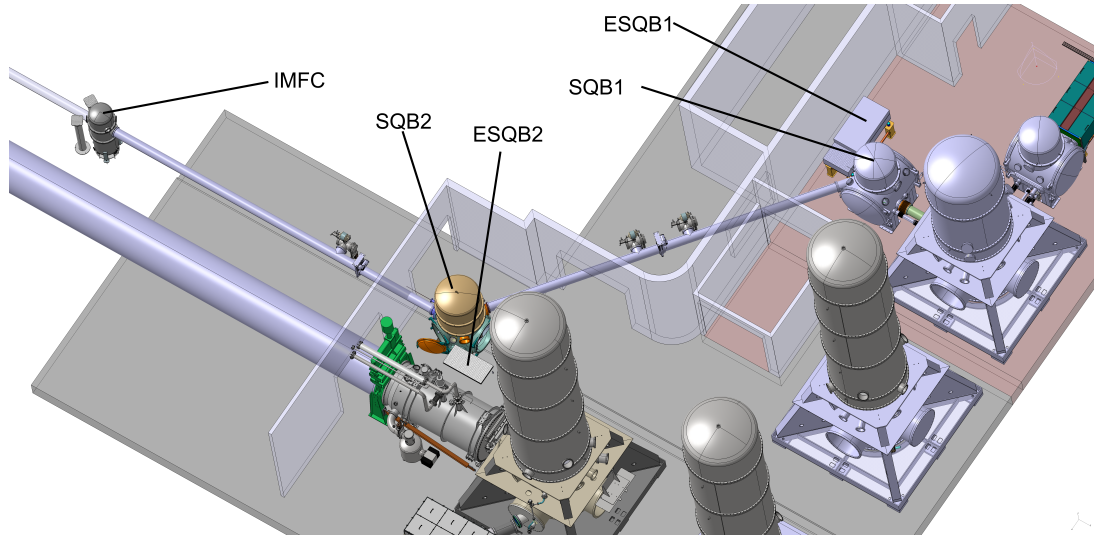


Figure 7.8: CAD view of central building area surrounding the ESQB1 and vacuum chambers hosting the SQB1, the SQB2 with surrounding walls. Credit : B. Lieunard

This infrastructural constraints translate into constraints on the squeezed beam optical path as illustrated in figure 7.9. The IMFC and the SQB2 are separated by a 41.26 m long vacuum pipe whereas the SQB2 and the SQB1 are separated by a 11.25 m long vacuum pipe with an angle of 38° with respect to the Filter Cavity pipe (or equivalently the flange between the SQB1 and the SDB1).

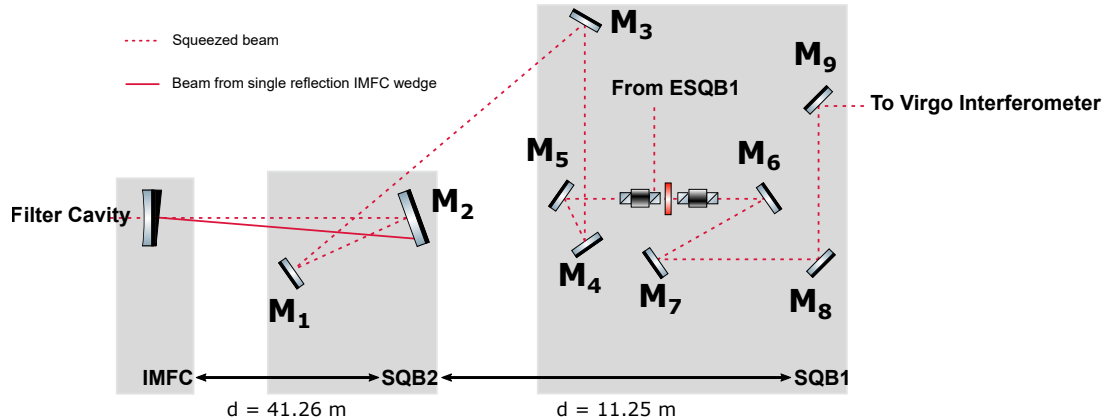


Figure 7.9: Simplified optical layout of the main beam represented in red dotted line with the beam undergoing a single reflection on the anti-reflective surface of the IMFC and being separated from the main beam due to the IMFC wedge. Note that the distances d correspond to the distances between the center of the vacuum chambers

First, it means that the beam size is naturally increasing from the 1.2 cm beam size radius on the IMFC to the SQB2 optics : the beam size on the SQB2 is at the order of 1.4 cm.

This beam size has to be compared with the optic diameter. Indeed, their comparison allows to compute clipping losses which accounts as optical losses for the squeezed beam.

The optical losses or equivalently the power lost P_{lost} by a Gaussian beam of power P_0 and size w during its transmission through a circular aperture of radius r is expressed as

:

$$P_{lost} = P_0 e^{-2\frac{r^2}{w^2}} \quad (7.1)$$

This relationship is represented in figure 7.10.

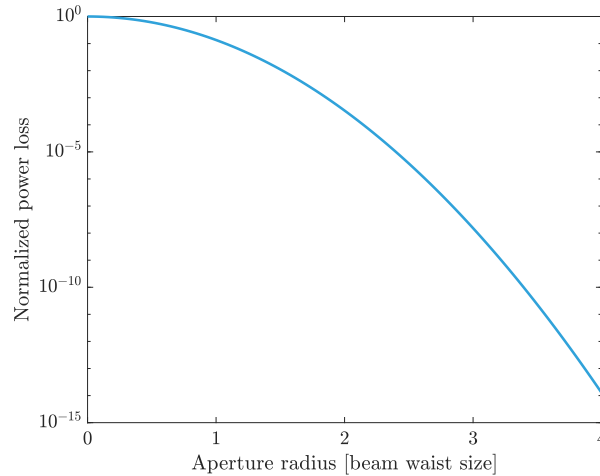


Figure 7.10: Normalized power loss of a Gaussian beam when propagating through a circular aperture. The lost power is plotted as a function of the aperture radius expressed in beam radius

It can be seen that the clipping losses decrease quickly when the aperture radius increases. For instance, the clipping losses start to be totally negligible when the aperture radius is three times larger than the beam size. Indeed for this aperture size, less than 1 ppb of the incident beam power is lost.

On the other hand, there is a maximal radius allowed for optics on the SQB1 or the SQB2. Indeed, the beam height is defined by the beam height on the SQB1 Faraday isolators. Therefore, the beam height on these benches has been set to 11.0 cm. As the usual mirror size above few inches diameter is defined as multiples of 2" (which also means lower price and lower polishing time), the maximal mirror diameter is 6". Indeed, in addition to the mirror radius, one has also to take into account the height required for the mirror mount.

Combining these two constraints, the first mirror seen by the squeezed beam reflected of the Filter Cavity has a 6" diameter.

The IMFC wedge

It has been presented last chapter in section 6.6 that there is no need for the etalon effect. In order to avoid these unwanted multiples reflections inside the IMFC, it is foreseen to tilt the anti-reflective surface of the IMFC. This tilt is called a wedge and allows to separate the main beam from the unwanted beams that reflect inside the IMFC.

Furthermore, due to the anti-reflective coating, the larger the number of reflections on this surface, the lower the power on the beam. Meaning that the beam that undergoes a direct reflection on the IMFC surface 2 is the most powerful one.



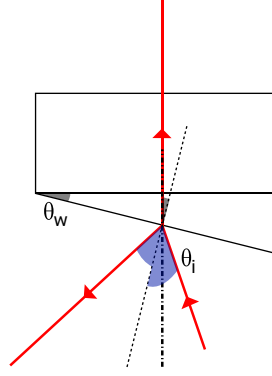


Figure 7.11: Effect of a wedge (represented by the gray angle) of the IMFC surface 2 on an incident beam. Only the transmitted beam and the beam directly reflected of the surface 2 are represented. The blue angle represents the incident and reflection angle with respect to the surface 2 normal (black dashed line). The dashed-dotted black line corresponds to the Filter Cavity optical axis. The gray angles are equal to the wedge angle θ_W . The blue angles are equal to the incident angle θ_i

Its separation with the main beam can be extracted from figure 7.11.

In this figure, θ_W corresponds to the wedge angle. In order to have the incident beam aligned with the Filter Cavity optical axis, the beam incident on the IMFC can not be at normal incidence. This implies that the transmitted angle θ_t is equal to the wedge angle θ_W . Using the Snell-Descartes laws of refraction, the incidence angle is $\theta_i = n \theta_W$ and $n = 1.45$ is the refractive index of the IMFC

As the reflection angle θ_r is equal to θ_i , the longitudinal separation δ between the main (incident) beam and the spurious reflected beam is expressed at a distance d from the IMFC as

$$\delta = 2 \cdot n \cdot d \cdot \theta_W \quad (7.2)$$

where $d = 41.78$ m is the distance between the IMFC and the mirror M1 on the SQB2.

The resulting longitudinal separation on M1 as a function of the wedge angle is presented in figure 7.12.

The wedge angle is constrained by two parameters.

On one hand, it is needed to have the spurious reflected beam hitting the mirror M1 on the SQB2. Indeed, with a waist of the order of 1.4 cm, it is still too large to be properly dumped on this bench. Therefore, it has to be propagated through the Filter Cavity matching telescope before being dumped on the SQB1 where it has a smaller size. This constraints the beam separation on the M2 to a maximal value given by the M2 radius dimension (3").

On the other hand, it is required that at least three times the spurious beam waist is hitting the SQB2 mirror. It means that no light from the spurious beam is scattered outside the M2 mirror. It has already been presented that the scattered light was troublesome during the O3 run and with this condition, no scattered light from the spurious beam is

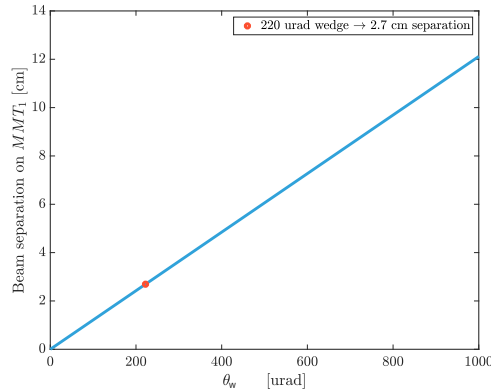


Figure 7.12: Longitudinal separation between the main beam and the spurious reflected beam as a function of the IMFC wedge at the mirror M1 on the SQB2

introduced on the SQB2.

Therefore, the IMFC wedge has chosen to be 220 μrad . This also allows to be insensitive to the wedge polishing accuracy typically of 10 %.

7.3.2 The matching telescopes design

Goal and constraints

The goal of both the matching telescope between the squeezed beam and the Filter Cavity as well as the matching telescope between the squeezed beam and the interferometer is to reach more than 99 % of mode-matching.

Another requirement of this overall squeezing system is that it should be easy to switch between the frequency-dependent squeezing injection and the frequency-independent squeezing injection.

A convenient way to realize the frequency-independent squeezing injection is to have the waist of the squeezed beam located on the SQB1. Indeed, one can then easily inject the frequency-independent squeezing by installing a single mirror at the waist position and insuring the proper geometrical properties of the squeezed beam. More precisely, this beam waist needs to be located between the SQB1 Faraday isolators and the mirror M3. With this condition, the frequency-independent squeezed beam will still go through the Faraday isolators chain. This insures a proper reduction of the scattered light which might be increased by placing a mirror on the beam waist. Furthermore, the squeezed beam is still propagating through the matching telescope for the interferometer which insures the proper geometrical properties of the squeezed beam with respect to the interferometer.

Also, the beam size on the SQB1 has to be small enough to not be clipped inside the Faraday isolators polarizers that are rectangles of size 25 mm \times 55 mm.

Finally, a last constraint is coming from the polishing. Indeed, the RoC of the mirror can be precise at the order of 2 %. Meaning that the telescope design has to be able to

Parameter	Interferometer beam on M9	Filter Cavity beam on IMFC
Sagittal size [mm]	1.35	8.02
Tangential size [mm]	1.35	8.02
Distance to Sagittal waist [m]	3.84	-142.15
Distance to Tangential waist [m]	3.77	-142.15

Table 7.1: Geometrical properties of the Filter Cavity and interferometer beam to match. The sign follows the Optocad convention [102]

compensate deviations of any curved mirror RoC.

The starting parameters

The geometrical parameters of the squeezed beam are defined by the Filter Cavity length and the IMFC and EMFC RoC. On the other hand, the interferometer main beam on the SDB1 are given by an Optocad simulation of the entire interferometer [102]. As the interferometer beam is present on the SQB1, its geometrical parameters are given on the mirror M9 on the SQB1.

The geometrical parameters of the squeezed beam inside the Filter Cavity and the interferometer beam on the mirror M9 are given in table 7.1.

Using the ABCD formalism [92], it is possible to propagate the squeezed beam from the Filter Cavity to the SDB1. At that point, the squeezed beam has to match the interferometer beam geometrical parameters.

In between these two locations, only mirrors are present to avoid absorption losses. These mirrors are either flat and used to steer the squeezed beam alignment or curved to mode-match the squeezed beam to the Filter Cavity or to the interferometer. In this formalism, the only mirror parameters that matter are its position with respect to the beam waist and its RoC. The goal of this section is to derive the required parameters of the curved mirrors between the Filter Cavity and the main interferometer.

A Gaussian beam is described using its complex beam parameter q which is defined as a function of its distance to the waist z as : $q = z + i \cdot \frac{\pi\omega_0^2}{\lambda}$ where ω_0 is the beam size at its waist and λ the wavelength. By defining the complex beam parameter for both the sagittal and tangential directions, it is possible to take into account astigmatism effects.

The interaction of a medium with a Gaussian beam is described by a 2×2 matrix. Table 7.2 presents the transfer matrices used to design the matching telescopes.

In this table, n is the refractive index, d the propagation distance, θ the incidence angle on the mirror and r the mirror RoC.

The action of optical components on an incident Gaussian beam can be expressed by

Action	Matrix
propagation	$\begin{pmatrix} 1 & nd \\ 0 & 1 \end{pmatrix}$
Sagital reflection	$\begin{pmatrix} 1 & 0 \\ \frac{2 \cos(\theta)}{r} & 1 \end{pmatrix}$
Tangential reflection	$\begin{pmatrix} 1 & 0 \\ \frac{2}{r \cos(\theta)} & 1 \end{pmatrix}$

Table 7.2: Transfer matrix used to design the matching telescopes

actions on its complex beam parameter q_{in} such that :

$$q_{out} = \frac{A \cdot q_{in} + B}{C \cdot q_{in} + D} \quad (7.3)$$

where the propagation of the Gaussian beam through the optical system is described by

the transfer matrix : $T_{prop} = \begin{pmatrix} A & B \\ C & D \end{pmatrix}$.

Finally, the mode-matching between two optical beams (or equivalently between one beam and the fundamental mode of a cavity) is described by their overlap integral :

$$MM = \frac{|\iint E_1 \cdot E_2^* dS|}{\iint |E_1|^2 dS \iint |E_2|^2 dS} \quad (7.4)$$

where E_k is either a Gaussian optical field or the fundamental mode of an optical cavity.

From this equation, it is possible to estimate the mode-matching losses as :

$$\Lambda_{MM}^2 = 1 - MM \quad (7.5)$$

The matching telescope design

The matching telescope corresponds to the *MM ITF*, *M2* and *M4* of figure 7.7.

Indeed, it is the most constrained telescope for the frequency-dependent squeezing injection. Especially, the large angle between the SQB1 and the SQB2 could create a large amount of astigmatism losses if no care is taken when designing this telescope.

The proposed matching telescope uses four curved mirrors labeled *M2* located on the SQB2 and *M4*, *M6*, *M7* located on the SQB1. The last two mirrors correspond to the *MM ITF*. Their respective parameters are described in table 7.3.

Mirror	RoC [m]	Incidence angle [deg]
M2	25.5	-5
M4	2.125	-8
M6	-2.125	-9
M7	1.35	11

Table 7.3: Curved optics used to match the Filter Cavity to the interferometer

Parameter	Interferometer beam	Filter Cavity beam
Sagital size [mm]	1.35	1.35
Tangential size [mm]	1.35	1.36
Distance to Sagital waist [m]	3.84	-3.84
Distance to Tangential waist [m]	3.77	-3.71

Table 7.4: Beams parameters on the M9 mirror. Distance are with respect to the M9. The sign follows the Optocad convention [102]

Using the Virgo description made in Optocad, it is possible to accurately position all the optical benches required for the frequency-dependent squeezing injection into the Virgo framework. This allows to check the effects of this telescope with the nominal beam parameters.

As can be seen in figure 7.13, several of the constraints previously presented are achieved.

- First, this matching telescope insures 99.99 % of mode-matching between the Filter Cavity and the interferometer. The geometrical parameters of the Filter Cavity beam and the interferometer beams propagated up to the mirror M9 are presented in table 7.4. Note that the difference in sign between the squeezed beam and the interferometer beam arises only from the Optocad convention [102].
- The beam separation due to the IMFC wedge can be performed on the SQB1 before entering the Faraday isolators. Indeed, at the position marked by the *SQB1 Iris*, the beams are separated by more than 5 cm. This separation has to be compared with their sizes that are below 1.7 mm. First, the comparison of the beam sizes with their separation shows that there is enough space to put a diaphragm at this position to dump the beams due to the IMFC wedge. Second, it also insures negligible clipping losses of the main beam (as in 7.10).
- There is an intermediate waist located 67 mm before the SQB1 Faraday isolators (coming from the Filter Cavity). It is marked by the green and pink triangles in figure 7.13. It can also be seen that the sagital and tangential waist locations are almost overlap (the sagital and tangential waist locations are separated by 0.5 mm).

It implies that putting a mirror at this position (facing the SDB1) can insure an easy injection of frequency-independent squeezing.



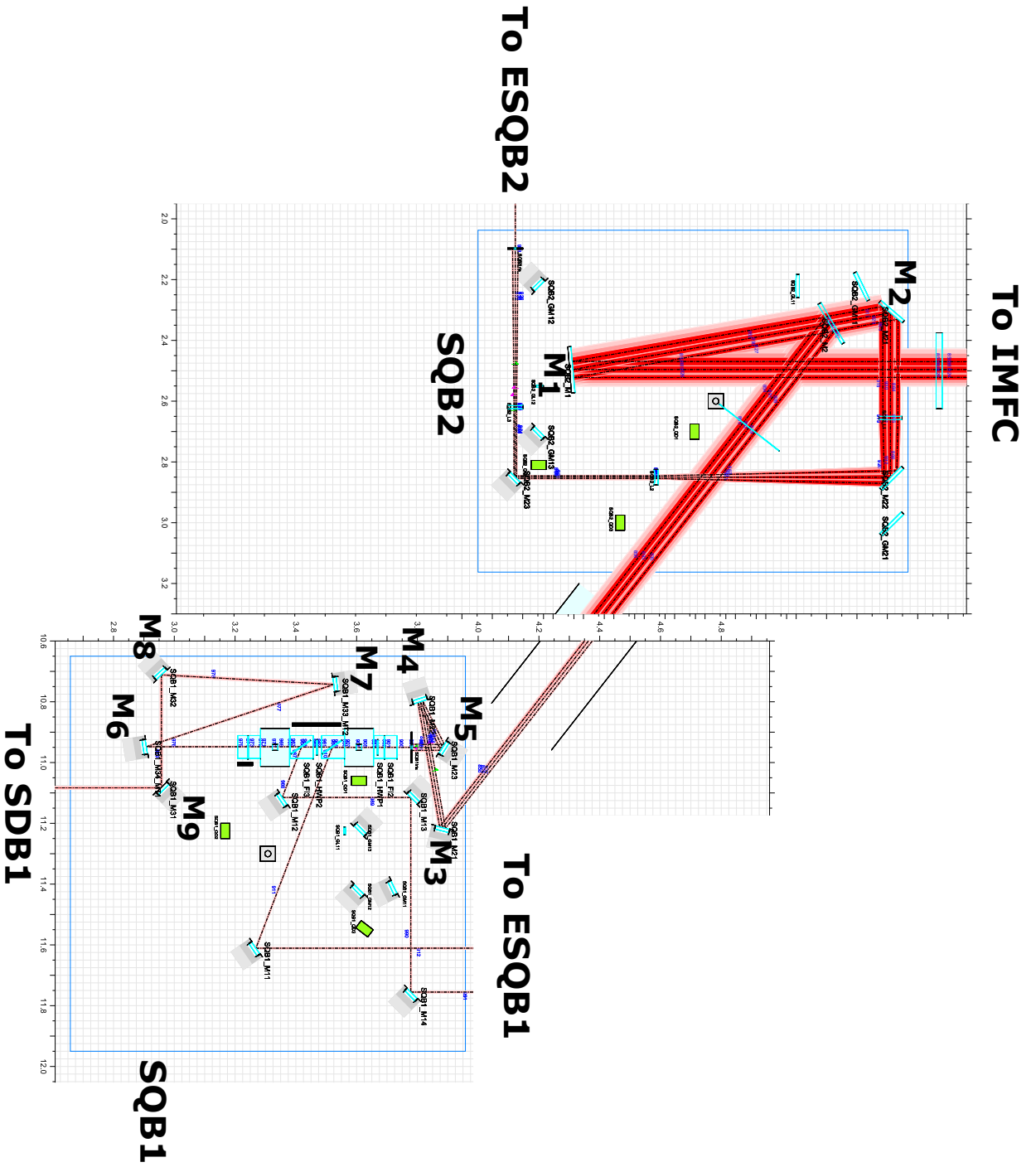


Figure 7.13: Propagation of the squeezed beam from the Filter Cavity to the SDB1 performed in Optocad [102]

7.3.3 The matching telescope tolerances

The mode-matching telescope is able to reach the mode-matching goal while insuring the proper separation of the spurious beam and having an intermediate waist on the SQB1. In practice, the curved mirrors RoC will have some errors arising from the polishing. A reasonable polishing can lead to a precision on the RoC of curved mirror at the order of $\pm 2\%$. While the matching telescope provides a high level of mode-matching with nominal RoC, the deviation of any of the RoC with respect to their nominal values might affect the mode-matching and not meet the 99 % requirement. It is therefore required to check if the mode-matching telescope is able to reach the mode-matching goal even if some mirrors RoC are not at their nominal value.

To compensate this effect, it is possible to change the position and the angle of incidence of the mirrors. In this section, it will be checked that reasonable displacement and tilt of the curved mirror of the matching telescope are enough to compensate RoC error at the order of $\pm 2\%$.

This section presents the tolerances of the matching telescope to any parameter changes with respect to their nominal value. It also consider variations on the position and RoC of either the IMFC or the EMFC.

As can already be seen in table 7.2, the difference between the sagittal and tangential reflection matrices on a curved mirror arises from the the angle of incidence on this mirror. While, this does not have any effects for a flat mirror (RoC= ∞) This shows that by acting on the angle of incidence of a curved mirror, it should be possible to correct the astigmatism induced by a non-nominal value of a mirror RoC. Furthermore, the position of a curved mirror is also affecting the telescope performances. There are therefore two degrees of freedom to act on in order to compensate a shift of its RoC : the position and the angle of incidence of the mirror.

However, as presented in figure 7.9, the maximal displacement of the mirrors is limited as several other optical components are also installed on the SQB1 and the SQB2.

Thus, this tolerance study considers that a mirror M is moved by a distance Δd . Its angle of incidence θ is changed to θ' in order to keep the incidence position of the optical beam on an identical position on a subsequent mirror $M1$. In order to keep identical the beam reflected by the $M1$, the angle of incidence of the $M1$ is also changed. This is presented in figure 7.14.

From this figure, it is possible to extract the impact of the displacement Δd of the mirror M on the optical path. The angle of incidence on M is decreased by $\delta\theta = \frac{1}{2} \arcsin\left(\frac{\Delta d}{d_1 \cdot \sin\theta}\right)$, the distance d_1 is changed to $d'_1 = d_1 \cdot \frac{\sin\theta}{\sin\theta'}$ and the angle of incidence of $M1$ is increased by $\delta\theta$.

Applying these changes to the four curved mirrors of the matching telescope, it is then possible to see if it is possible to compensate their RoC deviation.

The result is presented in figure 7.15. In this figure, each row corresponds to a variation of the RoC of a particular mirror. Each column corresponds to a variation of the position and incidence angle of a particular mirror as previously described.



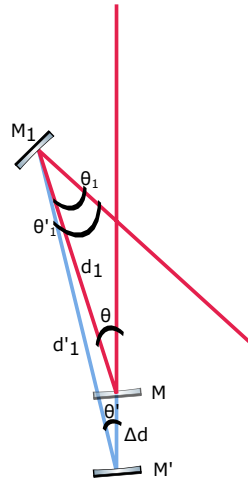


Figure 7.14: Effects of the displacement of a mirror M on the optical path. The angles of incidence of both M and $M1$ are also modified in order to keep the beam. The red trace shows the original beam path while the blue trace shows the modified optical path due to the displacement of the mirror M

Note that the effects of a 2 % error on the RoC of the IMFC and the EMFC are also presented. However, because a shift of their positions had no effect on the mode-matching, only variations of their RoC are represented.

On each sub-figure, the pink dot shows the mode-matching achieved in nominal conditions. The red, black and blue contour lines corresponds respectively to 98 %, 99 % and 99.9 % of mode-matching (the mode-matching goal being 99 %).

It can be seen that the variation of the $M1$ RoC degrades the most the mode-matching. Also, the position of the $M6$ has a large impact on the mode-matching. It is therefore foreseen to install the $M6$ on a translation stage in order to precisely control its position. Furthermore, the $M6$ could be move to correct a too large deviation of the $M2$ RoC.

In the case of the largest variation of the $M1$ RoC, moving both the $M2$ and $M6$ allows to meet the mode-matching goal.

7.4 Conclusion

This chapter has presented how the frequency dependent squeezing can be injected into the Advanced Virgo interferometer. For instance, the 285 m long Filter Cavity can be installed inside the Virgo north arm tunnel. The infrastructural work that minimizes the interferometer downtime led to constraints on the optical paths. Taking these constraints into account, it was possible to design a mode-matching telescope insuring more than 99% of mode-matching between the Filter Cavity and the interferometer (the goal of the squeezing degradation budget) even when taking into account the unavoidable uncertainties on the matching telescope RoC.

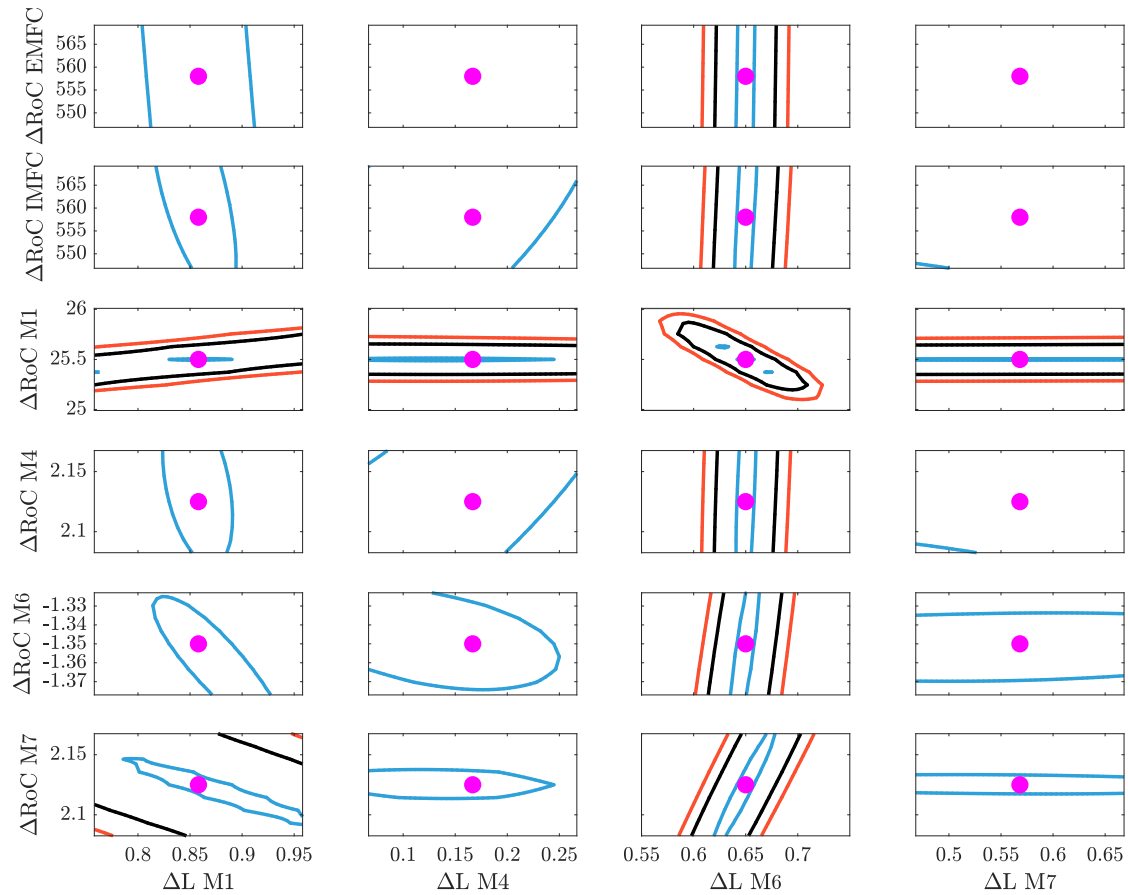


Figure 7.15: Effects of position (columns) and RoC (rows) variations of each curved mirror of the matching telescope on the mode-matching between the Filter Cavity and the interferometer. The pink dot shows the nominal configuration. The red, black and blue contours correspond respectively to 98 %, 99 % and 99.9 % of mode-matching (the mode-matching goal being 99 %). All the RoC and position variations are in meter



Conclusion

Since the first detection of gravitational waves in 2015 by the LIGO-Virgo collaboration, the sensitivity of gravitational wave detectors has drastically improved. This has allowed to increase the detection rate of gravitational waves from one per several months in 2015 to one per week in 2019.

All current gravitational wave detectors have a large part of their sensitivity limited by quantum noise. Thus for the O3 observation period, the LIGO and Virgo detectors have injected frequency-independent squeezed vacuum states.

To this purpose, it was first necessary to ensure that these squeezed vacuum states were introduced into the interferometer with the right geometrical parameters and the right phase with respect to the interferometer signal. Control loops were implemented to keep these geometrical and phase parameters stable during the eleven month long observation period. The duty cycle of the injection of squeezed vacuum states was greater than 96% over the O3 duration. The effects of light back-scattered into the interferometer by the squeezer optical components have also been studied. This showed that only few components were inducing such back-scattered light.

The mechanisms that affected the squeezed vacuum states performances, namely the optical losses and the phase noise, have been characterized.

First, the level of effective optical losses has been measured to be at $(40 \pm 2)\%$. In addition, the sources of these effective optical losses were analyzed and are divided as follows: 16.7 % are due to injection losses, 12 % to detection losses and 15.2 % to high-frequency technical noises equivalent to optical losses.

One of the main challenges for future observation periods is to reduce these optical losses. For this purpose, it is planned to use temperature controls of the different Faraday isolators and to change the design of the OMCs from two cavities to one. It could also be interesting to implement an active mode-matching control in order to further reduce the mode-mismatch between the OMC and the interferometer. It is planned to install such active mode-matching controls for the squeezed beam. The reduction of high-frequency technical noises appears to be particularly important to further improve the reduction of shot noise at high frequency.

Finally, the level of phase noise have been measured to be at a 55 mrad]. The phase noise is mainly due to residual phase fluctuations in the phase control loops. It will therefore be particularly important to reduce these residual phase fluctuations that couple the



squeezing to the anti-squeezing.

The squeezer used at Virgo was able to generate up to 13.7 dB of squeezing. During O3, between 6 and 8 dB of squeezing have been injected into Virgo interferometer. This allowed to reduce the shot noise by more than 2 dB during O3, and consequently to increase the observation rate of gravitational waves emitted by binary neutron stars by 15 %. The maximal achieved high-frequency sensitivity improvement was more than 3 dB. It was also seen that by removing the effects of technical noises, up to 5 dB of shot noise reduction could have been achieved.

The increase of the radiation pressure noise has also been observed for the first time at the Virgo detector (and at a similar time in the LIGO detectors).

The use of the Filter Cavity for the O4 observation period will allow to exploit the full potential of the squeezing source. The mechanisms that affect the Filter Cavity have been studied and were used to estimate the frequency-dependent squeezed vacuum states performances.

For instance it has been shown that a 285 m long Filter Cavity achieves a quantum noise reduction similar to the one of a Filter Cavity with the maximal length possible within the Virgo infrastructure. A 285 m long Filter Cavity allows the Advanced Virgo detector to reach indeed 99 % of the binary black holes and binary neutron stars ranges that would be achieved using a 3 km long Filter Cavity. This shorter cavity presents also the advantage of being easier to implement.

The Filter Cavity finesse and detuning that allows to rotate the squeezed vacuum states have also been derived to be respectively 10300 and 25 Hz. The drawback of a such high finesse is that the effects of the cavity round-trip losses are enhanced.

The Filter Cavity mirrors have been designed to achieve 40 ppm of round-trip losses. For instance, the impact of the mirror surface quality on the cavity round-trip losses have been studied. Two mirror surface qualities were considered and will be used respectively for O4 and O5.

Two optical configurations have been studied for the Filter Cavity : one with a plane input mirror and a curved end mirror and another one with two curved mirrors with identical radii of curvature. The effects of these optical configurations on the beam size in the Filter Cavity and on the Filter Cavity round-trip losses were studied. This study showed that the optical configuration with two curved mirrors with identical radii of curvature is less sensitive to round-trip losses and has therefore been chosen for the Filter Cavity.

The Filter Cavity mirror radius of curvature have been chosen to avoid degeneracies where the squeezed beam can couple to the Filter Cavity higher-order modes. The radius of curvature was chosen to be 558 m which allows to avoid degeneracies over the 20 m of the radius of curvature uncertainties during the polishing.

Finally, the mode-matching between the squeezed beam reflected by the Filter Cavity and the interferometer appeared to be a critical source of degradation of the frequency-dependent squeezed vacuum states performances. A mode-matching telescope has therefore been designed. It is composed of four curved mirrors. Especially, the telescope tolerance to errors on the curved mirror radii of curvature have been studied. This showed that more than 99 % of mode-matching between the squeezed beam reflected by the Filter

Cavity and the interferometer is achievable despite the error on any of these four curved mirror radii of curvature.

The injection of frequency-dependent squeezed vacuum states in the Virgo detector is a particularly challenging task.

One of the challenges concerns the control of this cavity. For this purpose, different beams will be used. The experiment of TAMA showed that it was possible to control the Filter Cavity using a green beam. However, it appeared that this control is very sensitive to the relative alignment between the green beam and the squeezed beam. It will therefore be particularly important to ensure the relative alignment of these two beams. It is also planned to use an infra-red beam to control the Filter Cavity which should ensure that the Filter Cavity control beam is superimposed on the squeezing beam.

The light back-scattered from the squeezer optics to the interferometer was particularly sensitive to the relative alignment between the squeezer and the interferometer. Starting from the O4 observation period, the squeezing beam will be injected into the interferometer through optics located on a bench suspended under vacuum. This should drastically reduce the effects of back-scattered light.

To conclude, the injection of vacuum squeezed states should allow the Virgo detector to reach a binary neutron stars range above 100 Mpc. It means that the number of gravitational waves detected by Virgo will significantly increase. This is an important step for ground-based gravitational wave detectors as it allows to probe ever more varied and distant sources in the Universe.



Appendix A : Phase shift induced by thermal fluctuations

The mirror substrate is made of bulk silica (of molecular formula SiO_2) because of its low thermal noise. The mirror coating is made of ion beam sputtered [103] pairs of layers of silica and tantalum (of molecular formula Ta_2O_5) allowing for low optical and mechanical losses. Each layer is described by its thickness and refractive index.

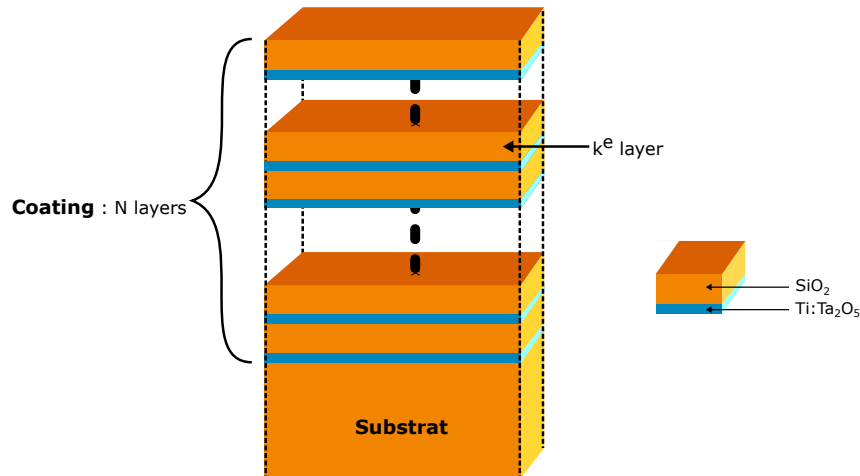


Figure 7.16: View of a coated mirror. The substrate is made of silica (SiO_2). The coating is made of pairs of silica and Titania doped tantalum (Ta_2O_5) layers. Each layer is defined by their thickness and refractive index

Such a multilayer coating is described by its characteristic matrix [104] :

$$\begin{pmatrix} B_\lambda \\ C_\lambda \end{pmatrix} = \left[\prod_{k=1}^N \begin{pmatrix} \cos \delta_k & i \frac{\sin \delta_k}{n_k} \\ i n_k \sin \delta_k & \cos \delta_k \end{pmatrix} \right] \cdot \begin{pmatrix} 1 \\ n_s \end{pmatrix} \quad (7.6)$$

where B_λ and C_λ can be assimilated respectively to the normalized electric and magnetic field amplitudes and n_s is the substrate refractive index. The wavelength dependency appearing in the B_λ and C_λ is due to the presence of the layer refractive index following Cauchy formula. Also, the optical path inside each layer $\delta_k = 2\pi n_k \frac{d_k}{\lambda}$ is dependent on both the wavelength λ and the layer thickness d_k .



From this characteristic matrix, it is possible to compute the mirror complex amplitude reflectivity as :

$$\rho_\lambda = \frac{1 - \frac{C_\lambda}{B_\lambda}}{1 + \frac{C_\lambda}{B_\lambda}} \quad (7.7)$$

Finally, we can express the coating induced phase shift as :

$$\phi_\lambda^M = \arctan \frac{\Im(\rho_\lambda)}{\Re(\rho_\lambda)} \quad (7.8)$$

This exhibits that the reflection of a beam on a coating induces a phase shift between optical beam with different wavelengths.

The thermal effects appear through the thermal expansion coefficient α and the thermo-refractive coefficient $\beta = \frac{\partial n}{\partial T}$. These coefficients allow to express the refractive index and thickness of the layer dependency to the temperature as [105] :

$$\begin{aligned} n(T) &= n - \beta T \\ d(T) &= d + \alpha T \end{aligned} \quad (7.9)$$

This formalism allows to compute the round-trip phase ϕ_λ accumulated by both the green and infrared beams inside the filter cavity as the sum of the phase accumulated during the beam round-trip inside the filter cavity with the phase due to thermal effects inside the coatings of the IMFC and the EMFC.

$$\phi_G = \phi_G^{IMFC} + \phi_G^{EMFC} + 2 \frac{2\pi}{\lambda_G} \cdot L_{FC} \quad (7.10)$$

$$\phi_{IR} = \phi_{IR}^{IMFC} + \phi_{IR}^{EMFC} + 2 \frac{2\pi}{\lambda_{IR}} \cdot L_{FC} \quad (7.11)$$

As the filter cavity is locked using the green beam, the green beam is kept at resonance meaning that $\phi_G = 2\pi N$ with N being an integer (assumed to be null in the following).

A thermal fluctuations ΔT induce a green phase fluctuation defined as :

$$\Delta\phi_G = \left(\frac{\partial\phi_G^{IMFC}}{\partial T} + \frac{\partial\phi_G^{EMFC}}{\partial T} \right) \Delta T + 2 \frac{2\pi}{\lambda_G} \delta L_{FC} = 0 \quad (7.12)$$

In the following, the IMFC and the EMFC coating phase shift are combined into a single term $\frac{\partial\phi_\lambda^M}{\partial T} = \left(\frac{\partial\phi_\lambda^{IMFC}}{\partial T} + \frac{\partial\phi_\lambda^{EMFC}}{\partial T} \right)$. From this equation, it is possible to extract the filter cavity length fluctuations induced by the thermal fluctuations ΔT . Note that the thermal fluctuations in Virgo vacuum chambers are of the order of 30 mK over one week.

$$\delta L_{FC} = -\frac{\lambda_G}{4\pi} \frac{\partial\phi_G^M}{\partial T} \Delta T \quad (7.13)$$

This allow to compute the phase shift induced for the infrared beam as :

$$\Delta\phi_{IR} = \frac{\partial\phi_{IR}^M}{\partial T}\Delta T + 2\frac{2\pi}{\lambda_{IR}}\delta L_{FC} \quad (7.14)$$

$$= \left(\frac{\partial\phi_{IR}^M}{\partial T} - \frac{1}{2} \frac{\delta\phi_G^M}{\partial T} \right) \cdot \Delta T \quad (7.15)$$

From TAMA style coating [98], $\frac{\partial\phi}{\partial T} = 65.3 \mu\text{rad/K}$. This computation shows that the effects of thermal induced phase shift on the relative phase between the green and the infra-red beams used to control the Advanced Virgo+ Filter Cavity should be negligible.



Bibliography

- [1] Franzen A. “ComponentLibrary, vector graphics library for illustrations of optics experiments.” (2006) (cit. on p. v).
- [2] A. Einstein. “Die Grundlage der allgemeinen Relativitätstheorie”. *Annalen der Physik* 354.7 (1916), 769–822. DOI: [10.1002/andp.19163540702](https://doi.org/10.1002/andp.19163540702) (cit. on p. 1).
- [3] Albert Einstein. “Über Gravitationswellen”. *Sitzungsber. Preuss. Akad. Wiss. Berlin (Math. Phys.)* 1918 (1918), 154–167 (cit. on p. 1).
- [4] LIGO Scientific Collaboration and Virgo Collaboration. “Observation of Gravitational Waves from a Binary Black Hole Merger”. *Phys. Rev. Lett.* 116 (6 Feb. 2016), p. 061102. DOI: [10.1103/PhysRevLett.116.061102](https://doi.org/10.1103/PhysRevLett.116.061102) (cit. on pp. 1, 25).
- [5] F. Tisserand. “Les travaux de Le Verrier”. *Annales de l’Observatoire de Paris* 15 (Jan. 1880), 23–43 (cit. on p. 2).
- [6] P. R. Saulson. *Fundamentals of Interferometric Gravitational Wave Detectors*. WORLD SCIENTIFIC, 1994. DOI: [10.1142/2410](https://doi.org/10.1142/2410) (cit. on pp. 2–4).
- [7] Sascha Husa. “Michele Maggiore: Gravitational waves. Volume 1: theory and experiments”. *General Relativity and Gravitation* 41.7 (July 2009), 1667–1669. DOI: [10.1007/s10714-009-0762-5](https://doi.org/10.1007/s10714-009-0762-5) (cit. on p. 3).
- [8] J.M. Weisberg, D.J. Nice, and J.H. Taylor. “Timing Measurements of the Relativistic Binary Pulsar PSR B1913+16”. *Astrophys. J.* 722 (2010), 1030–1034. DOI: [10.1088/0004-637X/722/2/1030](https://doi.org/10.1088/0004-637X/722/2/1030) (cit. on p. 4).
- [9] Lee Samuel Finn and David F. Chernoff. “Observing binary inspiral in gravitational radiation: One interferometer”. *Physical Review D* 47.6 (Mar. 1993), 2198–2219. DOI: [10.1103/PhysRevD.47.2198](https://doi.org/10.1103/PhysRevD.47.2198) (cit. on p. 5).
- [10] LIGO Scientific Collaboration and Virgo Collaboration. “All-sky search for short gravitational-wave bursts in the first Advanced LIGO run”. *Physical Review D* 95.4, 042003 (Feb. 2017), p. 042003. DOI: [10.1103/PhysRevD.95.042003](https://doi.org/10.1103/PhysRevD.95.042003) (cit. on p. 5).
- [11] LIGO Scientific Collaboration and Virgo Collaboration. “All-sky search for short gravitational-wave bursts in the second Advanced LIGO and Advanced Virgo run”. *Physical Review D* 100.2, 024017 (July 2019), p. 024017. DOI: [10.1103/PhysRevD.100.024017](https://doi.org/10.1103/PhysRevD.100.024017) (cit. on p. 5).



- [12] LIGO Scientific Collaboration and Virgo Scientific Collaboration. “First Search for Gravitational Waves from Known Pulsars with Advanced LIGO”. *Astrophysical Journal* 839.1, 12 (Apr. 2017), p. 12. DOI: [10.3847/1538-4357/aa677f](https://doi.org/10.3847/1538-4357/aa677f) (cit. on p. 5).
- [13] LIGO Scientific Collaboration and Virgo Scientific Collaboration. “A directed search for continuous Gravitational Waves from the Galactic Center”. *Physical Review D* (Sept. 2013). DOI: [10.1103/PhysRevD.88.102002](https://doi.org/10.1103/PhysRevD.88.102002) (cit. on p. 5).
- [14] Max Camenzind. *Compact objects in astrophysics : white dwarfs, neutron stars, and black holes*. 2007. DOI: [10.1007/978-3-540-49912-1](https://doi.org/10.1007/978-3-540-49912-1) (cit. on p. 5).
- [15] LIGO Scientific Collaboration and Virgo Scientific Collaboration. “Tests of general relativity with the binary black hole signals from the LIGO-Virgo catalog GWTC-1”. *Physical Review D* 100.10, 104036 (Oct. 2019), p. 104036. DOI: [10.1103/PhysRevD.100.104036](https://doi.org/10.1103/PhysRevD.100.104036) (cit. on p. 5).
- [16] LIGO Scientific Collaboration and Virgo Scientific Collaboration and INTEGRAL. “Gravitational Waves and Gamma-Rays from a Binary Neutron Star Merger: GW170817 and GRB 170817A”. *Astrophysical Journal Letters* 848.2, L13 (Oct. 2017), p. L13. DOI: [10.3847/2041-8213/aa920c](https://doi.org/10.3847/2041-8213/aa920c) (cit. on pp. 5, 6, 25).
- [17] LIGO Scientific Collaboration and Virgo Scientific Collaboration. “A gravitational-wave standard siren measurement of the Hubble constant”. *Nature* 551.7678 (Nov. 2017), 85–88. DOI: [10.1038/nature24471](https://doi.org/10.1038/nature24471) (cit. on p. 6).
- [18] The LIGO Scientific Collaboration and the Virgo Collaboration. “A gravitational-wave measurement of the Hubble constant following the second observing run of Advanced LIGO and Virgo”. *arXiv e-prints*, arXiv:1908.06060 (Aug. 2019), arXiv:1908.06060 (cit. on p. 6).
- [19] Planck Collaboration et al. “Planck 2015 results. XIII. Cosmological parameters”. *Astron. Astrophys.* 594, A13 (Sept. 2016), A13. DOI: [10.1051/0004-6361/201525830](https://doi.org/10.1051/0004-6361/201525830) (cit. on p. 6).
- [20] S.H. et al. Suyu. “H0LiCOW – I. H0 Lenses in COSMOGRAIL’s Wellspring: program overview”. *Mon. Not. Roy. Astron. Soc.* 468.3 (2017), 2590–2604. DOI: [10.1093/mnras/stx483](https://doi.org/10.1093/mnras/stx483) (cit. on p. 6).
- [21] Hsin-Yu Chen, Maya Fishbach, and Daniel E. Holz. “A two per cent Hubble constant measurement from standard sirens within five years”. *Nature* 562.7728 (Oct. 2018), 545–547. DOI: [10.1038/s41586-018-0606-0](https://doi.org/10.1038/s41586-018-0606-0) (cit. on p. 6).
- [22] Michael Zevin, Chris Pankow, Carl L. Rodriguez, Laura Sampson, Eve Chase, Vasiliki Kalogera, and Frederic A. Rasio. “Constraining Formation Models of Binary Black Holes with Gravitational-wave Observations”. *Astrophysical Journal* 846.1, 82 (Sept. 2017), p. 82. DOI: [10.3847/1538-4357/aa8408](https://doi.org/10.3847/1538-4357/aa8408) (cit. on p. 6).
- [23] LIGO Scientific Collaboration and Virgo Collaboration. “Binary Black Hole Population Properties Inferred from the First and Second Observing Runs of Advanced LIGO and Advanced Virgo”. *Astrophysical Journal Letters* 882.2, L24 (Sept. 2019), p. L24. DOI: [10.3847/2041-8213/ab3800](https://doi.org/10.3847/2041-8213/ab3800) (cit. on p. 6).
- [24] E. Pian et al. “Spectroscopic identification of r-process nucleosynthesis in a double neutron star merger”. *Nature* 551 (2017), 67–70. DOI: [10.1038/nature24298](https://doi.org/10.1038/nature24298) (cit. on p. 6).

- [25] Darach Watson, Camilla J. Hansen, Jonatan Selsing, Andreas Koch, Daniele B. Malesani, Anja C. Andersen, Johan P. U. Fynbo, Almudena Arcones, Andreas Bauswein, Stefano Covino, Aniello Grado, Kasper E. Heintz, Leslie Hunt, Chryssa Kouveliotou, Giorgos Leloudas, Andrew J. Levan, Paolo Mazzali, and Elena Pian. “Identification of strontium in the merger of two neutron stars”. *Nature* 574.7779 (Oct. 2019), 497–500. DOI: [10.1038/s41586-019-1676-3](https://doi.org/10.1038/s41586-019-1676-3) (cit. on p. 6).
- [26] C. J. Moore, R. H. Cole, and C. P. L. Berry. “Gravitational-wave sensitivity curves”. *Classical and Quantum Gravity* 32.1, 015014 (Jan. 2015), p. 015014. DOI: [10.1088/0264-9381/32/1/015014](https://doi.org/10.1088/0264-9381/32/1/015014) (cit. on p. 7).
- [27] M. E. Gertsenshtein and V. I. Pustovoit. “On the Detection of Low-Frequency Gravitational Waves”. *Soviet Journal of Experimental and Theoretical Physics* 16 (Jan. 1963), p. 433 (cit. on p. 7).
- [28] Weiss R. “Gravitation Research: Electromagnetically Coupled Broadband Gravitational Antenna”. *Quarterly Progress Report - MIT Research Lab of Electronics* (1972) (cit. on p. 7).
- [29] Eric D. Black and Ryan N. Gutenkunst. “An introduction to signal extraction in interferometric gravitational wave detectors”. *American Journal of Physics* 71.4 (Apr. 2003), 365–378. DOI: [10.1119/1.1531578](https://doi.org/10.1119/1.1531578) (cit. on p. 9).
- [30] B.J. Meers. “Recycling in Laser Interferometric Gravitational Wave Detectors”. *Phys. Rev. D* 38 (1988), 2317–2326. DOI: [10.1103/PhysRevD.38.2317](https://doi.org/10.1103/PhysRevD.38.2317) (cit. on p. 12).
- [31] Brian J. Meers. “Recycling in laser-interferometric gravitational-wave detectors”. *Phys. Rev. D* 38 (8 Oct. 1988), 2317–2326. DOI: [10.1103/PhysRevD.38.2317](https://doi.org/10.1103/PhysRevD.38.2317) (cit. on p. 12).
- [32] Fabrice Ardhuin, Eleonore Stutzmann, Martin Schimmel, and Anne Mangeney. “Ocean wave sources of seismic noise”. *Journal of Geophysical Research (Oceans)* 116.C9, C09004 (Sept. 2011), p. C09004. DOI: [10.1029/2011JC006952](https://doi.org/10.1029/2011JC006952) (cit. on p. 15).
- [33] F. Acernese. “Properties of seismic noise at the Virgo site”. *Classical and Quantum Gravity* 21.5 (Mar. 2004), S433–S440. DOI: [10.1088/0264-9381/21/5/008](https://doi.org/10.1088/0264-9381/21/5/008) (cit. on p. 15).
- [34] Scott A. Hughes and Kip S. Thorne. “Seismic gravity-gradient noise in interferometric gravitational-wave detectors”. *Phys. Rev. D* 58.12, 122002 (Dec. 1998), p. 122002. DOI: [10.1103/PhysRevD.58.122002](https://doi.org/10.1103/PhysRevD.58.122002) (cit. on p. 16).
- [35] Shuichi Sato, Shinji Miyoki, Souichi Telada, Daisuke Tatsumi, Akito Araya, Masatake Ohashi, Yoji Totsuka, Mitsuhiro Fukushima, and Masa-Katsu Fujimoto. “Ultra-stable performance of an underground-based laser interferometer observatory for gravitational waves”. *Phys. Rev. D* 69.10, 102005 (May 2004), p. 102005. DOI: [10.1103/PhysRevD.69.102005](https://doi.org/10.1103/PhysRevD.69.102005) (cit. on p. 16).
- [36] F. Badaracco et al. “Machine learning for gravitational-wave detection: surrogate Wiener filtering for the prediction and optimized cancellation of Newtonian noise at Virgo” (May 2020) (cit. on pp. 16, 131).



- [37] Herbert B. Callen and Richard F. Greene. “On a Theorem of Irreversible Thermodynamics”. *Phys. Rev.* 86 (5 June 1952), 702–710. DOI: [10.1103/PhysRev.86.702](https://doi.org/10.1103/PhysRev.86.702) (cit. on p. 16).
- [38] G Ballardin, L Bracci, S. Braccini, C Bradaschia, C Casciano, G Calamai, R Cavalieri, R Cecchi, Giancarlo Cella, E ambrosio, V Dattilo, A. Virgilio, L Fabbroni, Francesco Fidecaro, F. Frasconi, A Gaddi, A Gennai, G Gennaro, Adalberto Giuzotto, and Zhijiao Zhang. “Measurement of the VIRGO superattenuator performance for seismic noise suppression”. *Review of Scientific Instruments - REV SCI INSTR* 72 (Sept. 2001). DOI: [10.1063/1.1392338](https://doi.org/10.1063/1.1392338) (cit. on p. 20).
- [39] Marine Ducrot. “Etude des cavités optiques de filtrage de sortie du détecteur d’ondes gravitationnelles Advanced Virgo”. 2016GREAY046. PhD thesis. 2016 (cit. on pp. 21, 68, 105).
- [40] M Mehmet and H Vahlbruch. “High-efficiency squeezed light generation for gravitational wave detectors”. *Classical and Quantum Gravity* 36.1 (2018), p. 015014. DOI: [10.1088/1361-6382/aaf448](https://doi.org/10.1088/1361-6382/aaf448) (cit. on pp. 21, 60, 62, 105, 110, 181).
- [41] F. Acernese et al. “The advanced Virgo longitudinal control system for the O2 observing run”. *Astroparticle Physics* 116, 102386 (Mar. 2020), p. 102386. DOI: [10.1016/j.astropartphys.2019.07.005](https://doi.org/10.1016/j.astropartphys.2019.07.005) (cit. on p. 22).
- [42] Lee Samuel Finn and David F. Chernoff. “Observing binary inspiral in gravitational radiation: One interferometer”. *Phys. Rev. D* 47.6 (Mar. 1993), 2198–2219. DOI: [10.1103/PhysRevD.47.2198](https://doi.org/10.1103/PhysRevD.47.2198) (cit. on p. 22).
- [43] Peter Shawhan. “Rapid alerts for following up gravitational wave event candidates”. *Proc SPIE* (June 2012). DOI: [10.1117/12.926372](https://doi.org/10.1117/12.926372) (cit. on p. 23).
- [44] F Acernese et al. “Advanced Virgo: a second-generation interferometric gravitational wave detector”. *Classical and Quantum Gravity* 32.2 (Dec. 2014), p. 024001. DOI: [10.1088/0264-9381/32/2/024001](https://doi.org/10.1088/0264-9381/32/2/024001) (cit. on pp. 23, 84).
- [45] LIGO Scientific Collaboration and Virgo Collaboration. “GW170814: A Three-Detector Observation of Gravitational Waves from a Binary Black Hole Coalescence”. *Phys. Rev. Lett.* 119.14, 141101 (Oct. 2017), p. 141101. DOI: [10.1103/PhysRevLett.119.141101](https://doi.org/10.1103/PhysRevLett.119.141101) (cit. on p. 23).
- [46] Terra Hardwick. “Status of Advanced LIGO detectors at the start of the third observing run”. In: *American Astronomical Society Meeting Abstracts #233*. Vol. 233. American Astronomical Society Meeting Abstracts. Jan. 2019, 210.02, p. 210.02 (cit. on p. 23).
- [47] KAGRA Collaboration. “The status of KAGRA underground cryogenic gravitational wave telescope”. In: *Journal of Physics Conference Series*. Vol. 1342. Journal of Physics Conference Series. Jan. 2020, 012014, p. 012014. DOI: [10.1088/1742-6596/1342/1/012014](https://doi.org/10.1088/1742-6596/1342/1/012014) (cit. on p. 23).

- [48] K. L. Dooley, J. R. Leong, T. Adams, C. Affeldt, A. Bisht, C. Bogan, J. Degallaix, C. Gräf, S. Hild, J. Hough, A. Khalaidovski, N. Lastzka, J. Lough, H. Lück, D. Macleod, L. Nuttall, M. Prijatelj, R. Schnabel, E. Schreiber, J. Slutsky, B. Sorazu, K. A. Strain, H. Vahlbruch, M. Waş, B. Willke, H. Wittel, K. Danzmann, and H. Grote. “GEO 600 and the GEO-HF upgrade program: successes and challenges”. *Classical and Quantum Gravity* 33.7, 075009 (Apr. 2016), p. 075009. DOI: [10.1088/0264-9381/33/7/075009](https://doi.org/10.1088/0264-9381/33/7/075009) (cit. on p. 23).
- [49] James Lough, Emil Schreiber, Fabio Bergamin, Hartmut Grote, Moritz Mehmet, Henning Vahlbruch, Christoph Affeldt, Marc Brinkmann, Aparna Bisht, Volker Kringel, Harald Lück, Nikhil Mukund, Séverin Nadji, Borja Sorazu, Kenneth Strain, Michael Weinert, and Karsten Danzmann. “First demonstration of 6 dB quantum noise reduction in a kilometer scale gravitational wave observatory”. *arXiv e-prints*, arXiv:2005.10292 (May 2020), arXiv:2005.10292 (cit. on p. 23).
- [50] LIGO Scientific collaboration KAGRA collaboration and VIRGO collaboration. “Prospects for Observing and Localizing Gravitational-Wave Transients with Advanced LIGO, Advanced Virgo and KAGRA”. *Living Rev. Rel.* 21.1 (2018), p. 3. DOI: [10.1007/s41114-018-0012-9](https://doi.org/10.1007/s41114-018-0012-9) (cit. on pp. 24, 142, 148).
- [51] B.P. et al. Abbott. “GW170817: Observation of Gravitational Waves from a Binary Neutron Star Inspiral”. *Phys. Rev. Lett.* 119.16 (2017), p. 161101. DOI: [10.1103/PhysRevLett.119.161101](https://doi.org/10.1103/PhysRevLett.119.161101) (cit. on p. 25).
- [52] B.P. et al. Abbott. “GWTC-1: A Gravitational-Wave Transient Catalog of Compact Binary Mergers Observed by LIGO and Virgo during the First and Second Observing Runs”. *Phys. Rev. X* 9.3 (2019), p. 031040. DOI: [10.1103/PhysRevX.9.031040](https://doi.org/10.1103/PhysRevX.9.031040) (cit. on p. 25).
- [53] Christopher Gerry and Peter Knight. *Introductory Quantum Optics*. Cambridge University Press, 2004. DOI: [10.1017/CB09780511791239](https://doi.org/10.1017/CB09780511791239) (cit. on pp. 30, 31, 33, 35, 37).
- [54] Roy J. Glauber. “Coherent and Incoherent States of the Radiation Field”. *Physical Review* 131.6 (Sept. 1963), 2766–2788. DOI: [10.1103/PhysRev.131.2766](https://doi.org/10.1103/PhysRev.131.2766) (cit. on p. 31).
- [55] Emil Schreiber. “Gravitational-wave detection beyond the quantum shot-noise limit: The integration of squeezed light in GEO 600”. PhD thesis. PhD thesis. 2018 (cit. on pp. 34, 48, 49, 108).
- [56] E. Wigner. “On the Quantum Correction For Thermodynamic Equilibrium”. *Physical Review* 40.5 (June 1932), 749–759. DOI: [10.1103/PhysRev.40.749](https://doi.org/10.1103/PhysRev.40.749) (cit. on p. 36).
- [57] C. M. Caves and B. L. Schumaker. “New formalism for two-photon quantum optics. I. Quadrature phases and squeezed states”. *Phys. Rev. A* 31.5 (May 1985), 3068–3092. DOI: [10.1103/PhysRevA.31.3068](https://doi.org/10.1103/PhysRevA.31.3068) (cit. on pp. 40, 41).
- [58] Bonny L. Schumaker and Carlton M. Caves. “New formalism for two-photon quantum optics. II. Mathematical foundation and compact notation”. *Phys. Rev. A* 31.5 (May 1985), 3093–3111. DOI: [10.1103/PhysRevA.31.3093](https://doi.org/10.1103/PhysRevA.31.3093) (cit. on p. 40).



- [59] P. Kwee, J. Miller, T. Isogai, L. Barsotti, and M. Evans. “Decoherence and degradation of squeezed states in quantum filter cavities”. *Phys. Rev. D* 90 (6 Sept. 2014), p. 062006. DOI: [10.1103/PhysRevD.90.062006](https://doi.org/10.1103/PhysRevD.90.062006) (cit. on pp. 41, 56, 131, 133, 134, 139).
- [60] R. E. Slusher, B. Yurke, J. C. Mertz, J. F. Valley, and L. W. Hollberg. “Observation of squeezed states generated by four-wave mixing in an optical cavity”. *Phys. Rev. Lett.* 55.22 (Nov. 1985), 2409–2412. DOI: [10.1103/PhysRevLett.55.2409](https://doi.org/10.1103/PhysRevLett.55.2409) (cit. on p. 42).
- [61] Henning Vahlbruch, Moritz Mehmet, Karsten Danzmann, and Roman Schnabel. “Detection of 15 dB Squeezed States of Light and their Application for the Absolute Calibration of Photoelectric Quantum Efficiency”. *Physical Review Letters* 117 (Sept. 2016). DOI: [10.1103/PhysRevLett.117.110801](https://doi.org/10.1103/PhysRevLett.117.110801) (cit. on pp. 42, 105).
- [62] D. F. Walls and Gerard J. Milburn. *Quantum Optics*. 2008 (cit. on p. 43).
- [63] Jürgen Appel, Dallas Hoffman, Eden Figueroa, and A. I. Lvovsky. “Electronic noise in optical homodyne tomography”. *Phys. Rev. A* 75 (3 Mar. 2007), p. 035802. DOI: [10.1103/PhysRevA.75.035802](https://doi.org/10.1103/PhysRevA.75.035802) (cit. on p. 48).
- [64] Sheila E. Dwyer. “Quantum noise reduction using squeezed states in LIGO”. PhD thesis. 2013 (cit. on pp. 49, 110, 111).
- [65] S. Dwyer, L. Barsotti, S. S. Y. Chua, M. Evans, M. Factourovich, D. Gustafson, T. Isogai, K. Kawabe, A. Khalaidovski, P. K. Lam, M. Landry, N. Mavalvala, D. E. McClelland, G. D. Meadors, C. M. Mow-Lowry, R. Schnabel, R. M. S. Schofield, N. Smith-Lefebvre, M. Stefszky, C. Vorvick, and D. Sigg. “Squeezed quadrature fluctuations in a gravitational wave detector using squeezed light”. *Opt. Express* 21.16 (2013), 19047–19060. DOI: [10.1364/OE.21.019047](https://doi.org/10.1364/OE.21.019047) (cit. on pp. 49, 110).
- [66] Thomas Randall Corbitt. “Quantum noise and radiation pressure effects in high power optical interferometers”. PhD thesis. Massachusetts Institute of Technology, June 2008 (cit. on p. 50).
- [67] H. Kimble, Yuri Levin, Andrey Matsko, Kip Thorne, and Sergey Vyatchanim. “Conversion of conventional gravitational-wave interferometers into quantum non-demolition interferometers by modifying their input and/or output optics”. *Physical review D: Particles and fields* 65 (Dec. 2001). DOI: [10.1103/PhysRevD.65.022002](https://doi.org/10.1103/PhysRevD.65.022002) (cit. on pp. 50, 54, 55, 113, 115).
- [68] Carlton M. Caves. “Quantum-Mechanical Radiation-Pressure Fluctuations in an Interferometer”. *Phys. Rev. Lett.* 45 (2 July 1980), 75–79. DOI: [10.1103/PhysRevLett.45.75](https://doi.org/10.1103/PhysRevLett.45.75) (cit. on pp. 52, 112).
- [69] Carlton M. Caves. “Quantum-mechanical noise in an interferometer”. *Phys. Rev. D* 23 (8 Apr. 1981), 1693–1708. DOI: [10.1103/PhysRevD.23.1693](https://doi.org/10.1103/PhysRevD.23.1693) (cit. on pp. 54, 112).
- [70] J. Abadie et al. “A Gravitational wave observatory operating beyond the quantum shot-noise limit: Squeezed light in application”. *Nature Phys.* 7 (2011), 962–965. DOI: [10.1038/nphys2083](https://doi.org/10.1038/nphys2083) (cit. on p. 59).
- [71] J. Aasi et al. “Enhancing the sensitivity of the LIGO gravitational wave detector by using squeezed states of light”. *Nature Photon.* 7 (2013), 613–619. DOI: [10.1038/nphoton.2013.177](https://doi.org/10.1038/nphoton.2013.177) (cit. on p. 60).

- [72] H. Grote, K. Danzmann, K. L. Dooley, R. Schnabel, J. Slutsky, and H. Vahlbruch. “First Long-Term Application of Squeezed States of Light in a Gravitational-Wave Observatory”. *Phys. Rev. Lett.* 110 (18 2013), p. 181101. DOI: [10.1103/PhysRevLett.110.181101](https://doi.org/10.1103/PhysRevLett.110.181101) (cit. on p. 60).
- [73] Simon Chelkowski, Henning Vahlbruch, Karsten Danzmann, and Roman Schnabel. “Coherent control of broadband vacuum squeezing”. *Physical Review A* 75 (May 2007). DOI: [10.1103/PhysRevA.75.043814](https://doi.org/10.1103/PhysRevA.75.043814) (cit. on pp. 61, 72, 74).
- [74] Jean-Yves Vinet, Violette Brisson, and Stefano Braccini. “Scattered light noise in gravitational wave interferometric detectors: Coherent effects”. *Phys. Rev. D* 54 (2 1996), 1276–1286. DOI: [10.1103/PhysRevD.54.1276](https://doi.org/10.1103/PhysRevD.54.1276) (cit. on p. 64).
- [75] URL: https://websvn.ego-gw.it/listing.php?repname=AdvVirgo&path=%2FAdvSens%2FGWINC_AdV%2F&#a59d067692a7c250112c5686a30d3594c (cit. on pp. 64, 100, 104, 126).
- [76] L. Conti, A. Bertolini, A. Chiummo, S. Chua, I. Fiori, E. Genin, J. Harms, M. Leonardi, G. Pillant, and J.P. Zendri. *Update on stray light noise from AEI squeezer in Adv*. (Cit. on pp. 64, 84).
- [77] Eric Genin, Maddalena Mantovani, Gabriel Pillant, Camilla De Rossi, Laurent Pinard, Christophe Michel, Matthieu Gosselin, and Julia Casanueva. “Vacuum-compatible low-loss Faraday isolator for efficient squeezed-light injection in laser-interferometer-based gravitational-wave detectors”. *Appl. Opt.* 57.32 (2018), 9705–9713. DOI: [10.1364/AO.57.009705](https://doi.org/10.1364/AO.57.009705) (cit. on pp. 64, 65, 104, 105, 136, 181).
- [78] Marco Vardaro. “Toward a fully automated and digitally controlled squeezed vacuum source”. PhD thesis. 2018 (cit. on p. 70).
- [79] Kirk McKenzie, Nicolai Grosse, Warwick Bowen, Stanley Whitcomb, Malcolm Gray, David McClelland, and Ping Koy Lam. “Squeezing in the Audio Gravitational-Wave Detection Band”. *Physical review letters* 93 (Nov. 2004), p. 161105. DOI: [10.1103/PhysRevLett.93.161105](https://doi.org/10.1103/PhysRevLett.93.161105) (cit. on p. 72).
- [80] Henning Vahlbruch, Simon Chelkowski, Boris Hage, Alexander Franzen, Karsten Danzmann, and Roman Schnabel. “Coherent Control of Vacuum Squeezing in the Gravitational-Wave Detection Band”. *Physical review letters* 97.1, 011101 (July 2006), p. 011101. DOI: [10.1103/PhysRevLett.97.011101](https://doi.org/10.1103/PhysRevLett.97.011101) (cit. on p. 72).
- [81] T Accadia et al. “Noise from scattered light in Virgo’s second science run data”. 27.19 (Sept. 2010), p. 194011. DOI: [10.1088/0264-9381/27/19/194011](https://doi.org/10.1088/0264-9381/27/19/194011) (cit. on p. 84).
- [82] F. Acernese, M. Agathos, L. Aiello, Annalisa Allocca, A. Amato, S. Ansoldi, Sarah Antier, M. Arène, N. Arnaud, S. Ascenzi, P. Astone, F. Aubin, Svitlana Babak, Philippe Bacon, Francesca Badaracco, M. K. M Bader, J. Baird, F. Baldaccini, G. Ballardín, and Karsten Danzmann. “Increasing the Astrophysical Reach of the Advanced Virgo Detector via the Application of Squeezed Vacuum States of Light”. *Physical Review Letters* 123 (Dec. 2019). DOI: [10.1103/PhysRevLett.123.231108](https://doi.org/10.1103/PhysRevLett.123.231108) (cit. on pp. 99, 105, 129).



- [83] Sebastian Khan, Sascha Husa, Mark Hannam, Frank Ohme, Michael Pürrer, Xisco Jiménez Forteza, and Alejandro Bohé. “Frequency-domain gravitational waves from nonprecessing black-hole binaries. II. A phenomenological model for the advanced detector era”. *Phys. Rev. D* 93 (4 Feb. 2016), p. 044007. DOI: [10.1103/PhysRevD.93.044007](https://doi.org/10.1103/PhysRevD.93.044007) (cit. on p. 100).
- [84] Jürgen Appel, Dallas Hoffman, Eden Figueroa, and A. I. Lvovsky. “Electronic noise in optical homodyne tomography”. *Phys. Rev. A* 75 (3 Mar. 2007), p. 035802. DOI: [10.1103/PhysRevA.75.035802](https://doi.org/10.1103/PhysRevA.75.035802) (cit. on p. 108).
- [85] F. Acernese et al. “Quantum Backaction on kg-Scale Mirrors: Observation of Radiation Pressure Noise in the Advanced Virgo Detector”. *Phys. Rev. Lett.* 125 (13 Sept. 2020), p. 131101. DOI: [10.1103/PhysRevLett.125.131101](https://doi.org/10.1103/PhysRevLett.125.131101) (cit. on p. 112).
- [86] LIGO Scientific Collaboration. “Quantum-Enhanced Advanced LIGO Detectors in the Era of Gravitational-Wave Astronomy”. *Phys. Rev. Lett.* 123 (23 Dec. 2019), p. 231107. DOI: [10.1103/PhysRevLett.123.231107](https://doi.org/10.1103/PhysRevLett.123.231107) (cit. on p. 112).
- [87] V.B. Braginskii and A. B. Manuki. “Ponderomotive Effects of Electromagnetic Radiation”. *JETP* 26 (1967), p. 831 (cit. on p. 112).
- [88] T. P. Purdy, R. W. Peterson, and C. A. Regal. “Observation of Radiation Pressure Shot Noise on a Macroscopic Object”. *Science* 339.6121 (2013), 801–804. DOI: [10.1126/science.1231282](https://doi.org/10.1126/science.1231282) (cit. on p. 112).
- [89] M. Was, P. Kalmus, J. R. Leong, T. Adams, N. Leroy, D. M. Macleod, C. Pankow, and F. Robinet. “A fixed false alarm probability figure of merit for gravitational wave detectors”. *Classical and Quantum Gravity* 31.8, 085004 (Apr. 2014), p. 085004. DOI: [10.1088/0264-9381/31/8/085004](https://doi.org/10.1088/0264-9381/31/8/085004) (cit. on p. 128).
- [90] Virgo collaboration. URL: <https://wiki.virgo-gw.eu/AdvancedVirgoPlus/WPDpages> (cit. on p. 136).
- [91] Sebastian Khan, Sascha Husa, Mark Hannam, Frank Ohme, Michael Pürrer, Xisco Jiménez Forteza, and Alejandro Bohé. “Frequency-domain gravitational waves from nonprecessing black-hole binaries. II. A phenomenological model for the advanced detector era”. *Phys. Rev. D* 93.4, 044007 (Feb. 2016), p. 044007. DOI: [10.1103/PhysRevD.93.044007](https://doi.org/10.1103/PhysRevD.93.044007) (cit. on p. 147).
- [92] H. Kogelnik and T. Li. “Laser beams and resonators”. *applied optics* 5.10 (1966), p. 1550. DOI: [10.1364/AO.5.001550](https://doi.org/10.1364/AO.5.001550) (cit. on pp. 152, 190).
- [93] D. Z. Anderson. “Alignment of resonant optical cavities”. *Applied Optics* 23.17 (Sept. 1984), 2944–2949. DOI: [10.1364/AO.23.002944](https://doi.org/10.1364/AO.23.002944) (cit. on p. 153).
- [94] Nicholas Straniero, Jérôme Degallaix, Raffaele Flaminio, Laurent Pinard, and Gianpietro Cagnoli. “Realistic loss estimation due to the mirror surfaces in a 10 meters-long high finesse Fabry-Perot filter-cavity”. *Optics Express* 23 (Aug. 2015), p. 21455. DOI: [10.1364/OE.23.021455](https://doi.org/10.1364/OE.23.021455) (cit. on p. 158).
- [95] J. C. Stover. *Optical Scattering: Measurement and Analysis, Third Edition*. SPIE Press Book, 2012. DOI: [10.1117/3.975276](https://doi.org/10.1117/3.975276) (cit. on p. 158).
- [96] R. Bonnand J. Degallaix M. Galimberti and Q. Benoit. *Defining the arm cavity loss for Advanced Virgo* (cit. on pp. 161, 166).

- [97] Jérôme Degallaix. “OSCAR a Matlab based optical FFT code”. *Journal of Physics: Conference Series* 228 (July 2010), p. 012021. DOI: [10.1088/1742-6596/228/1/012021](https://doi.org/10.1088/1742-6596/228/1/012021) (cit. on p. 162).
- [98] Eleonora Capocasa, Matteo Barsuglia, Jérôme Degallaix, Laurent Pinard, Nicholas Straniero, Roman Schnabel, Kentaro Somiya, Yoichi Aso, Daisuke Tatsumi, and Raffaele Flaminio. “Estimation of losses in a 300 m filter cavity and quantum noise reduction in the KAGRA gravitational-wave detector”. *Physical Review D* 93 (Apr. 2016). DOI: [10.1103/PhysRevD.93.082004](https://doi.org/10.1103/PhysRevD.93.082004) (cit. on pp. 164, 168, 173, 205).
- [99] E. Marchetti, M. Mazzoni, and I. Fiori. *Seismic investigation of the response of the 3 km arms of Virgo Interferometer*. URL: <https://tds.ego-gw.it/?content=3&r=1594> (cit. on p. 177).
- [100] Yuhang Zhao, Naoki Aritomi, Eleonora Capocasa, Matteo Leonardi, Marc Eisenmann, Yuefan Guo, Eleonora Polini, Akihiro Tomura, Koji Arai, Yoichi Aso, Yao-Chin Huang, Ray-Kuang Lee, Harald Lück, Osamu Miyakawa, Pierre Prat, Ayaka Shoda, Matteo Tacca, Ryutaro Takahashi, Henning Vahlbruch, and Raffaele Flaminio. “Frequency-Dependent Squeezed Vacuum Source for Broadband Quantum Noise Reduction in Advanced Gravitational-Wave Detectors”. *Physical Review Letters* 124 (Apr. 2020). DOI: [10.1103/PhysRevLett.124.171101](https://doi.org/10.1103/PhysRevLett.124.171101) (cit. on pp. 183–185).
- [101] Eric D. Black. “An introduction to Pound–Drever–Hall laser frequency stabilization”. *American Journal of Physics* 69.1 (2001), 79–87. DOI: [10.1119/1.1286663](https://doi.org/10.1119/1.1286663) (cit. on pp. 183, 184).
- [102] R. Schilling. “OPTOCAD: Tracing Gaussian TEM00 beams through an optical set-up” () (cit. on pp. 190, 192, 194).
- [103] The VIRGO Collaboration et al. “The VIRGO large mirrors: a challenge for low loss coatings”. *Classical and Quantum Gravity* 21.5 (Feb. 2004), S935–S945. DOI: [10.1088/0264-9381/21/5/083](https://doi.org/10.1088/0264-9381/21/5/083) (cit. on p. 203).
- [104] H.A. Macleod. *Thin-film optical filters*. Boca Raton: CRC Press, 2001. DOI: <https://doi.org/10.1201/9781420033236> (cit. on p. 203).
- [105] M. Evans, S. Ballmer, M. Fejer, P. Fritschel, G. Harry, and G. Ogin. “Thermo-optic noise in coated mirrors for high-precision optical measurements”. *Phys. Rev. D* 78 (2008), p. 102003. DOI: [10.1103/PhysRevD.78.102003](https://doi.org/10.1103/PhysRevD.78.102003) (cit. on p. 204).



